Bose-Einstein Condensation and Superfluidity in Two Dimensions

Richard Jonathan Fletcher
Trinity College

This dissertation is submitted for the degree of
Doctor of Philosophy

April 2015
Department of Physics

UNIVERSITY OF
CAMBRIDGE

To my parents Nick and Mary, my sister Liz and my brother Will.

Declaration

I declare that this thesis is my own work and is not substantially the same as any that I have submitted or am currently submitting for a degree, diploma or any other qualification at any other university. No part of this thesis has already been or is being concurrently submitted for any such degree, diploma or any other qualification. This thesis does not exceed the word limit of sixty thousand words, including tables, footnotes, bibliography and appendices, set out by the Faculty of Physics and Chemistry.

Abstract

It was known as early as 1934 that crystallisation is precluded in two dimensions. The requisite long-range order is destroyed by thermal fluctuations at any non-zero temperature, and therefore ordered phases such as a Bose-Einstein condensate (BEC) cannot exist in a uniform two-dimensional system. However, below a non-zero critical temperature a two-dimensional Bose fluid becomes superfluid, despite absence of the long-range coherence normally associated with this phenomenon. Remarkably, no symmetry is broken, but a topological order emerges which is sufficient to support superfluid behaviour; this Berezinskii-Kosterlitz-Thouless (BKT) transition is driven by the suppression of vortices, topological defects in the system phase.

Ultracold atomic gases offer an ideal system for addressing the low-temperature properties of a Bose fluid. Coherence properties are conveniently revealed in the atomic momentum distribution, flexible trapping geometries can be engineered using light potentials, interactions between atoms are sufficiently weak to allow a tractable theoretical description and crucially the interaction strength may be tuned via molecular resonances. Whilst in a uniform system the BKT transition is the sole low-temperature phenomenon, most experiments with ultracold atoms employ a harmonic trapping potential, which modifies the density of states and restores the possibility of conventional BEC in the ideal gas limit. Whether the low-temperature transition is BEC- or BKT-like, at the critical point one anticipates a sharp growth in the extent of coherence.

In the first part of this thesis, we offer some theoretical discussion of the low-temperature phase transitions in a two-dimensional Bose fluid, first in the context of a uniform trapping potential and subsequently extending this treatment to harmonic confinement. In addition to overviewing pure-two-dimensional physics, we explore to what extent residual excitations in the restricted dimension should modify behaviour.

The second part concerns an experimental work, in which we engineer a harmonically-trapped two-dimensional Bose gas with tuneable interactions, identify the onset of extended coherence over a decade of interaction strength, and show that the interaction-driven BKT transition smoothly converges onto the purely quantum-statistical BEC transition in the limit of vanishing interactions. Furthermore, we validate the predictions of a classical-field approach for the BKT critical point, which models the non-perturbative behaviour of interacting bosons using a tur-

bulent matter wave.

Acknowledgements

Very few theses represent the isolated efforts of a lone author, and it is a great pleasure to thank those who have helped, enabled and supported me over the preceding four years and acknowledge their part in this work. Foremost amongst these is Zoran, who has been an ever-present figure in my academic life since 2007. It has been a long journey from his initial casual offer of a summer placement to the completion of this thesis, and Zoran's boundless enthusiasm, sage advice and generous encouragement have been a constant and unwavering feature in this. In my opinion, one of the great features of the group is that members are judged solely on their input and efforts; merit always wins over seniority, and an undergraduate on a summer placement is taken as seriously as a wise elder, if they have something useful to say. This attitude largely (but not solely) originates with Zoran, and makes the lab a fresh, exciting and dynamic place to work.

Almost as consistent a figure has been Rob, who took Alex and me under his wing upon our arrival in the group. From the beginning Rob treated us with admirable patience and as academic equals (at least in Alex's case entirely justifiably), which retrospectively seems entirely ludicrous as I stumbled my way through the first term of work on superheating BECs. Since then I hope that my abilities have matured somewhat, but Rob's kind, helpful and ridiculously proficient input have been a continual font of support and progress.

Alex and I started our PhDs together, and we enjoyed countless discussions gradually, but not usually irrevocably, convincing ourselves we understood nothing about physics. His willingness to get to the heart of matters rather than accept dogmatic statement in place of understanding was a breath of fresh air. He has also been my (semi-voluntary) full-time consultant on all computing matters, and I hope he will forgive the endless teasing regarding his devotion to Microsoft, in which he remains steadfast despite ridicule, persecution and empirical evidence.

The previous year and a half has academically been dominated by work with Nir and Martin. Nir and I took the first 2D steps together, installing the new light and learning how to wield it. Working with him is fantastically good fun; the heady mixture of physics, Rocky clips, debate over food, wine, music and dinners, stories of mountains and snow and obsessing over the coffee machine makes 'being at work' something of a misnomer. He has been a strong influence on the evolution of my attitudes to science, research and 'living the good life'. Martin was my

teammate for the BKT experiment which constitutes this thesis, and which I sincerely doubt would exist without him. His steadfast enthusiasm, experimental talent and refusal to admit despair or frustration have been invaluable, and in addition he is one of the kindest people one could hope to meet. As another permanent feature of my PhD, I am also extremely grateful to our group secretary Pam, who dealt admirably with all the lost invoices, confused emails and last-minute requests I could muster.

I have been fortunate to spend at least part of my time overlapping with various group members who have passed on (to greater things), all of whom improved life in some way. Naaman and Robbie were endlessly willing to help out a hapless undergraduate, and largely built the machine which allowed my own work to happen. Stuart and Scott welcomed me into the ring team; a cynic would suggest that a willing new graduate student was exactly what an experiment demanding unreasonable levels of menial labour demanded, but I choose to adopt a more charitable view and thank them for adopting me onto their project in my early days, essentially teaching me everything I know about the machine, and being willing competitors in numerous games and challenges.

In addition to our lab, rumours swirled of another experiment across the narrow sea; ruled by Toby and Igor, it was a strange and exotic world of pull-up bars, balance boards and well-organised, neatly labelled, well-stocked cupboards. I pillaged more of their supplies than I care to admit, talked of life and science with Toby over coffee of varying quality but boundless quantity, and marvelled at Igor's tales of cliffs, ravines and the high seas. Aziza was with us for only a year, but her contribution is a cycle time a full minute faster than the old machine. The new generation of students, Jay, Konrad and Christoph are already making their mark. Jay had the pleasure(?) of joining the 2D experiment partway through and single-handedly set up the high-field imaging light, with little more than vague assertions that 'it's probably doable' to guide her. Konrad joined more recently and immediately threw himself into paper discussions (even at version 20+, which is an accolade few can claim), whilst installing our new Bragg setup. Christoph inhabits the 'new machine', and given their rate of progress must be doing a sterling job.

Despite what some might claim (new students look away now), life does persist outside of the lab and mine was populated by people who made my graduate years rich, absorbing and superbly good fun. There are too many to attempt to list here, partially for fear of omission but principally for the inability to do people justice. The life of formals, feasts, brunches, BA events, breakfast club, Portugal Street parties, cycling adventures, ski trips and gents rowing was a good one, and I thank all those who lived it with me.

The only, and outstanding, exception to this blanket omission is Sun. She offers, without conditions or demands, a seemingly inexhaustible source of compassion, care and support, and has listened with astounding humour to more rants about lasers, air-conditioning units and Matlab than any person has any right to expect. She has been my partner on innumerable exploits, schemes and adventures, and

I'm immensely fortunate to have her in my life.

Finally, and surpassing all others, I thank my family: my parents Nick and Mary, my sister Liz, and my brother Will. It feels trivial and absurd to attempt to elucidate anything specific; their impact on my life cannot be quantified. A certainty is that without their unconditional love, belief and support my life would be incomparably poorer, and this thesis is as much theirs as mine.

Contents

What is a scientist after all?
It is a curious man looking through a keyhole,
the keyhole of nature,
trying to know what's going on.

JACQUES YVES COUSTEAU

Chapter 1

Introduction

Quantum mechanics can have a somewhat undeserved reputation; it is the physics of the microscopic, the esoteric, the unfamiliar. But regardless of their ability to shock and surprise, many-body interacting quantum systems constitute the universe we inhabit and consequently understanding their physics is of both fundamental and practical importance. Remarkably, whilst the richness of observed quantum phenomena seems almost limitless - from superconductivity in MRI magnets to quantum magnetism, stability of neutron stars to behaviour of the quark-gluon plasma - such apparent diversity arises from the interplay of very few ingredients; quantum statistics, the form and strength of the inter-particle interactions, temperature, gauge fields and any external potentials.

Many of these interesting behaviours arise out of the interactions between particles. In an ideal gas, every constituent member follows a single-particle trajectory, and the behaviour of the whole cannot be more than the sum of its parts. Once interactions are introduced, the concept of collective behaviour becomes meaningful, whereby a macroscopic phenomenon such as superfluidity emerges from the complexity of the underlying microscopic physics. One of the great goals of modern physics is to elucidate how this emergence occurs.

There is however an inherent difficulty in both theoretical and computational approaches to this question. Theoretically, the high densities of real-world quantum systems create great difficulties; interactions between particles are strong, of various and complicated forms, and are generally many-body. Computationally, it is extremely demanding to simulate many-particle quantum systems of even modest size. Whereas the state-vector of an N-particle classical system has length $6N$, a quantum system of N particles each with M possible states requires M^N complex numbers to specify its state completely, which rapidly becomes computationally infeasible[1].

---

[1] As a concrete example, the state of 3 spin-1/2 particles is naturally written in the basis $|\psi\rangle = c_1|\uparrow\uparrow\uparrow\rangle + c_2|\uparrow\uparrow\downarrow\rangle + c_3|\uparrow\downarrow\uparrow\rangle ...$ which could be denoted by a 8-dimensional vector c_n. For N particles, the length of c_n would be 2^N. Assuming that storage of a complex number involves ~ 10 bytes, the quantum state of $N = 100$ spins would consume 10^{19} TB.

Ultracold Gases as Quantum Simulators

A measure of the importance of quantum behaviour is provided by the phase-space density $\mathcal{D} = n\lambda_{\mathrm{th}}^3$, where n is the particle number density and $\lambda_{\mathrm{th}} = h/\sqrt{2\pi m k_{\mathrm{B}} T}$ is the thermal wavelength associated with a particle of mass m at temperature T. This approximately corresponds to the occupation of individual states, and hence quantum statistics become relevant for $\mathcal{D} \gtrsim 1$. In macroscopic, 'real-world' quantum systems such as liquid He or the electron sea in a metal, $n \sim 10^{29}$ m^{-3}, and the onset of quantum behaviour occurs at relatively high characteristic temperatures of ~ 10 K and $\sim 10^4$ K respectively[1].

In ultracold atomic gases, one can access this same quantum limit of $\mathcal{D} \gg 1$, but at much lower densities, and commensurately lower temperatures of order 100 nK. This enables many-body quantum phenomena to be addressed at densities $\sim 10^{10}$ times lower than real-world systems; as will be outlined in the next Section, this greatly simplifies the treatment of interactions, permitting tractable theoretical progress. Furthermore, the control and tuneability afforded by these systems make them ideal 'simulators' of quantum physics [1]. Intricate sculpting of optical and magnetic fields create arbitrary confining potentials, interactions may be tuned by means of molecular resonances [2], and the recent advent of artificial gauge potentials enables neutral atoms to effectively behave as particles of arbitrary charge subjected to electromagnetic fields [3]. In the spirit of the quantum simulator envisaged by Feynman [4], the philosophy is to engineer custom Hamiltonians and observe the subsequent behaviour in a clean, controllable and addressable environment.

The exquisite control over geometry and interactions afforded by the techniques of ultracold atomic gases has enabled researchers to address a wide variety of interesting quantum states. Bose-Einstein condensation (BEC) was first observed in 1995 [5], and requires the fewest ingredients, being driven purely by quantum statistics. Once the complications of geometry and interactions are included, numerous phase transitions are possible, including the superfluid-to-Mott insulator [6], normal-to-superfluid [7–9], Anderson localisation [10], and the Dicke transition [11].

Tuning Interactions

One of the most important tools in the ultracold atom arsenal is the ability to arbitrarily tune the strength and sign of interactions between atoms. The quantum-mechanical problem of scattering is in general rather involved. If two atoms located at $\mathbf{r}_1$ and $\mathbf{r}_2$ interact via a potential $V(\mathbf{r}_2 - \mathbf{r}_1)$, the natural coordinates are centre-of-mass position $\mathbf{R}$ and relative position $\mathbf{r}$. The overall wavefunction straightforwardly takes the separable form $\Psi(\mathbf{r}, \mathbf{R}) = \exp(i\mathbf{K} \cdot \mathbf{R})\psi(\mathbf{r})$, where $\mathbf{K}$

---

[1] For a more extreme example, the number density inside a neutron star is $n \sim 10^{44}$ m^{-3}, meaning that quantum behaviour is dominant for temperatures below 10^{12} K!

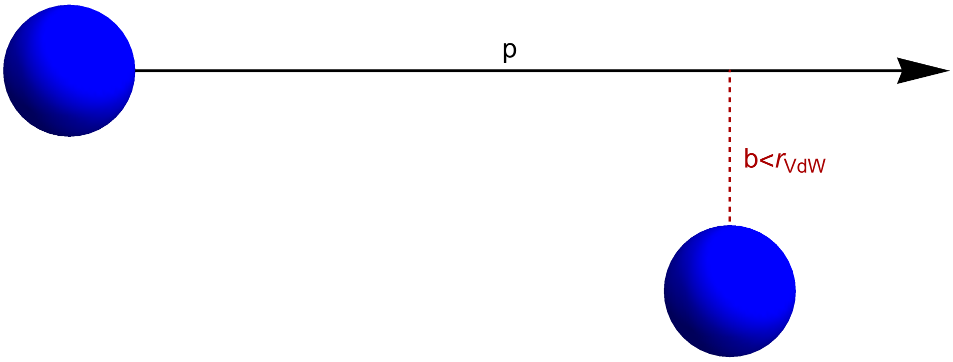

Figure 1.1: *Two atoms colliding. In order to interact, their impact parameter b must be smaller than the range of interaction r_{VdW}. This limits collisional angular momentum to $L \lesssim pr_{VdW}$, where p is the typical atomic momentum.*

is the centre-of-mass wavevector, and the relative wavefunction ψ is the solution to the time-independent Schrödinger equation

$$\left[\frac{-\hbar^2}{2\mu}\nabla^2_{\mathbf{r}} + V(\mathbf{r})\right]\psi(\mathbf{r}) = E\psi(\mathbf{r}), \tag{1.1}$$

where $\mu = m/2$ is the reduced mass. In general, the potential $V(\mathbf{r})$ may be rather complex; however, the interatomic potentials via which ultracold gases interact have two properties that afford a simplified approach.

1. The Van der Waals scattering potentials are short-ranged, falling faster than r^{-1} [12].

2. Collisional energies are sufficiently low that the scattering wavefunction contains an extremely small contribution from $l > 0$ angular momentum states[1]. For two particles colliding with momentum p and impact parameter b, their relative angular momentum is $L = pb$; this is illustrated in Fig 1.1. For interaction range r_0, the relative momentum necessary to appreciably admix states with $l > 0$ into the scattering wavefunction is

$$p \gtrsim \frac{\hbar}{r_0}. \tag{1.2}$$

   For typical interactions ranges[2] of $\sim 100\ a_0$, where a_0 is the Bohr radius, this momentum scale corresponds to temperatures of $T \gtrsim 100\ \mu$K. This is larger than typical temperatures in ultracold gases by a factor $\sim 10^3$, and scattering is dominated by the s-wave channel $l = 0$.

---

[1] Eigenstates of the angular momentum operator $\hat{L}^2$ labelled by quantum number l.
[2] For ^{39}K, the Van der Waals radius $r_{\text{VdW}} = 64\ a_0$ [13].

The scattering length If both simplifying assumptions are valid, far from the scattering centre at $r = 0$ the wavefunction ψ takes the form

$$\psi(\mathbf{r}) \approx \underbrace{e^{ikz}}_{\substack{\text{Incident}\\ \text{plane wave}}} + \underbrace{\frac{f}{r}e^{ikr}}_{\substack{\text{Scattered}\\ \text{spherical wave}}} . \tag{1.3}$$

An unperturbed plane wave $\exp(ikz)$ contains an admixture of l-components, with $l = \{0, 1, 2...\}$. In general, each component is modified by the presence of a potential, resulting in an outgoing scattered wave with amplitude and phase encoded in the scattering amplitude $f(\theta, \phi)$. If scattering is s-wave then only the $l = 0$ component is coupled into the scattered wave, which is consequently spherically-symmetric. Furthermore, in the case of elastic scattering the only effect of a potential can be to impart a phase shift δ on the $l = 0$ component.

A phase shift is dimensionless; the incident plane wave provides an associated wavevector k, and so the scattering potential must be characterised by a *scattering length* a, defined as

$$\lim_{k \to 0} k \cot \delta = -\frac{1}{a}. \tag{1.4}$$

The scattering amplitude is related to the phase-shift δ via[1]

$$\begin{aligned} f &= \frac{1}{k} e^{i\delta} \sin \delta, \\ &= \frac{-a}{1 + ika}. \end{aligned} \tag{1.5}$$

The scattering potential, which in general may be extremely complex, is thus parametrised by a single scalar parameter a. Furthermore, *any* two potentials characterised by the same value of a will result in completely identical behaviour, regardless of how different their specific functional forms are[2]. The ability to replace the complicated actual potential $V(\mathbf{r})$ by a simplified model potential greatly facilitates tractable theoretical descriptions of many-body, interacting quantum systems, and is a tremendous advantage of ultracold atomic systems.

Feshbach resonances The scattering length a is thus simply set by the phase shift δ imparted by a scattering potential. In ultracold gases one may tune δ via a Feshbach resonance [2], whereby two free atoms in one spin state are brought into resonance with a bound molecule in another spin state. Since different spin states possess different magnetic moments, the relative energy of the two can be tuned simply by application of a uniform magnetic field, and the scattering phase

---

[1] This is calculated within the theoretical framework of partial-wave decomposition, see for example [14].

[2] Typically one considers contact interactions $V(\mathbf{r}) = g\delta(\mathbf{r})$, where the coupling constant $g = 4\pi\hbar^2 a/m$ [12].

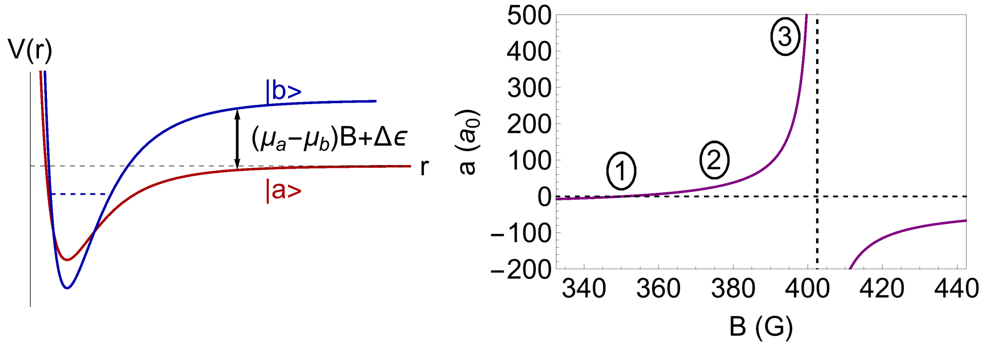

Figure 1.2: *A Feshbach resonance. On the left is the interatomic potential $V(r)$ for two-particle spin states $|a\rangle$ and $|b\rangle$, which have energy difference $\Delta\varepsilon$ at zero magnetic field. We assume the atoms are in state $|a\rangle$; a magnetic field can be used to tune the difference between the free-atom energy (dashed black line) and bound molecular state (dashed blue line). In the vicinity of the resonance a can take any value, illustrated on the left for a resonance at 402.5 G in the $|4\ {}^2S_{1/2}, F=1, m_F=1\rangle$ state of ^{39}K.*

---

shift set to an arbitrary value. In the vicinity of a resonance, the scattering length varies with field strength B according to

$$a(B) = a_\infty \left(1 - \frac{\Delta}{B - B_0}\right), \tag{1.6}$$

where a_∞ is the scattering length far from the resonance, which is located at B_0 and has width Δ. In our experiment we employ a resonance exhibited by ^{39}K in the hyperfine state $|4\ {}^2S_{1/2}, F=1, m_F=1\rangle$, for which these parameters are $a_\infty = -29\ a_0$, $B_0 = 402.5$ G and $\Delta = 52$ G [15, 16]. This B-dependence is illustrated in Fig. 1.2.

This flexibility allows all interaction regimes - from non-interacting, to attractive, to repulsive - to be addressed in a highly controllable manner, within a single experimental arena. Over the course of my PhD, working with ^{39}K in a variety of trapping geometries I addressed interaction-driven physics in various regions of Fig. 1.2, indicated by circled numerals; an overview of these works [17–19] is given in the next Section.

This Thesis

The principal topic of this thesis concerns the nature of the low-temperature phases exhibited by a two-dimensional Bose system. Low-temperature phase transitions are commonly associated with the appearance of some order in a system. When water freezes into ice, the previously random and chaotic arrangement of molecules is replaced by a regular configurational order. Likewise, more exotic transitions display comparable behaviour; BEC is characterised by a global phase coherence and magnetism results from a regular ordering of spins.

In a harmonically-trapped two-dimensional gas, tuning interactions can qualitatively change the nature of this transition. For an interacting gas, the emergence of a topological order below some critical temperature gives rise to superfluidity, mediated by the Berezinskii-Kosterlitz-Thouless (BKT) transition, whereas BEC is precluded by the requisite critical density being infinite. On the other hand, an ideal gas cannot exhibit superfluid dynamics, but can undergo BEC resulting in a homogeneous phase. Using a harmonically-trapped two-dimensional Bose gas, we identify the low-temperature phase transition over a decade of interaction strengths, and show that the interaction-driven BKT transition smoothly converges onto the purely quantum-statistical BEC transition in the limit of vanishing interactions; this corresponds to region ② of Fig. 1.2 [19].

In addition to this work, during my PhD we also addressed two extreme interaction regimes in a three-dimensional gas, denoted by regions ① and ③. The ability to entirely switch off interactions grants access to the ideal gas limit in which momentum states are decoupled from each other, prohibiting the redistribution of particles in response to changing global variables such as energy and number. We were able to engineer a 'superheated' BEC which was decoupled from the surrounding thermal reservoir, persisting at temperatures much higher than the critical temperature [17].

In the opposite limit, turning attention to the strongest interactions allowed by quantum mechanics we accessed the unitary regime; rather than interactions becoming ever more important, one in fact observes an emergence of universal physics where the exact strength of interactions becomes irrelevant [18]. These two works on tuneable interactions in a three-dimensional gas are briefly summarised below, before we turn our attention to two-dimensional physics for the remainder of this thesis.

All papers resulting from my PhD work, including a study of the effect of spinor degrees of freedom on the stability of superfluid flow [20, 21], are presented for completeness in Appendix A.

Stability of a Unitary Bose Gas *Richard J. Fletcher, Alexander L. Gaunt, Nir Navon, Robert P. Smith, and Zoran Hadzibabic*

The scattering length, which provides a lengthscale for all interaction-driven behaviour of a system, can be tuned to arbitrarily large values close to a Feshbach resonance. Rather than interactions becoming ever more important, as a diverges the scattering amplitude $f \to i/k$. Quite remarkably, in the limit of the strongest interactions allowed by quantum mechanics, one uncovers a situation where no details whatsoever of the interaction potential appear in any system description.

This is illustrated in Fig. 1.3, which shows the probability density $|\psi|^2$ of Eq. (1.3) around a scattering potential, along with the s-wave component $|\psi_{l=0}|$ for ka =0.2, 1 and 1000. As the scattering length increases, both the strength of scattering and the phase shift δ rise commensurately. However, for $ka \gtrsim 1$ the dependence

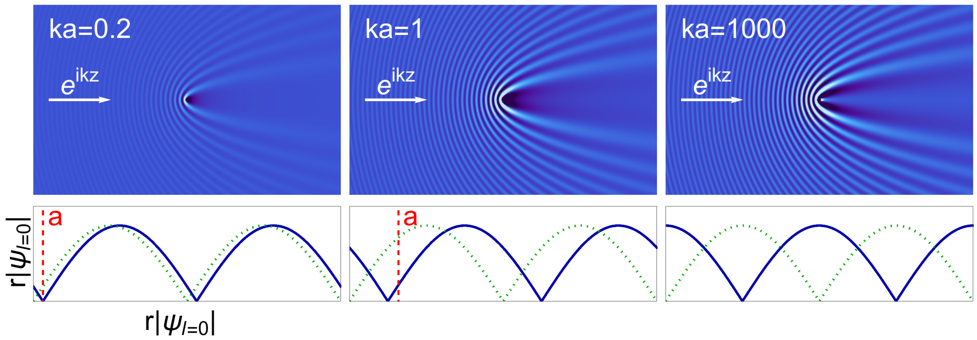

Figure 1.3: *The relative-coordinate wavefunction $\psi(r)$ in the vicinity of a scattering potential. The density plots depict $|\psi|^2$ in the plane $y = 0$, with the colour range corresponding to modulations of $\pm 20\%$ compared to an unperturbed plane wave. The line plots show the $l = 0$ component $|\psi_{l=0}|$ of both an unpertubed plane wave (dotted green line) and the wavefunction of Eq. (1.3) (solid blue line). The vertical red lines mark the scattering length a. With increasing ka, initially the strength of wavefunction modulation and phase shift both rise. As ka exceeds unity, the system remains frozen; behaviour is 'unitarity limited'.*

---

on a vanishes, and ψ remains static, being set purely by the wavevector k. In this *unitary limit*, for a thermal gas the diverging a is replaced by the natural lengthscale λ_{th} [22–25].

In a degenerate gas, the interparticle spacing $n^{-1/3}$ provides the natural lengthscale at which the scattering length saturates [26–29]. This can also be viewed as a competition of energy scales [22]; the characteristic energy of a thermal gas is $k_B T \sim \hbar^2/(m\lambda_{\text{th}}^2)$, whereas for a degenerate gas it is interaction energy $\hbar^2 an/m$. These exceed the energy scale associated with the scattering length $\hbar^2/(ma^2)$ when $a \gtrsim \lambda_{\text{th}}$ and $a \gtrsim n^{-1/3}$ respectively.

The irrelevance of interaction strength in this regime leaves λ_{th} or $n^{-1/3}$ as the only lengthscale that can appear in the system description, and behaviour is set by simple parameters such as temperature or density; in this sense the physics becomes universal. For example, in a degenerate unitary Bose gas one should observe an effective 'fermionization', in which density sets all energy, time and lengthscales [26–29], and the equation of state becomes that of an ideal Fermi gas [26–28, 30]

Over the past decade, there has been extensive theoretical and experimental work concerning the unitary Fermi gas [31]. In the vicinity of a Feshbach resonance one observes a crossover between a BCS superfluid of momentum-paired fermions, and a BEC of fermionic molecules. Despite extensive theoretical interest [22, 24–28, 32–41], experimental studies of the unitary Bose gas have been more limited [25, 29, 30, 42–44]. This is principally due to an inherent instability of such systems; whilst two-body collisions are necessarily elastic due to energy and momentum conservation, three bosons can react to form a tightly-bound molecule and a free atom. The energy released in the process leads to heating of the gas, and generally

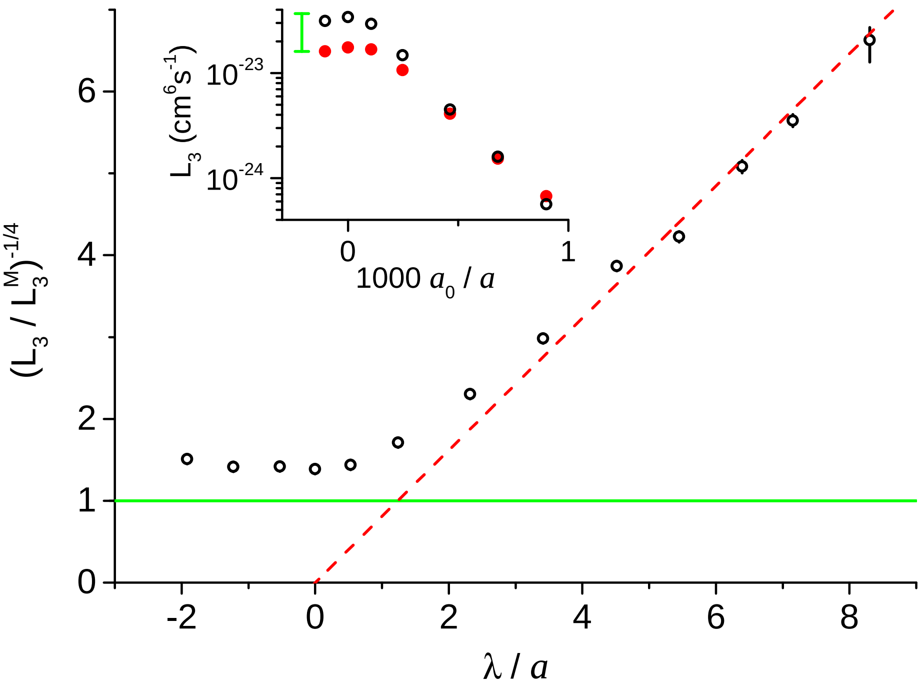

Figure 1.4: *The three-body loss coefficient L_3, scaled to the theoretical unitarity-limited upper bound L_3^M [25] (green line). Away from unitarity L_3 displays the anticipated a^4 scaling (red line), before saturating at $\sim 30\%$ of the upper limit. Inset is a plot of L_3 as a function of a for two different temperatures; as unitarity is approached, losses exhibit a temperature-dependent saturation.*

---

ejects all participants from a trapped sample. The rate of recombination rises as a^4 [45], dramatically shortening attainable lifetimes as the enticing unitary regime is approached.

In this study we measured the general scaling laws relating the particle-loss and heating rates to the temperature, scattering length, and atom number. The three-body loss coefficient is defined as $L_3 = -\dot{N}/(\langle n^2 \rangle N)$, where N is the total atom number and $\langle ... \rangle$ denotes an average over a trapped gas. In addition to confirming the $L_3 \propto a^4$ scaling for $a \ll \lambda_{\text{th}}$, in the regime $a \gtrsim \lambda_{\text{th}}$ we confirm for the first time the expected saturation at a unitarity-limited upper bound $L_3 \propto T^{-2}$, illustrated in Fig. 1.4. This is a dramatic manifestation of universal physics, in which temperature rather than interaction strength controls a fundamentally interaction-driven process. Furthermore, species-specific Efimov physics [25] are found to give a unitarity-limited L_3 three times lower than the theoretical upper bound, making ^{39}K particularly promising for studies of unitary physics in the Bose gas.

Additionally, we characterise the recombination heating of the gas in various interaction regimes, discerning the effect of molecular state binding energy and unitarity-enhanced losses for low-momentum atoms. Our work is one of the first experimental efforts to address the stability of the unitary Bose gas [25, 29].

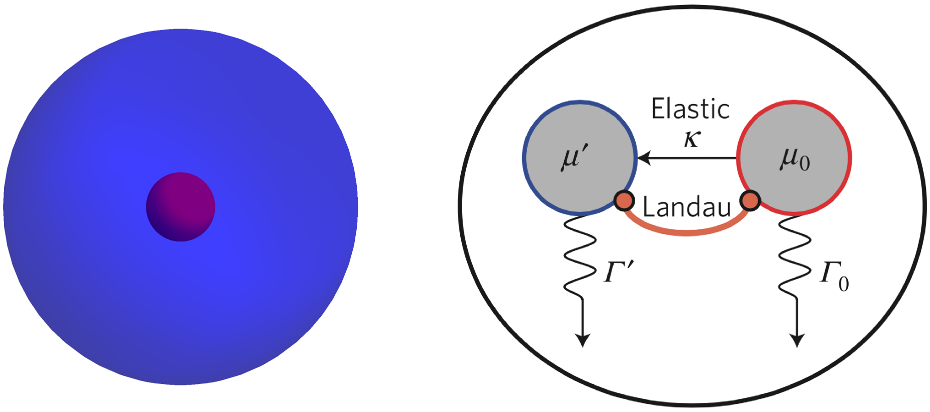

Figure 1.5: *A partially-condensed Bose gas, which can be viewed as two coupled subsystems; a BEC and thermal reservoir, with chemical potentials μ_0 and μ' respectively. Kinetic equilibrium is mediated by Landau damping, whereby the population of collective BEC excitations comes to thermal equilibrium with the surrounding thermal bath. However, phase equilibrium is achieved via elastic scattering, which redistributes particles amongst states. Each subsystem also experiences some inelastic loss rate Γ.*

A Superheated Bose-Condensed Gas _Alexander L. Gaunt*, Richard J. Fletcher*, Robert P. Smith, and Zoran Hadzibabic_

Formulating a quantitative description of systems containing very many particles might at first seems rather daunting. However, statistical physics turns this complexity to its advantage, concerning itself with the average behaviour of an ensemble rather than particular constituents. The ergodic hypothesis posits that a system explores all available[1] microscopic configurations equally; this effective averaging over individual arrangements means that whilst the behaviour of a *single* particle within an ensemble might be beyond theoretical reach, the physics of the system as a whole follows simple, powerful relations.

The study of non-equilibrium processes is a major challenge, since they do not obviously exhibit simple, universal governing laws. A familiar example of a non-equilibrium system is superheated water; in the absence of nucleation centres, water may be heated to $T > T_\mathrm{c} = 100°\mathrm{C}$ whilst remaining liquid. The water, and the surrounding environment, can be viewed as two subsystems in mutual kinetic equilibrium, both being characterised by the same temperature $T > T_\mathrm{c}$. However, the system is not in global phase equilibrium, since the phase transition from water to steam is energetically inhibited.

Cold atomic gases are ideal for studies of non-equilibrium physics. The distribution of particles amongst energy states is easily accessible via the momentum distribution, and interactions can be tuned by molecular resonances. In this

---

[1] Under the appropriate constraints, for example conservation of particle number or energy.

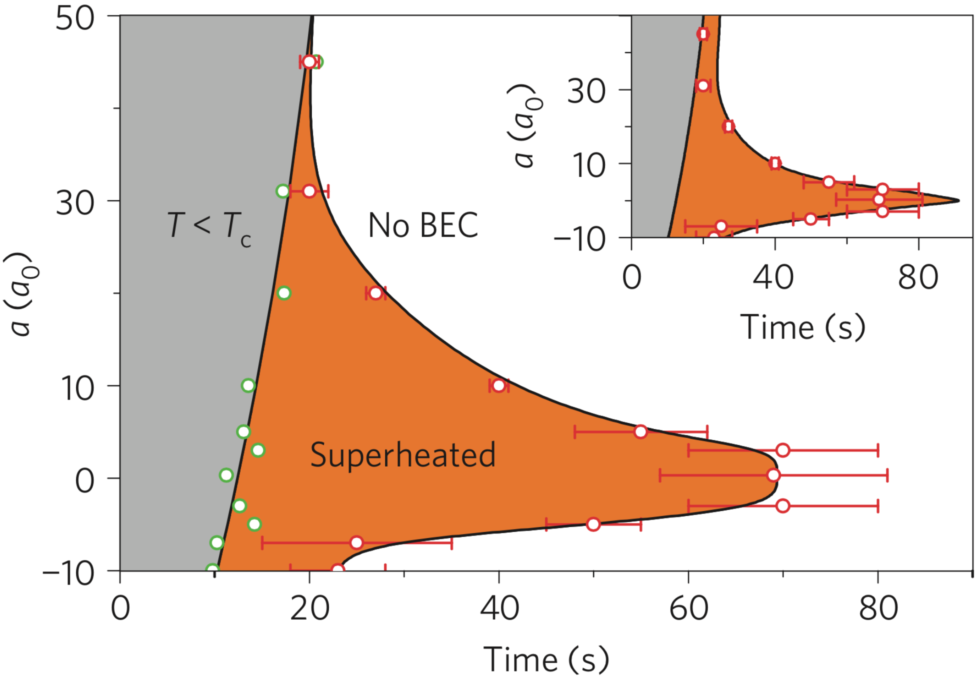

Figure 1.6: *Temporal phase diagram. For each value of a we plot the equilibrium time at which the BEC should vanish (green points) and the time at which the BEC actually vanishes (red points). Solid curves are spline fits to the data. For $a \approx 0$ the BEC survives in the superheated regime for a whole minute. The inset shows the results of numerical calculation which simulates the gas as two partially-decoupled subsystems, and reproduces our data (red points) extremely well.*

experiment, a gas of ^{39}K in the vicinity of a Feshbach resonance was used to demonstrate dynamic stalling of a continuous phase transition. We initially prepare a partially-condensed gas, before rapidly reducing the interaction strength to a low value. In the subsequent evolution, the energy-per-particle rises through light scattering, and atoms are lost via background gas collisions and three-body recombination.

One can view the Bose gas as two subsystems; a BEC, and the surrounding thermal reservoir, illustrated in Fig. 1.5. These are coupled in two ways, both dependent on the scattering length a. First, the kinetic thermal equilibrium between the collective excitations in the BEC (phonons) and the thermal bath is ensured by Landau damping, whose rate is $\propto \sqrt{a}$ [12, 46]. Second, elastic scattering mediates the redistribution of particles amongst momentum states in response to changing global parameters and drives global phase equilibrium, at a rate $\propto a^2$ [47]. The different rate scalings enable one to engineer a superheated Bose-condensed gas, which displays kinetic, but not phase, equilibrium. The BEC and thermal bath are both at the same temperature $T > T_c$, but the condensed fraction remains non-zero.

The lack of phase equilibrium is manifested as different chemical potentials for each component. Remarkably, these are observed to diverge with time, meaning that we are not simply observing a relaxation towards equilibrium, but rather a persistent out-of-equilibrium state in which a coherent object is protected against annihilation by the closure of its decay channel. In Fig. 1.6 we show a temporal phase diagram, indicating the time at which the BEC would vanish in an equilibrium system (green points), and the time at which the observed condensed fraction reaches zero (red points). At our lowest interaction strengths we observe a BEC persisting into the superheated regime for up to minute. In terms of temperature, the weakest-interacting systems display a BEC up to temperatures $T \approx 1.5T_\mathrm{c}$, equivalent to water remaining in a liquid state at 287°C.

Chapter 2

Low-Temperature Phases in Two Dimensions

It was known as early as 1934 [48] that crystallisation is precluded in two dimensions. The requisite long-range order (LRO) is destroyed by thermal fluctuations at any non-zero temperature; this is formalised as the Mermin-Wagner theorem [49], and implies that ordered phases such as BEC cannot exist in a uniform two-dimensional system. However, below a non-zero critical temperature a two-dimensional Bose fluid becomes superfluid, despite absence of the long-range coherence normally associated with this phenomenon. Remarkably, no symmetry is broken, but a topological order emerges which is sufficient to support superfluid behaviour; this BKT transition is driven by the suppression of vortices, topological defects in the system phase [50–52].

Whilst in a uniform system this is the sole low-temperature transition, the modified density of states induced by a harmonic trapping potential restores the possibility of conventional BEC in the ideal gas limit. It is this interplay between BKT and BEC physics which is considered in this thesis.

In the current Chapter we present a theoretical overview of two phenomena which may be exhibited by a system of degenerate, interacting bosons: Bose-Einstein condensation and superfluidity. This discussion is made without any speculation on their possibility, which is considered in the case of a uniform two-dimensional system in Chapter 3. In contrast to experiments on liquid ^{4}He [53] and other condensed matter systems [52, 54] which are typically uniform in-plane, most experiments with ultracold bosonic gases confine atoms in-plane using a harmonic potential [9, 55–68]. The relationship between BEC and superfluidity in harmonically-trapped two-dimensional gases is the subject of Chapter 4, where we also consider the effect of residual freedom in the 'frozen' dimension and ask what it means to be 'two-dimensional'.

Having completed our discussion from a theoretical perspective, the second part of the thesis concerns an experimental work on a harmonically-trapped two-dimensional ultracold Bose gas. By tuning the strength of interactions, we were able to observe the unification of BKT and BEC transitions in the limit of vanishing interactions, and quantitatively compare the measured critical parameters to theoretical predictions made over a decade ago. An overview of the experiment is given in Chapter 5, the experimental setup is presented in Chapter 6, and the method and results are discussed in Chapter 7. Finally, in Chapter 8 we give some experimental conclusions and offer an outlook on future research directions.

2.1 Low-Temperature Phases

Our general problem under consideration is the following: we imagine a uniform system of bosons of mass m confined to a two-dimensional world with number density n and temperature T, interacting via some repulsive contact potential characterised by a dimensionless interaction strength $\tilde{g}$. Our question is, what state (if any) should emerge as the phase-space density $\mathcal{D} = n\lambda_{\mathrm{th}}^2$ is increased to values $\mathcal{O}(1)$? This thesis is concerned with the interplay between BEC and superfluidity in two-dimensional systems, and in this Section we overview these phenomena.

2.1.1 Bose-Einstein Condensation

The quantum statistics of bosons are described by the Bose-Einstein distribution, which controls how bosons should occupy the energy levels of a system:

$$f(\varepsilon) = \frac{1}{e^{\beta(\varepsilon-\mu)} - 1}, \tag{2.1}$$

where $\beta = (k_{\mathrm{B}}T)^{-1}$ and k_{B} is the Boltzmann constant, μ is the chemical potential, ε is the energy of the state under consideration, and $f(\varepsilon)$ the occupation number.

Unlike their fermionic counterparts, multiple bosons may occupy a single energy state which offers the possibility of BEC, whereby a macroscopic fraction $\mathcal{O}(1)$ of particles accumulate in a single eigenstate. Unlike many familiar phase transitions, BEC is not driven by the interactions between particles but is a natural consequence of their quantum statistics. Put quantitatively, the single-particle density matrix exhibits an eigenvalue of order the total particle number N, with a macroscopically-occupied single-particle wavefunction given by the corresponding eigenstate [69].

In a uniform system, the density matrix $\hat{\rho}$ is diagonal in momentum-space; letting $|\mathbf{k}\rangle$ denote a state of momentum $\hbar\mathbf{k}$,

$$\hat{\rho} = \sum_{\mathbf{k}} N_{\mathbf{k}} |\mathbf{k}\rangle\langle\mathbf{k}|, \tag{2.2}$$

where $N_{\mathbf{k}}$ is the occupation number of state $|\mathbf{k}\rangle$. The existence of a BEC implies that $N_0 \sim N$, which is necessarily accompanied by the appearance of long-range order. This is quantified by the first-order correlation function,

$$g^{(1)}\left(\mathbf{r}\right)=\left\langle\hat{\Psi}^{\dagger}\left(\mathbf{r}\right)\hat{\Psi}\left(0\right)\right\rangle, \tag{2.3}$$

where the bosonic field operator $\hat{\Psi}^{\dagger}\left(\mathbf{r}\right)$ creates a particle in the position state $|\mathbf{r}\rangle$. Evaluating $g^{(1)}$ for the density matrix of Eq. (2.2) one finds[1]

$$\begin{aligned} g^{(1)}(\mathbf{r}) &= \sum_{\mathbf{k}}\frac{N_{\mathbf{k}}}{L^2}e^{i\mathbf{k}\cdot\mathbf{r}}, \\ &= \frac{N_0}{L^2}+\int\frac{\mathrm{d}^2\mathbf{k}}{(2\pi)^2}n(\mathbf{k})e^{i\mathbf{k}\cdot\mathbf{r}}, \end{aligned} \tag{2.4}$$

where $n(\mathbf{k})$ is the system momentum distribution[2], and the conversion of a sum to an integral is valid assuming the system extent $L\to\infty$. The condensate density N_0/L^2 is therefore revealed as the infinite-distance limit of $g^{(1)}$, and the existence of a BEC implies a well-defined phase relation between infinitely-separated points[3].

2.1.2 Superfluidity

The presence of phase coherence generally engenders a non-zero 'macroscopic wavefunction' $\psi=\left\langle\hat{\Psi}\right\rangle$, where the average is over a region much larger than interparticle spacing but smaller than the lengthscale of any macroscopic flows or potentials [70]. The case of $\psi\neq0$ is intimately linked to the phenomenon of superfluidity, first observed in liquid ^{4}He [71, 72] in which it was posited to be a consequence of BEC by London [73]. Whereas bulk flow of a classical fluid gradually decays into elementary excitations, a superfluid flows without dissipation.

To understand the origins of this behaviour, one can consider the available dissipation channels.

1. Decay into excitations with linear momentum, which transfers energy and momentum of the bulk flow into creation of quasi-particles[4]. The Landau critical velocity [74] relates the form of the quasi-particle dispersion relation $\varepsilon(k)$ to a critical velocity v_c, below which excitations cannot be created whilst conserving both momentum and energy,

$$v_c=\min\left(\frac{\varepsilon\left(k\right)}{\hbar k}\right). \tag{2.5}$$

---

[1] We make use of the relation $\left\langle\hat{A}\right\rangle=\mathrm{Tr}(\hat{\rho}\hat{A})$ for some observable $\hat{A}$, and the position-space representation of a momentum state $\langle\mathbf{r}|\mathbf{k}\rangle=L^{-1}\exp(i\mathbf{k}\cdot\mathbf{r})$.

[2] Defined as the number of particles in the momentum-space element $\mathrm{d}^2\mathbf{k}/(2\pi)^2$.

[3] The definition of the BEC density as $n_0=\lim_{r\to\infty}g^{(1)}(\mathbf{r})$ is known as the Penrose-Onsager criterion [69].

[4] The label 'quasi-particle', refers to a collective excitation of the system with a definite energy and momentum. In that sense an excitation can be treated as particle-like.

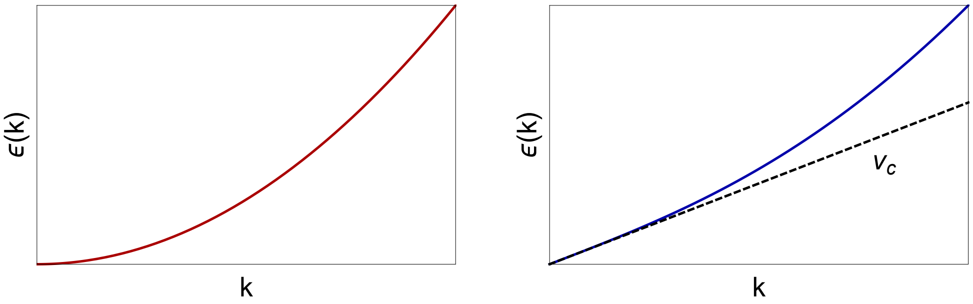

Figure 2.1: *Examples of dispersion relations corresponding to a normal fluid (red) and a superfluid (blue). Whereas the Landau critical velocity of Eq. (2.5) vanishes in the case of a normal fluid, in a superfluid one obtains some* $v_c > 0$*, given by the gradient of the black dashed line. Below this velocity the bulk motion cannot transfer energy into an excitation whilst conserving energy and momentum.*

Examples of the dispersion relations for a normal fluid, and superfluid are shown in Fig. 2.1.

2. Angular momentum of the bulk fluid can dissipate into elementary rotational excitations (vortices). In the case of $\psi \neq 0$, vortices become quantised [70, 75]. Fixing the density n to be constant, one may include dynamics in the macroscopic wavefunction by permitting modulation of its phase $\theta(\mathbf{r})$, giving

$$\psi(\mathbf{r}) = \sqrt{n}e^{i\theta(\mathbf{r})}. \tag{2.6}$$

The fluid velocity can be defined via the quantum-mechanical flux[1] $\mathbf{j} = (\hbar/(2mi)) \left[\psi^* \nabla \psi - \psi \nabla \psi^*\right]$, and making the identification $\mathbf{j} = n\mathbf{v}$ yields the velocity field

$$\mathbf{v}\left(\mathbf{r}\right) = \frac{\hbar}{m} \nabla \theta \left(\mathbf{r}\right), \tag{2.7}$$

a simple looking equation with a profound consequence; the requirement for phase $\theta(\mathbf{r})$ to be single-valued forces quantisation of flow around any closed loop,

$$\oint \mathbf{v} \cdot \mathrm{d}\mathbf{r} = \frac{\hbar}{m} 2\pi\nu \qquad , \qquad \nu \in \mathbb{Z}. \tag{2.8}$$

For the case of rotation around some point at radius $r = 0$, the azimuthal velocity is then $v(r) = \nu\hbar/(mr)$. The flow associated with a single vortex has energy E_{vortex} and angular momentum J_{vortex} given by

$$E_{\text{vortex}} = \int_{\xi}^{R} \frac{1}{2} n m v^2 \left(r\right) \mathrm{d}^2\mathbf{r} = \nu^2 \frac{\pi \hbar^2}{m} n \ln \left(\frac{R}{\xi}\right), \tag{2.9}$$

$$J_{\text{vortex}} = \int_{\xi}^{R} n m v \left(r\right) r \mathrm{d}^2\mathbf{r} = \nu \hbar N, \tag{2.10}$$

---

[1] This is derived by demanding that the probability density $\rho = |\psi|^2$ obeys the continuity equation $\frac{\partial \rho}{\partial t} = -\nabla \cdot \mathbf{j}$.

> where R is the system radius, N the total particle number and ξ the radius of the central zero-density region demanded by the undefined phase $\theta(r = 0)$. The quantisation displayed by Eqs. (2.9, 2.10) means that below some finite critical velocity [70], vortex excitation is not possible whilst conserving both energy and angular momentum.
>
> In a classical fluid, very many single-particle states are occupied and there is no macroscopic wavefunction. Whilst individual single-particle states must have quantised circulation, the bulk fluid can exhibit arbitrary vorticity leading to dissipation at any flow velocity.

If neither decay channel outlined above is available, bulk motion cannot dissipate and the system is superfluid.

A familiar example is provided in three dimensions, where the appearance of BEC in an interacting system heralds the onset of superfluid behaviour [7, 8]; the existence of a macroscopic wavefunction results in quantised vortices, and interactions suppress density fluctuations on long lengthscales such that the low-k excitations are phase-waves (phonons) with a linear dispersion relation. As a consequence, below some non-zero velocity neither vortices nor phonons may be excited, and the energy associated with macroscopic flow cannot decay into elementary excitations.

It is worth mentioning that although an interacting BEC exhibits superfluid flow, in general one neither equates to nor even entails the other. The canonical example is that a non-interacting BEC has a 100% condensed fraction, but does not display superfluid flow which may be seen by application of Eq. (2.5) to a free-particle dispersion relation. Conversely, liquid ^{4}He, whilst possessing a superfluid fraction of order unity as $T \to 0$, has a condensed fraction (defined through the largest density matrix eigenvalue) of $\sim$ 10% [69, 76]. As we shall see, the possibility for superfluidity without condensation at all is dramatically demonstrated by the Bose gas in two dimensions.

Chapter 3

The Uniform Two-Dimensional Bose Gas

Having outlined possible low-temperature phases for a collection of bosons in Chapter 2, we now turn our attention to their feasibility in a uniform two-dimensional Bose gas. The possibility of BEC and superfluidity is addressed in Section 3.1, which necessitates a description of the collective excitations; a Bogoliubov-type approach is the topic of Section 3.3, which predicts the interacting two-dimensional Bose gas to support superfluid behaviour. The superfluid critical point is identified in Section 3.4, where vortex excitations are included 'by-hand', and the BKT transition is introduced as the mechanism behind the superfluid-normal transition. A more quantitative classical-field description is presented in Section 3.5, which makes explicit predictions for the superfluid critical point and equation of state.

3.1 BEC and Superfluidity in the Uniform Gas

The original conception of BEC by Einstein was as a phase transition driven by the saturation of thermal states [77], and is a natural consequence of bosonic quantum statistics. For a particular system, one can imagine gradually adding particles (increasing μ) and ask whether a single state becomes macroscopically occupied.

In a uniform system the eigenstates are momentum states $|\mathbf{k}\rangle$, with corresponding energies $\varepsilon_0(k) = \hbar^2 k^2/(2m)$ in the case of an ideal gas. The particle density n_{th} corresponding to the thermally-populated states $|k > 0\rangle$ is obtained by integrating the Bose distribution over momentum states,

$$n_{\text{th}} = \int \frac{\mathrm{d}^2\mathbf{k}}{(2\pi)^2} \left[e^{\beta(\varepsilon_0(k)-\mu)} - 1 \right]^{-1} = -\lambda_{\text{th}}^{-2} \ln\left(1 - e^{\beta\mu}\right), \tag{3.1}$$

where $|\mathbf{k} = 0\rangle$ is excluded by the integration measure $\mathrm{d}^2\mathbf{k}$. As the chemical potential μ approaches its upper bound of $\varepsilon_0(0) = 0$, this density diverges. The thermal states may therefore hold an arbitrarily large number of particles, and the state $|\mathbf{k} = 0\rangle$ is never macroscopically occupied for any finite phase-space density. This result is reassuring: the presence of a BEC would imply long-ranged coherence $\lim_{r\to\infty} g^{(1)}(\mathbf{r}) = \text{const.}$, violating the Mermin-Wagner theorem [49].

It is worth commenting on the effect of interactions on this argument. As we shall see in Section 3.2 they can be introduced at a mean-field (MF) level via an 'interaction potential' $V_{\text{int}} = 2gn$, accomplished by the replacement $\mu \to \mu - 2gn_{\text{th}}$ in Eq. (3.1). Our conclusion is unchanged; thermal density remains divergent with increasing μ, which may now grow indefinitely rather than being restricted to $\mu < 0$.

Given the absence of BEC in the uniform two-dimensional system, one might wonder whether this precludes superfluidity. Without phase coherence, how is one to define superfluid flow $v \sim \nabla\theta$? However, the absence of BEC merely implies that $\lim_{r\to\infty} g^{(1)}(\mathbf{r}) = 0$. Whilst coherence over specifically *infinite* distance is precluded, if phase coherence falls slowly enough this shall turn out to be sufficient for superfluidity.

Even qualitatively, we can argue that BEC and superfluidity must be distinct from each other. Condensation is driven by the quantum statistics of particles; interactions certainly modify a system's behaviour [78–80], but are not intrinsic to the transition. Superfluidity however is a collective, dynamic phenomenon; for a macroscopic wavefunction to support interesting dynamics such as vortices or superfluid flow, one requires a spatially-varying phase $\theta(\mathbf{r})$. This necessitates dynamic admixing of multiple eigenstates, which is driven by interactions[1]. Furthermore, the low-k dispersion relation of an ideal gas is quadratic in any number of dimensions; a non-zero critical velocity arises out of interaction-induced deformation of this spectrum.

Any discussion of superfluidity therefore requires a formalism for interactions, which is the topic of Section 3.2. Once equipped with this, the coherence properties and quasi-particle excitations for the uniform Bose gas are considered within a Bogoliubov approach, which provides a framework from which to address superfluid behaviour.

3.2 Interactions in Two Dimensions

Whilst the form of interatomic interactions is generally complicated and system dependant, the low temperatures and densities of ultracold gases afford an assumption of two-body contact interactions[2]. The Hamiltonian is then given by

$$\mathcal{H} = \int \left[\hat{\Psi}^\dagger(\mathbf{r}) \frac{-\hbar^2}{2m} \nabla^2 \hat{\Psi}(\mathbf{r}) + \frac{g}{2} \hat{\Psi}^\dagger(\mathbf{r}) \hat{\Psi}^\dagger(\mathbf{r}) \hat{\Psi}(\mathbf{r}) \hat{\Psi}(\mathbf{r}) - \mu \hat{\Psi}^\dagger(\mathbf{r}) \hat{\Psi}(\mathbf{r}) \right] \mathrm{d}^2\mathbf{r}, \tag{3.2}$$

---

[1] More specifically, the interaction energy must be greater than the typical spacing between single-particle eigenenergies for an appreciable state admixture.

[2] This was justified in the Introduction.

where g is a coupling constant setting the strength of interactions. The field operator $\hat{\Psi}(\mathbf{r})$ is two-dimensional, and must have dimensions *length*$^{-1}$. Therefore $\hat{\Psi}^\dagger\nabla^2\hat{\Psi}$ and $\hat{\Psi}^\dagger\hat{\Psi}^\dagger\hat{\Psi}\hat{\Psi}$ are dimensionally identical, and the coupling constant g must on dimensional grounds be $\propto (\hbar^2/m)$. We can thus parameterise interactions by a dimensionless strength $\tilde{g}$, such that

$$g \equiv \frac{\hbar^2}{m}\tilde{g}. \tag{3.3}$$

For the purposes of future discussions, several salient points are worth making here.

Scale invariance In contrast to its counterpart in three dimensions, the Hamiltonian of Eq. (3.2) is scale-invariant, being unchanged under the rescaling of space $\mathbf{r} \to \Lambda\mathbf{r}$. This means that interactions cannot provide any absolute length (or energy) scale; we already showed that interactions are parameterised by a dimensionless strength $\tilde{g}$, whereas in three dimensions the scattering length a sets an absolute lengthscale[1] [12]. The remaining energy scales are the chemical potential μ and temperature T, and only their ratio rather than absolute values can be physically meaningful.

Effect of bosonic exchange symmetry The average interaction energy density of a system with Hamiltonian (3.2) is given by $(g/2)\langle n^2\rangle$. An ideal non-degenerate Bose gas displays Gaussian density fluctuations, such that $\langle n^2\rangle = \gamma n^2$ with $\gamma = 2$, whereas in the case of suppressed fluctuations $\gamma = 1$. The energy cost V_{int} of locally adding a particle is therefore given by

$$V_{\text{int}} = \frac{\partial}{\partial n}\left[\frac{g}{2}\gamma n^2\right] = \gamma g n. \tag{3.4}$$

Density fluctuations can be simply understood as arising from the demand of bosonic exchange symmetry: defining a pairwise contact potential of strength A as $U(\mathbf{r}_1, \mathbf{r}_2) = A\delta(\mathbf{r}_2 - \mathbf{r}_1)$, it is straightforward to evaluate the interaction energy of two bosons in properly symmetrised wavefunctions. For a d-dimensional uniform system of extent L, let two single-particle states be denoted $\psi = L^{-d/2}\exp(i\mathbf{k}_1 \cdot \mathbf{r})$ and $\phi = L^{-d/2}\exp(i\mathbf{k}_2 \cdot \mathbf{r})$: in the degenerate case,

$$\Psi(\mathbf{r}_1, \mathbf{r}_2) = \phi(\mathbf{r}_1)\phi(\mathbf{r}_2) \qquad \to \qquad \langle\Psi|U|\Psi\rangle = A, \tag{3.5}$$

whereas in the non-degenerate case,

$$\Psi(\mathbf{r}_1, \mathbf{r}_2) = \frac{\phi(\mathbf{r}_1)\psi(\mathbf{r}_2) + \phi(\mathbf{r}_2)\psi(\mathbf{r}_1)}{\sqrt{2}} \qquad \to \qquad \langle\Psi|U|\Psi\rangle = 2A. \tag{3.6}$$

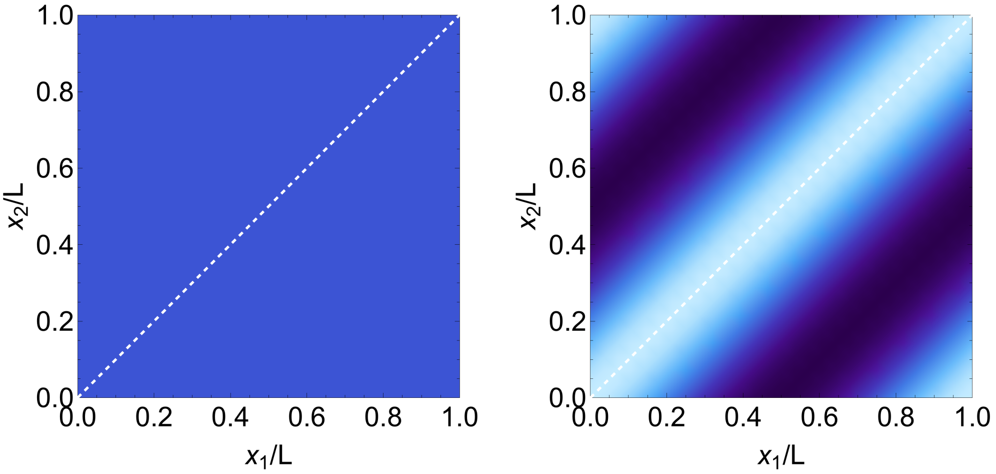

Figure 3.1: *Particle density* $|\Psi(x_1, x_2)|^2$ *for two particles in symmetrised degenerate (left) and non-degenerate (right) wavefunctions (see text). Axes are in units of system extent L. The white dashed lines denote* $x_1 = x_2$.

This is illustrated in Fig. 3.1, where we plot the particle density $|\Psi(x_1, x_2)|^2$ for two particles in one dimension. The chosen eigenstates are $\phi = L^{-1/2} \exp(i2\pi x/L)$ and $\psi = L^{-1/2} \exp(i4\pi x/L)$, which obey periodic boundary conditions. In the non-degenerate case, particle density is enhanced along the line $x_1 = x_2$.

Suppression of density fluctuations As the degeneracy of a system increases, neglecting interactions one might expect γ to smoothly reduce from its fully fluctuating value of $\gamma = 2$ to the non-fluctuating value $\gamma = 1$. In fact, without BEC this reduction is small: for simplicity, we imagine K states each containing an equal, and very large, number of bosons. If we randomly select two particles, the probability of them being in the same state is $1/K$. The expected value of γ is then

$$\langle \gamma \rangle = \left(1 \times \frac{1}{K}\right) + \left(2 \times \frac{K-1}{K}\right) = 2 - \frac{1}{K}. \tag{3.7}$$

Thus without the presence of a BEC ($K = 1$), suppression of fluctuations is rather small.

There is however an energetic advantage to reducing fluctuations: assuming fixed average density n, minimising the interaction energy density $(g/2)\gamma n^2$ equates to minimising γ. A careful population of the phase-density excitations [51] in a two-dimensional gas finds this is significant for $\mathcal{D} \gg 1$.

---

[1] Specifically, in three dimensions the relevant coupling constant is given by $g_{3\mathrm{D}} = (\hbar^2/m)4\pi a$.

3.3 Bogoliubov Analysis of Excitations

In order to establish whether a given system is superfluid, one must have some knowledge of the dispersion relation of excitations. In the case of a BEC, one typically uses a Bogoliubov analysis [81] to obtain the collective quasi-particle excitations; one assumes a single mode to contain the majority of particles, and expands the Hamiltonian in a small parameter corresponding to the weakly-occupied modes. In the case of a two-dimensional Bose gas there is generally no BEC at any non-zero temperature, and no single mode dominates. However, if one assumes that density fluctuations are small, these provide a convenient small parameter in which to expand the Hamiltonian, enabling a Bogoliubov-type analysis despite the absence of BEC [51, 82].

Such a treatment was performed within a classical-field approach in [51]. At $T = 0$ all particles occupy the lowest eigenstate, giving a macroscopic wavefunction $\psi(\mathbf{r}) = \sqrt{n}$. One includes spatial variation in phase and small density perturbations,

$$\psi(\mathbf{r}) = \sqrt{n\left(1 + 2\eta\left(\mathbf{r}\right)\right)}e^{i\theta(\mathbf{r})}, \tag{3.8}$$

and substitutes into the Hamiltonian of Eq. (3.2). Replacement of the quantum field operator with the classical-field $\hat{\Psi} \to \psi$ is justified if quantities of interest involve only modes with energies $\varepsilon(k) \ll k_{\mathrm{B}}T$, the occupation numbers of which are much larger than unity [83–85].

Application of the Gross-Pitaevskii equation (GPE) [86, 87] yields equations of motion for $\eta(\mathbf{r})$ and $\theta(\mathbf{r})$ which characterise the collective excitations supported by the system.

3.3.1 Dispersion Relation

From the equations of motion for $\eta(\mathbf{r})$ and $\theta(\mathbf{r})$ one obtains the quasi-particle spectrum [51], which sets the energy cost $\varepsilon(k)$ to create an excitation with momentum $\mathbf{k}$:

$$\varepsilon(k) = \sqrt{\frac{\hbar^2 k^2}{2m}\left(\frac{\hbar^2 k^2}{2m} + 2gn\right)}. \tag{3.9}$$

This spectrum is illustrated in Fig. 3.2; one can understand it in two limits:

- A linear low-k regime $\varepsilon(k) \approx k\sqrt{\hbar^2 gn/m}$ of phonon excitations.
- A quadratic high-k regime $\varepsilon(k) \approx \hbar^2 k^2/(2m) + gn$ of free-particle excitations. One might wonder why the free particles see a repulsive potential $1gn$ rather than the $2gn$ expected due to Bose exchange symmetry; this is because the excitation spectrum describes the energy *cost* associated with creating a quasi-particle, and so is referenced to the interaction energy of $\psi(\mathbf{r}) = \sqrt{n}$, equal to $1gn$.

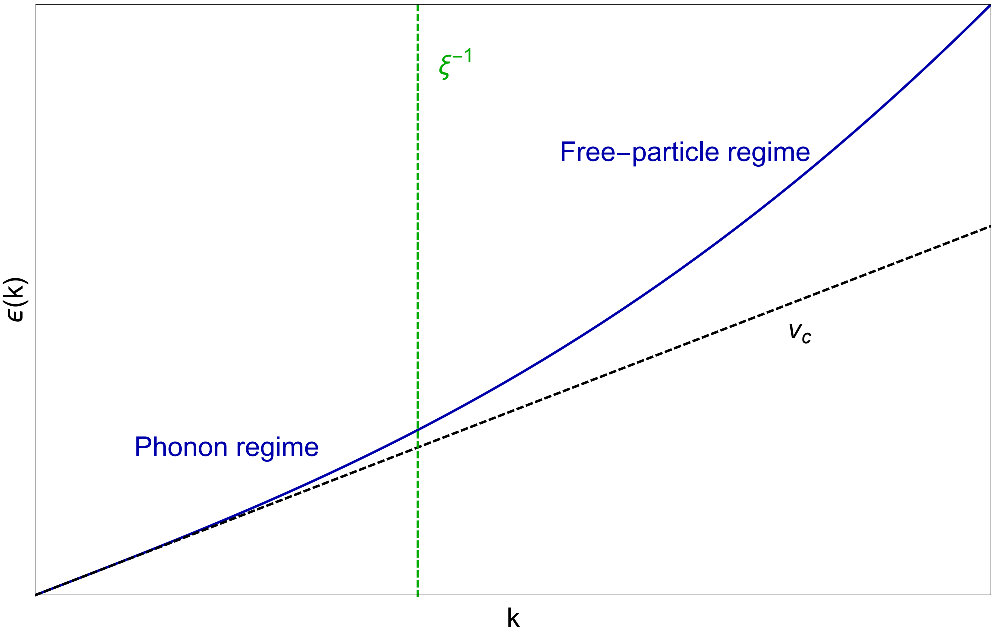

Figure 3.2: *The quasi-particle spectrum of a two-dimensional Bose gas with small density fluctuations. At $k \ll \xi^{-1}$ the spectrum is that of phonons, and is linear in k. This gives a non-zero superfluid critical velocity v_c according to the Landau criterion of Eq. (2.5). At higher $k \gg \xi^{-1}$ the quasi-particles become free-particle-like, with a quadratic dispersion relation.*

The effect of repulsive interactions is to modify the free-particle $\varepsilon_0(k) \propto k^2$, which develops a linear regime at low-k. The crossover between the linear and quadratic regimes is given by the *healing length* ξ,

$$\xi = \sqrt{\frac{\hbar^2}{nmg}} = \sqrt{\frac{1}{\tilde{g}n}}. \tag{3.10}$$

According to Eq. (2.5) we expect the low-T uniform Bose gas to be superfluid, with critical velocity set by the phonon speed $\sqrt{gn/m}$.

Composition of excitations The quasi-particles of Eq. (3.9) are collective phase-density excitations, and it is interesting to consider their composition. Intuitively, the energy cost of modulating the density is finite even in the limit $k \to 0$, whereas the cost of phase fluctuations vanishes and phonons should consequently be dominated by phase modulation. Repulsive interactions thus suppress density fluctuations on lengthscales $> \xi$ [51].

3.3.2 Correlation Function

The zero-temperature state $\psi(\mathbf{r}) = \sqrt{n}$ displays true LRO, characterised by $g^{(1)}(\mathbf{r}) = n$. As the temperature T is increased from zero, quasi-particles will be thermally generated, and consequently decrease the coherence between separated points. Since the long-distance correlations will be dominated by long-wavelength phonons which are primarily phase-waves, a reasonable approximation is to neglect density fluctuations[1]. The Hamiltonian of Eq. (3.2) reduces to the simpler form,

$$H_{\mathrm{XY}} = \frac{\hbar^2}{2m} n_{\mathrm{s}} \int \left|\nabla\theta\left(\mathbf{r}\right)\right|^2 \mathrm{d}^2\mathbf{r}. \tag{3.11}$$

The 'by-hand' substitution of the total density n for the superfluid density n_{s} accounts for the fact that density fluctuations are never totally suppressed, so we heuristically include them via the (unknown) quantity n_{s} [51, 88]. This is consistent within the two-fluid model[2]; the effect of $T > 0$ is to generate Bogoliubov quasi-particles which together constitute the normal component. Therefore the existence of a normal component and the presence of density fluctuations both arise from the same physical source. Additionally, one can define the superfluid density via a system's resistance to twisting of its phase [89], and so it is plausible that the energy cost associated with $\nabla\theta \neq 0$ is associated with a superfluid component.

The Hamiltonian H_{XY} is the two-dimensional XY model for a lattice of spins $\mathbf{s}_i$ with interactions $\propto \mathbf{s}_i \cdot \mathbf{s}_j$. The correlation function for this model at low temperatures is known [90, 91], and gives the important result for the low-T uniform Bose gas:

$$g^{(1)}(\mathbf{r}) = n_{\mathrm{s}} \left(\frac{\xi}{r}\right)^{\frac{1}{n_{\mathrm{s}}\lambda_{\mathrm{th}}^2}}, \tag{3.12}$$

where the healing length ξ provides an upper momentum cutoff; modes with $k > \xi^{-1}$ have been incorporated into $n \to n_{\mathrm{s}}$. The lack of true coherence at any $T > 0$ is a manifestation of the Mermin-Wagner theorem. As opposed to three-dimensions, the density of states for phonon modes goes as k rather than k^2. The weaker suppression of $k \to 0$ modes in the two-dimensional space is insufficient to preserve phase order at distances $\to \infty$.

However, the extent of coherence is sufficient to support superfluidity. As noted in [92, 93], Josephson provides a direct relation between the correlation function and superfluid density [94],

$$n_{\mathrm{s}} = \lim_{k\to 0} \frac{n_0 m}{k^2 G(k,0)}, \tag{3.13}$$

where $G(k,z)$ is the single-particle Green's function at imaginary frequency z. For spatial correlation function $r^{-\eta}$ one has $G(k,0) \sim k^{\eta-2}$ [92]. In a system of extent L the condensate density $n_0 \sim L^{-\eta}$ and the lowest $k \sim 1/L$. Taking the limit $L \to \infty$ Eq. (3.13) approaches a non-zero value, indicating a non-zero superfluid density.

---

[1] See [51] for a more complete discussion of the justification for this assumption.

[2] See Section 3.4.1.

3.3.3 Consistency of Bogoliubov Approach

At the start of the present Section, we noted that the Bogoliubov analysis of the two-dimensional Bose gas relies upon density fluctuations being small. Additionally, the classical-field of Eq. (3.8) has a phase which is assumed to vary in a well-defined way. However, an ideal Bose gas would display large density fluctuations $\langle n^2 \rangle = 2n^2$, and we have shown above that at any $T > 0$ the two-dimensional Bose gas is not coherent. Each of these points is addressed here.

- The presence of repulsive interactions suppresses density fluctuations on lengthscales $> \xi$. If total density fluctuations are significantly reduced, expansion around a state with fixed density remains reasonable. A simple estimate of this regime comes from demanding that only phonon modes (principally phase fluctuations) are significantly populated[1]. This condition $k_\mathrm{B}T \ll gn$ yields $\mathcal{D} \gg (2\pi/\tilde{g})$. More carefully, populating the spectrum of Eq. (3.9) and calculating the resulting density fluctuations finds that $\mathcal{D} \gg 1$ is in fact sufficient [51].

  At finite temperature, we can associate the residual density fluctuations with the presence of a normal component [51], heuristically replacing $n \to n_\mathrm{s}$ and expanding around a state $\psi(\mathbf{r}) = \sqrt{n_\mathrm{s}} e^{i\theta(\mathbf{r})}$. This assumes that only the superfluid component supports Bogoliubov quasi-particles; unlike the normal fluid, the energy cost associated with a phase gradient is non-zero [89].

- The correlation function of Eq. (3.12) decays algebraically with distance, vanishing as $r \to \infty$. This is consistent with the absence of BEC; we saw in Eq. (2.4) that a macroscopic occupation of $|\mathbf{k} = 0\rangle$ would give a finite limit [69].

  Whilst over sufficiently large separations the phase order is destroyed, one can always define a local phase, and coherence decays slowly enough to give a non-zero macroscopic wavefunction. The algebraic form of Eq. (3.12) means there is no lengthscale associated with the decay of correlations; one therefore cannot define a low-k validity cutoff in the derived collective excitations.

These results provide a framework for introducing excitations to the two-dimensional Bose gas. The question we are concerned with is how the presence of these excitations should modify superfluid properties, and is the topic of the next Section.

---

[1] This approach simply indicates the typical $\mathcal{D}$ at which density fluctuations are suppressed. One might worry about the validity of the classical-field approximation if occupations of phonon modes become small.

3.4 Superfluid Fraction, and the BKT Transition

Previously, we showed that the two-dimensional Bose gas should be superfluid at $T = 0$. In this Section, we imagine slowly increasing the temperature and ask how the superfluid fraction should change under the thermal generation of Bogoliubov quasi-particles. However, regardless of its internal consistency the Bogoliubov approach is inherently perturbative, only accounting for smooth deformations of ψ. The inclusion of topological excitations is addressed in Section 3.4.2, where we introduce the topological BKT transition.

3.4.1 Superfluid Fraction

At finite temperature, quasi-particles will be thermally generated according to the Bose distribution, and will not themselves exhibit superfluid behaviour. This problem is conveniently treated within a 'two-fluid model', with two constituent parts [12]:

1. A superfluid component of density n_s, which exhibits dissipationless flow and is described by the macroscopic wavefunction $\psi(\mathbf{r}) = \sqrt{n_\mathrm{s}} e^{i\theta(\mathbf{r})}$ [70].
2. A normal component of density n_n, consisting of a thermal gas of quasi-particles. Since these are in general not free particles, this density is defined according to the momentum density $\mathbf{j}$ of a quasi-particle gas moving with velocity $\mathbf{v}$.

$$\mathbf{j} = n_\mathrm{n} m \mathbf{v} \tag{3.14}$$

We introduce the effect of finite temperature by thermally populating the dispersion relation of Eq. (3.9), and integrating to find the total momentum of the resultant excitation gas. Consider a quasi-particle of momentum $\mathbf{p}$ in the superfluid frame, which has an energy cost of $\varepsilon(p)$. If the normal component has a velocity $\mathbf{v}$, then the energy cost in the normal frame is $\varepsilon(p) - \mathbf{p} \cdot \mathbf{v}$; this is depicted in Fig. 3.3.

We can assume that quasi-particles interact sufficiently that the normal component is in thermal equilibrium; quasi-particles are then populated according to the Bose distribution,

$$f(p) = \frac{1}{e^{\beta(\varepsilon(p) - \mathbf{p}\cdot\mathbf{v})} - 1}, \tag{3.15}$$

and the net momentum density of the quasi-particle gas is

$$\mathbf{j} = \int \frac{\mathrm{d}^2\mathbf{p}}{(2\pi\hbar)^2} \mathbf{p} f(p). \tag{3.16}$$

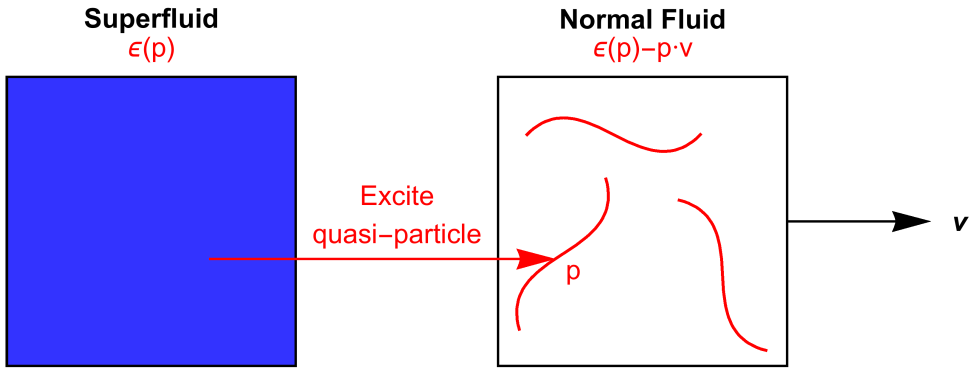

Figure 3.3: *The two-fluid model, consisting of a superfluid component of density $\mathcal{D}_s$, and collective excitations which constitute a normal fluid of density $\mathcal{D}_n$. If the superfluid is in motion, there is some relative velocity $\boldsymbol{v}$ between the superfluid and normal components; for convenience of calculation we work in the frame of the superfluid. The energy cost to create a quasi-particle of momentum $\boldsymbol{p}$ is $\varepsilon(p)$ in the superfluid frame, whereas in the normal frame it is $\varepsilon(p) - \boldsymbol{p}\cdot\boldsymbol{v}$.*

From Eq. (3.14) we obtain the normal density

$$\begin{aligned} n_{\mathrm{n}} &= \mathbf{j}\cdot\mathbf{v}/(mv^2), \\ &= \int \frac{\mathrm{d}^2\mathbf{p}}{(2\pi\hbar)^2}\frac{\mathbf{p}\cdot\mathbf{v}}{v^2}\frac{1}{e^{\beta(\varepsilon(p)-\mathbf{p}\cdot\mathbf{v})}-1}. \end{aligned} \tag{3.17}$$

If the normal fluid velocity is much smaller than $\varepsilon(p)/p$ for any populated excitation[1], the Bose distribution in Eq. (3.17) can be written as an expansion about the stationary case:

$$\begin{aligned} n_{\mathrm{n}} &= \int \frac{\mathrm{d}^2\mathbf{p}}{(2\pi\hbar)^2}\frac{(\mathbf{p}\cdot\mathbf{v})^2}{v^2}\frac{\partial f_0}{\partial\varepsilon}, \\ &= \int \frac{\mathrm{d}^2\mathbf{p}}{(2\pi\hbar)^2}\frac{p^2}{2}\frac{\partial f_0}{\partial\varepsilon}, \end{aligned} \tag{3.18}$$

where f_0 is the Bose distribution of Eq. (3.15) evaluated at $\mathbf{v} = 0$, and we have made use of the average absolute projection of any two-dimensional vector $\mathbf{p}$ along some direction being $p/\sqrt{2}$.

We can now insert the Bogoliubov excitation spectrum of Eq. (3.9) with the substitution $n \to n_{\mathrm{s}}$. Transforming variables into the dimensionless normal density $\mathcal{D}_{\mathrm{n}} = n_{\mathrm{n}}\lambda_{\mathrm{th}}^2$ and superfluid density $\mathcal{D}_{\mathrm{s}} = n_{\mathrm{s}}\lambda_{\mathrm{th}}^2$, we obtain the integral equation

$$\mathcal{D}_{\mathrm{n}}(\mathcal{D}_{\mathrm{s}}) = \int_0^\infty \mathrm{d}u \frac{u e^{\sqrt{u(u+\tilde{g}\mathcal{D}_{\mathrm{s}}/\pi)}}}{\left(e^{\sqrt{u(u+\tilde{g}\mathcal{D}_{\mathrm{s}}/\pi)}}-1\right)^2}, \tag{3.19}$$

---

[1] Equivalently, the velocity difference between superfluid and normal components should be much less than the critical velocity of Eq. (2.5).

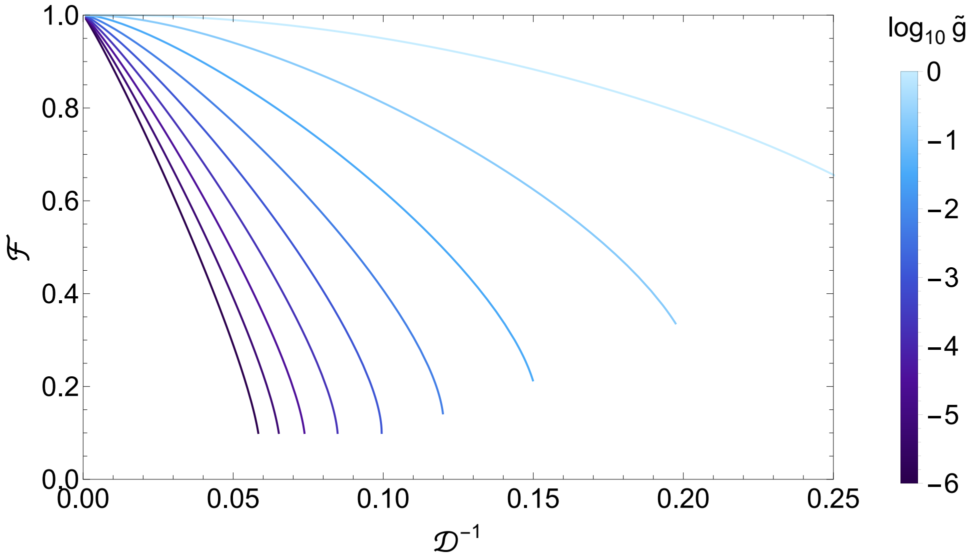

Figure 3.4: *The decay in superfluid fraction $\mathcal{F}$ with decreasing phase-space density $\mathcal{D}$. Curves are generated by thermal population of Bogoliubov quasi-particles, which form a normal component (see text). Progressive shades of blue indicate the strength of interactions $\tilde{g}$.*

---

which assumes that the quasi-particle spectrum depends solely upon $\mathcal{D}_{\mathrm{s}}$; this should be valid for high superfluid fractions.

In experiments, the quantity most easily controlled and measured is the total density $\mathcal{D}$. As this is varied, one can use Eq. (3.19) to obtain an implicit equation for the superfluid density $\mathcal{D}_{\mathrm{s}}$,

$$\mathcal{D} = \mathcal{D}_{\mathrm{n}}\left(\mathcal{D}_{\mathrm{s}}\right) + \mathcal{D}_{\mathrm{s}}. \tag{3.20}$$

This can be solved numerically, and Fig. 3.4 plots the variation of superfluid fraction $\mathcal{F} = \mathcal{D}_{\mathrm{s}}/\mathcal{D}$ with total density $\mathcal{D}$ for various interaction strengths $\tilde{g}$. As one would intuitively expect, the superfluid fraction falls from unity as $\mathcal{D}$ decreases. Larger values of $\tilde{g}$ make the superfluid more resilient to thermal depletion, due to the stronger deformation of the low-k limit of $\varepsilon(k)$ from quadratic to linear. By contrast, the ideal gas superfluid fraction would be zero for any $T > 0$.

At this stage, one might naively feel that the picture is complete. Starting from the superfluid $T = 0$ limit, with increasing T the normal density smoothly increases, until the superfluid fraction has fallen to zero. However, a flaw is revealed by considering the Hamiltonian $\mathcal{H}_{\mathrm{XY}}$ of Eq. (3.11). At low temperatures, the correlation function $g^{(1)}(\mathbf{r})$ takes the algebraic form of Eq. (3.12). At high-T however, correlations decay exponentially $g^{(1)}(\mathbf{r}) \sim \exp(-r/\zeta)$ where ζ is some temperature dependent lengthscale [95]. This can be simply understood in a lattice model by noting that at very high temperatures, adjacent lattice sites are very weakly correlated. Therefore correlations should fall by some fixed fraction per lattice site, resulting in exponential decay.

What is troubling is that there is no smooth deformation which maps an algebraic function onto an exponential, and it is unclear how $g^{(1)}(\mathbf{r})$ should evolve with increasing T; as noted by Berezinskii this is suggestive of a phase transition [90]. Furthermore, an algebraic function possesses no lengthscale; this is again suggestive of some phase transition, at which the correlation length diverges and $g^{(1)}$ switches from exponential to algebraic. This reasoning is correct; a phase transition does occur, but is not predicted within the perturbative Bogoliubov approach.

3.4.2 The BKT Transition

The Bogoliubov calculation of the superfluid fraction does not predict any phase transition. However, such a perturbative approach can only capture smooth deformations of the order parameter; the topology of $\psi(\mathbf{r})$ is unchanged by the addition of Bogoliubov quasiparticles, which deform it in a continuous manner. By construction, this approach cannot account for topological excitations such as vortices, singularities in $\psi(\mathbf{r})$ around which $\theta(\mathbf{r})$ winds by $\pm 2\pi$, which involve a discrete change in the structure of $\psi(\mathbf{r})$. The global phase winding associated with a vortex is very destructive to coherence, and the presence of vortices leads to a breakdown of the slow, algebraic decay of Eq. (3.12).

The favourability of thermally nucleating a vortex depends on the resultant change in the system free energy $\Delta F = E_{\text{vortex}} - TS_{\text{vortex}}$ where E_{vortex} is the kinetic energy of a vortex velocity field and S_{vortex} the entropy associated with the vortex position. From Eq. (2.9) we obtain the energy of a single-charged vortex as $E_{\text{vortex}} = (1/2)\mathcal{D}_{\text{s}} k_{\text{B}} T \ln(R/\xi)$ where R is the system radius, and ξ the healing length of Eq. (3.10). This provides the length scale over which $|\psi(\mathbf{r})|$ can vary from its bulk value to zero at the vortex centre, and gives the size of a vortex core. The vortex entropy S_{vortex} depends on the number of ways one can place a single vortex into the gas, giving $S_{\text{vortex}} = k_{\text{B}} \ln(R^2/\xi^2)$. Consequently,

$$\Delta F = (\mathcal{D}_{\text{s}} - 4)\,\frac{1}{2} k_{\text{B}} T \ln\left(\frac{R}{\xi}\right). \tag{3.21}$$

One therefore recovers a critical superfluid density, below which ΔF becomes negative and the proliferation of free vortices becomes energetically favourable,

$$\mathcal{D}_{\text{s}}^{\text{BKT}} = 4. \tag{3.22}$$

For a superfluid with $\mathcal{D}_{\text{s}} > 4$, whilst the formation of single vortices is energetically unfavourable, vortices may exist as bound pairs of opposite circulation. There is no net phase winding around a pair, hence whilst its associated entropy diverges with system size, its energy does not [51,52]. Vortex pairs have $\Delta F < 0$ at all nonzero temperatures; they have no long-range effect on the phase, but will reduce the superfluid density compared with a phonon-only model.

Once vortices are included, a modified superfluid evolution emerges as T is increased from zero. The superfluid density $\mathcal{D}_{\text{s}}$ initially falls smoothly due to rising

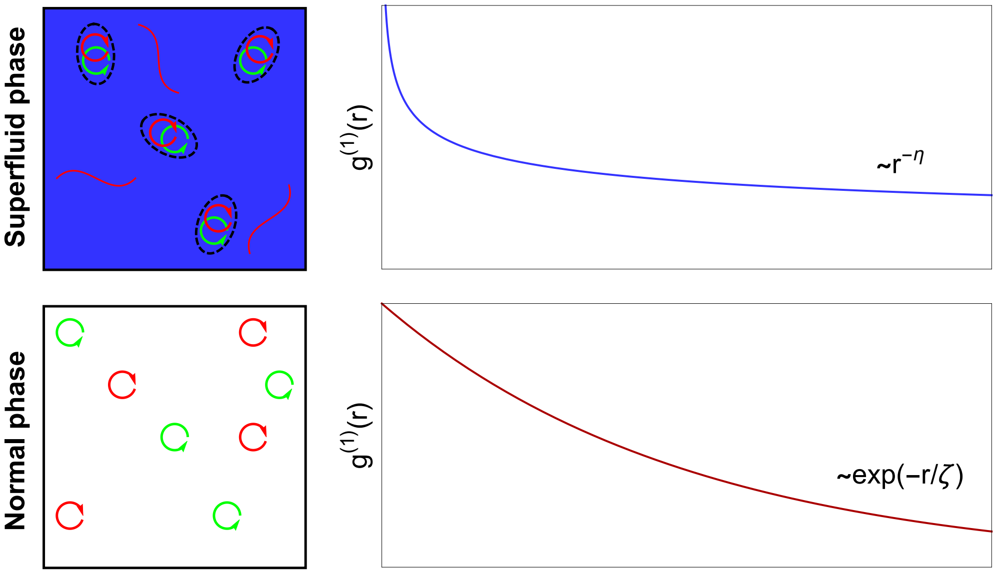

Figure 3.5: *The BKT transition. For superfluid densities $\mathcal{D}_s > 4$ vortices can only exist in bound pairs (black ovals), which have no long-range effect on coherence. The correlation function $g^{(1)}(\boldsymbol{r})$ decays algebraically, driven by the phase distortions associated with collective excitations (red lines). As temperature is increased, the superfluid fraction progressively falls until the BKT criterion Eq. (3.22) is reached. The proliferation of free vortices becomes energetically favourable, leading to destruction of the superfluid and exponentially-decaying correlations.*

---

temperature and generation of quasi-particle excitations. Free vortices are energetically suppressed, and vortices can only exist in bound pairs of opposite circulation which do not affect coherence over large distances. In accordance with the Mermin-Wagner theorem true LRO is absent, but the correlation function $g^{(1)}(\mathbf{r})$ falls to zero only algebraically, giving a 'quasi-LRO' sufficient to support superfluidity [92]. At the critical point $\mathcal{D}_\mathrm{s} = \mathcal{D}_\mathrm{s}^\mathrm{BKT}$, a proliferation of free vortices destroys the superfluid and leads to a universal jump in superfluid density $\Delta\mathcal{D}_\mathrm{s} = 4$. The long-range phase distortions of unbound vortices give rise to an exponentially-decaying correlation function [95]. This defect-driven loss of superfluidity is known as the Berezinskii-Kosterliz-Thouless (BKT) transition [50, 90], and is illustrated in Fig. 3.5.

It is interesting to consider the behaviour of vortex pairs just before the BKT transition is reached. The energy of a pair of oppositely charged vortices separated by a distance l is [52],

$$E_\mathrm{p}(l) = k_\mathrm{B} T \mathcal{D}_\mathrm{s} \ln \frac{l}{\xi}. \tag{3.23}$$

Noting that a pair of separation l is $\sim l$-fold degenerate, we find the average pair separation $\langle l \rangle$ as

$$\begin{aligned} \langle l \rangle &= \frac{\int_\xi^\infty l^{2-\mathcal{D}_\mathrm{s}} \mathrm{d}l}{\int_\xi^\infty l^{1-\mathcal{D}_\mathrm{s}} \mathrm{d}l}, \\ &= \frac{\mathcal{D}_\mathrm{s} - 2}{\mathcal{D}_\mathrm{s} - 3} \xi. \end{aligned} \tag{3.24}$$

For large superfluid densities $\mathcal{D}_\mathrm{s} \gg 1$ vortex pairs are tightly bound, with size of order the healing length. As the density falls, the pair size starts to diverge. Even this simple argument would predict the pair size to diverge at $\mathcal{D}_\mathrm{s} = 3$; in reality the presence of other pairs reduces the energy cost [51] of Eq. (3.23), making Eq. (3.24) a lower bound and the transition occurs at $\mathcal{D}_\mathrm{s} = 4$.

Critical density Although Eq. (3.22) gives a universal value for the critical superfluid density, it does not set the critical total density $\mathcal{D}^\mathrm{BKT}$. This will depend upon system-specific microscopic physics, which controls the superfluid fraction $\mathcal{F}(\mathcal{D})$. Experimentally, in ultracold gases $\mathcal{D}$ is more straightforwardly measured and controlled than $\mathcal{D}_\mathrm{s}$, and knowledge of the critical total density $\mathcal{D}^\mathrm{BKT}$ is desirable.

Quantitatively predicting D_BKT requires an accurate description of the non-perturbative behaviour of interacting bosons in the fluctuation region near the critical point. Classical-field simulations [96] model this behaviour by a turbulent matter-wave field [97]; this approach is introduced in Section 3.5. As a toy model, we can use our Bogoliubov model to make an estimate by fixing $\mathcal{D}_\mathrm{s}$ in Eq. (3.20), and evaluating $\mathcal{D}^\mathrm{BKT} = \mathcal{D}_\mathrm{n}(4) + 4$. This can be evaluated for various value of $\tilde{g}$, and the results are plotted in Fig. 3.6.

We empirically find a logarithmic dependence of $\mathcal{D}^\mathrm{BKT}$ upon $\tilde{g}$, illustrated by the excellent linear fit (black line) of $\mathcal{D}^\mathrm{BKT}(\tilde{g}) = 4.9 - 0.99 \ln \tilde{g}$. For comparison, the classical-field result [96] is $\mathcal{D}^\mathrm{BKT}(\tilde{g}) = 5.9 - \ln \tilde{g}$ (dashed red line); the two are in excellent agreement, with a small constant offset. It is unsurprising that our 'phonon-only' model of Eq. (3.19) over-estimates the superfluid density, since it neglects the reduction in superfluid fraction associated with vortex-pairs.

Graphically, in Fig. 3.7 we plot the smooth, quasi-particle driven decay of superfluid density identically to Fig 3.4, in addition to the BKT criterion (black dashed line) of Eq. (3.22). The BKT critical point is identified as where this is crossed, causing a $\tilde{g}$-dependent jump in superfluid fraction $\mathcal{F}$.

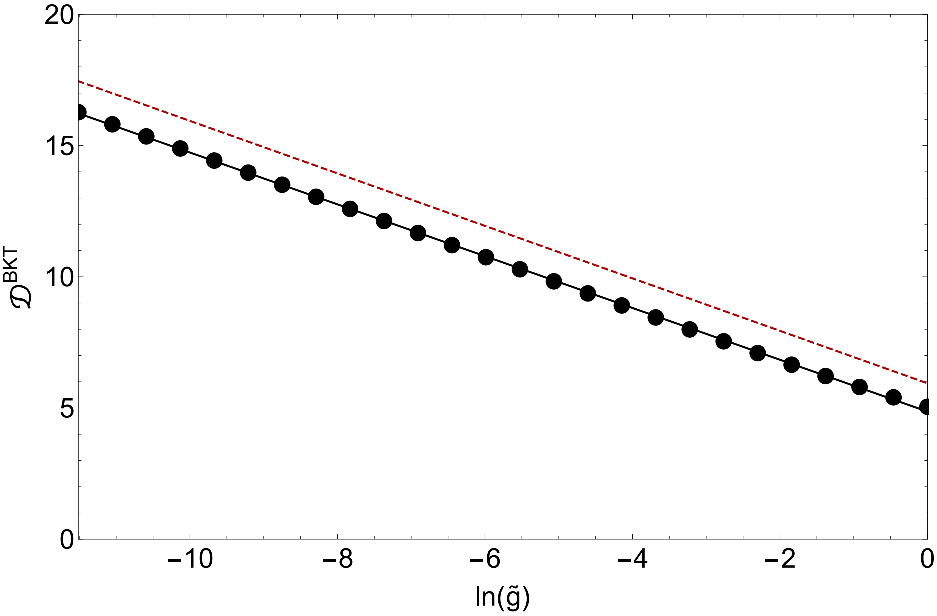

Figure 3.6: *BKT critical density from the 'phonon-only' model of Section 3.3 (see text). Black points denote numerical values for the critical density at specific interaction strengths, and the black line is an empirical linear fit. For comparison, the red dashed line denote the results of a classical-field prediction [96] introduced in Section 3.5.*

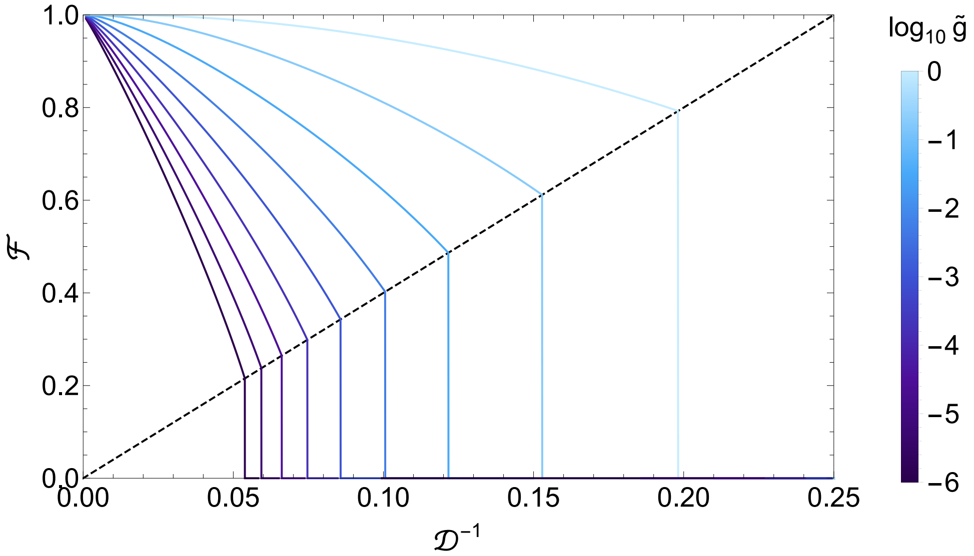

Figure 3.7: *The decay in superfluid fraction $\mathcal{F}$ with decreasing phase-space density $\mathcal{D}$, including the BKT transition point of Eq. (3.22). When the black dashed line is reached, the proliferation of free vortices becomes energetically favourable leading to destruction of the superfluid.*

3.5 Classical-Field Approach

Although the arguments of Section 3.3 provide an intuitive picture of the superfluid critical point, there are several approximations that one may have trouble with. Perhaps foremost, the dispersion relation of Eq. (3.9) was derived for $T = 0$ and based on small perturbations about the state $\psi(\mathbf{r}) = \sqrt{n}$; it is therefore unclear how far it should support a $T > 0$ description. Second, we have entirely neglected the influence of bound vortex pairs in the superfluid state. Third, our approach does not automatically predict the BKT transition, and says nothing regarding the normal side of the transition or the equation of state.

A more careful approach was made in [96, 98], where a classical-field method was used to address the low-T properties of the two-dimensional Bose gas. In this Section we give an overview of their method, and present some salient results.

3.5.1 Overview of Classical-Field Method

In a homogeneous ideal gas, eigenstates are momentum states $|\mathbf{k}\rangle$, whose dispersion relation is free-particle-like. Interactions couple different momenta [12], and modify this dispersion relation[1]. If this coupling is weak, then the problem can be treated perturbatively within MF theory; the energy of each $|\mathbf{k}\rangle$ is simply shifted by a MF potential $2gn$.

This approach is not sufficient for a two-dimensional gas close to the BKT critical point. It does not predict any transition, does not contain any suppression of fluctuations and cannot include superfluid dynamics or vortices. These phenomena arise out of strong coupling between momentum states; the system can no longer be described via small corrections to the ideal gas picture and the problem becomes non-perturbative [96, 98, 99]. This regime is reached when interactions become of order the energy of a particular $|\mathbf{k}\rangle$; therefore non-perturbative effects are confined to low-k states[2] [99].

The authors of [96, 98] employ a classical-field approach, describing the system by a classical-field ψ:

$$\mathcal{H} = \int \left[\frac{\hbar^2}{2m} |\nabla\psi|^2 + \frac{g}{2}|\psi|^4 - \mu|\psi|^2 \right] \mathrm{d}^2\mathbf{r}. \tag{3.25}$$

By evolving this field under the GPE until steady state is observed, equilibrium properties of the gas are obtained. The classical-field method accounts for the non-perturbative dynamics of all strongly occupied low-k modes of ψ [83, 85, 100]; the description should fail for low-occupation higher-k modes, but these are weakly coupled and can be described within an ideal gas picture [96, 100].

---

[1] If the system remains translationally-invarient, k should remain a good quantum number.

[2] We already saw a similar phenomenon in the Bogoliubov approach of Section 3.3; states with $k > 1/\xi$ simply had their energies shifted, whereas those with $k < 1/\xi$ were coupled into phonon modes with a linear rather than quadratic dispersion relation.

3.5.2 Critical Point

The BKT transition was identified by the requirement of $\mathcal{D}_{\mathrm{s}} = 4$, giving a critical total density $\mathcal{D}^{\mathrm{BKT}}$ and chemical potential μ^{BKT}:

$$\mathcal{D}^{\mathrm{BKT}} = \ln\left(\frac{380}{\tilde{g}}\right) \quad , \quad \mu^{\mathrm{BKT}} = k_{\mathrm{B}}T\frac{\tilde{g}}{\pi}\ln\left(\frac{13.2}{\tilde{g}}\right). \tag{3.26}$$

Several points deserve to be made about these expressions:

- The critical phase-space density is reasonably close to the value obtained by our simple Bogoliubov model of Section 3.3; the comparison between the two is illustrated in Fig. 3.6.
- In the limit of vanishing interactions $\tilde{g} \to 0$, $\mathcal{D}^{\mathrm{BKT}}$ diverges. This makes it manifest that the BKT transition is fundamentally interaction driven; in an ideal gas, superfluid dynamics are prohibited and the healing length diverges, making vortices conceptually impossible.
- The critical chemical potential is an interaction-dependent rescaling of the temperature. This is a consequence of scale-invariance[1]. The only relevant energy scales are μ and $k_{\mathrm{B}}T$, therefore only their ratio $\tilde{\mu}$ can be physically meaningful,
$$\tilde{\mu} = \frac{\mu}{k_{\mathrm{B}}T}. \tag{3.27}$$

The divergence of $\mathcal{D}^{\mathrm{BKT}}$ as $\tilde{g} \to 0$ illustrates the breakdown of the BKT picture in the ideal gas limit. According to Eq. (3.1), in an ideal gas $\mathcal{D}$ diverges as $\mu \to 0$. Therefore the $\tilde{g} \to 0$ limits of $\mathcal{D}^{\mathrm{BKT}}$ and μ^{BKT} are mutually consistent, and it is interesting that the BKT critical point, derived from considering the superfluid transition of an interacting gas, approaches the critical point for ideal gas BEC. It is this connection which is the topic of the experimental work presented in Chapters 5 - 7.

3.5.3 Equation of State

In addition to locating the BKT critical point, classical-field simulations also provide the equation of state for the two-dimensional Bose gas [98]. Naively this would take the form $\mathcal{D}(\mu, T, \tilde{g})$, but two factors simplify matters.

- The scale-invarience of the two-dimensional Bose gas Hamiltonian means $\mathcal{D}(\mu, T, \tilde{g})$ reduces to $\mathcal{D}(\tilde{\mu}, \tilde{g})$.
- By referencing phase-space density and chemical potential to their critical values, which absorb all interaction-dependence, in the vicinity of the BKT

---

[1] See Section 3.2.

point the equation of state takes the universal form $\Delta\mathcal{D} = (\mathcal{D} - \mathcal{D}^{\mathrm{BKT}}) = 2\pi\lambda(X)$, where $\lambda(X)$ is a universal function of the dimensionless parameter,

$$X = \frac{\tilde{\mu} - \tilde{\mu}^{\mathrm{BKT}}}{\tilde{g}}. \tag{3.28}$$

The function $\lambda(X)$ is tabulated in [98] and provides the corresponding $\mathcal{D}$ for any set $(\mu, T, \tilde{g})$. It is illuminating to consider an intuitive limit for $X \ll 0$, where one expects a low density gas exhibiting full bosonic density fluctuations. A MF approach is therefore reasonable, introducing interactions perturbatively via a potential $2gn$. Inclusion in our semiclassical equation of state Eq. (3.1) yields

$$\mathcal{D} = -\ln\left(1 - e^{\tilde{\mu} - \mathcal{D}\tilde{g}/\pi}\right). \tag{3.29}$$

Changing to the variables X and $\Delta\mathcal{D}$, we obtain

$$\Delta\mathcal{D} = -\ln\left(1 - e^{\tilde{g}\left[X - \frac{1}{\pi}\left(\Delta\mathcal{D} + \ln\frac{13.2}{380}\right)\right]}\right) - \ln\frac{380}{\tilde{g}}. \tag{3.30}$$

One immediately notices that that Eq. (3.30) does not exhibit a universal form. It does however *approach* a universal form close to the transition, which can be used to quantify where a universal description becomes valid within a MF picture. This requires the exponent in Eq. (3.30) to become small, specifically

$$\tilde{g}\left[X - \frac{1}{\pi}\left(\Delta\mathcal{D} + \ln\frac{13.2}{380}\right)\right] \ll 1. \tag{3.31}$$

In this limit, our MF equation of state reduces to

$$\Delta\mathcal{D} = -\ln\left(-380\left[X - \frac{1}{\pi}\left(\Delta\mathcal{D} + \ln\frac{13.2}{380}\right)\right]\right), \tag{3.32}$$

where all dependence on $\tilde{g}$ is absorbed into the parameter X.

In Fig. 3.8, we plot the universal, classical-field equation of state $\Delta\mathcal{D} = 2\pi\lambda(X)$ along with the MF approximation of Eq. (3.32). This result is important, and several points are worth making:

- The intuitive MF approach (green dashed line) gives an excellent description of the classical-field results (red line) for $X \ll 0$. As $X = 0$ is approached the classical-field curve rises *above* the MF; this is a consequence of the gradual suppression of fluctuations, which reduces the interaction potential from its fully fluctuating value of $2gn$. This enhances the density at a given $\tilde{\mu}$ compared with a MF approach. Empirically, this suppression is significant within a *fluctuation region* $-1 \lesssim X < 0$ denoted by the shading. A fully fluctuating, MF description fails when

$$\left(\tilde{\mu}^{\mathrm{BKT}} - \tilde{\mu}\right) \lesssim \tilde{g}, \tag{3.33}$$

  which could have been predicted on purely dimensional grounds [96]. The fluctuation region marks the onset of non-perturbative physics in the low-k states, and the failure of MF theory [99].

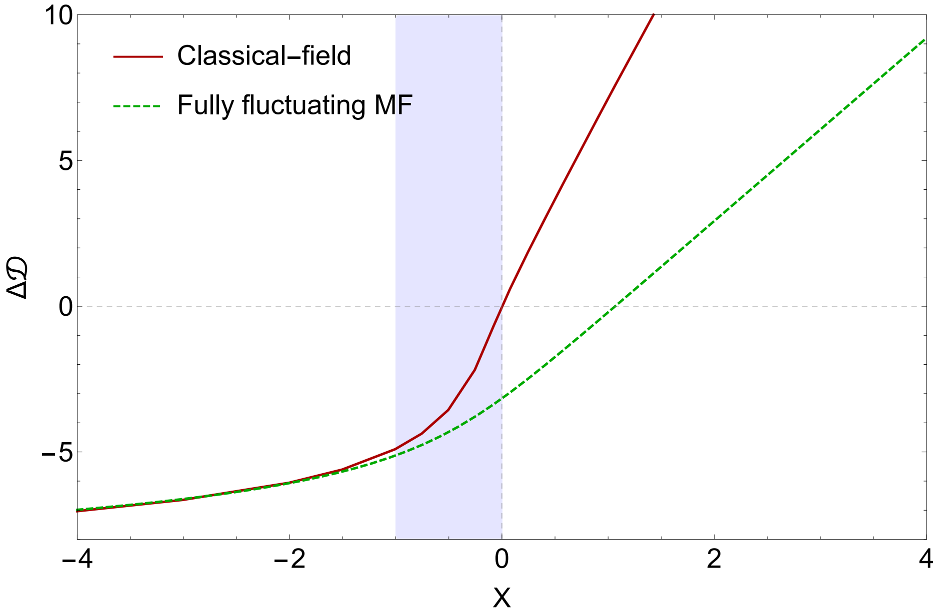

Figure 3.8: *The universal equation of state for a two-dimensional Bose gas, showing the numerical classical-field results of [98] and a MF approximation of Eq. (3.32). The blue shading demarcates the 'fluctuation region' in the vicinity of the critical point, where suppression of density fluctuations becomes significant and a MF approach fails.*

- There is no discontinuity in either $\mathcal{D}$ or its derivative at the BKT point $X = 0$. This is a consequence of the 'infinite-order' of the BKT transition; no symmetry is broken, unlike second-order transitions such as BEC in three dimensions where the system arbitrarily chooses a global phase. All derivatives of the free energy are continuous across the transition.

- For $X \gg 0$ one recovers a linear growth in $\mathcal{D}$, characteristic of a Thomas-Fermi regime where the chemical potential is set by interaction energy alone.

It is also enlightening to consider the equation of state at fixed $\tilde{g}$, for comparison with approximations lacking a universal form. In Fig. 3.9 we show the equation of state $\mathcal{D}(X)$, for $\tilde{g} = 0.05$. The plot shows the classical-field equation of state (red line) and the MF model for a fully fluctuating Bose gas of Eq. (3.30) (green dashed line). In addition, the equivalent MF curve for the case of fully suppressed density fluctuations (green dotted line) is shown, obtained by replacing $2gn \rightarrow 1gn$ in Eq. (3.29). There are several points of interest to be made:

- As X increases into the fluctuation region, the classical-field result rises away from the fully fluctuating MF curve, towards the non-fluctuating MF curve. The non-fluctuating model provides an upper bound for the equation of state; to rise above would require density anti-bunching ($\gamma < 1$ in Eq. (3.4)).

- For large $X \gg 0$ the classical-field result approaches the non-fluctuating MF result.

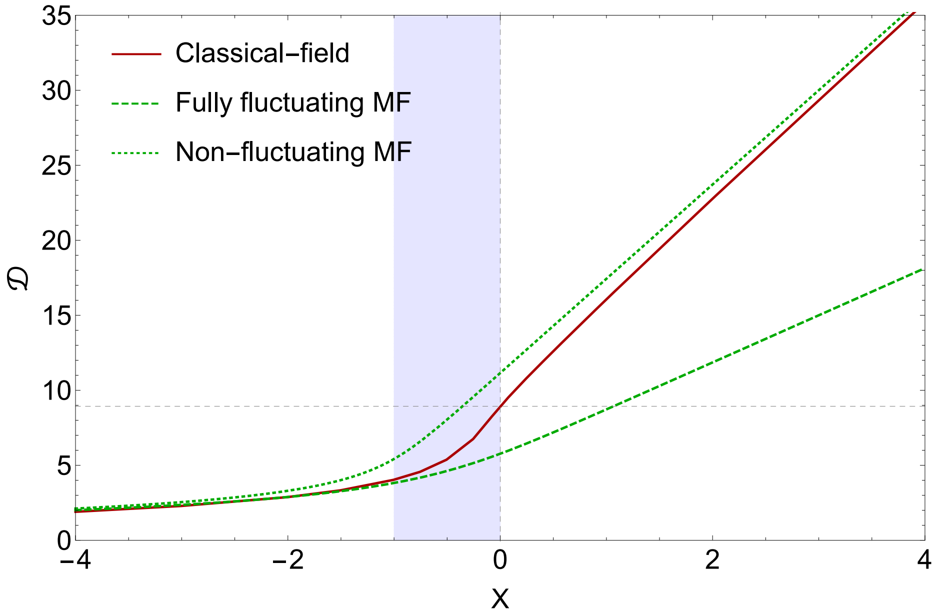

Figure 3.9: *The equation of state for a two-dimensional Bose gas with* $\tilde{g} = 0.05$ *(red line). For comparison, also plotted are MF curves for a gas with full fluctuations (green dashed line) and fully suppressed fluctuations (green dotted line).*

As Figs. 3.8 and 3.9 illustrate, it is the gradual suppression of density fluctuations as the BKT transition is approached that makes an analytic form for the equation of state difficult. This is in sharp contrast to three dimensions, where fluctuation suppression is usually negligible in a normal gas, and complete in a BEC. In this case, suppression is driven by degeneracy. In the two-dimensional case however, it is primarily the energetic advantage to reducing density fluctuations that drives fluctuation suppression in an interacting gas.

In terms of the interaction potential $\gamma g n$ of Eq. (3.4), the case $\gamma = 2$ corresponds to a fully fluctuating Bose gas, and $\gamma = 1$ to fully suppressed fluctuations. One might be tempted to consider fractional $1 < \gamma < 2$ to heuristically represent the partial suppression of fluctuations. However, we recall that the interaction potential is defined as the cost in interaction energy associated with adding a particle (see Eq. (3.4)). For partial suppression of fluctuations, one can write $\langle n^2 \rangle = \gamma(n) n^2$, where γ is now some function of n. This gives an interaction potential

$$\begin{aligned} V_{\text{int}} &= \frac{\partial}{\partial n}\left(\frac{g}{2}\gamma(n) n^2\right), \\ &= g\gamma(n) n + \frac{g}{2}\frac{\partial \gamma}{\partial n} n^2. \end{aligned} \tag{3.34}$$

Therefore one cannot in this case introduce an interaction potential linear in n; there is an additional quadratic term, with a generally complicated prefactor $\partial\gamma/\partial n$ which lacks a simple analytic form. Only in the two extremes of full fluctuations and fully suppressed fluctuations does the second term disappear, permitting a simple $V_{\text{int}} \propto n$.

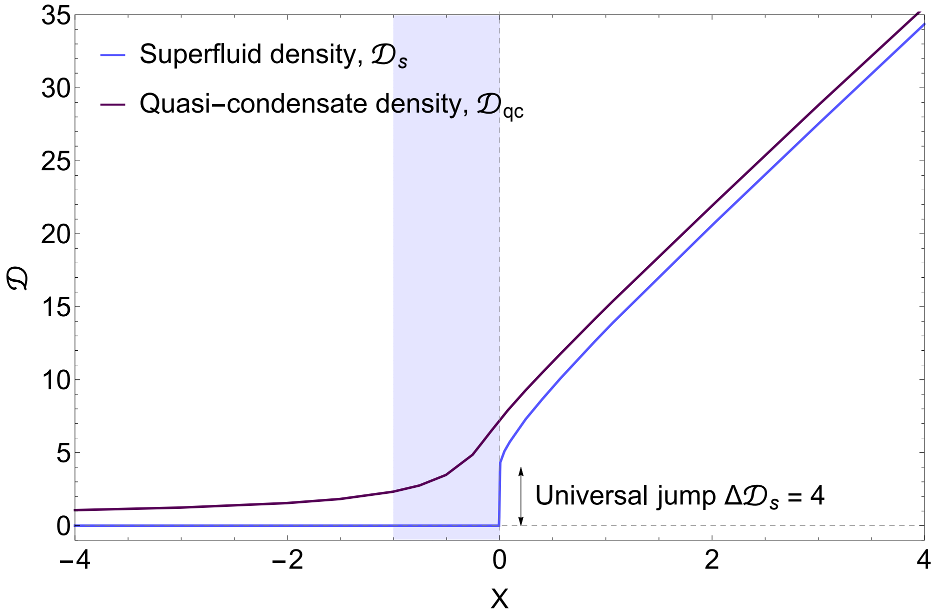

Figure 3.10: *The variation in superfluid density (blue line) and quasi-condensate density (purple line) across the BKT transition.*

Finally, the classical-field results of [98] additionally provide the superfluid density $\mathcal{D}_\mathrm{s}$, and the 'quasi-condensate' density $\mathcal{D}_\mathrm{qc}$. The latter is defined as $\mathcal{D}_\mathrm{qc} \equiv \lambda_\mathrm{th}^2\sqrt{2\left\langle n\right\rangle^2 - \left\langle n^2\right\rangle}$. In the limit of vanishing fluctuations, one simply obtains $\mathcal{D}_\mathrm{qc} = \mathcal{D}$, whereas for a fully fluctuating Bose gas $\mathcal{D}_\mathrm{qc} = 0$. The quasi-condensate density therefore provides a measure of the extent to which fluctuations have been suppressed. These quantities are plotted in Fig. 3.10. First, the jump in $\mathcal{D}_\mathrm{s}$ is recovered within the classical-field approach. This jump is universal, independent of interactions strength or particle specifics. Second, the quasi-condensate density takes a universal form across the transition. In particular, at the BKT transition point $X = 0$, one obtains $\mathcal{D}_\mathrm{qc} = 7.16$ [98]. For experimentally realistic values of $\tilde{g} \in [0.01, 1]$, the critical density $\mathcal{D}^\mathrm{BKT} \approx 6 \to 10$, and so already at the transition $\mathcal{D}_\mathrm{qc}$ is a significant fraction[1] of $\mathcal{D}$.

This now completes our discussion of the infinite, uniform Bose gas in two dimensions. Having identified and characterised the BKT superfluid-normal transition, and introduced the uniform-system equation of state, we now turn our attention to more experimentally realistic systems. In Chapter 4 we consider how to apply understanding of a pure-two-dimensional uniform gas to a quasi-two-dimensional, harmonically-trapped system.

---

[1] The quasi-condensate density exceeding the total density at the critical point suggests an inconsistency with the classical-field results [51, 101]. This occurs for $\mathcal{D}^\mathrm{BKT} < 7.16$, or $\tilde{g} > 0.3$.

Chapter 4

Two-Dimensional Physics in Trapped Gases

The discussion of Chapter 3 focused upon a pure-two-dimensional system of infinite, uniform extent. Whilst this model is theoretically accessible, experiments with cold gases differ in two crucial ways. First, the cold-atom researcher unavoidably inhabits a three-dimensional world, and no system can ever be perfectly two-dimensional. Second, in most experimental studies using ultracold atomic gases, the planar trapping potential is harmonic rather than uniform. These considerations are the topic of this Chapter; in Section 4.1 we ask how the presence of higher axial states should modify pure-two-dimensional behaviour, and in Section 4.2 we consider both how to apply uniform system results to the case of harmonic trapping, and how the interplay between BEC and BKT might be modified.

4.1 Effect of Residual Axial Freedom

In real-world experiments on two-dimensional systems, axial confinement is provided by some trapping potential, with a discrete spectrum of eigenenergies. For specificity we consider a harmonic trapping potential of frequency ω_z; for an ideal gas this potential has energy levels $E_j = j\hbar\omega_z$[1] and eigenstates $|j\rangle$. However, interactions modify both the energies and eigenstates, which are denoted $\overline{E}_j$ and $\overline{|j\rangle}$.

In the limit of ω_z becoming very large[2] the trap provides truly two-dimensional confinement, with no excitation or dynamics possible in the axial direction. However, in most ultracold atomic systems this spacing is comparable in magnitude to temperature and interaction energy.

One can identify two distinct limits of superfluid behaviour, depending upon the trap spacing ω_z:

---

[1] We neglect zero point energy $(1/2)\hbar\omega_z$ to simplify the notation.

[2] This will be quantified later in the Section.

- A kinematically two-dimensional gas. In-plane, excitations are collective Bogoliubov modes, labelled by a two-dimensional wavevector $\mathbf{k} = (k_x, k_y)$. Axially, excitations take the form of thermal promotion to higher axial states, which are well-spaced compared to other energy scales.
- A kinematically three-dimensional gas. In this case, all possible excitations are collective Bogoliubov modes, labelled by a three-dimensional wavevector $\mathbf{k} = (k_x, k_y, k_z)$.

The crossover between these regimes is set by comparing interaction energy with axial level spacing. Dynamics or collective excitations in the axial direction require admixture of multiple axial states; conversely, occupation of a single state ensures that the superfluid phase cannot vary axially, and the superfluid order parameter is two-dimensional. It is the superfluid interaction energy gn_s which admixes axial trap levels; one therefore expects a crossover between kinematically two- and three-dimensional behaviour when

$$gn_\mathrm{s} \sim \hbar\omega_z. \tag{4.1}$$

This can also be simply understood as when the superfluid healing length $\xi = 1/\sqrt{\tilde{g}n_\mathrm{s}}$ becomes comparable with the axial lengthscale $\sqrt{\hbar/(m\omega_z)}$.

In this Section, we consider each of these limits, and ask how the 'pure-two-dimensional' BKT picture should be modified.

4.1.1 Kinematically Two-Dimensional Superfluid

Taking our inspiration from Section 3.3 we start at $T = 0$, where atoms form a superfluid in the axial ground state $\overline{|j = 0\rangle}$. We now imagine switching on $T > 0$, and ask how the system behaviour should differ from a pure-two-dimensional gas.

In Section 3.3 we calculated the spectrum for quasi-particles, collective excitations of the superfluid which are thermally populated by increasing temperature. This resultant gas of excitations defined the normal component (Eq. (3.14), and the superfluid fraction steadily reduces as T rises. With the presence of higher axial levels, we now have *two* channels by which the superfluid fraction falls.

1. Thermal generation of quasi-particles, identically to the pure-two-dimensional case. These are collective excitations of the superfluid, labelled by a two-dimensional wavevector $\mathbf{k}$. We assume that the presence of atoms in higher axial states $\overline{|j > 0\rangle}$ does not modify the dispersion relation of Eq. (3.9). Therefore the normal density $\mathcal{D}_\mathrm{n}$ ($\mathcal{D}_\mathrm{s}$) defined in Eq. (3.19) should remain valid.
2. Thermal promotion of atoms to higher axial levels $\overline{|j > 0\rangle}$. Making the assumption that the density in these higher levels is small, their dispersion

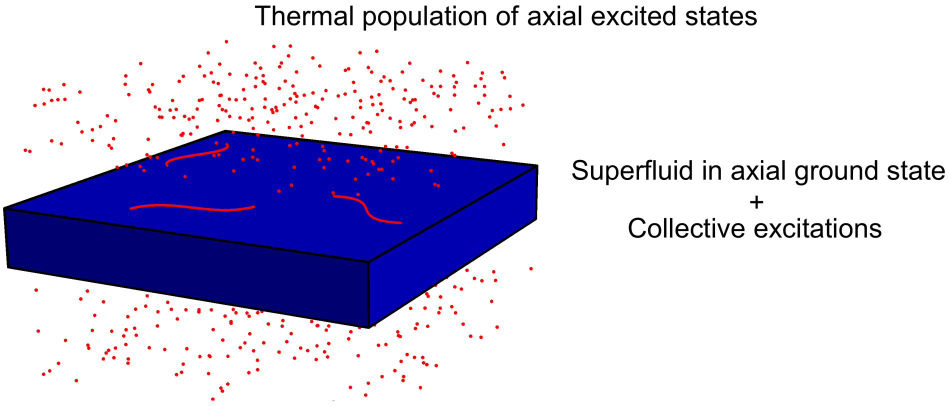

Figure 4.1: *A cartoon depicting a slab of superfluid (blue cuboid), which occupies the axial ground state* $\left|j=0\right\rangle$*. The effect of finite temperature is to thermally generate both collective quasi-particles in the superfluid (red lines), and promote atoms to higher axial states* $\left|j>0\right\rangle$ *(red points). Each of these channels reduces the superfluid density.*

relation relative to the superfluid should be free-particle-like,

$$\varepsilon_{j>0}\left(k\right)=\left(\overline{E_j}-\overline{E_0}\right)+\frac{\hbar^2k^2}{2m}, \tag{4.2}$$

where k is the planar momentum.

We employ Eq. (3.19) to evaluate the normal density associated with these atoms. Substituting the dispersion relation Eq. (4.2), and making use of integration by parts we find that

$$\begin{aligned}\mathcal{D}_{\mathrm{n}}&=\sum_{j>0}\int_0^\infty \mathrm{d}u\frac{ue^{u+\beta\left(\overline{E_j}-\overline{E_0}\right)}}{\left(e^{u+\beta\left(\overline{E_j}-\overline{E_0}\right)}-1\right)^2},\\ &=\sum_{j>0}\int_0^\infty \mathrm{d}u\frac{1}{\left(e^{u+\beta\left(\overline{E_j}-\overline{E_0}\right)}-1\right)},\\ &=-\sum_{j>0}\ln\left(1-e^{-\beta\left(\overline{E_j}-\overline{E_0}\right)}\right).\end{aligned} \tag{4.3}$$

This rather obvious result states that the normal density associated with atoms in excited axial states is equivalent to their density, assuming a free-particle dispersion relation and that $\mu\approx\overline{E_0}$.

These two channels via which the superfluid fraction falls are illustrated in Fig. 4.1. To calculate the superfluid fraction at fixed total density, we calculate and subtract the normal densities associated with each channel. Generalising Eq. (3.20) to the case of a quasi-two dimensional system gives an implicit equation for $\mathcal{D}_\mathrm{s}$:

$$\underbrace{\mathcal{D}_0}_{\substack{\text{Density in axial}\\ \text{ground state}}} + \underbrace{\mathcal{D}_{j>0}}_{\substack{\text{Density in axial}\\ \text{excited states}}} = \underbrace{\mathcal{D}_\mathrm{s}}_{\substack{\text{Superfluid}\\ \text{density}}} + \underbrace{\mathcal{D}_\mathrm{n}\left(\mathcal{D}_\mathrm{s}\right)}_{\substack{\text{Normal density due to}\\ \text{two-dimensional collective}\\ \text{excitations of superfluid}}} + \underbrace{\mathcal{D}_{j>0}}_{\substack{\text{Normal density}\\ \text{due to thermal}\\ \text{population of axial}\\ \text{excited states}}} . \tag{4.4}$$

It trivially follows that the axial excited state population appears identically on both sides. Subtracting, one uncovers a modified implicit equation,

$$\mathcal{D}_0 = \mathcal{D}_\mathrm{s} + \mathcal{D}_\mathrm{n}\left(\mathcal{D}_\mathrm{s}\right). \tag{4.5}$$

This looks identical to the superfluid density equation for a pure-two-dimensional system, Eq. (3.20), with the simple substitution $\mathcal{D} \to \mathcal{D}_0$. Importantly, the function $\mathcal{D}_\mathrm{n}\left(\mathcal{D}_\mathrm{s}\right)$ accounts for two-dimensional collective excitations of the superfluid, and so is unchanged by the presence of atoms in excited levels. The total two-dimensional superfluid density $\mathcal{D}_\mathrm{s}$ is determined solely by the axial ground state density $\mathcal{D}_0$, which is therefore the relevant density that determines when the BKT transition is crossed. One thus expects the axial ground state to support pure-two-dimensional physics, with the only caveat being that the superfluid should be kinematically two-dimensional.

In terms of comparing experiment with the classical-field theoretical expectations of [96, 98], we note that the classical-field ψ represents the heavily-occupied, low-k modes of a pure-two-dimensional system. Since ψ is two-dimensional, its dynamics cannot account for axial excitations. In the case of a kinematically two-dimensional system, there are no axial collective excitations available; ψ is then a valid representation of the axial ground state. Excitation to higher axial states is free-particle-like; these atoms are well-described by MF theory [99] and can be included/removed in theories 'by-hand'. The critical parameters and equation of state provided by [96, 98] therefore correspond to the axial ground state.

This argument that pure-two-dimensional BKT physics should be observed in the axial ground state is supported by comparison with the results of Quantum Monte-Carlo (QMC) simulation [99, 102] of quasi-two-dimensional gases. These simulations are for the more experimentally common case of harmonic in-plane trapping; BKT physics in a harmonic trap is the topic of Section 4.2, and the QMC results are presented in Section 4.2.4. The assumption that the axial ground state supports pure-two-dimensional physics, in accordance with the arguments of this Section, is found to give superb agreement with the BKT transition point obtained from QMC.

4.1.2 Kinematically Three-Dimensional Superfluid

One can imagine making the superfluid progressively more three-dimensional, by decreasing the axial level spacing $\hbar\omega_z$ to values comparable to the superfluid

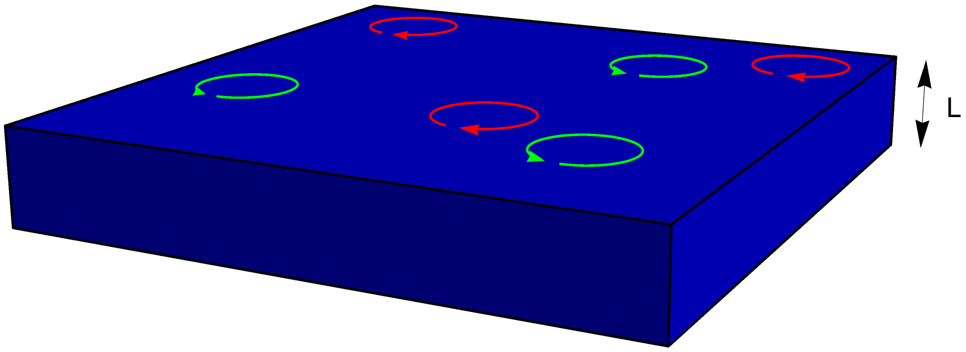

Figure 4.2: *A 'slab' of superfluid (blue cuboid) of axial extent L. Vortices (red and green circles) can exist as topological defects, whose energy is minimised by aligning their cores normal to the superfluid plane. The arrowheads indicate the vortex charge. We imagine increasing the axial thickness L, which increases the admixture of higher axial states into the superfluid wavefunction and results in the onset of axial dynamics (see text).*

interaction energy gn_s. The resultant admixture of higher axial levels into the superfluid wavefunction will progressively permit superfluid dynamics and collective excitations in the axial direction.

We can immediately note that the classical-field predictions for a pure-two-dimensional system should not be valid, since the field ψ does not incorporate axial dynamics. We can no longer circumvent this problem by separating the system into an axial ground state supporting two-dimensional excitations, and a set of free-particle excitations in higher axial states. Therefore we can no longer apply pure-two-dimensional physics, unlike in the kinematically two-dimensional case.

However, it is still interesting to ask how the BKT picture is modified in this regime. For a simple toy model, we consider a uniform 'slab' of superfluid, with infinite extent in-plane and axial thickness L, illustrated in Fig. 4.2. Reducing ω_z is equivalent to increasing L. In reality, the superfluid axial profile is not a top-hat; we do not expect this to qualitatively alter our conclusions.

The quantities of interest are the two-dimensional density[1] $\mathcal{D}^{\mathrm{2D}} = n^{\mathrm{2D}}\lambda_{\mathrm{th}}^2$, three-dimensional density $\mathcal{D}^{\mathrm{3D}} = n^{\mathrm{3D}}\lambda_{\mathrm{th}}^3$, and superfluid fraction $\mathcal{F}$. One may trivially relate these densities by

$$\mathcal{D}^{\mathrm{2D}} = \frac{L}{\lambda_{\mathrm{th}}}\mathcal{D}^{\mathrm{3D}}. \tag{4.6}$$

Assuming that vortex cores remain axially-aligned, the energetic arguments for the proliferation of vortices in Section 3.4.2 should still apply to the two-dimensional superfluid density, and one expects the universal jump of Eq. (3.22) to remain valid. However, we are interested in how the jump in superfluid fraction varies with increasing thickness L.

---

[1] In all other Sections, densities are assumed to refer to the two-dimensional density. Here we explicitly include the superscript '2D' since discussion also concerns three-dimensional densities.

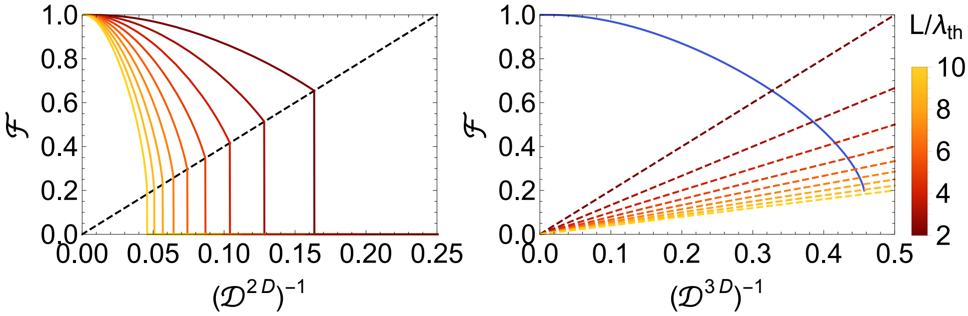

Figure 4.3: *The decay in superfluid fraction $\mathcal{F}$ as a function of two-dimensional density $\mathcal{D}^{2D}$ (left) and three-dimensional density $\mathcal{D}^{3D}$ (right), for a kinematically three-dimensional gas with $(a/\lambda_{th}) = 0.1$. The black dashed line illustrates where the BKT criterion of Eq. (3.22) is satisfied. Whereas the righthand curve has no L-dependence, the lefthand curve does, illustrated by progressive shadings. The coloured dashed lines on the righthand plot indicate the BKT criterion of Eq. (3.22) expressed in terms of three-dimensional density.*

For a kinematically three-dimensional gas, the superfluid fraction $\mathcal{F}$ is a function of $\mathcal{D}^{\mathrm{3D}}$; it is derived entirely analogously to Eq. (3.19), with the result

$$\mathcal{D}_{\mathrm{n}}^{\mathrm{3D}}\left(\mathcal{D}_{\mathrm{s}}^{\mathrm{3D}}\right) = \frac{4}{3\sqrt{\pi}} \int_0^\infty \mathrm{d}u \frac{u^{3/2} e^{\sqrt{u(u+4\mathcal{D}_{\mathrm{s}}^{\mathrm{3D}} a/\lambda_{\mathrm{th}})}}}{\left(e^{\sqrt{u(u+4\mathcal{D}_{\mathrm{s}}^{\mathrm{3D}} a/\lambda_{\mathrm{th}})}} - 1\right)^2}. \tag{4.7}$$

This function $\mathcal{F}(\mathcal{D}^{\mathrm{3D}})$ has no L-dependence; we can make use of the mapping of Eq. (4.6), to infer the variation with two-dimensional density, $\mathcal{F}(\mathcal{D}^{\mathrm{2D}})$ which is now dependent on L. The resulting sketches of superfluid fraction are illustrated in Fig. 4.3. In this regime, as $(L/\lambda_{\mathrm{th}})$ is increased, the magnitude of the jump in superfluid fraction $\Delta\mathcal{F}$ falls. As a system enters the kinematically three-dimensional regime, one should observe the smooth disappearance of any discontinuity in superfluid fraction as the transition is crossed.

4.1.3 Condition for Two-Dimensional Behaviour

Based on the arguments above, the possibility to observe pure-two-dimensional BKT physics in a quasi-two-dimensional system depends upon two factors:

1. The superfluid must be kinematically two-dimensional. According to Eq. (4.1), this demands

$$g n_{\mathrm{s}} \ll \hbar\omega_z \tag{4.8}$$

   to be satisfied at the critical point; substituting the critical value of $n_{\mathrm{s}} = 4/\lambda_{\mathrm{th}}^2$, we obtain

$$\frac{2\tilde{g} k_{\mathrm{B}} T}{\pi} \ll \hbar\omega_z. \tag{4.9}$$

In terms of axial extent $L = \sqrt{\hbar/(m\omega_z)}$, this becomes $(L/\lambda_{\mathrm{th}}) \ll 2\tilde{g}^{-1/2}$ which is of order unity for typical values of $\tilde{g} \in [0.01, 1]$.

2. The occupation of excited states should be small, such that atoms in higher axial states do not influence the behaviour of axial ground state atoms. This requires

$$k_{\mathrm{B}}T \lesssim \hbar\omega_z. \tag{4.10}$$

For example, assuming $E_j = j\hbar\omega_z$, at a temperature $k_{\mathrm{B}}T = \hbar\omega_z$ the axial ground state contains 72% of atoms[1]. In a uniform system this condition equates to $(L/\lambda_{\mathrm{th}}) \lesssim (2\pi)^{-1/2}$.

It is unsurprising that $L/\lambda_{\mathrm{th}} \ll 1$ sets the condition for two-dimensional behaviour; the typical coherence length should be larger than the gas thickness, such that the phase on one axial face is strongly correlated with the opposite face, resulting in a two-dimensional order parameter $\psi(\mathbf{r})$.

Summary of uniform system results All previous discussion has focused on the case of an infinite uniform in-plane potential. In this geometry, we have demonstrated that conventional, saturation-driven BEC is impossible. Instead, an interacting gas will undergo a normal-superfluid transition via the BKT mechanism. The critical phase-space density for this transition[2] diverges in the ideal gas limit, $\tilde{g} \to 0$, and therefore the ideal gas should not undergo a phase transition for any finite $\mathcal{D}$.

In the following Section 4.2, we shall apply the uniform system results of Chapter 3 to the case of a harmonic planar trapping potential. Not only is this situation more relevant to experiments with ultracold atoms, but also qualitatively changes the nature of the ideal gas limit.

4.2 Effect of Harmonic Trapping

Harmonic potentials are the most natural trapping geometry if atoms are confined with optical or magnetic fields, being the leading-order power close to a potential minimum. Depending upon the question addressed this can either be a help or hindrance; inhomogeneity means that different regions do not cross phase transitions coincidentally, complicating the study of critical phenomena or transition dynamics. On the other hand, equations of state can be obtained 'single-shot', since the spatially varying potential effectively scans the local chemical potential [1, 103]. In this Section, we ask how the presence of a harmonic potential changes the low-temperature phases available to a two-dimensional Bose gas. The case of an ideal gas is addressed in Section 4.2.1, and an interacting gas in Section 4.2.2. Finally,

---

[1] This is evaluated for an ideal gas with $\mu = 0$, such that the atomic fraction in the axial ground state $= g_2(1)/\sum\limits_{j=0}^{\infty} g_2(e^{-j})$, where $g_2(z)$ is the polylogarithm of order two.

[2] See Eq. (3.26).

in Section 4.2.5 we identify a crossover from interacting BKT physics to ideal gas BEC physics as interactions are taken to zero.

4.2.1 The Ideal Gas

In Section 3.1 we imagined gradually increasing the chemical potential of a uniform ideal two-dimensional gas, and showed that the density $\mathcal{D}$ of thermally-populated states diverges as $\mu \to 0$. This means physically that if one were to continually increase $\mathcal{D}$, no single state would ever become macroscopically occupied.

In a harmonic trap, the relevant global quantity is the atom number N; to ascertain whether BEC is possible, we ask how the number of thermal particles should scale with the chemical potential μ. Within the LDA one can straightforwardly generalise the thermal density of Eq. (3.1) to a harmonic trap with in-plane potential $V(r)$, via the substitution $\mu \to \mu - V(r)$. This results in

$$\mathcal{D}\left(r\right) = -\ln\left(1 - e^{\beta(\mu - V(r))}\right). \tag{4.11}$$

Assuming a harmonic potential $V(r) = (1/2)m\omega_r r^2$ integration is straightforward, yielding,

$$N = \left(\frac{k_\mathrm{B}T}{\hbar\omega_r}\right)^2 g_2\left(e^{\beta\mu}\right), \tag{4.12}$$

where $g_2(z) = \sum_{n=0}^{\infty} z^n/n^2$ is the polylogarithm function of order two. Setting $\mu = 0$ gives an upper bound to the number of thermal atoms,

$$N_\mathrm{c}^0 = \frac{\pi^2}{6}\left(\frac{k_\mathrm{B}T}{\hbar\omega_r}\right)^2. \tag{4.13}$$

The presence of the harmonic trapping potential therefore restores the possibility for conventional BEC, driven by the saturation of thermal states. The transition occurs when the central phase-space density $\mathcal{D}(r = 0)$ reaches infinity, just as in a uniform system. However, the presence of a trap permits the infinite uniform gas critical density to be locally attained at the centre, whilst requiring a finite total number of atoms.

4.2.2 The Interacting Gas

BEC In a three-dimensional gas, ideal-gas BEC occurs at a critical atom number of $N_\mathrm{c}^0 \approx 1.202(k_\mathrm{B}T/(\hbar\omega))^3$, and a central phase-space density $\mathcal{D}^\mathrm{3D} \approx 2.612$. If weak repulsive interactions are switched on, both of these numbers are slightly shifted [79, 80]. To lowest order in a/λ_th, the critical atom number rises since more atoms are required to attain the critical central density [79]. However, interactions do not alter the BEC-like nature of the transition, which remains statistically driven by the saturation of excited states [78].

In a two-dimensional gas, even qualitatively a problem rears its head. The divergence of the critical ($\mu = 0$) density profile of Eq. (4.11) at the trap centre is acceptable for an ideal gas, but non-zero interactions would entail locally infinite energy density. More quantitatively, one may introduce interactions at a MF level by the substitution $\mu \to \mu - 2gn$ in Eq. (4.11), yielding an implicit equation for $\mathcal{D}$,

$$\mathcal{D}\left(r\right) = -\ln\left(1 - e^{\beta(\mu - V(r)) - \tilde{g}\mathcal{D}/\pi}\right). \tag{4.14}$$

The total atom number N is found by integration of $\mathcal{D}$ over the trap; this can either be done numerically, or by noting that integration over a two-dimensional area is equivalent to linear integration over the trap potential energy [104], since both vary as r^2. We introduce an effective potential

$$u\left(r\right) = \frac{1}{2}m\omega_r^2 r^2 + \frac{\tilde{g}}{\beta\pi}\left[\mathcal{D}\left(r\right) - \mathcal{D}\left(0\right)\right], \tag{4.15}$$

which for simplicity of subsequent integration limits we have defined such that it vanishes at $r = 0$. In terms of $u(r)$, the equation of state Eq. (4.14) becomes

$$\mathcal{D}\left(u\right) = -\ln\left(1 - e^{\beta(\Delta - u)}\right), \tag{4.16}$$

where the modified chemical potential $\Delta = \mu - \tilde{g}\mathcal{D}(0)/(\beta\pi)$ is referenced to the MF interaction potential at the trap centre.

The total atom number may now be obtained by converting the spatial integral into an integral over the effective potential $u(r)$,

$$\begin{aligned} N &= \frac{\pi}{\lambda_{\text{th}}^2}\int_{r=0}^{\infty}\mathrm{d}\left(r^2\right)\mathcal{D}\left(r\right) = \frac{\pi}{\lambda_{\text{th}}^2}\int_{u=0}^{\infty}\mathrm{d}u\left(\frac{\partial r^2}{\partial u}\right)\mathcal{D}\left(u\right), \\ &= \frac{2\pi}{m\omega_r^2\lambda_{\text{th}}^2}\int_{u=0}^{\infty}\mathrm{d}u\left(1 - \frac{\tilde{g}}{\beta\pi}\frac{\partial\mathcal{D}}{\partial u}\right)\mathcal{D}\left(u\right), \\ &= \left(\frac{k_{\text{B}}T}{\hbar\omega_r}\right)^2\left[g_2\left(e^{\beta\Delta}\right) + \frac{\tilde{g}}{2\pi}\mathcal{D}\left(0\right)^2\right]. \end{aligned} \tag{4.17}$$

Conventional, saturation-driven BEC should occur in the limit $\Delta \to 0$, which corresponds to the chemical potential reaching the lowest trap energy level. In the ideal gas case $\tilde{g} = 0$, Eq. (4.17) reassuringly recovers N_{c}^0 of Eq. (4.13). However, for any finite interactions $\tilde{g} > 0$ we note that the second term of Eq. (4.17) diverges with the central density. Therefore N grows indefinitely with increasing μ, the thermal states can accommodate any number of particles and BEC never occurs.

Another viewpoint is that the density of a critical ideal gas reaches infinity, but over an infinitesimal area resulting in a finite total atom number. However, in an interacting gas, the central curvature of the effective potential smoothly vanishes with increasing μ [92]. The gas becomes progressively 'more uniform' at the trap centre, leading to an infinite critical atom number and suppressing BEC. This

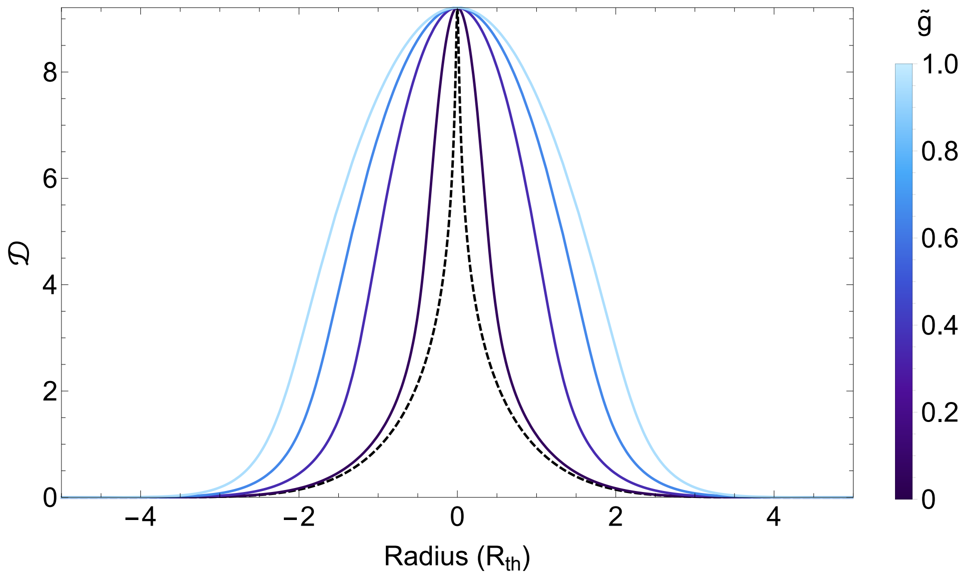

Figure 4.4: *The radial density profiles for a harmonically trapped two-dimensional Bose gas of various interactions strengths. The black dashed profile is an ideal gas with* $\tilde{\mu} = -10^{-4}$*. The blue lines are profiles for interacting gases, with* $\tilde{\mu}$ *chosen so that the central density coincides with the ideal gas. The radius is in units of thermal radius* $R_{th} = \sqrt{k_{\mathrm{B}}T/(m\omega_r^2)}$*, where* ω_r *is the planar harmonic trap frequency.*

---

is illustrated in Fig. 4.4, where we plot density profiles for various values of $\tilde{g}$ obtained by numerical solution of Eq. (4.14). All central phase-space densities are fixed to that of an ideal gas close to BEC, with $\tilde{\mu} = \beta\mu = -10^{-4}$. As the interaction strength is increased, the density profile broadens and more atoms are required to reach a given central density.

BKT Having seen that interactions suppress the occurrence of BEC, we now turn our attention to the possibility of a superfluid transition. Intuitively, in a harmonically trapped gas we anticipate a local BKT transition when the central density reaches $\mathcal{D}^{\mathrm{BKT}}$; within the LDA, the trap centre should locally behave as a uniform gas.

The critical number for BKT to occur in a harmonic trap, $N_{\mathrm{c}}^{\mathrm{BKT}}$, is therefore the trap population such that the central density reaches $\mathcal{D}^{\mathrm{BKT}}$. An intuitive approach would be to use our MF relation Eq. (4.17) which relates the central phase-space density $\mathcal{D}(0)$ and total atom number N. For large central densities $\beta|\Delta| \ll 1$, and $g_2\left(e^{\beta\Delta}\right) \approx g_2(1) = \pi^2/6$. This yields the MF result for the BKT critical number [92, 104],

$$\frac{N_{\mathrm{c}}^{\mathrm{BKT}}}{N_{\mathrm{c}}^{0}} = 1 + \frac{3\tilde{g}}{\pi^3}\ln^2\left(\frac{380}{\tilde{g}}\right). \tag{4.18}$$

In the ideal gas limit $\tilde{g} = 0$ one recovers the ideal gas critical number for BEC, a consequence of the central density for both BEC and BKT being infinite. This approach assumes that the gas displays full bosonic density fluctuations, implicit in our inclusion of a MF interaction potential $2gn$. One might worry about this for two reasons:

1. As the classical-field results of Section 3.5 indicate [96, 98], the suppression of density fluctuations is already significant at the BKT critical point. This enhances the density at a given chemical potential $\tilde{\mu}$, which permits $\mathcal{D}^{\mathrm{BKT}}$ to be reached at the trap centre with fewer total atoms than a MF approach would suggest.

2. An inconsistency is already manifest between the MF equation of state Eq. (4.14) and classical-field critical point Eq. (3.26). If one demands a critical phase-space density $\mathcal{D}^{\mathrm{BKT}}$ according to classical-field predictions, MF theory predicts a critical chemical potential,

$$\begin{aligned}\tilde{\mu}_{\mathrm{MF}} &= \frac{\tilde{g}\mathcal{D}^{\mathrm{BKT}}}{\pi} + \ln\left(1 - e^{-\mathcal{D}^{\mathrm{BKT}}}\right), \\ &= \frac{\tilde{g}}{\pi}\ln\frac{380}{\tilde{g}} + \ln\left(1 - e^{-\mathcal{D}^{\mathrm{BKT}}}\right), \\ &\approx \tilde{\mu}^{\mathrm{BKT}} + \tilde{g}\left(\frac{1}{\pi}\ln\frac{380}{13.2} - \frac{1}{380}\right), \\ &= \tilde{\mu}^{\mathrm{BKT}} + 1.07\tilde{g}. \end{aligned} \tag{4.19}$$

   Thus a MF approach overestimates the chemical potential predicted by classical-field theory for any non-zero interactions, again suggesting that the critical number of Eq. (4.18) should be an overestimate.

An attempt to improve upon the MF prediction of Eq. (4.18) was made in [99]. A hybrid model is adopted, which assumes that most of the trapped cloud is well-described by MF theory; from Eq. (3.33) we see that MF theory fails when the local chemical potential satisfies

$$\mu^{\mathrm{BKT}} - [\mu - V(r)] < \tilde{g}k_{\mathrm{B}}T. \tag{4.20}$$

When $\mu = \mu^{\mathrm{BKT}}$ the trap centre is critical. This condition then defines a fluctuation radius $R_{\mathrm{fluct}} = \sqrt{2\tilde{g}}\sqrt{k_{\mathrm{B}}T/(m\omega_r^2)}$, inside of which MF theory fails.

Within the fluctuation radius, the authors introduce a local *correlation density*, defined as the difference between the classical-field density of [98], and MF theory. The total density profile can then be constructed by summing a MF profile with chemical potential $\mu = \mu^{\mathrm{BKT}}$, and the correlation density within the fluctuation radius.

This hybrid profile is illustrated in Fig. 4.5, where we plot the density profiles at $\tilde{g} = 0.2$ corresponding to a MF critical profile neglecting suppression of fluctuations (green dashed line), a MF profile with chemical potential μ^{BKT} (blue dashed line) and the correlation density (red line).

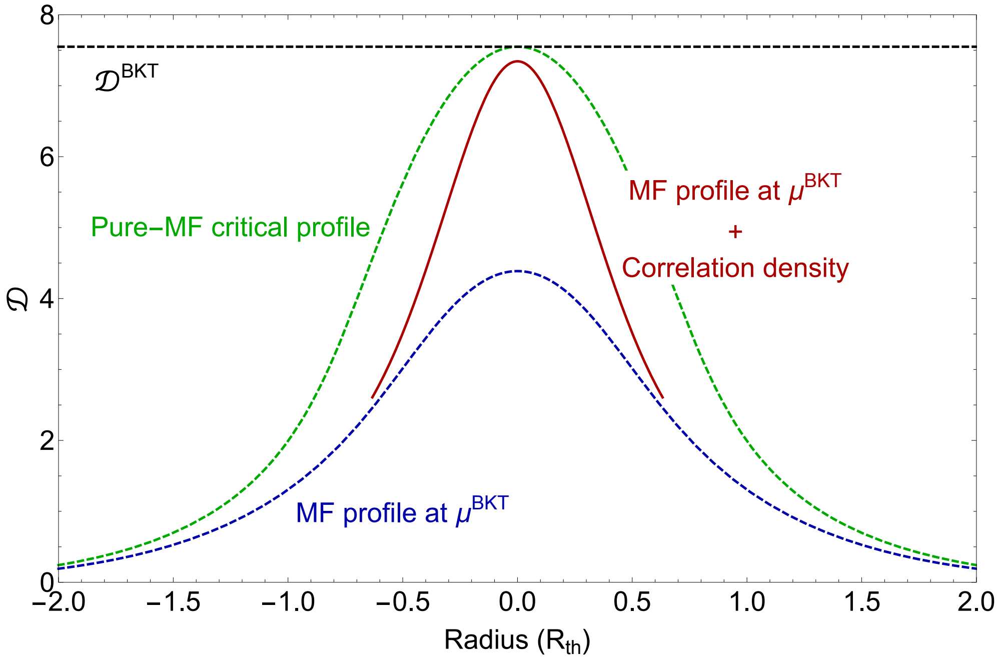

Figure 4.5: *The critical radial density profile at $\tilde{g} = 0.2$ for a fully fluctuating two-dimensional gas (green dashed line) and a model which takes into account suppression of fluctuations near the critical point; this hybrid profile is constructed from a MF profile at $\mu = \mu^{BKT}$ (blue dashed line) and a correlation density (red line) which accounts for the discrepancy between the MF and classical-field equations of state. Both profiles have a peak density $\mathcal{D}^{BKT}$ (black dashed line) at $r = 0$ where the BKT transition occurs. The small discrepancy between the hybrid profile and critical density is due to non-exactness of the heuristic analytic function for the correlation density (see text, and [99]).*

The MF critical number of Eq. (4.18) corresponds to the area underneath the green dashed curve, which overestimates the atom number required. To obtain the critical atom number accounting for suppression of fluctuations, we sum the contributions from a MF profile at $\mu = \mu^{\text{BKT}}$, and the correlation density. The former can be easily obtained from Eq. (4.17), by setting $\mu = \mu^{\text{BKT}}$. The correlation density is well-described by a heuristic analytic function of chemical potential [99], which is then integrated over the central region $r < R_{\text{fluct}}$. The result is,

$$\frac{N_{\text{c}}^{\text{BKT}}}{N_{\text{c}}^{0}} = \underbrace{1 + \frac{3\tilde{g}}{\pi^3}\ln^2\left(\frac{\tilde{g}}{16}\right) + \frac{6\tilde{g}}{16\pi^2}\ln\left(\frac{\tilde{g}}{16}\right)}_{\substack{\text{Contribution from MF} \\ \text{profile at } \mu = \mu^{\text{BKT}}}} + \underbrace{\frac{90\tilde{g}}{16\pi^2}}_{\substack{\text{Contribution from} \\ \text{correlation density}}} . \tag{4.21}$$

This result is plotted in Fig. 4.6, along with the MF result of Eq. (4.18). The discrepancy between the two is dramatic, and the curves only converge for exponentially small $\tilde{g}$.

The significant difference for small values of $\tilde{g}$, is a consequence of the slow divergence of $\mathcal{D}^{\text{BKT}}$ as $\tilde{g} \to 0$ and the universal value for the quasi-condensate density. The quasi-condensate fraction at the BKT critical point is $7.16/\ln(380/\tilde{g})$ [96],

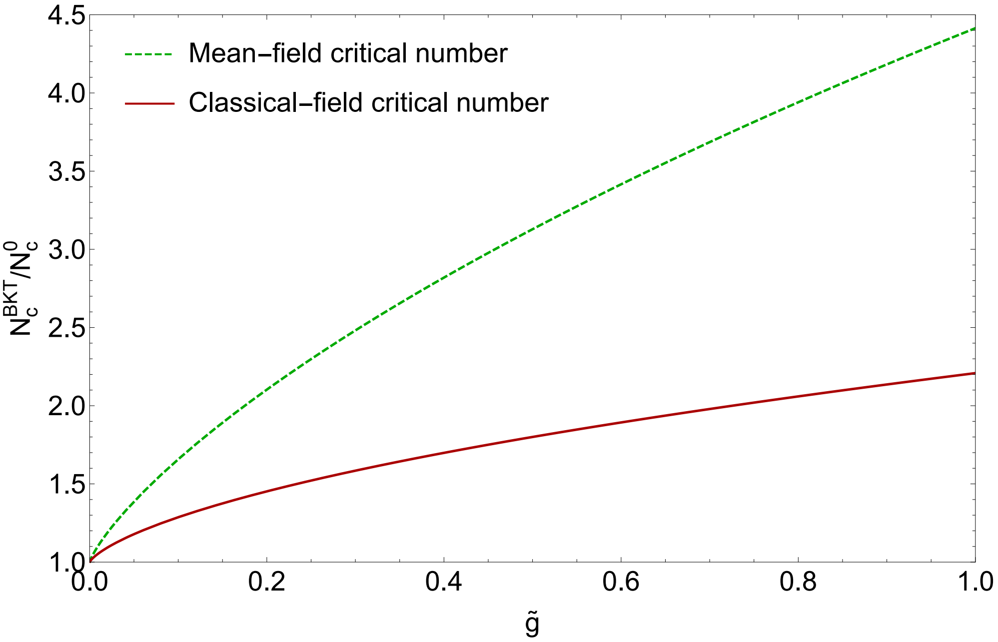

Figure 4.6: *The BKT critical number N_c^{BKT} for a harmonically trapped two-dimensional gas, scaled to the ideal gas BEC number N_c^0. The green dashed line is predicted using a MF model for a fully fluctuating Bose gas. The red line is based on a hybrid profile which accounts for the suppression of density fluctuations close to the BKT transition (see text).*

which falls to zero only logarithmically with reducing $\tilde{g}$; for illustration, it only falls below 0.5 at $\tilde{g} = 2 \times 10^{-4}$.

The suppression of fluctuations is therefore significant at the critical point even for extremely small interaction strength, allowing the central density to peak strongly above the MF theory. The majority of atoms lie outside the fluctuation radius R_{fluct}, are well-described by MF theory, and experience the full $2gn$ interaction potential. The net result is that the cloud density peaks strongly in excess of MF theory within a small central region, attaining the critical density with (globally) significantly fewer atoms than MF theory would suggest.

4.2.3 Applicability of Uniform System Results

The understanding of BKT in a harmonic trap of this Chapter arose from applying infinite uniform system results within the LDA. However, 'real-world' harmonic trapping potentials are of finite extent, with a lengthscale set by $\sqrt{\hbar/(m\omega_r)}$ and the planar eigenstates have a finite energy spacing $\hbar\omega_r$.

The BKT mechanism is mediated by the proliferation of free vortices in a superfluid, which requires the possibility of in-plane dynamics in order to have a spatially varying superfluid phase. This necessitates that the superfluid wavefunction has contributions from multiple planar trap eigenstates; thus at the critical point the superfluid interaction energy $gn_{\mathrm{s}} = 2\tilde{g}k_{\mathrm{B}}T/\pi$ should be much larger than the planar eigenenergy spacing. One can therefore apply infinite uniform system results to the centre of a harmonic trap if

$$\hbar\omega_r \ll \frac{2\tilde{g}k_{\mathrm{B}}T}{\pi}. \tag{4.22}$$

The legitimacy of LDA is also discussed in [57]. The authors demand that when the trap centre is locally critical, the healing length should be much smaller than the radius R_{fluct} of the fluctuation region in which beyond-MF effects contribute. This gives an essentially identical condition to Eq. (4.22).

BEC-BKT crossover in a finite system Whereas in the thermodynamic limit of $\omega \to 0$, $N\omega^2 = \text{const.}$ the transition would be BKT-like for all $\tilde{g} > 0$, and BEC-like strictly for $\tilde{g} = 0$, Eq. (4.22) implies that in a finite system the two transitions actually meet in a crossover region of finite width in $\tilde{g}$-space. The BEC transition also extends into $\tilde{g} > 0$; for finite planar level spacing $\hbar\omega_r$ BEC is reached[1] for a finite critical $\mathcal{D}$.

For our planar trapping frequency[2] of $\omega_r \approx 2\pi \times 37.7$ Hz the critical phase-space density for BEC is ~ 13 [51], which is smaller than $\mathcal{D}^{\mathrm{BKT}}$ for $\tilde{g} \lesssim 10^{-3}$. Furthermore, Eq. (4.22) indicates that the BKT transition should become badly defined for $\tilde{g} \lesssim 10^{-2}$. In our experiment of Chapters 5 - 8 we investigate $0.05 \lesssim \tilde{g} \lesssim 0.5$, with the lower limit set by our finite momentum resolution[3] and this crossover is not relevant in our case.

Fig. 4.7 illustrates the various criteria which must be satisfied if one is to observe the pure-two-dimensional BKT transition in the axial ground state of a harmonically-trapped gas. The horizontal lines denote the criterion that the superfluid be kinematically two-dimensional, quantified by Eq. (4.9). The curved lines denote the criterion that planar superfluid dynamics are possible at the BKT critical point, quantified by Eq. (4.22). Each criterion is interaction-dependent, and are sketched for a range of $\tilde{g}$. The horizontal dashed black line marks the condition $k_{\mathrm{B}}T = \hbar\omega_z$, which gives an approximate temperature scale such that the presence of atoms in axial excited states do not significantly affect the ground state physics. The red point denotes our specific experimental conditions which satisfy all criteria; we therefore expect pure-two-dimensional BKT physics to be addressable in our system for $\tilde{g} \gtrsim 10^{-2}$.

---

[1] The definition of BEC outside the thermodynamic limit is slightly difficult; here it is taken as a point beyond which the ground state occupation grows sharply whilst the occupation of excited states remains approximately constant.

[2] See Chapter 6.

[3] This is discussed in Section 6.3.3.

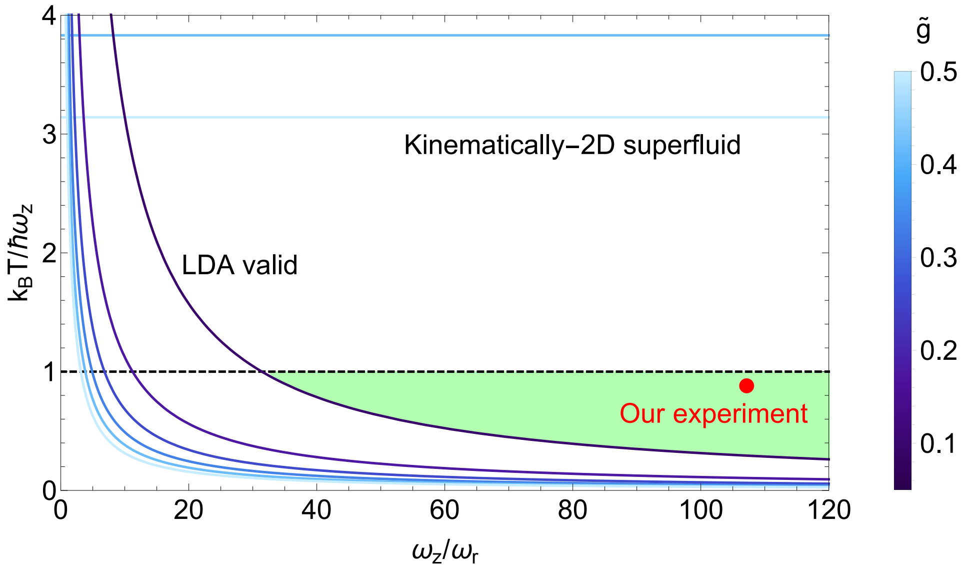

Figure 4.7: *Necessary criteria for a 'pure-two-dimensional' BKT transition to occur in a harmonically-trapped gas (see text). Three conditions must be satisfied: the superfluid must be kinematically two-dimensional (horizontal coloured lines), planar superfluid dynamics must be possible (curved coloured lines), and the majority of atoms should reside in the axial ground state (dashed black line). The green shading denotes the region in which all conditions are satisfied. Our experiment (red point) satisfies all conditions for* $\tilde{g} \gtrsim 10^{-2}$. *The minimum and maximum values of* $\tilde{g}$ *plotted, 0.05 and 0.5 respectively, correspond to the bounds of interaction strength addressed in our experiment.*

4.2.4 Comparison with Quantum Monte-Carlo

Our understanding of the BKT transition in a harmonically trapped gas is based upon two assumptions, which have been addressed and justified in preceding Sections.

- That in the case of a kinematically two-dimensional system, the axial ground state should display pure-two-dimensional physics. This was discussed in Section 4.1.
- That uniform gas results for the BKT transition can be applied to a harmonic gas, within the LDA. We expect that this should be valid in the limit of Eq. (4.22).

As a check of this approach, we can compare our predictions for the BKT critical point to the results of QMC simulations for a harmonically trapped, quasi-two-dimensional system [99, 102]. Two results are provided for different trap parameters, based upon specifics of experiments at ENS [9] and NIST [57]. These specifics are noted in Table 4.1, along with the QMC predictions for the BKT critical temperature T^{BKT}.

These results can be compared with the predictions based on applying pure-two-dimensional theory to the axial ground state. Setting $T = T^{\mathrm{BKT}}$ from Table 4.1,

	ENS	**NIST**
$\boldsymbol{\tilde{g}}$	0.13	0.02
$\boldsymbol{\omega_z/2\pi}$	3 kHz	1 kHz
$\boldsymbol{\omega_r/2\pi}$	50 Hz	20 Hz
$\boldsymbol{N}$	$20,000$	$17,900$
$\boldsymbol{T}^{\mathrm{BKT}}$ **(nK)**	186	74

Table 4.1: *BKT critical temperatures T^{BKT}, calculated by QMC [99, 102], for two different trap configurations.*

Eq. (4.21) gives the critical axial ground state numbers as 13,200 and 10,600 for the ENS and NIST experiments respectively. The axial excited state population can be calculated within a MF model for the axial levels (presented in Section 7.2.3), and one finds excited state numbers of 6,800 and 7,500 respectively.

This results in total critical numbers of 20,000 and 18,100 for the two experiments, in superb agreement with the results of QMC. This lends support to the applicability of pure-two-dimensional results to the axial ground state, and the validity of Eq. (4.21) which applies uniform system classical-field results to the case of harmonic trapping.

4.2.5 Unification of BEC and BKT

The results presented in this Section suggest that the two very different transitions, the statistically-driven BEC and interaction-driven BKT, should continuously connect as interactions are tuned to zero. Whereas in a uniform system one is precluded from following the BKT transition to the ideal gas limit $\tilde{g} \to 0$ by the diverging critical atom number, the presence of a harmonic trap results in a finite critical number at all interaction strengths. The harmonic potential of most ultracold atomic systems therefore offers an opportunity to observe this crossover, and ascertain exactly how the BKT critical point converges onto that for BEC. An experimental work confirming this unification is the topic of the remainder of this thesis.

Chapter 5

Experimental Overview

5.1 Introduction

In Chapters 3 and 4, we discussed the low-temperature phases available in a two-dimensional Bose gas. In a uniform planar trapping potential, BEC is precluded since the associated critical phase-space density is infinite. However, an interacting gas undergoes the BKT superfluid-normal transition at a critical phase-space density $\mathcal{D}^{\mathrm{BKT}} = \ln(380/\tilde{g})$ where $\tilde{g}$ is a dimensionless measure of interaction strength. This is a fundamentally-interaction driven transition mediated by the proliferation of free vortices, topological defects which can only exist in an interacting system.

As the interaction strength approaches zero, the critical density $\mathcal{D}^{\mathrm{BKT}}$ diverges, and approaches the infinite critical density for BEC. Furthermore, the critical chemical potential $\mu^{\mathrm{BKT}} \to 0$, again recovering the BEC result. This suggests that the critical points of the two conceptually very different phase transition should be continuously connected as a function of $\tilde{g}$, where the BEC critical point is recovered as the ideal-gas limit of the BKT transition. In a uniform system it is not possible to follow this connection, due to the divergent atom number required. However, as Section 4.2 addressed, in the case of harmonic in-plane trapping the critical atom number for both ideal-gas BEC and interacting-gas BKT is finite. The transition occurs when the trap centre locally reaches the uniform-system critical density and one is effectively probing uniform system physics; however, the presence of the harmonic trapping potential results in a finite critical atom number at all interaction strengths.

Whereas most condensed matter experiments in two-dimensional systems such as superfluid He films [53], exciton-polariton condensates [54] and thin-film superconductors [52] utilise a uniform trapping potential which precludes explicit observation of this unification, experiments with ultracold atomic gases typically employ harmonic trapping potentials [9, 55–68]. In this experimental work, we directly observe the unification of the BKT transition with the ideal-gas BEC limit in a harmonically-trapped two-dimensional gas with tuneable interaction strength.

In Section 5.2 we outline previous work on trapped two-dimensional atomic gases, in particular studies of the BKT transition. Section 5.3 overviews the relationship between the correlation function of a gas and its momentum distribution, which forms the basis of our method for identifying the onset of extended coherence; this provides an experimentally convenient signature of either the BKT or BEC transition.

Our experimental setup for trapping and probing two-dimensional gases is described in Chapter 6. The experiment itself, extraction of relevant gas quantities and resulting critical parameters for the BKT transition are presented in Chapter 7, and finally Chapter 8 summarises the conclusions which may be drawn from our work, and offers an outlook on future research possibilities.

5.2 Previous Experimental Work

The BKT transition was first conclusively observed experimentally in thin-films of liquid ^{4}He [53], where the characteristic discontinuous jump in superfluid density was detected as a shift in the frequency of a torsional pendulum. In the following years, aspects of BKT physics have been addressed in systems as diverse as thin-film superconductors [52], Josephson-junction arrays [52] and exciton-polariton systems [54].

Whilst well-suited to superfluid fraction measurements, condensed matter experiments are somewhat limited in the parameters which may be controlled. In liquid He experiments for example, temperature can be set by the film substrate, and two-dimensional density varied by changing the film thickness, but neither density, interaction strength nor trapping geometry can easily be tuned. Furthermore, the interaction parameter $\tilde{g}$ in liquid ^{4}He films is estimated to be of order unity [98], making theoretical approaches difficult.

By contrast, both the density and temperature of two-dimensional ultracold gases can easily be controlled. Trapping potentials are provided by sculpted optical and magnetic fields; the resultant potentials are extremely flexible, and have enabled experiments to address the cases of harmonic [9, 55–68], uniform [105] and two-dimensional lattice [66] planar trapping geometries.

Importantly, the precise control over interaction strength afforded by Feshbach resonances [2] opens the possibility of addressing any interaction regime, from strongly interacting to the ideal gas limit [61, 66], within a single experimental arena. The realisation of two-dimensional cold gases within the weakly-interacting limit $\tilde{g} \ll 1$ opens a regime in which quantitative, theoretical descriptions become possible [51, 96, 98], and which is precluded by condensed matter systems.

In the context of investigative ease, cold two-dimensional gases can be addressed in both real-space and momentum-space, and interference techniques give access

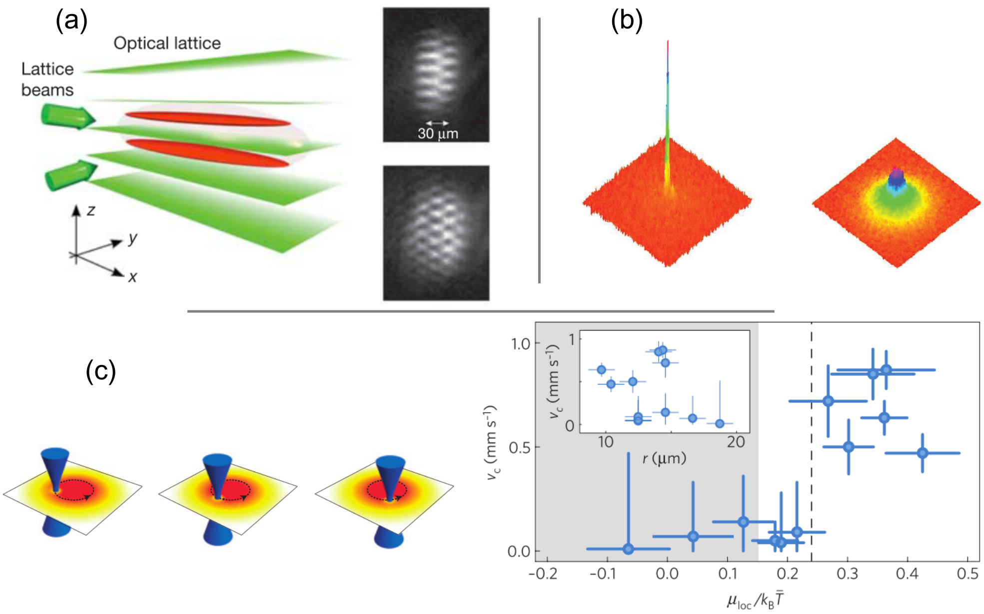

Figure 5.1: *Various signatures of the BKT transition have been observed in ultracold gases. (a) Interference between two quasi-two-dimensional planes of atoms revealed a proliferation of vortices above a critical temperature [9]; these are revealed as discontinuities in the interference fringes. (b) Complimentary momentum-space (left) and real-space (right) images show a sharp increase in the extent of coherence [58], whilst spatially nothing dramatic is observed. (c) Stirring a harmonically trapped two-dimensional gas at various radii reveals a discontinuous jump in the critical velocity for heating, signifying a jump in superfluid density at some critical chemical potential [63].*

---

to the phase of the order parameter, yielding information regarding correlation functions [9, 57], proliferation of vortex phase defects [9, 65] and phase fluctuations [64, 106]. Cold atom systems therefore offer a tantalising combination of experimental feasibility and theoretical tractability, permiting quantitative predictions [51, 96, 98] to be rigorously tested in a controllable, tuneable system.

The BKT transition was first observed in ultracold gases in 2006 at ENS [9]. The proliferation of vortices above a critical temperature was revealed by interfering two two-dimensional atomic planes; vortices manifested themselves as dislocations in the interference pattern. In the following years, experiments identified the anticipated growth in the extent of coherence close to the transition [9, 56–58, 60, 61, 68], and the discontinuous appearance of a non-zero superfluid fraction [63]; some of these experiments are depicted in Fig. 5.1.

In addition to confirming important features of the BKT transition, cold gas experiments have made manifest the importance of beyond-MF critical physics. As the transition is approached a marked departure from MF physics is apparent even on the normal side; various studies identified a gradual suppression of density fluctuations [61], reduction in compressibility [58], reduction in interaction energy [62] and enhanced occupation of low-momentum states [57, 60] with respect to MF theory.

In Section 3.5 we introduced the classical-field analysis of weakly-interacting two-dimensional gases [96, 98], which attempts to account for such non-perturbative, beyond-MF critical behaviour. The resultant equation of state [98], was observed to provide a superb description of quasi-two-dimensional trapped Bose gases, in experiments at ENS [59, 62] and Chicago [61, 66]. Not only were the measured density profiles at fixed interaction strength reproduced very well by theory, but the ability to tune interaction strength allowed confirmation of the predicted universal form for the equation of state [61, 66]. Additionally, density was observed to depend purely upon $\tilde{\mu} = \mu/(k_{\mathrm{B}}T)$, confirming the predicted scale invariance of the weakly-interacting two-dimensional Bose gas.

Whilst many experiments provided information about the behaviour of a two-dimensional gas in the vicinity of the BKT point, relatively few quantitatively identified the critical parameters. This is rendered difficult by two factors: First, the infinite order of the BKT transition precludes any dramatic or sudden behaviour in real-space [57, 58, 61, 62, 68]. The equation of state displays no discontinuity or sharp feature at the critical point, aside from the superfluid fraction which is not straightforward to quantify in an ultracold gas[1]. Second, the wide fluctuation region surrounding the BKT critical point [96, 98, 99] means that MF theory gradually becomes invalid as the transition is approached, rather than any sudden failure at the transition [60].

Therefore, whilst various aspects of the BKT transition have been addressed at specific interaction strengths, a systematic study of the BKT critical point, how it varies with interaction strength, and in particular how it approaches the ideal gas limit, has been lacking. The only previous experiment to employ tuneable interactions, in Chicago, has focused on the interaction dependence of the equation of state [61, 66]. Recent experiments offered confirmation of both scale invariance and universality, but being limited to *in situ* measurements could not directly reveal the critical point.

In the next Section, we overview our method for identifying the BKT transition, before moving on to our particular experimental work, which forms the remainder of this thesis.

5.3 Identifying the Critical Point

There are several experimental signatures of the BKT transition that might be employed to identify the critical point. As outlined in Section 5.2, previous experiments have observed the onset of superfluid behaviour [67], the proliferation of vortices [9], the width of the *in situ* density profile [57] and the appearance of a significant low-momentum fraction [56–58, 60, 68].

In this work, we systematically identify the critical point for the onset of extended coherence for a wide range of interaction strengths, $0.05 < \tilde{g} < 0.5$. Whether the

---

[1] This discontinuity was directly observed in a trapped Bose gas in [63].

low-temperature transition is BEC- or BKT-like, at the critical point one anticipates a sharp growth in the range of coherence [51, 100, 102, 107]. In the case of BEC this is a consequence of condensation into a single state[1], whereas in the BKT case it is due to the transition to a correlation function that decays algebraically rather than exponentially with separation[2]. The appearance of extended coherence provides an experimentally convenient probe of the critical point, since in a uniform system the correlation function $g^{(1)}(\mathbf{r})$ is revealed as the Fourier transform of the momentum distribution $n(\mathbf{k})$.

This relation is slightly modified for the case of an inhomogenous system. The momentum distribution $n(\mathbf{k})$ is the number of atoms in a momentum-space element $\mathrm{d}^2\mathbf{k}/(2\pi)^2$, and is related to momentum occupation numbers by $n(\mathbf{k}) = A\left\langle \hat{a}^{\dagger}_{\mathbf{k}}\hat{a}_{\mathbf{k}}\right\rangle$ where A is some system area which will not appear explicitly in our final result. The momentum distribution can be rewritten in spatial field operators,

$$\begin{aligned} n\left(\mathbf{k}\right) &= A\left\langle \hat{a}^{\dagger}_{\mathbf{k}}\hat{a}_{\mathbf{k}}\right\rangle, \\ &= \int \mathrm{d}^2\mathbf{r} \int \mathrm{d}^2\mathbf{r}'\; e^{i\mathbf{k}\cdot(\mathbf{r}-\mathbf{r}')} \left\langle \hat{\Psi}^{\dagger}\left(\mathbf{r}\right)\hat{\Psi}\left(\mathbf{r}'\right)\right\rangle, \qquad \mathbf{a} = \mathbf{r}-\mathbf{r}' \\ &= \int \mathrm{d}^2\mathbf{r} \left[\int \mathrm{d}^2\mathbf{a}\; e^{i\mathbf{k}\cdot\mathbf{a}} \left\langle \hat{\Psi}^{\dagger}\left(\mathbf{r}\right)\hat{\Psi}\left(\mathbf{r}-\mathbf{a}\right)\right\rangle\right]. \end{aligned} \tag{5.1}$$

We can identify $g^{(1)}(\mathbf{r}, \mathbf{a}) = \left\langle \hat{\Psi}^{\dagger}\left(\mathbf{r}\right)\hat{\Psi}\left(\mathbf{r}-\mathbf{a}\right)\right\rangle$ as a local correlation function, whose Fourier transform with respect to $\mathbf{a}$ integrated over the entire sample is revealed in the momentum distribution.

A change in the functional form of $g^{(1)}(\mathbf{r})$ leads to a dramatic change in its values at distances much larger than the thermal wavelength λ_{th} [51]. The Fourier relation of Eq. (5.1) implies that the appearance of increased coherence over a large lengthscale L will manifest itself as enhanced population of momentum states $k \lesssim 2\pi/L$. Any change in the functional form of $g^{(1)}$ should be increasingly pronounced at larger L, and the consequent change in the momentum distribution should be progressively more dramatic with lower k. Thus, unlike the in-trap density distribution, which varies very smoothly through the BKT critical point [57, 58, 61, 62], $n(\mathbf{k})$ can provide a dramatic signature of the phase transition [58].

---

[1] See Section 2.1.1.

[2] See Section 3.3.

Chapter 6

Experimental Setup and Characterisation

Our experiment was carried out with a gas of ^{39}K atoms at a temperature $T \approx 170$ nK, confined in an optical harmonic trap with radial and axial trapping frequencies $(\omega_r, \omega_z) \approx 2\pi \times (37.7, 4040)$ Hz, giving a trap-frequency ratio $> 10^2$. As illustrated in Fig. 4.7, the axial level spacing is sufficiently large such that the superfluid is kinematically two-dimensional[1], planar superfluid dynamics are possible[2], and the majority of atoms reside in the axial ground state[3].

A great advantage of a large aspect ratio ω_z/ω_r is that the critical atom numbers scale quadratically with this quantity. Since $N_{\mathrm{c}}^{\mathrm{BKT}} \sim (k_{\mathrm{B}}T/(\hbar\omega_r))^2$, the aspect ratio $(\omega_z/\omega_r)^2$ provides an upper bound to the allowed critical numbers if the transition is to be crossed in the quasi-two-dimensional limit. In our system this results in $N_{\mathrm{c}}^{\mathrm{BKT}} \lesssim 10^4$, sufficiently high to be easily observable, whilst $\hbar\omega_z/k_{\mathrm{B}} \approx 193$ nK, an easily attainable temperature regime.

Interactions were tuned by means of a Feshbach resonance centred on 402.5 G [15, 16]. The momentum distribution $n(\mathbf{k})$ was obtained via the 'momentum focusing' method [58,68,108,109] which obtained the momentum distribution exactly, with no admixture from the *in situ* spatial distribution. Imaging of the cloud was performed along the axial direction, giving access to the full planar momentum distribution.

Each of these components shall be addressed in turn. For each, we first give a conceptual overview, followed by more specific experimental characterisation.

---

[1] See Section 4.1.

[2] See Section 4.2.3.

[3] See Section 4.1.

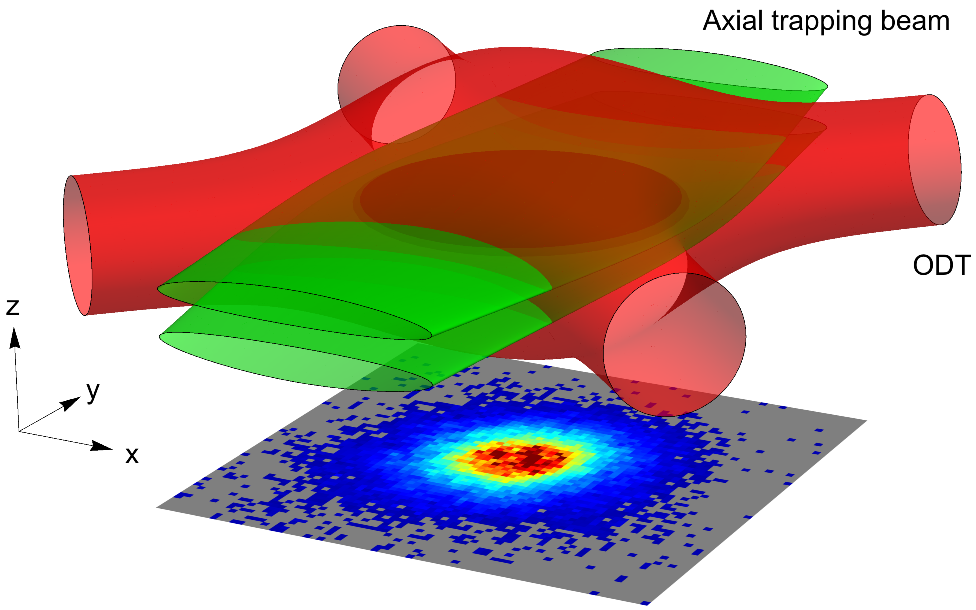

Figure 6.1: *The constituent beams of our optical trapping setup. Tight axial confinement is provided by two 'blades' of blue-detuned light, whereas a crossed red-detuned beam (ODT) provides in-plane confinement; surfaces represent equipotentials of their respective beams. A typical vertical absorption image of a trapped two-dimensional atomic cloud (dark disk) is projected below the trap.*

6.1 Optical Trap for Two-Dimensional Confinement

Our atomic trapping potential is generated by light potentials, which are a central tool in ultracold atomic physics. By tuning a laser to be either red- or blue-detuned from an atomic resonance, atoms experience either an attractive or repulsive potential proportional to the light intensity. Available trapping potentials are limited only by the ability to sculpt light into the desired geometry; such diverse trapping configurations as harmonic traps, uniform box traps [110] and optical lattices in one, two and three dimensions [111] have been realised. An overview of light potentials and the use of Fourier optics to generate intricate optical patterns is given in Appendix B.

In our system, two-dimensional confinement is generated by two repulsive 'blades' of light at $\lambda = 532$ nm which tightly confine atoms in the axial direction. To provide harmonic in-plane trapping, we superimpose our axial potential with an attractive optical dipole trap (ODT) consisting of a red-detuned beam at $\lambda = 1064$ nm crossed in a bow-tie configuration. The complete optical trapping setup is illustrated in Fig. 6.1, along with an absorption image of a trapped two-dimensional cloud, taken along the axial (vertical) direction.

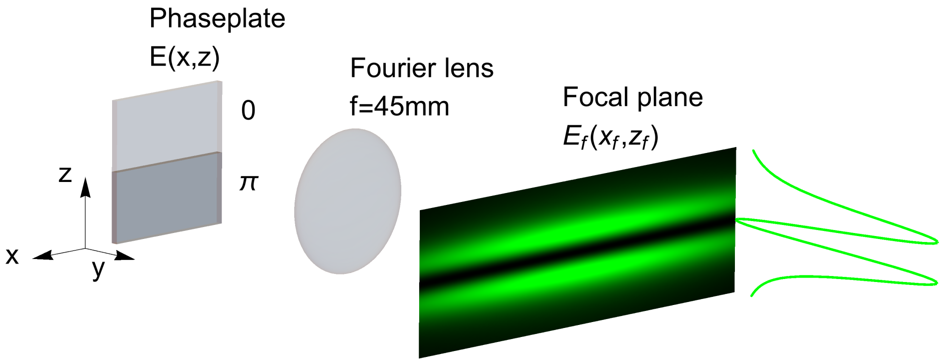

Figure 6.2: *The phaseplate used to generate our axial trapping potential. The plate imprints a 0-π phase pattern onto a Gaussian beam, and a lens projects the Fourier transform of the resulting amplitude pattern $E(x,z)$ onto its focal plane, giving $E_f(x_f,z_f)$. The atoms occupy the resulting potential landscape; the intensity pattern is illustrated, along with a 1D cut through $x_f = 0$.*

6.1.1 Axial Trapping

Our axial potential is derived from the Fourier spectrum of a 0-π phase pattern imprinted on a blue-detuned Gaussian beam. The beam is first passed through a phaseplate, which imposes a relative retardation of $\lambda/2$ between vertical halves, and the resulting spectrum is projected onto the atoms by a 'Fourier lens'. The phaseplate is depicted in Fig. 6.2. Qualitatively, one expects destructive interference between the two phaseplate halves to produce a nodal intensity plane between two sheets of light. This technique for two-dimensional trapping is also employed in [59,112], and our optical setup was designed by Naaman Tammuz [113].

Quantitatively, for a Gaussian incident beam with waist w_z in the z-direction, the associated 1D amplitude profile at the phaseplate is,

$$E_{\text{p.p.}}(z) \sim e^{-z^2/w_z^2} \times \begin{cases} 1 & : z < 0 \\ -1 & : z > 0 \end{cases} \tag{6.1}$$

Decomposing this amplitude pattern into wavenumbers q in the z-direction, we obtain the spectrum:

$$\begin{aligned} \tilde{E}_{\text{p.p.}}(q) &\sim e^{-q^2 w_z^2/4}\left[\int_{-\infty}^{-iqw_z/2} \mathrm{d}t\ e^{-t^2} - \int_{-iqw_z/2}^{\infty} \mathrm{d}t\ e^{-t^2}\right], \\ &\sim e^{-q^2w_z^2/4}\operatorname{erfi}\left(\frac{qw_z}{2}\right). \end{aligned} \tag{6.2}$$

where erfi(z) denotes the imaginary error function[1]. By placing a lens after the phaseplate, a focal distance f before the atoms, this spectrum is mapped onto

---

[1] $\operatorname{erfi}(z) = -\frac{2i}{\sqrt{\pi}}\int_0^{iz} e^{-t^2}\mathrm{d}t$.

amplitude at the atoms $E_f(z_f)$ according Eq. (B.7):

$$E_f(z_f) \sim e^{-z_f^2/W_z^2} \mathrm{erfi}\left(\frac{z_f \pi w_z}{\lambda f}\right), \tag{6.3}$$

which is a modulated Gaussian of waist $W_z = \lambda f/(\pi w_z)$. The atoms occupy the resulting nodal plane, which provides a tight axial confinement.

The prefactor of Eq. (6.3) is fixed by the total power P of the beam. Including x-dependence gives an intensity pattern:

$$I_f(x_f, z_f) = \frac{2P}{\pi W_x W_z}\, e^{-2x_f^2/W_x^2}\, e^{-2z_f^2/W_z^2} \left|\mathrm{erfi}\left(\frac{z_f}{W_z}\right)\right|^2. \tag{6.4}$$

The trapping frequency can be found by relating light intensity to the induced atomic potential via Eq. (B.3) and expanding about $z_f = x_f = 0$. We make use of $\mathrm{erfi}(z) \approx 2z/\sqrt{\pi}$ for $z \ll 1$, and equate the resulting quadratic-z_f potential to $(1/2)m\omega_z^2 z_f^2$. This yields a trapping frequency:

$$\omega_z(x_f) = 2\pi \times 0.721 \left(1 - \frac{x_f^2}{W_x^2}\right) \sqrt{\frac{P}{W_x W_z^3}}\ \mathrm{MHz}, \tag{6.5}$$

where P is the total beam power in watts, and waists W_x, W_z are in microns.

The full optical setup is illustrated in Fig. 6.3. A compact diode laser[1] provides 1.8 W of light at 532 nm, with a beam waist of 750 μm. The laser output is first passed through an AOM, and the first-order diffracted beam used for the axial trapping which permits fast (< 1 μs) switching of the axial trap. A telescope expands the beam to a 1.5 mm waist, and a $\lambda/2$ waveplate followed by PBS ensures that a clean and stable polarisation propagates to the atoms.

It is beneficial for the axial light to propagate along the horizontal imaging axis, to facilitate alignment. Two dichroic mirrors[2], one before the Fourier lens and one after the atoms, are used to direct the green light whilst remaining transparent to $\lambda = 767$ nm which is used for the horizontal imaging.

In the x-direction, a cylindrical lens ($f = 500$ mm) focuses the beam and together with the Fourier lens ($f = 45$ mm) gives an x-collimated beam at the atoms, with $W_x = 135$ μm.

At the Fourier lens, the beam is collimated in the z-direction with waist $w_z = 1.5$ mm, giving a waist at the atoms of $W_z = \lambda f/(\pi w_z) = 5.1$ μm. We therefore anticipate an axial frequency upper bound[3] from Eq. (6.5) of $\omega_z \approx 2\pi \times 7.2$ kHz. This frequency would correspond to a temperature $\hbar\omega_z/k_{\mathrm{B}} = 344$ nK, setting an easily attainable temperature scale for quasi-two-dimensional behaviour.

---

[1] Laser Quantum, Excel 532 nm.

[2] Semrock Inc. LM01-552-25.

[3] The laser outputs 1.8 W, some fraction of which is lost *en route* to the atoms.

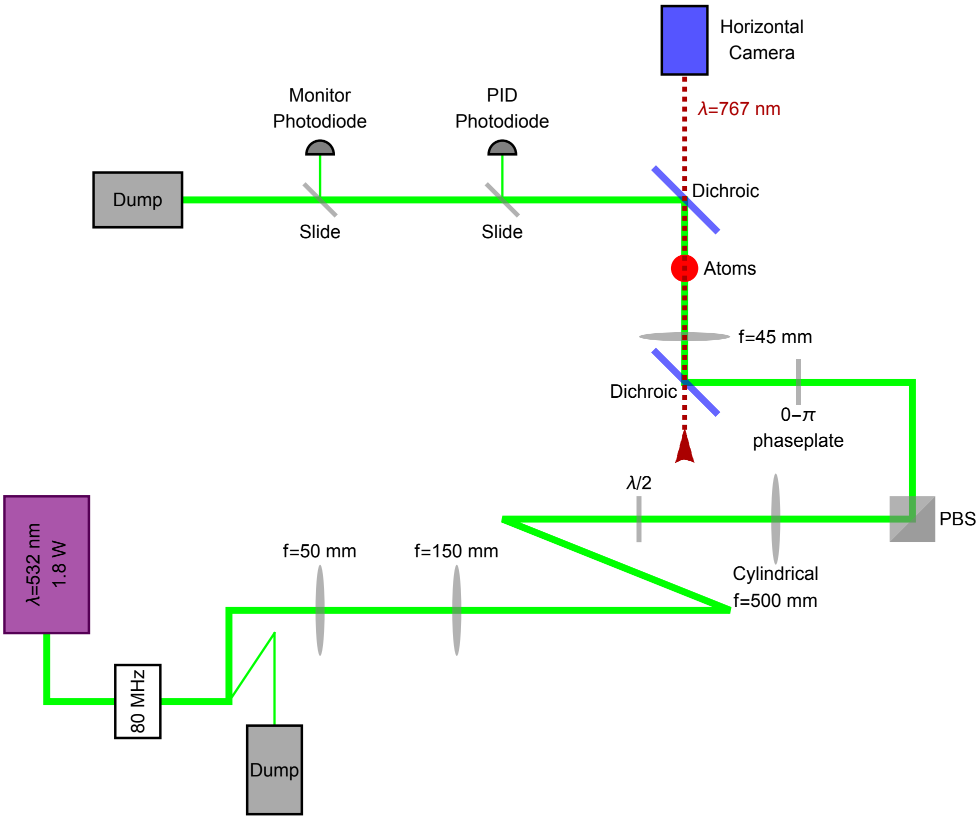

Figure 6.3: *The optical setup for the axial trapping potential (see text). For clarity all reflective mirrors are omitted.*

Anti-trapping The maximum ω_z is found exactly at $x_f = 0$, in the Fourier lens focal plane. Away from this point, the zero-point energy $E_0(x_f, y) = \hbar\omega_z(x_f, y)/2$ will fall, giving an effective 'anti-confinement'. From Eq. (6.5), the zero-point energy displays a quadratic x-dependence:

$$\begin{aligned} E_0(x) &= E_0(0)\left(1 - \frac{x_f^2}{W_x^2}\right), \\ &= E_0(0) - \frac{1}{2}m\varpi_x^2 x_f^2. \end{aligned} \tag{6.6}$$

We can therefore identify an anti-trapping transverse potential, of frequency $\varpi_x = \sqrt{\hbar\omega_z(0)/(mW_x^2)}$. For the numbers given above, this evaluates to $\varpi_x \approx 2\pi \times 10.1$ Hz.

Along the propagation direction of the beam, $\hat{y}$, a similar anti-trapping potential arises due to divergence of the z-focused beam. W_z displays a variation with distance y away from the focus,

$$W_z(y) = W_z(0)\sqrt{1 + \frac{y^2}{y_R^2}}, \tag{6.7}$$

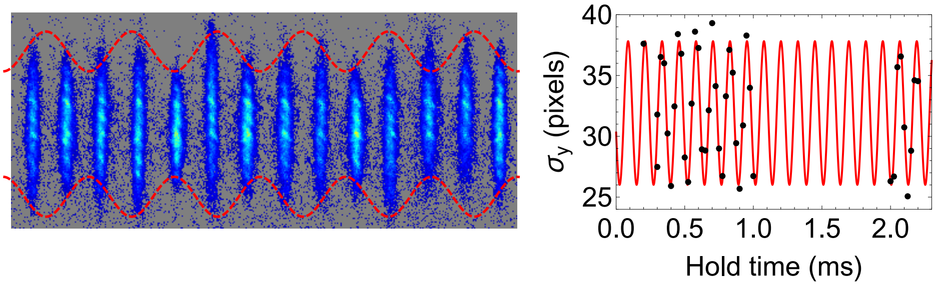

Figure 6.4: *Measurement of axial trapping frequency. The black points depict the variation in axial width σ_y of a BEC, after 17 ms ToF, for various trap hold times after exciting a monopole breathing mode. The red dashed lines are superimposed on the images to guide the eye.*

---

where $y_R = \pi W_z^2/\lambda = 154\ \mu$m is the Rayleigh length for a Gaussian beam focussed to W_z. Inserting into Eq. (6.5) and keeping quadratic terms in y^2/y_R^2, yields a variation in zero-point energy with y,

$$\begin{aligned} E_0(y) &= E_0(0)\left(1 - \frac{3y^2}{4y_R^2}\right), \\ &= E_0(0) - \frac{1}{2}m\varpi_y^2 y^2. \end{aligned} \tag{6.8}$$

The anti-trapping frequency in the propagation direction therefore evaluates to $\varpi_y = \sqrt{3\hbar\omega_z(0)/(4my_R^2)}$, which for the beam parameters above gives $\varpi_y \approx 2\pi \times 7.7$ Hz.

Power stabilisation After passing through the atom chamber, the axial trapping beam is terminated at a beam dump. A glass slide picks off a small beam fraction, which is directed onto a photodiode (see Fig. 6.3). The resulting photodiode output voltage is passed to a PID[1] whose error signal is fed back to the amplitude control of the initial AOM. This feedback permits control and stabilisation of the axial trapping power. We empirically find a bandwidth of $\gtrsim 5$ kHz, which is sufficient to avoid significant heating of atoms via fluctuations in the trapping beam power.

Axial trap frequency The frequency of axial trapping was determined from the breathing mode of an ideal gas BEC, and the experimental procedure is given in Appendix C. Fig. 6.4 shows a typical set of breathing mode ToF images, together with the variation in observed vertical Gaussian width σ_y with hold time.

---

[1] Made in-house by A. L. Gaunt.

We obtain[1] an axial frequency of

$$\omega_z = 2\pi \times (4040 \pm 6)\ \text{Hz}, \tag{6.9}$$

at a laser output power of 1.8 W. From the analytic frequency of Eq. (6.5) this implies a power of 560 mW incident on the atoms. Between the laser output and atoms, the axial trapping beam passes through 14 air-glass interfaces; some of the surfaces are AR coated for 532 nm, but we can estimate a potential compounded reduction of $0.96^{14} = 0.56$. Furthermore, the AOM diffraction efficiency of ≈ 0.8 would lead to a total power of $1.8 \times 0.56 \times 0.8 = 0.8$ W reaching the atoms. We also note that the axial trapping power after exiting the science cell is ~ 100 mW; however, this light has passed through the horizontal imaging optics, which are AR coated for 780 nm, and so this number can only provide a lower bound on the power at the atoms. Whether the lower axial frequency is purely due to power reduction, or whether imperfect beam profile and optic performance reduce the frequency, we make no definite conclusion on.

Nevertheless, this trapping frequency corresponds to an axial temperature scale of 193 nK, still easily achievable. Furthermore, the damping of the breathing mode is negligible over 18 oscillation cycles; fits were not improved by the inclusion of a damping envelope, implying excellent harmonic quality of the axial potential.

6.1.2 Planar Trapping

The axial trapping potential induces a large trapping frequency (~ 4 kHz) in the axial direction, and weak anti-trapping (~ 10 Hz) in-plane. Harmonic confinement is provided by two crossed attractive Gaussian beams; the optical setup of this ODT is outlined in [113, 114]. On each pass, the beam is focused to a waist of $\approx 140\ \mu$m. By design, the ODT waist, axial trapping transverse waist, and axial trapping Rayleigh length are all comparable. This ensures good matching between the two traps, such that atoms can inhabit the harmonic region of both beams without unnecessarily wasting laser power.

Planar trap frequency The planar trapping characteristics are determined by exciting an in-plane centre-of-mass oscillation of a BEC, and observing the resulting motion on the axial imaging system. From this evolution we can extract both eigenfrequencies of the planar trapping potential, and the eigenaxis orientations which are not generally along the camera (and hence image) axes. We assume that the planar trap is harmonic, with axes $\hat{x}'$, $\hat{y}'$ that lie at some angle θ to the camera axes. The trapping potential is then

$$V\left(x', y'\right) = \frac{1}{2} m\omega_{x'} x'^2 + \frac{1}{2} m\omega_{y'} y'^2. \tag{6.10}$$

---

[1] Taken 02.10.2014.

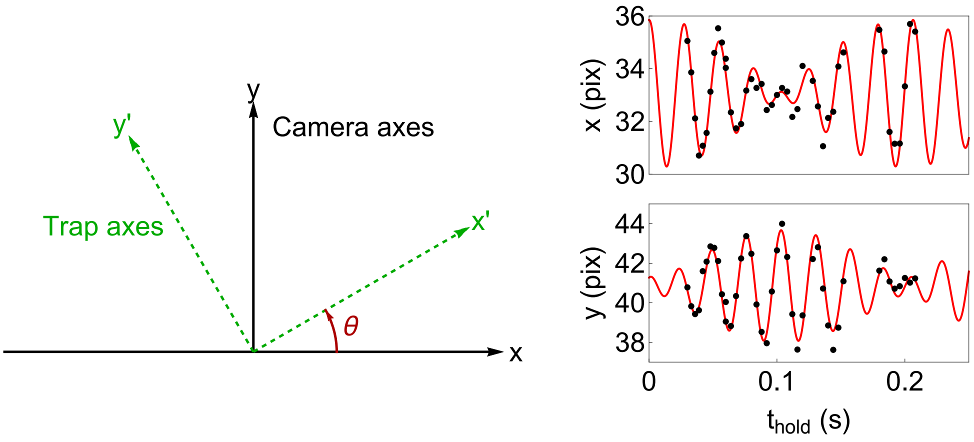

Figure 6.5: *In general, we assume trap axes to be related to camera axes by a rotation by θ. On the right we plot the displacement of an oscillating cloud along the horizontal (x) and vertical (y) camera axes. The red line is the coupled function of Eq. (6.12), fitted to an oscillating cloud in our focusing potential.*

A point in trap coordinates is related to camera coordinates via a rotation transformation,

$$\begin{pmatrix} x \\ y \end{pmatrix} = \begin{pmatrix} \cos\theta & -\sin\theta \\ \sin\theta & \cos\theta \end{pmatrix} \begin{pmatrix} x' \\ y' \end{pmatrix}. \tag{6.11}$$

We assume that the cloud oscillates independently along the trap eigenaxes; the observed motion along the camera axes should then be,

$$\begin{pmatrix} x(t) \\ y(t) \end{pmatrix} = \begin{pmatrix} \cos\theta & -\sin\theta \\ \sin\theta & \cos\theta \end{pmatrix} \begin{pmatrix} A\cos\left(\omega_{x'}t + \phi_{x'}\right) \\ B\cos\left(\omega_{y'}t + \phi_{y'}\right) \end{pmatrix}. \tag{6.12}$$

This yields a coupled fit function for $(x(t), y(t))$ with $\{A, B, \omega_{x'}, \omega_{y'}, \phi_{x'}, \phi_{y'}, \theta\}$ as fit variables[1]; we find trap parameters[2] of

$$\begin{aligned} \omega_{x'} &= 2\pi \times (33.9 \pm 0.5)\ \text{Hz}, \\ \omega_{y'} &= 2\pi \times (42.0 \pm 0.3)\ \text{Hz}, \\ \theta &= 64 \pm 6^\circ. \end{aligned} \tag{6.13}$$

We also repeated the frequency extraction in the absence of the axial trapping light[3]. This oscillation is illustrated in Fig. 6.5 and the extracted trap parameters

---

[1] A second method was to rotate the observed cloud coordinates $(x(t), y(t))$ by a variable angle, until the fitted amplitude of a single frequency component was maximised. The eigenfrequencies are obtained by single frequency fits to the rotated data sets. This approach yields identical frequencies to the first method, but slightly different eigenaxis angle θ. The two methods yield $\theta = 58^\circ$ and 70° with axial light present, $\theta = 41^\circ$ and 34° without. In practice we used an average of the two θ values, which corresponds to the value given in Eqs. (6.13) and (6.14).

[2] Taken 02.10.2014.

[3] Taken 03.10.2014.

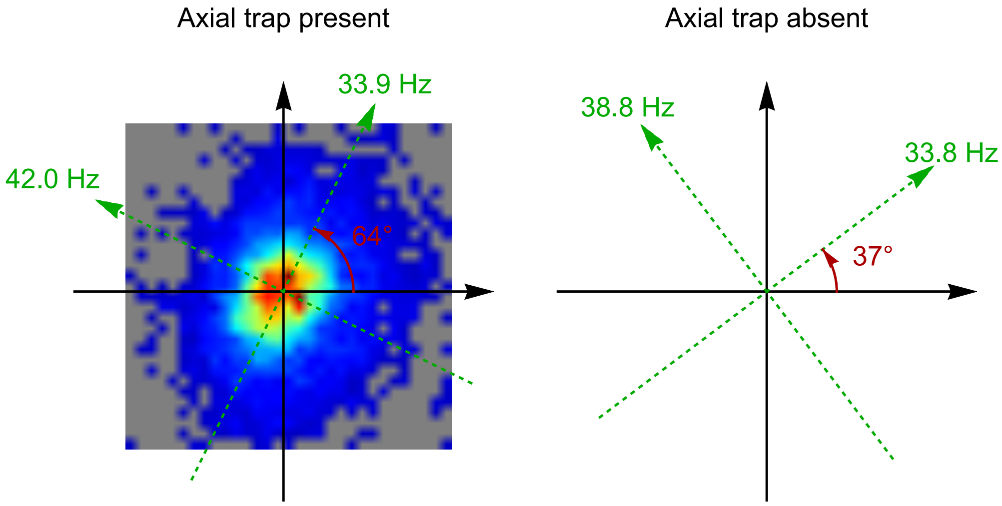

Figure 6.6: *The in-plane eigenaxes (green dashed lines) and frequencies both in the present of the axial trapping beam, and in their absence. The black lines are the axes of the vertical imaging camera. In the case of axial trapping being present, we also show an in situ image of a trapped cloud; the extracted eigenaxes agree excellently with the observed cloud asymmetry.*

are

$$\begin{aligned} \omega_{\text{foc},x'} &= 2\pi \times (33.8 \pm 0.2)\ \text{Hz}, \\ \omega_{\text{foc},y'} &= 2\pi \times (38.8 \pm 0.1)\ \text{Hz}, \\ \theta &= 37 \pm 3^\circ. \end{aligned} \tag{6.14}$$

These parameters will later be necessary to characterise the momentum focusing, used to extract the momentum distribution of a trapped gas (see Section 6.3).

We illustrate in Fig. 6.6 the planar trap geometry with and without axial trapping light present. In the case of axial trapping, we superimpose an *in situ* image of a two-dimensional cloud; the extracted eigenaxis orientation agrees excellently with the observed cloud asymmetry.

It is somewhat unanticipated that the presence of axial trapping light significantly modifies the planar trapping potential. In Section 6.1.1 we concluded that spatial variation of the axial trapping beam should lead to weak, approximately symmetric anti-trapping of ≈ 10 Hz; instead we observe an additional asymmetric trapping of ≈ 16 Hz. This may be caused by inhomogeneities in the axial trapping light, leading to an imperfect nodal plane. In the absence of the phaseplate, a Gaussian beam of 560 mW[1], wavelength 532 nm, and waists $(W_x, W_z) = (135, 5)$ μm would induce a potential of height 31 μK. For cloud temperatures of ∼ 100 nK, one needs imperfect destructive interference in the axial

---

[1] Estimated power at the atoms inferred from our measured axial frequency.

trapping nodal plane of only $\sim 0.3\%$ in order to appreciably distort the cloud shape.

Having characterised our two-dimensional trap, we conclude trapping frequencies of $(\omega_r, \omega_z) \approx 2\pi \times (37.7, 4040)$ Hz. Here, ω_r is the geometric mean of the in-plane trapping frequencies. Although the *in situ* cloud is anisotropic, we note that for any quantity Φ which depends upon the local potential $V(x,y) \propto \omega_x^2 x^2 + \omega_y^2 y^2$, an average or sum over the whole cloud can be recast as a circular integral:

$$\begin{aligned} &\int \Phi\left(\omega_x^2 x^2 + \omega_y^2 y^2\right)\, \mathrm{d}x\, \mathrm{d}y, \qquad \bar{x} = \frac{\omega_x}{\omega_r}\, x \quad , \quad \bar{y} = \frac{\omega_y}{\omega_r}\, y \\ = &\int \Phi\left(\omega_r^2 \bar{x}^2 + \omega_r^2 \bar{y}^2\right)\, \frac{\omega_r}{\omega_x}\, \frac{\omega_r}{\omega_y}\, \mathrm{d}\bar{x}\, \mathrm{d}\bar{y}, \\ = &\int \Phi\left(\omega_r^2 \bar{r}^2\right)\, \mathrm{d}^2\bar{r}. \end{aligned} \tag{6.15}$$

Therefore the momentum distribution and critical atom number in our anisotropic trap should be identical to a circular cloud of radial frequency ω_r, assuming validity of the LDA.

6.2 Tuning Interactions

In addition to sculpting the geometry of the confining potential, exploring the BEC-BKT crossover requires the ability to tune interatomic interactions. As discussed in Section 3.2, for a three-dimensional dilute Bose gas at low temperatures, the complicated actual interatomic potential can be represented by a contact potential, of strength $g_{3\mathrm{D}}$ [12]:

$$V\left(\mathbf{r}_1, \mathbf{r}_2\right) = g_{3\mathrm{D}}\delta\left(\mathbf{r}_2 - \mathbf{r}_1\right) = \frac{4\pi\hbar^2 a}{m}\delta\left(\mathbf{r}_2 - \mathbf{r}_1\right), \tag{6.16}$$

where a is the s-wave scattering length, a scalar scattering amplitude that is independent of the two-body relative momentum k. In a two-dimensional system, in which atoms are confined to the ground state of an axial harmonic potential with oscillator length $l_z = \sqrt{\hbar/(m\omega_z)}$, the scattering amplitude is in general k-dependent [115, 116]. However, in the limit $l_z \gg a$, usually well-satisfied by experiments, one can treat the gas as collisionally three-dimensional [51], whilst remaining kinematically two-dimensional.

The two-dimensional coupling constant g is then proportional to the three-dimensional scattering length: g is defined such that the interaction energy density is $(g/2)n^2$, where as usual n denotes the two-dimensional density. Then

$$\frac{g}{2}n^2 = \frac{g_{3\mathrm{D}}}{2} \int \mathrm{d}z\ n_{3\mathrm{D}}(z)^2 = \frac{2\pi\hbar^2 a}{m} \int \mathrm{d}z\ n_{3\mathrm{D}}(z)^2. \tag{6.17}$$

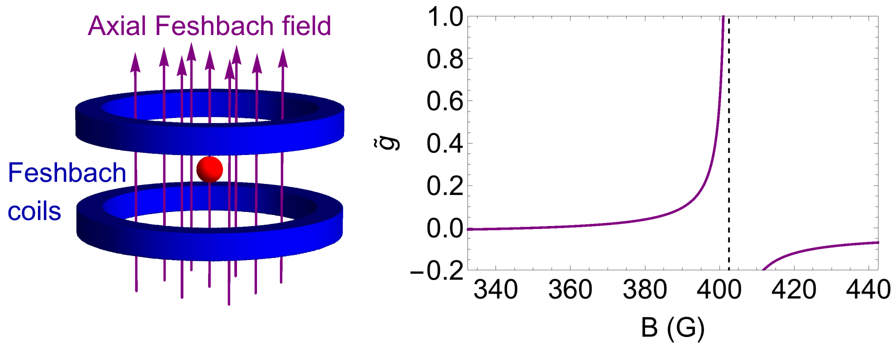

Figure 6.7: *The Feshbach coil arrangement, which produces a uniform magnetic field along the axial direction at the atoms (red sphere). On the graph we plot the variation in $\tilde{g}$ around a Feshbach resonance in the $|F, m_F\rangle = |1, 1\rangle$ state of ^{39}K, labelled in the low-field basis. The resonance is centred at* 402.5 *G, illustrated by the dashed black line. We assume an axial trapping frequency of 4 kHz.*

Inserting the axial ground state density $n_{3\mathrm{D}}(z) = ne^{-x^2/l_z^2}/(l_z\sqrt{\pi})$, yields

$$g = \frac{\hbar^2}{m}\sqrt{8\pi}\frac{a}{l_z} \qquad \rightarrow \qquad \tilde{g} = \sqrt{8\pi}\frac{a}{l_z}. \tag{6.18}$$

The tuneability of a via a Feshbach resonance[1] translates into the ability to tune $\tilde{g}$, allowing us to explore the crossover from ideal-gas BEC to interacting gas BKT within a single experimental setup[2].

Feshbach resonances were reviewed in the Introduction; we repeat some salient details here for convenience. For ^{39}K, the hyperfine state $|4\ ^2S_{1/2}, F = 1, m_F = 1\rangle$ (expressed in the low-field basis) displays a resonance centred at 402.5 G, with a width of 52 G [15, 16]. This is an easily attainable field strength, and the wide resonance permits accurate tuning of the scattering length.

The resultant variation in $\tilde{g}$ in the vicinity of the resonance is sketched in Fig. 6.7; for a sense of scale, we assume an axial trapping frequency of 4 kHz, and calculate $\tilde{g}$ via Eqs. (1.6) and (6.18).

Feshbach field setup Our Feshbach field is produced by a Helmholtz coil pair, which provides a uniform field at the atoms orientated in the axial direction. The coil setup is described in detail in [113, 114] and is illustrated in Fig. 6.7.

The coils are driven by a current-controlled power supply [113, 114], and the timescale for changing the field strength is ≈ 5 ms. Our analogue control voltage is accurate to 10^{-3} V, with the resonance centred on a control voltage of 3.805 V. This suggests a field error of ~ 0.1 G, leading to errors of 1% and 4% for our smallest ($\tilde{g} = 0.05$) and largest ($\tilde{g} = 0.5$) interaction strengths addressed.

---

[1] See Introduction, and [2].

[2] From Eq. (6.18) we note that the assumption of a collisionally-three-dimensional gas should break down for $\tilde{g} \approx \sqrt{8\pi} = 5$, an order of magnitude larger than values addressed in our work.

6.3 Momentum Focusing

Having addressed our setup for confining atoms to a quasi-two-dimensional environment and tuning their interactions, we now turn to our method for pinpointing the BKT critical point. As discussed in Section 5.3, we identify the onset of extended coherence by monitoring the in-plane momentum distribution, $n(\mathbf{k})$. The canonical technique for accessing the momentum distribution in trapped ultracold gases is time-of-flight (ToF) imaging [117], whereby the trapping potential is abruptly switched off, and the gas allowed to expand for a time t_{ToF} before recording the density distribution. Assuming ballistic expansion, the final position $\mathbf{r}(t_{\mathrm{ToF}})$ of an atom is given by $\mathbf{r}(t_{\mathrm{ToF}}) = \mathbf{r}(0) + \mathbf{p}(0)t_{\mathrm{ToF}}/m$, where $\mathbf{p}(0)$ is the initial momentum. Therefore, as t_{ToF} is increased, the imaged distribution maps smoothly from the initial spatial distribution onto the initial momentum distribution. One expects behaviour at the BKT transition to smoothly become more dramatic.

Since observing the exact momentum distribution would require waiting an infinite ToF, we instead employ a ‘momentum focusing’ method whereby the momentum distribution can be obtained exactly. This was previously demonstrated in 1D [108] where details of phase fluctuations within a condensate were extracted from the consequent broadening of the momentum distribution. The method was extended to harmonically-trapped two-dimensional gases in [58,68] where a sharp growth in low-k states was observed below a critical temperature, and attributed to the BKT transition. A theoretical overview of the focusing method is given in [109].

In this Section, we first outline the conceptual details of momentum focusing and offer some comparison to traditional ToF imaging. Some practical details of applying momentum focusing to our two-dimensional Bose gas are described in Section 6.3.2, and Section 6.3.3 concerns itself with the effect of a finite momentum-space resolution on identifying the BKT transition.

6.3.1 Conceptual Outline

Momentum focusing takes advantage of the symmetry of position and momentum in the harmonic oscillator Hamiltonian. For a particle undergoing harmonic motion, momentum is mapped over a quarter-period onto position, and vice versa. Quantitatively, for an oscillator of frequency ω_{foc} with Hamiltonian

$$\mathcal{H}_{\mathrm{HO}} = \frac{p^2}{2m} + \frac{1}{2}m\omega_{\mathrm{foc}}^2 x^2, \tag{6.19}$$

the time evolution is given by Hamilton’s equations:

$$\dot{x} = \frac{p}{m} \qquad , \qquad \dot{p} = -m\omega_{\mathrm{foc}}^2 x. \tag{6.20}$$

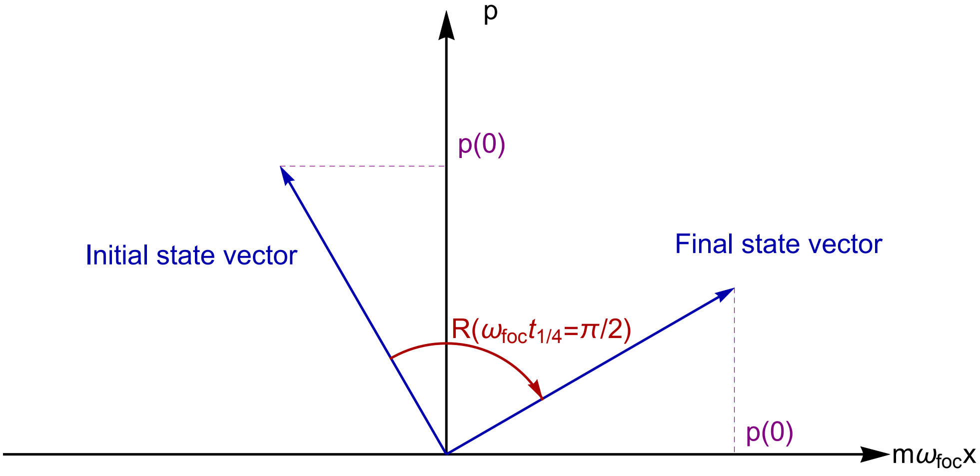

Figure 6.8: *The evolution of state vector* $(m\omega_{foc}x, p)$ *for a particle moving in a harmonic oscillator. The time-evolution is described by a rotation matrix* $R(\omega_{foc}t)$*, and after a quarter period, the spatial distribution reflects the initial momentum distribution.*

For some initial position and momentum $(x(0), p(0))$, the solution to Eq. (6.20) is,

$$\begin{pmatrix} m\omega_{\text{foc}}x(t) \\ p(t) \end{pmatrix} = \underbrace{\begin{pmatrix} \cos\omega_{\text{foc}}t & \sin\omega_{\text{foc}}t \\ -\sin\omega_{\text{foc}}t & \cos\omega_{\text{foc}}t \end{pmatrix}}_{R(\omega_{\text{foc}}t)} \begin{pmatrix} m\omega_{\text{foc}}x(0) \\ p(0) \end{pmatrix}. \tag{6.21}$$

The time-evolution matrix $R(\omega_{\text{foc}}t)$ is a rotation matrix in the oscillator phase-space. Its action is to rotate the vector $(m\omega_{\text{foc}}x, p)$ by an angle $\omega_{\text{foc}}t$, illustrated graphically in Fig. 6.8.

After a quarter-period $t_{1/4} = \pi/(2\omega_{\text{foc}})$, the position is

$$x(t_{1/4}) = \frac{p(0)}{m\omega_{\text{foc}}}. \tag{6.22}$$

This is the essence of momentum focusing; the initial momentum is mapped onto final position.

Comparison with ToF The great advantage of momentum focusing is that it grants experimental access to the infinite ToF limit, providing the exact momentum distribution. The disadvantage compared with ToF imaging is that the momentum resolution is fixed, whereas with ToF imaging resolution increases with expansion time. Since we expect the BKT transition to be revealed in the occupation of low-momentum states, the criterion of interest for the two methods is the lowest resolvable momenta in an ensemble.

For an imaging system of resolution δx, and a focusing trap of frequency ω_{foc}, the resolution in momentum-space follows straightforwardly from Eq. (6.22), $\Delta p =$

$m\omega_{\mathrm{foc}}\delta x$. The focusing method therefore gives the occupation of all momentum states $p < m\omega_{\mathrm{foc}}\delta x$, from the number of atoms within δx of an image centre.

If ToF imaging is used, the initial cloud size R sets a lower bound for the size of the imaged cloud. Even in the case of all atoms having zero momentum, after any ToF the spatial distribution would be of extent R. After a flight time t_{ToF}, the central image region of radius R approximately contains atoms with momenta $p < mR/t_{\mathrm{ToF}}$. Therefore, ToF imaging provides superior resolution of low-momentum atoms compared with focus imaging if

$$t_{\mathrm{ToF}} > \frac{1}{\omega_{\mathrm{foc}}}\frac{R}{\delta x}. \tag{6.23}$$

The definition of the cloud size R is somewhat arbitrary; the thermal radius $R_{\mathrm{th}} = \sqrt{k_{\mathrm{B}}T/(m\omega_r^2)}$ is a reasonable candidate. Generally speaking, for any imaging system which can reasonably resolve *in situ* clouds, the ratio $(R/\delta x) \gg 1$ leading to t_{ToF} being significantly larger than the focusing trap timescale.

For our system, $T \approx 170$ nK[1], $\omega_r \approx 2\pi \times 38$ Hz, and resolution is limited by the camera pixelsize[2] $\Delta x = 2.95$ μm. The same potential provides planar trapping and a focusing potential, hence $\omega_{\mathrm{foc}} \approx \omega_r$. This leads to a required $t_{\mathrm{ToF}} > 36$ ms, at which point the expanded cloud size $\sim t_{\mathrm{ToF}}\sqrt{k_{\mathrm{B}}T/m} \sim 10R$, and the optical density of an image has fallen by a factor of ~ 100 compared to an *in situ* image. The resulting poor signal-to-noise ratio[3], especially in the distribution wings, makes it difficult to extract cloud parameters such as number, temperature and chemical potential.

On the other hand, momentum focusing does not result in significant planar expansion of the cloud. It preserves good signal-to-noise in the wings of the momentum distribution whilst providing better low-momentum resolution than any ToF under 36 ms.

A subtlety is worth mentioning here: there is an additional advantage of momentum focusing over ToF imaging if we wish to observe a sharp feature in momentum-space. For either method, we require the cloud axial extent to not exceed the imaging system depth-of-field. For imaging resolution of δx, the depth of field b is approximately twice the Rayleigh length[4], $b = 2\pi\delta x^2/\lambda$. For a trapped quasi-two-dimensional cloud, the axial evolution after release is approximately that of a non-interacting Gaussian wavepacket, and after release time t the axial extent is $\approx \sqrt{1+\omega_z^2t^2}\sqrt{\hbar/(m\omega_z)}$. Demanding that this extent is less than the

---

[1] See Section 7.1.

[2] See Section 6.4.3.

[3] In principle, no information should be lost by imaging the same number of atoms spread over more pixels. In practice, the dominant source of imaging noise is photon count shot noise on each camera pixel. Since optical density (OD) is calculated from the number of photons absorbed by atoms, the ratio of shot noise to absorbed photons increases with falling OD. This causes signal-to-noise to fall with falling OD.

[4] This sets the extent of the focal point at the atoms, in the direction of imaging.

depth of field for our system parameters[1] restricts our release times to $t \lesssim 11$ ms. Our focusing time of ≈ 7 ms is within this limit. On the other hand, using a lengthy ToF would result in the axial extent of the cloud greatly exceeding the depth of field, resulting in blurring and distortion of the low-k peak.

6.3.2 Focusing our Two-Dimensional Bose Gas

In the case of an ensemble of particles, interactions must be negligible during focusing, which is a single-particle process. In a two-dimensional system, this can be accomplished by switching off the tight axial confinement of frequency ω_z [58, 68], whilst leaving the weak planar potential of frequency ω_r. Axial expansion causes interactions to vanish on a timescale $\omega_z^{-1} \ll \omega_r^{-1}$, and the in-plane evolution is essentially free-particle-like. Atoms must remain within the harmonic region of the ODT during focusing, and not be excessively displaced vertically. Focusing is therefore performed in the presence of a vertical magnetic field gradient which cancels the force downwards due to gravity; this is described in Appendix E. After a quarter-period, an absorption image taken along the axial direction reveals the planar momentum distribution.

Residual scattering Despite axial expansion being much faster than in-plane evolution, some residual inter-atomic collisions are inevitable during focusing. This can be estimated by noting that the axial expansion is driven by kinetic energy[2] and so the density should fall as $1/\sqrt{1+\omega_z^2 t^2}$ after release. The scattering rate at time t after release is then $\gamma/\sqrt{1+\omega_z^2 t^2}$, where γ is the in-trap scattering rate, and for a focusing time of t_{foc} the number of collisions per atom is

$$\begin{aligned} N_{\mathrm{coll}} &= \int_0^{t_{\mathrm{foc}}} \mathrm{d}t\ \gamma \frac{1}{\sqrt{1+\omega_z^2 t^2}}, \\ &= \gamma \frac{1}{\omega_z} \ln\left(\omega_z t_{\mathrm{foc}} + \sqrt{1+{\omega_z}^2 t_{\mathrm{foc}}^2}\right). \end{aligned} \tag{6.24}$$

Whilst this integral diverges with time, it does so logarithmically.

In our experiment a typical trapped atom number is 2×10^4 giving an *in situ* scattering rate[3] of $\approx 4000\tilde{g}^2$. Our focusing trap frequency[4] is $\omega_{\mathrm{foc}} \approx 2\pi \times 36$ Hz, and the range of interaction strengths considered is $0.05 < \tilde{g} < 0.5$. This results in $N_{\mathrm{coll}} \approx 0.2$ for our largest interaction strength, and $N_{\mathrm{coll}} \approx 0.002$ for our smallest, both much smaller than unity.

---

[1] The trap frequency $\omega_z = 2\pi \times 4040$ Hz (Section 6.1.1) and we take our resolution to be dominated by the pixelsize of our CCD, giving $\delta x \approx 3$ μm (Section 6.4.3).

[2] The definition of two-dimensional trapping is that the axial trap level spacing $\hbar\omega_z$ exceeds other energy scales in the gas.

[3] See Section 7.1.3.

[4] See Eq. (6.14).

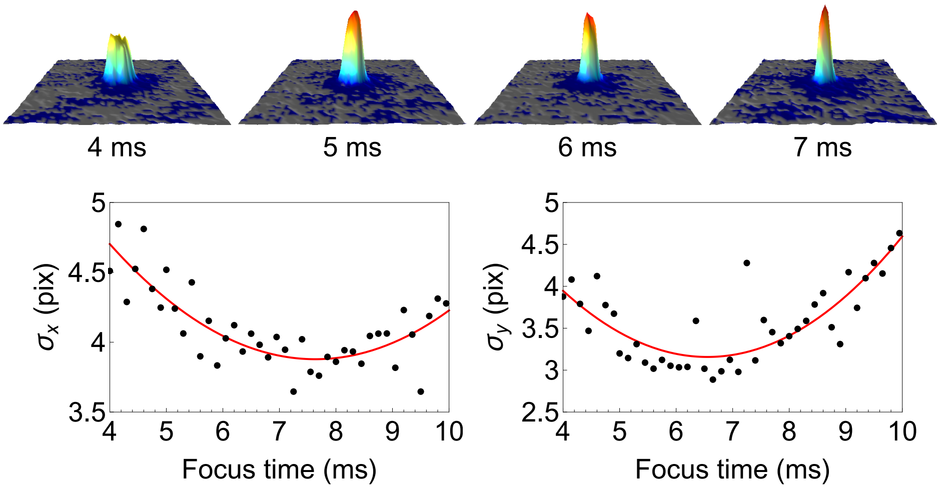

Figure 6.9: *Evolution of central peak with focusing time. As the focusing time is scanned, the sharp low-momentum peak displays a minimum width after a quarter-period of the focusing trap. We first rotate images by $\theta = 37°$ such that trap and camera axes align, then perform a two-dimensional fit using some heuristic two-curve function to extract a measure of the peak widths $\sigma_{x,y}$. A quadratic fit to the resulting evolution provides the focusing time at which the peak is minimised.*

Determination of focusing time We empirically determine the focusing time at which the momentum distribution is revealed, by preparing a weakly-interacting degenerate cloud at $a = 10\ a_0$ and monitoring the width of the sharp low-momentum peak as a function of focusing time; the experimental procedure is outlined in Appendix C and the evolution plotted in Fig. 6.9.

We fit a heuristic quadratic dip function, obtaining the focusing times t_0 as those for which the peak width is minimal. These are;

$$t_0^x = 7.5 \pm 0.1\ \text{ms} \qquad , \qquad t_0^y = 6.6 \pm 0.1\ \text{ms}. \tag{6.25}$$

To check that these are not overly sensitive to the choice of interaction strength, we repeat with a scattering length of 242 a_0, obtaining

$$t_0^x = 7.6 \pm 0.1\ \text{ms} \qquad , \qquad t_0^y = 6.5 \pm 0.1\ \text{ms}. \tag{6.26}$$

As representative focusing times we choose 7.5 ms and 6.5 ms respectively. From our measured trap frequencies of Eq. (6.14) we would predict focusing times of 7.4 ms and 6.4 ms; the slightly longer empirical times suggest the presence of a delay mechanism. One axial trap period is 0.25 ms, so a measured delay of 0.1 ms is entirely consistent with the time for interactions to vanish via axial expansion.

Focusing trap anisotropy The anisotropy of the focusing trap means that perfect focusing cannot be attained simultaneously in both directions. To first

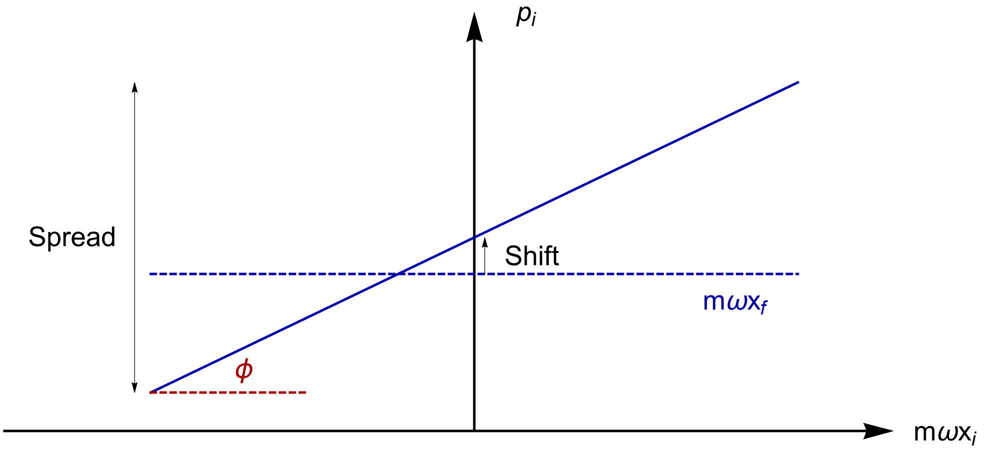

Figure 6.10: *The initial phase-space of a trapped gas; each point is populated according to the appropriate thermal distribution. The solid line is defined by Eq. (6.29); all atoms along this line will be mapped by momentum focusing onto the same final position. Imperfect focusing corresponds to finite $\phi = \omega_{foc}\Delta t$; this has the effect of both shifting the line, and introducing a non-zero gradient. Therefore there is a small overall shift in the momenta mapped onto some final position, and also a non-zero spread. The dotted line would be the result for $\phi = 0$, corresponding to the ideal mapping of Eq. (6.22).*

---

order, the inherent blurring of the momentum distribution will be isotropic if the focusing time error is an equal fraction of each axis period; we therefore choose a final focusing time t_{foc} according to

$$\frac{7.5 - t_{\text{foc}}}{7.5} = \frac{t_{\text{foc}} - 6.5}{6.5} \qquad \rightarrow \qquad t_{\text{foc}} = 6.96 \text{ ms}. \tag{6.27}$$

We can estimate the consequent blurring of the momentum distribution. For an error Δt in the focusing time, an initial state vector $(m\omega_{\text{foc}}x_{\text{i}}, p_{\text{i}})$ evolves onto a final state vector $(m\omega_{\text{foc}}x_{\text{f}}, p_{\text{f}})$ according to,

$$\begin{aligned}\begin{pmatrix} m\omega_{\text{foc}}x_{\text{f}} \\ p_{\text{f}} \end{pmatrix} &= \begin{pmatrix} \cos\left(\frac{\pi}{2}+\phi\right) & \sin\left(\frac{\pi}{2}+\phi\right) \\ -\sin\left(\frac{\pi}{2}+\phi\right) & \cos\left(\frac{\pi}{2}+\phi\right) \end{pmatrix} \begin{pmatrix} m\omega_{\text{foc}}x_{\text{i}} \\ p_{\text{i}} \end{pmatrix}, \\ &= \begin{pmatrix} -\sin\phi & \cos\phi \\ -\cos\phi & -\sin\phi \end{pmatrix} \begin{pmatrix} m\omega_{\text{foc}}x_{\text{i}} \\ p_{\text{i}} \end{pmatrix}, \end{aligned} \tag{6.28}$$

where $\phi = \omega_{\text{foc}}\Delta t$. Some final position x_{f} therefore corresponds to any initial state satisfying,

$$m\omega_{\text{foc}}x_{\text{f}} = \cos\phi \; p_{\text{i}} - \sin\phi \; m\omega_{\text{foc}}x_{\text{i}}. \tag{6.29}$$

This can conveniently be graphically represented, as in Fig. 6.10 where we plot the initial phase-space. Atoms populate this phase-space according to the Bose distribution, and any atoms along the line defined by Eq. (6.29) will be mapped onto the same final position x_{f}.

The effect of imperfect focusing $\phi \neq 0$ is thus twofold:

1. The central momentum mapped onto some final position is shifted by a factor $\cos\phi$. In our system, $T \approx 170$ nK and $\omega_{\text{foc}}\Delta t \approx 0.11$ along each focusing trap axis. The systematic shift of momentum is then of the order $\cos(\omega_{\text{foc}}\Delta t)p_{\text{th}} \approx 0.03\ \hbar\ \mu\text{m}^{-1}$, where $p_{\text{th}} = \sqrt{mk_{\text{B}}T}$ is the thermal momentum. This is an order of magnitude smaller than our momentum-space resolution set by the pixelsize, $m\omega_{\text{foc}}\Delta x = 0.4\ \hbar\ \mu\text{m}^{-1}$.

2. The momenta of atoms at a particular final position will have a finite spread, given by $\sin\phi\ m\omega_{\text{foc}}\delta x_{\text{i}}$, for some spread of initial position δx_{i}. This will be of order the cloud thermal radius, $\sqrt{k_{\text{B}}T/(m\omega_r^2)}$ for trap planar frequency ω_r. In our system $\omega_r \approx 2\pi \times 37.7$ Hz[1], giving a momentum spread of $0.4\ \hbar\ \mu\text{m}^{-1}$. By coincidence, this is equal to the accuracy enabled by our momenta resolution.

6.3.3 Effect of a Finite Momentum-Space Resolution

Our momentum resolution is $\Delta k \approx m\omega_{\text{foc}}\Delta x/\hbar = 0.4\ \mu\text{m}^{-1}$, imposed by the finite pixelsize Δx of our imaging system, and the anisotropy of the focusing trap. The rationale behind measuring the momentum distribution is that a change in the functional form of $g^{(1)}$ should be revealed in the occupation of low-momentum modes[2]. The lowest momentum atoms addressable are those with $k \lesssim \Delta k$, which are focused to within 1 pixel of the centre of an imaged cloud. Our best probe of extended coherence is then the measured peak height of the momentum distribution, denoted P_0. In terms of lengthscale, we are probing correlations over $L \approx 2\pi/\Delta k = 15.2\ \mu$m. At typical temperatures $T \approx 170$ nK, this corresponds to $(L/\lambda_{\text{th}}) = 22.4$, much larger than unity.

In the case of uniform trapping, L/λ_{th} should be as large as possible for detection of the transition. In the case of harmonic trapping, the critical point is reached when only the infinitesimal central region becomes superfluid; hence we should not expect to see any discontinuous jump in P_0, but rather a rapid growth as the cloud crosses the critical point. Importantly, in this case the cloud size sets an upper limit on desirable values of L. If we probe coherence over a long lengthscale L, then the BKT transition will only become apparent once a region of diameter $\sim L$ has become superfluid. We therefore require L to be much smaller than the thermal diameter of the cloud, $2R_{\text{th}} = 2\sqrt{k_{\text{B}}T/(m\omega_r^2)}$. This results in an overall condition on L (or equivalantly Δk),

$$\lambda_{\text{th}} \ll L \ll 2R_{\text{th}}. \tag{6.30}$$

In our system $\lambda_{\text{th}} \approx 0.7\ \mu$m, $L \approx 15\ \mu$m and $2R_{\text{th}} \approx 51\ \mu$m. The cloud inhomogeneity will unavoidably impose a shift in the apparent critical point, which is discussed in Appendix F.

---

[1] See Eq. (6.13).

[2] See Section 5.3.

How large should $L/\lambda_{\rm th}$ be? For the BKT transition to be detectable it must be accompanied by a sharp feature in P_0. Although we are working with a harmonic trap, we can take the uniform case as a toy model and ask how P_0 should change as the gas crosses from normal to superfluid. Measurement of P_0 equates to measuring the shaded area underneath the correlation function spectrum, $n(k)$, illustrated in Fig. 6.11.

For a degenerate two-dimensional ideal gas, the low-k momentum distribution is [51]:

$$n_{\mathbf{k}} \approx \frac{4\pi}{\lambda_{\rm th}^2}\frac{1}{k^2+k_c^2} \qquad , \qquad k_c \approx \frac{\sqrt{4\pi}}{\lambda_{\rm th}}e^{-\mathcal{D}/2}. \tag{6.31}$$

We note that this function becomes progressively peakier with increasing $\mathcal{D}$, leading to a diverging correlation length $\zeta = k_c^{-1}$ [51, 105]. For total system area A, the number of atoms with $k < \Delta k$ is

$$\begin{aligned} N_{\Delta k} &= \int_{k<\Delta k} \frac{\mathrm{d}^2\mathbf{k}}{(2\pi/\sqrt{A})^2} n_{\mathbf{k}} = A\frac{1}{\lambda_{\rm th}^2}\log\left[1+\left(\frac{\Delta k}{k_c}\right)^2\right], \\ &= A\frac{1}{\lambda_{\rm th}^2}\log\left[1+\pi\left(\frac{\lambda_{\rm th}}{L}\right)^2 e^{\mathcal{D}}\right]. \end{aligned} \tag{6.32}$$

The case of a BKT superfluid is more difficult; from Eq. (3.12) the correlation function $g^{(1)}(r) \sim r^{-\eta}$, where $\eta = 1/\mathcal{D}_{\rm s}$. On dimensional grounds the momentum distribution $n(k) \sim k^{\eta-2}$, but being more precise is difficult since the Fourier transform of the algebraic $g^{(1)}$ is not convergent. However, we can assume some maximum momentum $k_{\rm max}$ and write the fraction of atoms within the central region as

$$\frac{N_{\Delta k}}{N_{\rm Total}} \approx \frac{\int_0^{\Delta k} k^{\eta-1}\mathrm{d}k}{\int_0^{k_{\rm max}} k^{\eta-1}\mathrm{d}k} = \left(\frac{\Delta k}{k_{\rm max}}\right)^{\eta} \tag{6.33}$$

A convenient measure of the short-range lengthscale in the gas is the thermal wavelength, and so a reasonable estimate of the peak number is $N_{\Delta k} \approx An(\lambda_{\rm th}/L)^{\eta}$. At the BKT point $\eta = 1/4$, and so this expression is only very weakly dependent on the exact cutoff $k_{\rm max}$. We thus expect a relative change in P_0 at the BKT critical point,

$$\text{Relative change in } P_0 = \frac{\mathcal{D}^{\rm BKT}\left(\frac{\lambda_{\rm th}}{L}\right)^{1/4}}{\log\left[1+\pi\left(\frac{\lambda_{\rm th}}{L}\right)^2 e^{\mathcal{D}^{\rm BKT}}\right]}. \tag{6.34}$$

This ratio is plotted in Fig. 6.11 for various values of $\tilde{g}$. As expected, the transition is revealed at distances $L \gg \lambda_{\rm th}$, and becomes progressively more dramatic as longer lengthscales are probed.

In reality, this ratio should approach unity as $L \to 0$; this corresponds to counting atoms with $k < \infty$, and an '$L = 0$' measurement equates to summing the total atom number which does not change across the transition! This limit is not perfectly recovered by Eq. (6.34); the assumed upper momentum cutoff $k_{\rm max} = 2\pi/\lambda_{\rm th}$

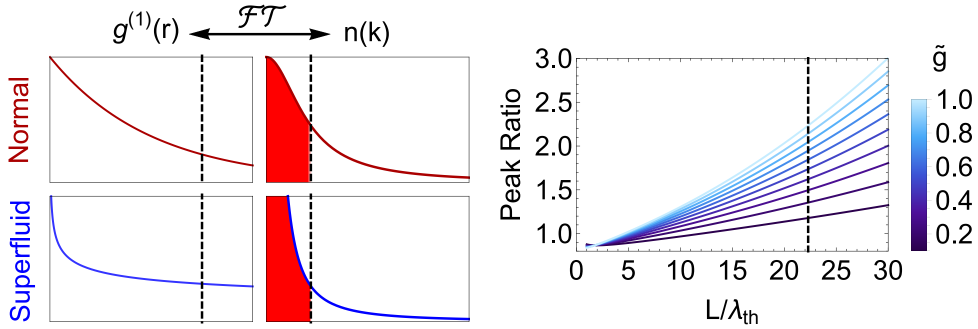

Figure 6.11: *The BKT transition causes $g^{(1)}(\boldsymbol{r})$ to change from exponential to algebraic decay, with a corresponding change in $n(\boldsymbol{k})$. Any change in the functional form of $g^{(1)}$ should be most dramatic at longer lengthscales, and lower momenta. The vertical dashed lines denote our momentum resolution Δk and the corresponding lengthscale $L = 2\pi/\Delta k$ on the appropriate plots. Measuring P_0 is equivalent to the number of atoms with $k < \Delta k$, denoted by the shaded red regions. P_0 should offer a clear transition signature if this area changes by an appreciable fraction at the critical point. Eq. (6.34) estimates the ratio of $N_{\Delta k}$ after crossing the BKT point to its value before; this ratio is plotted on the right for various values of $\tilde{g}$.*

---

is somewhat arbitrary, and the algebraic BKT superfluid correlation function is only valid for $L \gg \lambda_{\rm th}$. However, it is reassuring that the observed limit is ≈ 0.9, reasonably close to unity.

We note that our finite coherence lengthscale L implies that we cannot reliably detect the BKT transition below some value of $\tilde{g}$; physically, this is a consequence of the diverging normal gas correlation length with increasing $\mathcal{D}$. As a rough guide, the value of $\mathcal{D}^{\rm BKT}$ such that P_0 changes by 10% across the transition is $\mathcal{D}^{\rm BKT} = 8.67$, corresponding to $\tilde{g} = 0.07$. A slightly different argument asks the value of $\tilde{g}$ for which the normal gas correlation length $\lambda_{\rm th} \exp(\mathcal{D}^{\rm BKT}/2)/\sqrt{4\pi} = L$. At our typical temperatures of 170 nK, this results in $\mathcal{D}^{\rm BKT} = 8.75$ and $\tilde{g} = 0.06$, which gives an almost identical estimate.

The results of Eq. (6.34) and Fig. 6.11 offer good support for using the onset of coherence as a signature of the BKT transition; at least in a uniform system, crossing the transition leads to a significant jump in P_0 for sufficiently large $L/\lambda_{\rm th}$. In a harmonic system this should translate into a sharp (but continuous) growth in P_0.

An important point is worth mentioning here; we are specifically concerned with the peak height P_0 of the momentum distribution, not with its functional form. The former provides a model-free method to identify the onset of extended coherence, which in turn offers an experimental signature of the BKT phase transition [51, 102, 107, 118]. However, we make no theoretical assumption about the form of $n(k)$ at low-k. As a normal cloud approaches the critical point, $n(k)$ becomes narrower than a Gaussian fitted to the distribution wings, indicating coherence over lengthscales $> \lambda_{\rm th}$ [51, 57, 60] and even peaks above a pure-MF model [60, 99]. Thus unlike in three dimensions, where the presence of a bimodal distribution in $n(k)$ is a signature of BEC, such 'peakiness' does not provide a reliable signature of BKT [60].

6.4 Imaging

All information about our trapped gases comes from images of the atomic density. Imaging is principally along the vertical (axial) direction, which reveals the full planar atomic distribution. Our system also incorporates an imaging setup along the horizontal direction [113, 114], and is not discussed further here, being used solely for trap alignment. For ease of reference, the essential characteristics of each imaging direction are tabulated here in Table 6.1.

In this Section, we first briefly review the absorption imaging used to map the column density of an atomic sample. Since imaging of our cloud primarily takes place in the presence of the ($\sim$ 400 G) Feshbach field, Section 6.4.1 addresses the state structure of ^{39}K in this 'high-field' regime. At these magnetic fields, a residual admixture of $|m_J\rangle$ states leads to a 'depumping' effect, where the apparent OD falls with exposure to imaging light; a rescaling function to account for this effect is derived in Section 6.4.2. The characterisation of magnification and absolute imaging efficiency is the topic of Section 6.4.3.

Absorption imaging We probe our cloud using low-intensity absorption imaging, where the imaging light intensity I is much lower than the atomic transition saturation intensity I_s. Absorption imaging and our imaging procedure are described in more detail in Appendix D. Using this method, the optical density is obtained as

$$\text{OD} \approx -\ln\left(\frac{C_\text{atom}(\mathbf{r})}{C_\text{ref}(\mathbf{r})}\right), \tag{6.35}$$

where $C_\text{atom}(\mathbf{r})$ is a map of imaging light photon counts with atoms present, and $C_\text{ref}(\mathbf{r})$ the corresponding map without. Optical density is related to the number column density n via $\text{OD} = n\sigma_0$, where the zero-intensity cross section $\sigma_0 = 3\lambda^2/(2\pi)$ for a closed cycling transition [119].

Optimised reference image In practice, the light pattern $C_\text{ref}(\mathbf{r})$ obtained from the atom-free image will not be exactly identical to that incident on the atom cloud. The intensity of imaging light varies with time, and small frequency drifts lead to a changing interference pattern on propagation through the imaging optics. This leads to 'fringing' and distortion of calculated OD patterns. We eliminate this effect, via an optimal reference algorithm developed in [120]. For a particular data set, all of the atom-free images provide a basis $\{C_{\text{ref},i}\}$. For a particular C_atom, we select a region free from atoms, but with imaging light. This region is then decomposed into the basis $\{C_{\text{ref},i}\}$, giving a set of coefficients for

	Model	**QE**	$\boldsymbol{\Delta x}$	$\boldsymbol{M}$
Horizontal	PCO imaging, pixelfly QE	≈ 0.25	$\approx 2.43\ \mu$m	2.65
Vertical	Princeton Instruments, PIXIS 1024-BR	0.98	2.95 μm	4.41

Table 6.1: *Essential characteristics of the horizontal and vertical cameras and imaging systems. QE denotes quantum efficiency, Δx the in-trap length mapped onto a single CCD pixel, and M the magnification.*

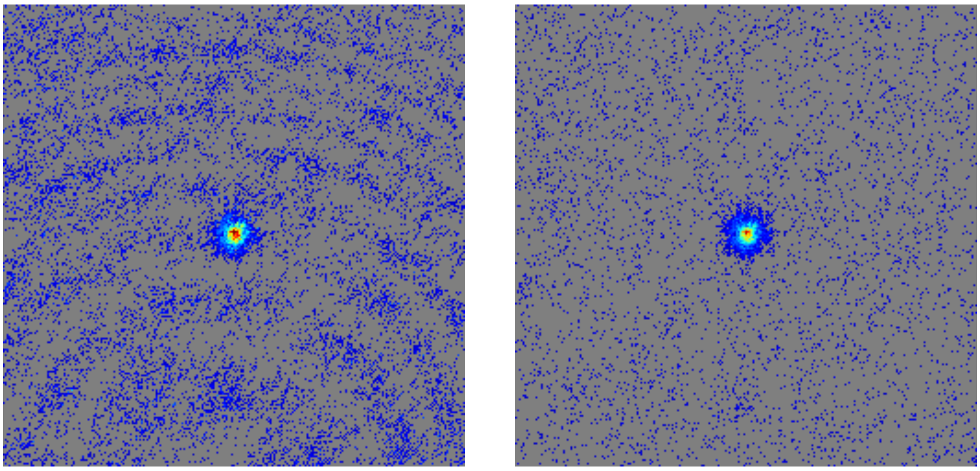

Figure 6.12: *A critical measured momentum distribution at $\tilde{g} = 0.28$, before (left) and after (right) applying the optimal reference algorithm.*

the admixture of each individual reference image. This set of coefficients is used to build an optimal reference image $C_{\mathrm{ref}}^{\mathrm{opt}}$.

Qualitatively, we use a region of light free from atoms to make a 'best guess' of the imaging light pattern originally incident on the atoms. By evaluating the OD of Eq. (6.35) using $C_{\mathrm{ref}}^{\mathrm{opt}}$, both offsets and fringing are significantly reduced; this is illustrated in Fig 6.12.

6.4.1 High-field State Structure

It is desirable to image our cloud in the presence of the Feshbach field, for two reasons. Foremost, our momentum focusing technique necessitates the cancellation of gravity during focusing which is provided by the superposition of the Feshbach field and a weak quadrupole field[1]. Furthermore, the timescale of ~ 5 ms to switch off the Feshbach field would make it impossible to image our cloud *in situ*; this is useful for alignment of the two-dimensional trap. We therefore use our Feshbach field as an imaging guide, and in this Section calculate the relevant atomic eigenstates.

At our field strengths of ~ 400 G, the magnetic energy of an atom will be $\sim \mu_{\mathrm{B}} B =$

---

[1] See Appendix E.

$0.6 \times h$ GHz. The fine-structure splitting for ^{39}K is $\sim 1700 \times h$ GHz [121], so we expect J to remain a good quantum number and there should be no admixture of the D1 and D2 line.

The zero-field hyperfine splitting on the other hand is $\approx 460 \times h$ MHz for the ground state 4 $^2\mathrm{S}_{1/2}$ [121], so F should no longer be a good quantum number at our field strengths. The hyperfine and Zeeman terms of the atomic Hamiltonian are,

$$\mathcal{H}_{\mathrm{mag}} = A\mathbf{I} \cdot \mathbf{J} + g_J \mu_{\mathrm{B}} J_z B + g_I \mu_{\mathrm{B}} I_z B. \tag{6.36}$$

Here we assume the magnetic field to define the z-axis, A is the hyperfine coefficient, g_J is the electronic g-factor, and g_I is the nuclear g-factor. This Hamiltonian is conveniently diagonalised in states $|m_I, m_J\rangle$ for a particular J state. We image on the D2 line;

$$4\ ^2\mathrm{S}_{1/2} \rightarrow 4\ ^2\mathrm{P}_{3/2}. \tag{6.37}$$

For ^{39}K the nuclear spin $I = 3/2$; this gives a basis of 8 spin-states $|\phi_i\rangle = |m_I, m_J\rangle_i$ for the ground manifold, and 16 for the excited manifold. For reference, the ground and excited state parameters are tabulated in Table 6.2.

	4 $^2\mathrm{S}_{1/2}$	**4 $^2\mathrm{P}_{3/2}$**
A (MHz $\hbar^{-1}$)	1450.5352809	38.283
g_J	2.0023193043622	4/3
g_I	-0.00014193489	

Table 6.2: *Hyperfine and Zeeman term parameters for the ground and excited states of the D2 line in ^{39}K [121].*

The Hamiltonian can be recast as a matrix $\mathcal{H}_{ij} = \langle\phi_i|\mathcal{H}_{\mathrm{mag}}|\phi_j\rangle$ for each manifold and diagonalised, yielding both the level energies and eigenstates at a particular field strength.

In Fig. 6.13 we plot the results for the ground and excited manifolds of the D2 line. At high-fields, the second term of Hamiltonian (6.36) dominates, and atomic eigenstates are approximately given by the basis states $|m_I, m_J\rangle$. Each m_J manifold is labelled, with the varying m_I splitting each into a number of parallel lines.

Choice of imaging states Our ground state at low-field is $|F = 1, m_F = 1\rangle$; at high field this connects to $|m_I = 3/2, m_J = -1/2\rangle$ which is plotted in blue in Fig. 6.13. As an upper state for absorption imaging we choose $|m_I = 3/2, m_J = -3/2\rangle$. This is (almost) a cycling transition when driven by σ^--polarised imaging light, maximising photon scattering per atom. This upper state is plotted in green.

Regardless of the Feshbach field at which the experiment is performed, at the beginning of the momentum focusing stage we jump the Feshbach field to its zero-crossing value of 350.5 G. Not only does this minimise the atomic interactions

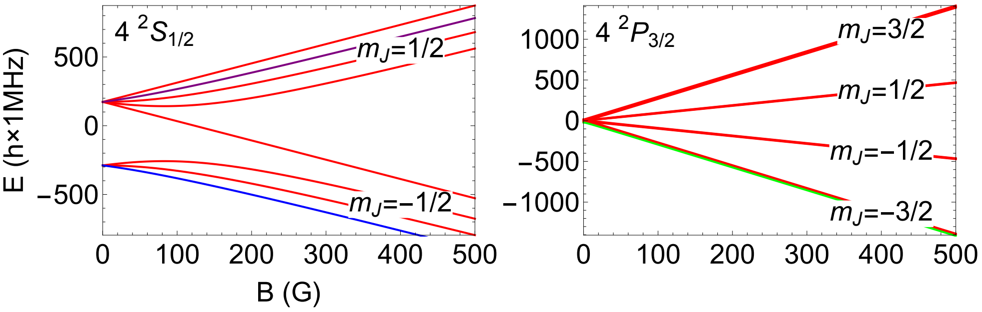

Figure 6.13: *The energy level structure corresponding to hyperfine and Zeeman energies, for the D2 ground state* ($4\ ^2S_{1/2}$) *and excited state* ($4\ ^2P_{3/2}$)*. The states at high field are approximately those of pure* m_J*, which are labelled. The blue (green) state denotes our ground (excited) state for absorption imaging. Although the blue and green states form an almost closed cycling transition, there is a small probability on each cycle of decaying to the purple state (see text).*

---

during the focusing, but also ensures that we always image at the same field strength, with the same eigenstate composition. At the zero-crossing, the ground eigenstate is,

$$|ground\rangle = 0.987\ |m_I = 3/2, m_J = -1/2\rangle - 0.158\ |m_I = 1/2, m_J = 1/2\rangle. \quad (6.38)$$

This means there is a small, ≈ 2.5% admixture of $m_J = 1/2$ into the ground state. Conversely, the $m_J = 1/2$ ground manifold contains a state approximately given by $|m_I = 1/2, m_J = 1/2\rangle$, but with a 2.5% admixture of $|m_I = 3/2, m_J = -1/2\rangle$; this state is plotted in purple. On each photon absorption/emission cycle, this leads to a 2.5% probability of an atom decaying into the dark $m_J = 1/2$ lower manifold. This 'depumping' leads to an effective cross section that falls with exposure to imaging light; calibration of this effect is discussed in Section 6.4.2.

Experimental imaging setup From Fig. 6.13, the energy splitting of our ground and excited states is -299 MHz relative to the D2 line at the zero-crossing field of 350.5 G. Frequency variation around this point is $-\mu_B/\hbar = -1.4$ MHz G^{-1}. We wish to work over a field range of ≈ 50 G, leading to a frequency tuneability requirement of ≈ 70 MHz.

Our high-field imaging light is derived from the MOT cooling light, detuned by $\approx -7.6\Gamma$ from the zero-field $|F = 2\rangle \rightarrow |F' = 3\rangle$ D2 transition [113,114]. This light is therefore already detuned by ≈ -205 MHz from the D2 line, and generating high-field imaging light requires a further negative shift of approximately $94 \rightarrow 164$ MHz.

The setup for preparation and delivery of high-field imaging light was designed and constructed by Jay Man [122]. After passing vertically through the atom cloud, it is focused onto the CCD camera using a objective and imaging lens setup designed and built by Alexandre Dareau [123], which has an imaging resolution

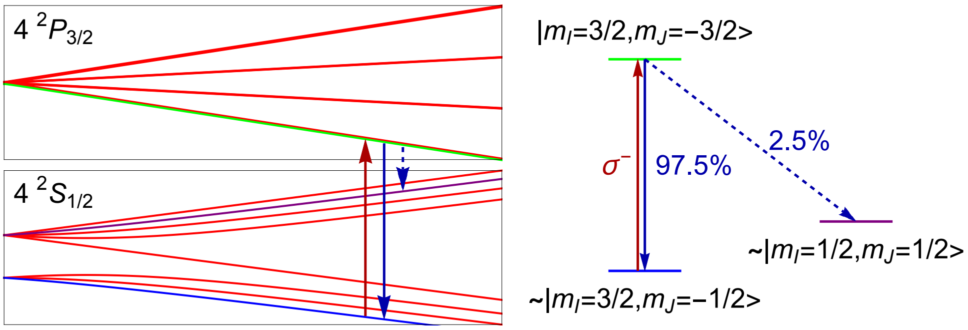

Figure 6.14: *The atomic states of* ^{39}*K as a function of magnetic field strength. Axes are identical to Fig. 6.13, labels are omitted here for clarity. The absorption imaging transition is from the ground state (blue) to an excited state (green), driven by a* σ^- *photon (solid red arrow). Atoms are most likely to decay back to the imaging ground state (solid blue arrow). However, the ground manifold state* $\sim |m_I = 1/2, m_J = 1/2\rangle$ *(purple) contains a small admixture of* $|m_I = 3/2, m_J = -1/2\rangle$*; there is therefore a small probability of an atom decaying into a dark state (dashed blue arrow) and exiting the cycling transition. All transitions and states are assumed to be at a field strength of* 350.5 *G; the transition arrows are displaced horizontally for clarity only.*

of $\lesssim 2\mu$m [21, 123]; these references contain a comprehensive description of the vertical imaging optics.

6.4.2 Rescaling Function

The residual impurity of our high-field imaging states results in a depumping effect, whereby some fraction of atoms are transferred to a dark state. This will reduce the apparent OD, by a factor which depends on the absolute number of absorption cycles.

In 'ideal' absorption imaging, the imaging light drives a perfectly closed cycling transition. Although there is a weak dependence of cross-section on imaging intensity[1], the measured OD is independent of the exact number of absorption/emission cycles each atom undergoes. However, the transition for our high-field imaging is not perfectly closed, leading to a $\approx 2.5\%$ probability for an atom to relax into a dark state on each absorption cycle[2]. This is illustrated in Fig. 6.14 and leads to an effective cross-section that depends upon the number of imaging photons. This can vary not merely shot-to-shot, but even pixel-to-pixel within a single image.

Empirical rescaling function To correct for this effect, we experimentally calibrate the relative variation of the observed OD with the camera counts in

---

[1] See Eq. (D.2).

[2] See Eq. (6.38).

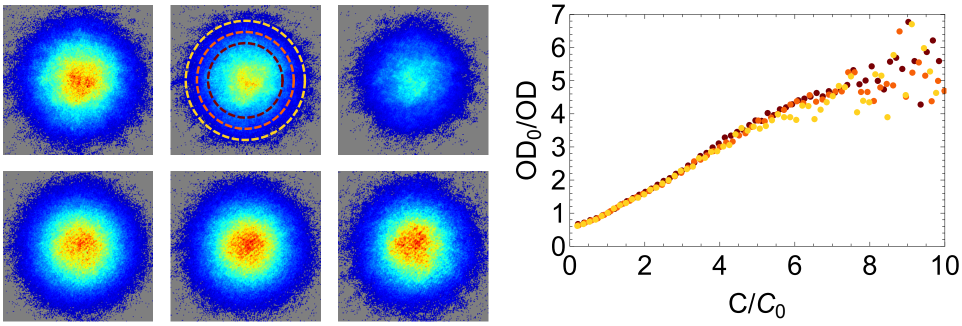

Figure 6.15: *Measurement of the OD rescaling function. The top row shows unprocessed absorption images of a thermal cloud at* $(C/C_0) = 1$*, 1.5 and 2.5 (left to right). For three particular radii, denoted by coloured rings, we construct a correlation plot of* (OD_0/OD) *vs* (C/C_0)*, which are plotted on the right. The bottom row shows the top images after OD rescaling (see text).*

the corresponding reference image, C. For this, we image a three-dimensional thermal cloud after expansion from the ODT. Assuming cylindrical symmetry of the cloud, any variations in OD observed around a ring concentric with the cloud centre we attribute to the variations in the probe intensity. Averaging over several images, we build, pixel by pixel, a correlation plot of $(\mathrm{OD}_0/\mathrm{OD})$ versus (C/C_0), where C_0 is a fixed reference value and OD_0 the corresponding OD. We construct such plots for various ring radii (i.e. various atomic column densities) and various (mean) probe intensities, and find that to a very good approximation the scaling of OD due to depumping depends only on the light intensity and not on the atomic column density. Finally, we construct a numerical interpolating function $(\mathrm{OD}_0/\mathrm{OD}) = \mathcal{F}(C/C_0)$ from the compiled correlation plots from all radii, illustrated in Fig. 6.16.

In practice, for an experimental shot we first obtain the optimal reference image $C_{\mathrm{ref}}^{\mathrm{opt}}(\mathbf{r})$, and then rescale each pixel of the OD image $\mathrm{OD}(\mathbf{r})$ according to

$$\mathrm{OD}(\mathbf{r}) \rightarrow \mathrm{OD}(\mathbf{r}) \times \mathcal{F}\left(\frac{C_{\mathrm{ref}}^{\mathrm{opt}}(\mathbf{r})}{C_0}\right). \tag{6.39}$$

This transformation accounts for any spatial or temporal variation in the imaging photon count. It not only takes the depumping effect into account, but also any other dependencies on imaging intensity, such as Doppler detuning of atoms during the imaging pulse and the effect of finite I/I_{s}.

In Fig. 6.15 we illustrate three identical thermal clouds, imaged with mean probe intensities $(C/C_0) = 1$, 1.5 and 2.5. We also plot the rescaling function extracted from three different ring radii (coloured rings) over ~ 40 images with a range of probe intensities. The radii of the rings are 50, 65 and 80 pixels, and a Gaussian fit gives the cloud radius as 36 pixels. The true OD therefore falls by a factor of ~ 2 between consecutive rings; however, the rescaling functions extracted at each radius overlap excellently. At the bottom of the figure are shown processed images, after applying the mapping of Eq. (6.39) pixel-by-pixel to the top images.

Analytic toy model As a sanity check, we can construct a simple model for the rescaling function $\mathcal{F}$. For a two-level transition illuminated by light of intensity I and frequency detuning δ, the resulting scattering rate and absorption cross-section are [119],

$$R_{\text{scatt}} = \frac{s\Gamma}{2}\frac{1}{1+s+(2\delta/\Gamma)^2} \quad , \quad \sigma = \frac{\sigma_0}{1+s+(2\delta/\Gamma)^2}, \tag{6.40}$$

where $s = I/I_{\text{s}}$. Assuming that $\delta = 0$ for a stationary atom, after scattering N photons the detuning experienced by an atom will be $\approx (2\pi/\lambda)Nv_r$, where $v_r = h/(m\lambda)$ is the recoil velocity induced by a single photon emission[1]. From Eq. (6.40) we have a differential equation for $N(t)$:

$$\frac{\partial N(t)}{\partial t} = R_{\text{scatt}} = \frac{s\Gamma}{2}\frac{1}{1+s+\left(\frac{4\pi v_r}{\lambda\Gamma}\right)^2 N(t)^2}. \tag{6.41}$$

This can be solved numerically. From Eq. (6.38) we anticipate a $\gamma = 97.5\%$ survival probability of an atom per absorption event. The visible column density should then decay during the imaging pulse as $n(t) = n(0)\gamma^{N(t)}$. This gives the effective OD as a function of time:

$$\begin{aligned} n(t)\sigma(t) &= [n(0)\sigma_0]\ \gamma^{N(t)}\ \frac{2}{s\Gamma}\ \frac{\partial N(t)}{\partial t}, \\ &= \text{OD}_{\text{true}}\ \gamma^{N(t)}\ \frac{2}{s\Gamma}\ \frac{\partial N(t)}{\partial t}, \end{aligned} \tag{6.42}$$

where $\text{OD}_{\text{true}} = n(0)\sigma_0$ would be the ideal optical density in the limit of zero-imaging intensity and no depumping. Over an imaging pulse of duration τ, the average transmitted intensity fraction is

$$\frac{\langle I\rangle_t}{I_0} = \frac{1}{\tau}\int_0^\tau \mathrm{d}t\ e^{-n(t)\sigma(t)}, \tag{6.43}$$

giving an overall apparent OD_{meas} of

$$\text{OD}_{\text{meas}} = -\ln\left(\frac{\langle I\rangle_t}{I_0}\right) = \ln\left(\frac{1}{\tau}\int_0^\tau \mathrm{d}t\ e^{-n(t)\sigma(t)}\right). \tag{6.44}$$

Assumpting that the optical density is small, expanding to first order gives,

$$\frac{\text{OD}_{\text{true}}}{\text{OD}_{\text{meas}}} \approx \tau\left[\int_0^\tau \mathrm{d}t\ \gamma^{N(t)}\ \frac{2}{s\Gamma}\ \frac{\partial N(t)}{\partial t}\right]^{-1}. \tag{6.45}$$

This results in an OD scaling function that is independent of atomic density, as we assumed for our empirical function. By normalising Eq. (6.45) to its value at

---

[1] We are neglecting the effect of photon re-emission. This is isotropic, so leads to a random walk in velocity space. Therefore the contribution of photon emission to net velocity along the imaging beam will scale as $\sqrt{N(t)}$, and will be much smaller than the contribution of absorption, scaling as $N(t)$.

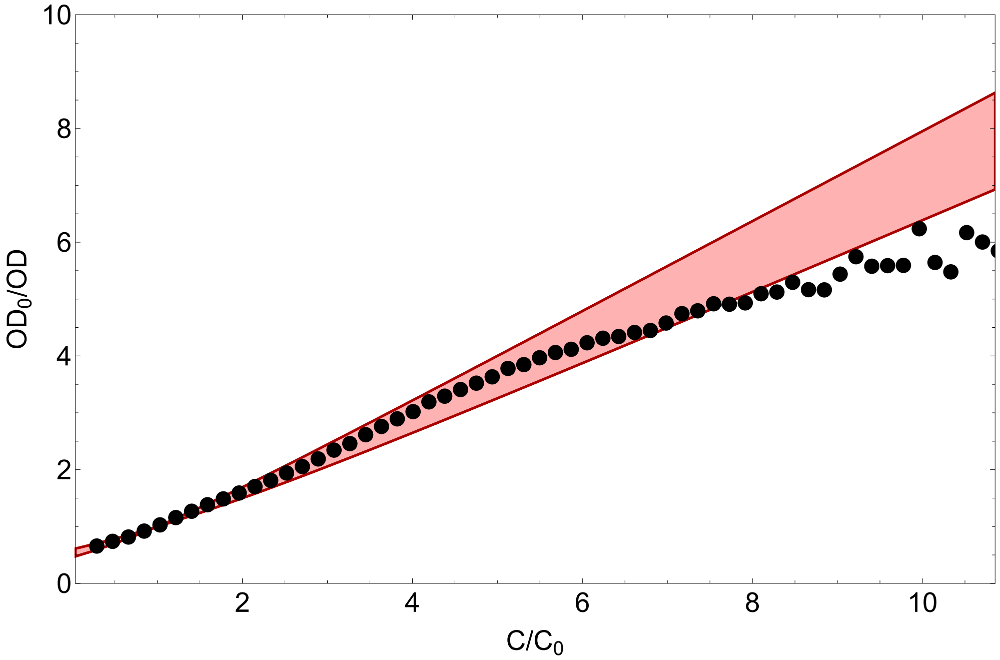

Figure 6.16: *The empirical rescaling function* $(OD_0/OD) = \mathcal{F}(C/C_0)$ *obtained from mapping the correlations between imaging photon count and observed optical density (black points). The rescaling function is referenced to the optical density at a reference imaging photon count of 1300, equivalent to* $(I/I_s) \approx 0.028$*. The red band is the toy model result of Eq. (6.45) referenced to its value at* $C = C_0$*. The band thickness reflects the uncertain ratio between imaging intensities at the atoms and camera (see text). This model assumes a depumping rate of* 2.5% *per absorption cycle, and has no other adjustable parameters.*

.

our reference count C_0, we obtain a model for our rescaling function $\mathcal{F}(C/C_0)$. In Fig. 6.16 we show both the empirically measured rescaling function, and this toy result. The band illustrates the uncertain ratio between the observed photon count and the photon count incident on the atoms; there are 12 air-glass interfaces between the atoms and camera, giving a potential compounded intensity reduction of $0.96^{12} = 0.61$. We observe a generally good agreement between the model and observations.

It is difficult to be more quantitative; our arguments assume that all atoms are depumped at the same rate, which is equivalent to assuming that all atoms experience the same light intensity[1]. In addition, this model neglects other factors which can reduce the observed OD, such as imperfections of the imaging polarisation, and the finite linewidth of the imaging laser. However, it is reassuring that it nevertheless reproduces our observations to within a few percent.

---

[1] We can make a rough estimate of when this should break down: the ratio of surviving fractions at opposite faces of a cloud is $\sim \gamma^N/\gamma^{N\exp(-\mathrm{OD})} \sim \gamma^{N\times\mathrm{OD}}$. Considering the typical number of scattered photons is $N \sim 10$, this leads to an extremely small OD limit for our simple model to be quantitatively accurate.

6.4.3 Imaging Characterisation

It is essential to properly characterise the imaging setup if quantitative information regarding trapped gases is to be obtained. First, to provide a lengthscale for images the imaging system magnification is required; this is essential for determining both atom number and temperature. Second, the effective cross-section is usually some fraction of σ_0; this can result from a multitude of factors, such as acceleration of atoms during the imaging pulse, imperfect imaging polarisation and a finite linewidth of the imaging laser. Knowledge of this imaging efficiency is essential for absolute measurement of atom numbers and densities.

Magnification The magnification of our horizontal imaging system is obtained by calibration against the vertical displacement of a free-falling cloud. The magnification of the vertical imaging system is then obtained by imaging a quasi-pure BEC on both imaging systems, and deducing the vertical magnification by relation to the horizontal. The experimental procedure is given in Appendix D, and results are in Table 6.1.

Imaging efficiency Although the rescaling function of the previous Section accounts for any spatio-temporal variations in imaging light intensity, it does not give an absolute cross-section for absorption of imaging light. Good knowledge of our imaging efficiency is essential if we are to quantitatively confirm the crossover from interacting gas BKT critical conditions, to the ideal gas BEC limit.

We obtain the absolute imaging efficiency by measurement of the critical point for conventional three-dimensional BEC, comparing the observed critical number with its theoretical value. The experimental procedure is described in Appendix D, and we find a ratio of theoretical to observed critical number of 4.3 ± 0.2 after the OD rescaling of Eq. (6.39).

Chapter 7

Mapping the BKT Phase Diagram

In Chapter 5, we outlined an experiment for identifying the BKT critical point in a harmonically-trapped Bose gas, over a range of interaction strengths. Chapter 6 overviewed our experimental setup for creating quasi-two-dimensional Bose gases, tuning their interactions and probing the resulting momentum distribution. In this Chapter, we describe the experimental method in more detail, and present our measurements of the critical point as a function of interaction strength.

Section 7.1 gives a typical experimental sequence for preparing a two-dimensional Bose gas and scanning the BKT critical point. The transition is identified by monitoring the extent of coherence as atom number slowly decays; measurement of this extent, along with thermodynamic variables such as temperature and chemical potential, is described in Section 7.2. Our results for the critical atom number and chemical potential are the topic of Section 7.3, with an analysis of systematic errors in Section 7.4.

7.1 Experimental Sequence

7.1.1 Sample Preparation

We initially prepare a cold gas of ^{39}K identically to the sequence described in [16], which results in $\approx 6 \times 10^6$ atoms in the ODT at a temperature of $\approx 4.4\ \mu$K. The geometric mean of trap frequencies is $\bar{\omega} \approx 2\pi \times 164$ Hz; the gas is thermal, with a central phase-space density of ≈ 0.03.

Our two-dimensional axial trapping beam[1] has a vertical waist of $\approx 5\ \mu$m; loading of an initially spherical cloud would be inefficient, resulting in only a thin 'slice' of atoms being captured. We therefore first cool and load our spherical ODT

---

[1] See Section 6.1.1.

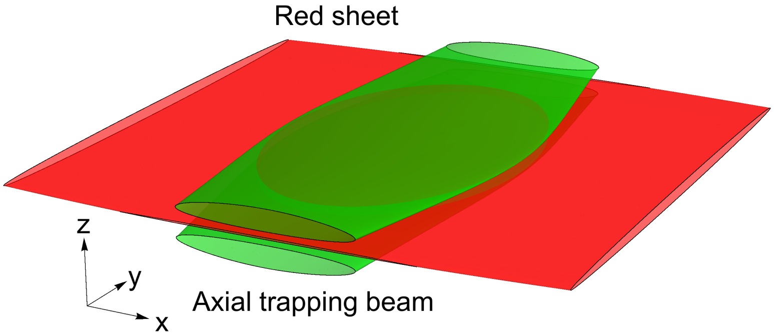

Figure 7.1: *The red sheet used for loading our cloud into the green axial trapping light. For clarity the ODT is not shown; in practice a combination of the red sheet and ODT provides a highly-flattened harmonic trap, which compresses the atomic cloud to lie between the green blades.*

---

cloud into a flattened trap, formed by superimposing the ODT with an attractive Gaussian beam propagating horizontally, with vertical waist 10 μm and transverse waist 500 μm. The optics for this 'sheet' beam are described in [21], and it is illustrated in Fig. 7.1.

We evaporatively cool the cloud by an exponential ramp-down of the ODT power. Over the first 3 s of this ramp, the sheet is increased from zero to its full power of 600 mW. The cloud is therefore simultaneously cooled and loaded into the combined ODT/sheet trap; a small condensate is visible at this point, indicating central phase-space densities $\mathcal{O}(1)$.

7.1.2 Loading of the Two-Dimensional Trap

In the ODT/sheet trap, the cloud temperature is $\sim$ 300 nK, and the axial frequency provided by the red sheet is $\sim$ 1 kHz. This gives an axial thermal diameter $\sim$ 2.5 μm which is much smaller than the separation between the green blades of the axial trapping light; by differentiating Eq. (6.4) the blade separation is calculated as 9.4 μm. This permits loading of the green nodal plane without capturing any atoms above or below the blades. Loading of the two-dimensional trap is accomplished by ramping on the green (axial) light to approximately a third of its eventual final power and then ramping the sheet beam to zero. Our loading efficiency from the sheet into the two-dimensional trap is approximately 50%. We do not observe any trapped atoms above or below the green blades, and so attribute these losses to heating and resultant in-plane losses during the transfer sequence.

After this transfer, the anti-gravity gradient is introduced, and the green light ramped to full power. The final in-trap cooling of the atoms is accomplished by a ramp-down of the ODT power resulting in planar evaporation. This yields $\approx 40,000$ atoms at $\approx$ 170 nK in our experimental trap configuration. Finally, the

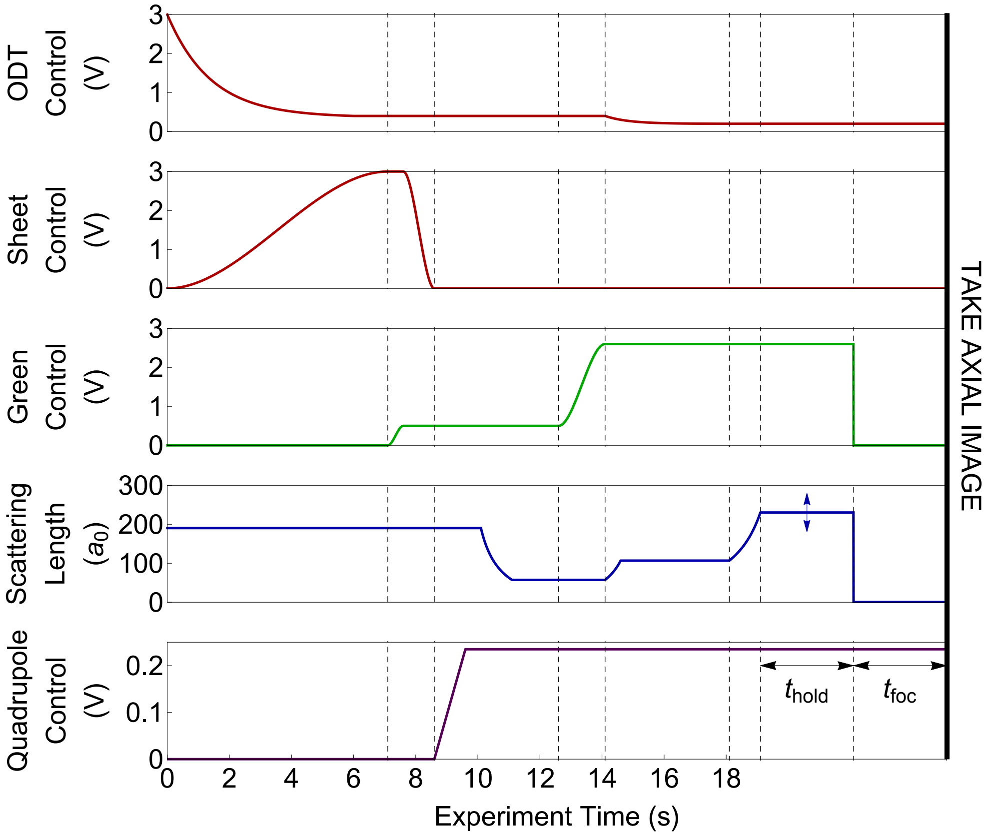

Figure 7.2: *The time evolution of ODT power, sheet beam power, axial green trap power, scattering length and anti-gravity coil control voltage.*

Feshbach field is adjusted to bring the interaction strength to its value of interest. The entire two-dimensional trap loading sequence is illustrated in Fig. 7.2.

Fig. 7.3 depicts the atom cloud after loading into the two-dimensional trap, and after final evaporative cooling. Images along both horizontal and vertical directions are shown; whilst *in situ* images are possible vertically thanks to the use of our Feshbach field as an imaging guide, the horizontal images use a small (~ 4 G) imaging guide along the imaging direction. We therefore ramp the Feshbach field to zero over 100 ms before taking horizontal *in situ* pictures; if a BEC is present this results in heating and depletion of the atoms. However, the method remains useful as an alignment tool.

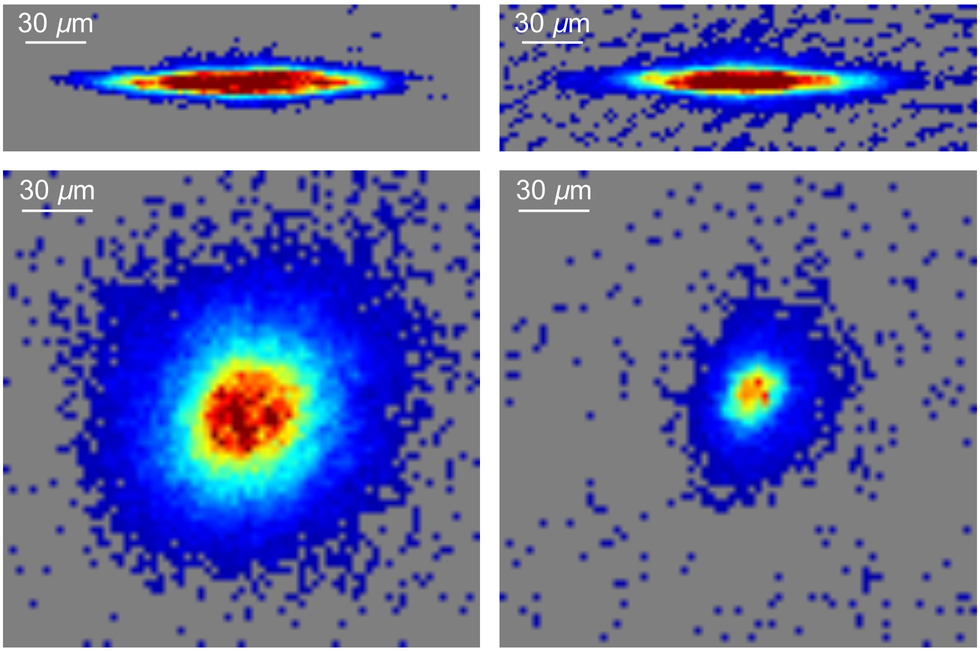

Figure 7.3: *Absorption images of the atom cloud immediately upon loading into the two-dimensional trap (left) and after the final ODT evaporation ramp (right). The main panels show images taken along the axial direction, with the corresponding horizontal images on top. Integration across the trapping plane leads to very high OD, and the horizontal images are saturated for a large fraction of the cloud (see Eq. (D.5)).*

7.1.3 Scanning of Atom Number

The cloud is prepared on the superfluid side of the BKT transition; this is apparent from a dramatic low-k peak in momentum-space [58, 68]. To scan the critical point, we simply wait a variable time in the final trap configuration. Atoms are lost from the trap via background gas collisions, scattering from trapping beams and three-body recombination. These result in a smooth and reproducible decay in atom number, and eventually the cloud centre crosses the superfluid-normal BKT transition.

It is important that the gas equilibrates faster than the rate of atom loss. We can estimate the elastic scattering rate by assuming an ideal gas density profile[1]; the average two-dimensional density $\langle n \rangle$ is then

$$\langle n \rangle = \frac{\int r\mathrm{d}r \left[\ln\left(1 - \exp\left(\tilde{\mu} - V(r)\right)\right)\right]^2}{\int r\mathrm{d}r \ln\left(1 - \exp\left(\tilde{\mu} - V(r)\right)\right)}, \tag{7.1}$$

where $V(r) = (1/2)m\omega_r^2 r^2$ is the in-plane trapping potential, and $\tilde{\mu}$ is fixed to give a characteristic critical central phase-space density $\mathcal{D} \approx 8$.

A similar approach provides the average wavevector: integrating the Bose distri-

---

[1] See Eq. (4.11).

bution over the trap yields the average in-plane momentum,

$$\left\langle k_r^2 \right\rangle = \frac{\int r\mathrm{d}r \int k^3 \mathrm{d}k \left[\exp\left(\beta\left(\frac{\hbar^2 k^2}{2m} + V(r) - \mu\right)\right) - 1\right]^{-1}}{\int r\mathrm{d}r \int k \mathrm{d}k \left[\exp\left(\beta\left(\frac{\hbar^2 k^2}{2m} + V(r) - \mu\right)\right) - 1\right]^{-1}}. \tag{7.2}$$

The axial momentum distribution follows trivially from noting that the harmonic oscillator ground state wavefunction is $\psi(z) \sim \exp(-z^2/(2l_z))$, where the oscillator length $l_z = \sqrt{\hbar/(m\omega_z)}$. The momentum distribution is simply the modulus square of the Fourier transform of $\psi(z)$, hence $n(k_z) \sim \exp(-k_z^2 l_z^2)$ and $\langle k_z^2 \rangle = 1/(2l_z^2)$.

We take the mean relative velocity between two atoms as $v_r = \sqrt{2}\sqrt{\langle k_r^2 \rangle + \langle k_z^2 \rangle}(\hbar/m)$. The mean elastic scattering rate is approximately $8\pi a^2 v_r \langle n \rangle$ [47], which is conveniently written as

$$\text{Mean scattering rate} \approx 0.2N\tilde{g}^2. \tag{7.3}$$

To be confident that our obtained value for a particular quantity Φ represents the equilibrium value, we require multiple thermalising scattering events in the time taken for Φ to change by its measurement error bar [79]. This limitation would make it impossible to reliably extract the critical point at $\tilde{g} = 0$; in our experiment $N \sim 2 \times 10^4$ and for weak interaction strengths we find gas parameters to vary measurably over[1] ~ 1 s. Demanding 5 scattering events in this time limits us to $\tilde{g} \gtrsim 0.04$.

7.1.4 Image Aquisition and Processing

After a variable wait time, during which the atom number smoothly falls, the axial potential is abruptly (< 1 μs) switched off whilst leaving the ODT present and unchanged. The Feshbach field is simultaneously jumped to its zero-crossing value[2] of 350.5 G. After waiting for the momentum focusing time[3] $t_{\mathrm{foc}} = 6.96$ ms we take an absorption image along the vertical direction. This reveals a ‘freeze-frame’ image of the momentum distribution at the moment the axial trapping was removed. By repeated this sequence for various hold times, the full evolution of the momentum distribution across the BKT transition is mapped out.

Typically, a full evolution sequence consists of images taken at ≈ 70 different hold times across the BKT transition. For each hold time we take two images; one at a relatively low intensity $I/I_{\mathrm{s}} \approx 0.023$ and one at a higher intensity of

---

[1] See Fig. 7.6.

[2] As the discussion of Section 6.3.2 indicates, interactions vanish on a timescale ω_z^{-1}, which is much faster than the timescale for the Feshbach field to change. The Feshbach field is changed during focusing because the OD rescaling function of Eq. (6.39) was measured for this imaging field only, and would be inapplicable to images taken at different fields. Furthermore, minimising interactions should reduce any effect of interactions upon the development of a low-momentum peak.

[3] See Eq. (6.27).

$I/I_s \approx 0.2$. The imaging depumping effect[1] leads to a trade-off between signal in the distribution wings and resolution of high OD at the distribution peak. We therefore use the 'low' intensity images for extraction of N, μ and T, and our 'high' intensity image for extraction of P_0.

There are three post-processing procedures applied to the raw experimental images:

1. Optimal reference images are calculated for each shot[2]. This provides a 'best-guess' for the imaging light pattern incident on each atomic sample.
2. The OD of each image is rescaled according to the transformation Eq. (6.39). This accounts for the dependency of imaging efficiency upon imaging photon count.
3. The entire image is scaled to take our imperfect imaging efficiency into account[3].

7.2 Image Analysis and Parameter Extraction

The output from a critical point scan is a sequence of images, showing the evolution of the momentum distribution across the BKT critical point. In Fig. 7.4 we show momentum distributions for an above-critical gas, critical gas, and normal gas. At high atom numbers, a sharp peak is evident in momentum-space, signifying extended coherence. As the number smoothly decays, this peak initially falls sharply, before decaying slowly with the profile wings. For comparison, we also show the corresponding *in situ* profiles; our imaging is not quantitatively reliable in this mode, but gives a qualitative impression of the spatial evolution. As expected, there is no dramatic signature of a transition in real-space[4].

For quantitative comparison with theoretical expectations, each image sequence must be converted into the evolution of various quantities of interest. In particular, we are interested in the degree of extended coherence, the total atom number N, the temperature T and chemical potential μ. The first two parameters can be extracted in a fit-free manner; the quantities (T, μ) however require a model for the gas distribution. In this Section, the extraction of each quantity is outlined.

---

[1] See Section 6.4.2.

[2] See Section 6.4.

[3] See Section 6.4.3.

[4] See Sections 5.2 and 5.3.

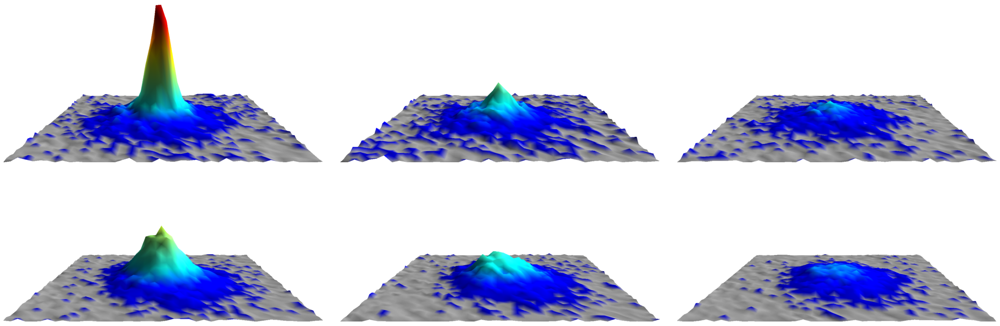

Figure 7.4: *The momentum-space (top) and real-space (bottom) distributions for a super-critical, critical, and normal gas. The interactions strength is* $\tilde{g} = 0.28$*, and these profiles correspond to the data of Fig. 7.6, with the hold times being 6 s, 11 s and 16 s respectively. Whereas momentum-space shows a sharp peak which rapidly falls and abruptly vanishes, the spatial distribution evolved smoothly across the transition.*

7.2.1 Coherence

To follow the evolution of extended coherence, we simply monitor the height of the low-momentum peak, P_0, by averaging the OD within 1 pixel of the peak centre[1]. This measurement is entirely free of any fitting assumptions.

The effect of our finite momentum resolution $\Delta k = 0.4\ \mu\mathrm{m}^{-1}$ was discussed in Section 6.3.3. The momentum distribution should show a sharp change at the BKT point for $(L/\lambda_{\mathrm{th}}) \gg 1$; our system probes[2] $(L/\lambda_{\mathrm{th}}) \approx 22.4$, and we anticipate that the BKT transition should be reliably identified for $\tilde{g} \gtrsim 0.06$.

7.2.2 Number

The total atom number is obtained by summing the OD over all pixels of an image, relying upon our absolute calibration of imaging efficiency. In practice, we restrict this sum to within 4 thermal momenta, $p < 4\sqrt{mk_{\mathrm{B}}T}$, to avoid contributions to noise from atom-free regions of an image. Again, extraction of this parameter makes minimal assumptions.

7.2.3 Thermodynamic Variables

In order to extract the temperature T and chemical potential μ, a fitting model for the momentum distribution is necessary. In three dimensions, for typical interaction strengths ideal-gas models are usually applicable; the ratio of interaction

---

[1] See Chapter 5 and Section 6.3.3.

[2] See Section 6.3.3.

to thermal energy is,

$$\begin{aligned}\frac{g_{3\mathrm{D}} n_{3\mathrm{D}}}{k_{\mathrm{B}} T} &= \frac{4\pi\hbar^2 a n_{3\mathrm{D}}}{m k_{\mathrm{B}} T}, \\ &= 2\frac{a}{\lambda_{\mathrm{th}}}\mathcal{D}^{3\mathrm{D}}. \end{aligned} \tag{7.4}$$

For typical values $a \approx 100a_0$ and $\lambda_{\mathrm{th}} \approx 0.5\ \mu\mathrm{m}$, even for degenerate thermal clouds $\mathcal{D}^{3\mathrm{D}} \approx 1$ this ratio evaluates to $\sim 1\%$ and ideal-gas models remain appropriate.

However, in two dimensions the situation is more complicated. For typical interaction strengths, interactions noticeably modify the gas distribution even in the thermal phase. In this case, the ratio of interaction to thermal energy is,

$$\begin{aligned}\frac{gn}{k_{\mathrm{B}} T} &= \frac{\hbar^2 \tilde{g} n}{m k_{\mathrm{B}} T}, \\ &= \frac{\tilde{g}}{2\pi}\mathcal{D}. \end{aligned} \tag{7.5}$$

In this case, close to the BKT point $\mathcal{D} \approx \mathcal{D}^{\mathrm{BKT}} \approx 10$, and for typical interaction strengths $0 < \tilde{g} < 1$ the ratio is close to unity meaning that interactions must be accounted for.

Moreover, the suppression of bosonic density fluctuations close to the BKT critical point[1] means that constructing a comprehensive model for the momentum distribution is very difficult. It is therefore necessary to restrict our fitting to momenta for which the occupations at a particular (T, μ) can be straightforwardly calculated.

First, we consider several possible candidates for the momentum distribution, and the momenta for which they are valid. Second, we outline the chosen model for the momentum distribution, based on a mean-field-Hartree-Fock (MFHF) approach [101].

Which model is appropriate? There are several approximations to the momentum distribution that we could consider.

1. Boltzmann gas, neglecting interactions and quantum statistics. This assumes both that the occupation per state is very small such that quantum statistics are irrelevant, and neglects interaction energy. In a harmonic system of trapping frequency ω_r, this distribution is,

$$n(p) = \left(\frac{2\pi k_{\mathrm{B}} T}{m\omega_r^2}\right)\sum_{j=0}^{\infty} e^{\beta\left(\mu - \frac{p^2}{2m} - j\hbar\omega_z\right)}. \tag{7.6}$$

   This approach should be valid for momenta $\frac{p^2}{2mk_{\mathrm{B}}T} \gg (1+\tilde{\mu})$, assuming thermal energy to exceed interaction energy.

---

[1] See Section 3.5.3.

2. Ideal quantum gas, neglecting interactions. Integrating the Bose distribution over position, one obtains $n(p)$ as,

$$n(p) = -\left(\frac{2\pi k_{\mathrm{B}}T}{m\omega_r^2}\right)\sum_{j=0}^{\infty}\ln\left(1 - e^{\beta\left(\mu - \frac{p^2}{2m} - j\hbar\omega_z\right)}\right), \tag{7.7}$$

   which reduces to the Boltzmann case for very large momenta. Such an approach is valid if the kinetic energy is much larger than any interaction energy scales, and hold for momenta $\frac{p^2}{2mk_{\mathrm{B}}T} \gg (\tilde{\mu} + \tilde{g}\mathcal{D}/\pi)$.

3. Quantum gas with mean-field interactions. The simplest way to account for interactions is to introduce an interaction potential, defined by the increase in interaction energy associated with adding a particle; according to Eq. (3.4) this is $2gn$ for a fully fluctuating Bose gas. Physically, this is a perturbative approach to interactions, where we assume planar eigenstates $|\mathbf{k}\rangle$ retain a quadratic dispersion relation, and calculate their first-order shift in energy due to the interaction term of Eq. (3.2). One can numerically calculate the momentum distribution in this case; such a calculation is the topic of the following Section.

   In terms of validity, this approach should fail for those momenta whose occupation numbers are significantly modified by correlations. Comparison with the classical-field results [98] of Section 3.5 showed that a fully fluctuating MF equation of state fails when $(\tilde{\mu}^{\mathrm{BKT}} - \tilde{\mu}) \lesssim \tilde{g}$. Assuming that this failure is dominated by the lowest momenta [99], we infer a momentum-space MF validity limit $\frac{p^2}{2mk_{\mathrm{B}}T} \gtrsim (\tilde{g} + \tilde{\mu} - \tilde{\mu}^{\mathrm{BKT}})$. This argument is not particularly rigorous; we shall later empirically show in Section 7.2.4 that this cutoff is appropriate.

Going beyond mean-field, correlations make a straightforward model of the momentum distribution difficult; strong coupling between momentum states changes both the eigenenergies and eigenstate themselves. We therefore adopt a MF perturbative model, the construction of which proceeds as follows.

Mean-Field-Hartree-Fock (MFHF) model Our momentum distribution model follows [101]. We work within the LDA, and assume that at in-plane position $\mathbf{r}$ within the trap the wavefunctions $|\psi\rangle$ are locally separable into planar momentum states $|\mathbf{k}\rangle$, and axial oscillator states $|\phi_j\rangle$,

$$|\psi\rangle_{\mathbf{k},j} = |\mathbf{k}\rangle|\phi_j\rangle. \tag{7.8}$$

This separable form means that eigenenergies are simply summations of planar kinetic energy $\hbar^2k^2/(2m)$, and axial eigenenergies ε_j, which are taken relative to the zero-point energy $\hbar\omega_z/2$.

The momentum distribution is found by integrating the Bose-Einstein distribution over the in-plane coordinate $\mathbf{r}$. For a planar trapping potential $V(\mathbf{r})$ we define the local chemical potential $\mu_{\mathrm{L}}(\mathbf{r}) = \mu - V(\mathbf{r})$, and take into account thermal occupation of higher axial states. This gives,

$$n(k) = \sum_j \int \mathrm{d}^2\mathbf{r} \left[e^{\beta\left(\frac{\hbar^2 k^2}{2m} + \varepsilon_j(\mathbf{r}) - \mu_{\mathrm{L}}(\mathbf{r})\right)} - 1 \right]^{-1} . \tag{7.9}$$

For a non-interacting system the axial energies would simply be $\varepsilon_j = j\hbar\omega_z$, but these are modified by the presence of interactions.

To evaluate the set $\{\varepsilon_j\}(\mu_{\mathrm{L}})$ at a particular radius r_0 we solve the axial Schrödinger equation,

$$\left[\frac{-\hbar^2}{2m}\frac{\partial^2}{\partial z^2} + \frac{m\omega_z^2 z^2}{2} - \frac{\hbar\omega_z}{2} + 2g_{3\mathrm{D}} n_{3\mathrm{D}}(z) \right] \phi_j(z) = \varepsilon_j \phi_j(z), \tag{7.10}$$

where the three-dimensional coupling constant $g_{3\mathrm{D}} = 4\pi\hbar^2 a/m$. The three-dimensional density is constructed from a particular set of axial eigenstates $\{|\phi_j(z)\rangle\}$ and energies $\{\varepsilon_j\}$ by integrating the Bose distribution of Eq. (7.9) over momentum rather than position, giving at the radius r_0,

$$n_{3\mathrm{D}}(z) = -\frac{1}{\lambda_{\mathrm{th}}^2} \sum_j \ln\left(1 - e^{\beta(\mu_{\mathrm{L}}(r_0) - \varepsilon_j)}\right) |\phi_j(z)|^2 . \tag{7.11}$$

Eqs. (7.10, 7.11) must be solved iteratively; an appropriate starting guess is a non-interacting system of states and energies. This method takes into account thermal populations of excited states, interaction-induced deformation of axial eigenstates[1] and interaction-induced shifts in eigenenergies including the differing overlaps between different axial states.

Practically, the Schrödinger equation of Eq. (7.10) is conveniently solved by matrix diagonalisation, in the basis of non-interacting axial states. The first three terms then simply give a contribution to on-diagonal elements

$$\mathcal{H}_{i,j}^{\mathrm{ideal}} = \langle\phi_i(z)| \frac{-\hbar^2}{2m}\frac{\partial^2}{\partial z^2} + \frac{m\omega_z^2 z^2}{2} - \frac{\hbar\omega_z}{2} |\phi_j(z)\rangle = i\hbar\omega_z\delta_{ij}, \tag{7.12}$$

and the only laborious step is the evaluation of the density term,

$$\mathcal{H}_{i,j}^{\mathrm{int}} = \langle\phi_i(z)|2g_{3\mathrm{D}} n_{3\mathrm{D}}(z)|\phi_j(z)\rangle. \tag{7.13}$$

Once the set of eigenenergies $\{\varepsilon_j\}(\mu_{\mathrm{L}})$ has been determined, the momentum distribution for a (μ, T) pair can be constructed via Eq. (7.9). By repeating this for appropriate ranges of μ and T, we construct a numerical interpolation function $n(p, T, \mu)$ for each interaction strength which can be used as a fit function for experimental images.

---

[1] At the BKT critical point, for $\tilde{g} = 0.5$ the critical chemical potential is $\mu^{\mathrm{BKT}} \approx 0.5 k_{\mathrm{B}}T$. Our typical temperatures are 170 nK and the trap spacing $\hbar\omega_z/k_{\mathrm{B}} = 193$ nK, hence interaction energy is roughly half the level spacing, resulting in some admixture between axial states.

Extracting μ and T Having equipped ourselves with numerical fit functions $n(p, T, \mu)$ for each interaction strength addressed, we can proceed to extract μ and T from images. To avoid the computational laboriousness of a two-dimensional fit, we first average each image over iso-momenta. A pixel at (x', y') in focusing trap coordinates maps onto momentum-space according to

$$\begin{pmatrix} p_{x'} \\ p_{y'} \end{pmatrix} = \begin{pmatrix} m\omega_{\mathrm{foc},x'}x' \\ m\omega_{\mathrm{foc},y'}y' \end{pmatrix}, \tag{7.14}$$

and therefore atoms with equal momentum magnitude p lie along a contour $p^2 = p_{x'}^2 + p_{y'}^2 = (m\omega_{\mathrm{foc},x'}x')^2 + (m\omega_{\mathrm{foc},y'}y')^2$ after momentum focusing. We can relate trap coordinates to image coordinates (x, y) by Eq. (6.11), giving image iso-momenta defined by

$$\begin{aligned} \frac{p^2}{m^2} =& x^2 \left(\omega_{\mathrm{foc},x'}^2 \cos^2\theta + \omega_{\mathrm{foc},y'}^2 \sin^2\theta\right) \\ &+ y^2 \left(\omega_{\mathrm{foc},x'}^2 \sin^2\theta + \omega_{\mathrm{foc},y'}^2 \cos^2\theta\right) \\ &+ xy \left(\omega_{\mathrm{foc},x'}^2 - \omega_{\mathrm{foc},y'}^2\right) \sin 2\theta. \end{aligned} \tag{7.15}$$

This is simply an ellipse, orientated at an angle θ relative to image coordinates. The values of $(\omega_{\mathrm{foc},x'}, \omega_{\mathrm{foc},y'}, \theta)$ are given by the focusing trap parameters of Eq. (6.14).

The resulting one-dimensional profiles are straightforwardly fitted with our numerical functions $n(p, T, \mu)$. To avoid a MF validity cutoff which depends upon the (initially unknown) $\tilde{\mu}$, we assume a 'worst-case' scenario of $\tilde{\mu} = \widetilde{\mu^{\mathrm{BKT}}}$ and fit only momenta $p^2 > 2mk_{\mathrm{B}}T\tilde{g}$. We set $T = 220$ nK, greater than the temperature of any single image.

In addition, since our one-dimensional data are derived from elliptically averaging a two-dimensional image, we weight points by $\sqrt{p}$. Our fitting procedure seeks to minimise the sum of squared errors between the data and fit model. This weighting artificially increases the contribution of each data point linearly with momentum, effectively simulating a two-dimensional fit.

An example of an elliptically-averaged momentum distribution $n(k)$ for a critical cloud with $\tilde{g} = 0.28$ is shown in Fig. 7.5, along with the fitted MFHF profile (green line). For illustration, we also indicate both the Boltzmann distribution of Eq. (7.6) and ideal quantum distribution of Eq. (7.7), shown as blue and purple lines respectively, for whom $\mu = 0$ and T is fixed to the result of the MFHF fit. It is clear that the Boltzmann model fails furthest into the wings, with the ideal quantum model performing better and the MFHF visibly superior to both. The vertical red line indicates the momentum bound below which we expect MF to fail.

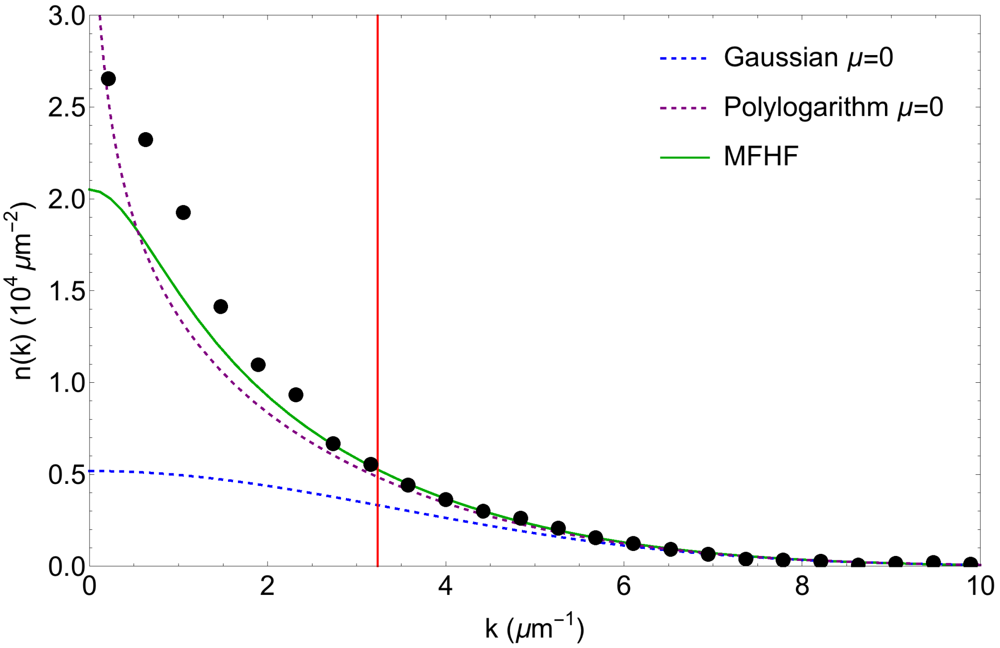

Figure 7.5: *The momentum distribution $n(k)$ of a critical cloud (black points) with $\tilde{g} = 0.28$, extracted by elliptically-averaging an image over increasing iso-momenta. The green solid line is the result of fitting a MFHF model for $n(k)$ (see Section 7.2.3), where the red vertical line denotes the lower bound to momenta for which this model should be applicable. Also plotted are distributions corresponding to a Boltzmann gas (blue) and ideal quantum gas (purple), with $\mu = 0$ and T fixed by the MFHF fit results.*

7.2.4 Critical Parameter Extraction

For a particular image, we obtain N, P_0, T and μ as described above. From a full sequence of images at various *in situ* hold times t, we obtain their evolutions $N(t)$, $P_0(t)$, $\mu(t)$ and $T(t)$. An example set of evolution curves is depicted in Fig. 7.6, for a sample at $\tilde{g} = 0.28$. Whilst N, μ and T display a smooth evolution with hold time, P_0 shows two clear regimes.

We attribute the sharp feature in the evolution of P_0 as indicating the disappearance of extended coherence. A change in the functional form of $g^{(1)}$ in a uniform system would induce a discontinuity in P_0; in a trapped system however, any transition first occurs at the centre over a vanishingly small region, and P_0 evolves continuously.

From the $P_0(t)$ curve, we extract the critical hold time t_c at which the transition occurs. We do not attempt to apply a specific model to the evolution of P_0; the exact evolution is influenced by changes in N, T and the specifics of our imaging system. We therefore choose a heuristic fit function, consisting of two piecewise segments joined at t_c.

$$P_0(t) = P_c + \begin{cases} a\left(1 - e^{-b|t-t_c|}\right) & : t < t_c \\ c\,|t - t_c| & : t > t_c \end{cases} \tag{7.16}$$

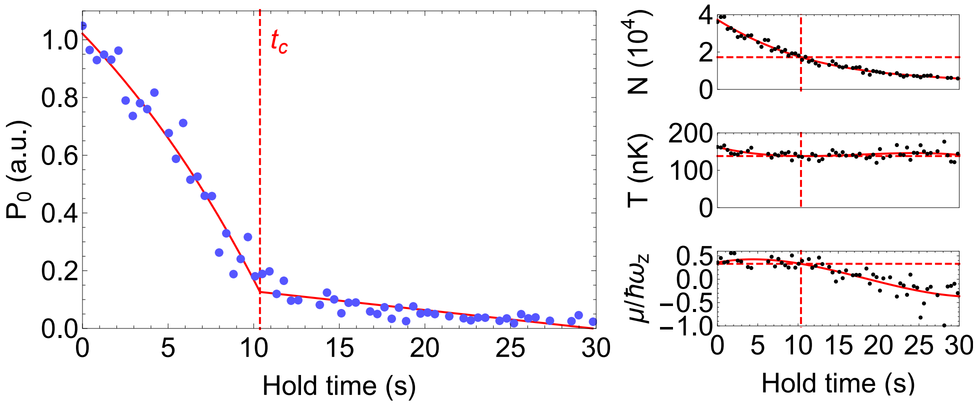

Figure 7.6: *The evolution of P_0, N, T and μ with hold time, for a sample with $\tilde{g} = 0.28$. The critical time t_c is identified via a piecewise fit to $P_0(t)$ (see text), indicated by the red solid line. Once determined, other parameters are fitted with third order polynomials (solid red lines) and their values at t_c interpolated. The red dashed lines denote t_c, and the interpolated critical values of each parameter.*

Close to t_c, the exponential segment simply reduces to a linear evolution $ab|t - t_\mathrm{c}|$. This piecewise function is effectively two linear segments, but allowing for OD saturation at early times.

The P_0 fit is superimposed on the example data set of Fig. 7.6 (solid red line). Having determined t_c, we fit $N(t)$, $T(t)$ and $\mu(t)$ with third-order polynomials and read off their critical values. A cubic is chosen merely to provide a smoothly evolving curve, and the method is effectively an interpolation with the demand of slow variation.

Finally, we arrive at a critical set of parameters $N_\mathrm{c} = N(t_\mathrm{c})$, $T_\mathrm{c} = T(t_\mathrm{c})$ and $\mu_\mathrm{c} = \mu(t_\mathrm{c})$. By repeating for various values of the interaction strength, we construct the variation of these critical parameters with $\tilde{g}$; this variation is presented and discussed in the following Section.

Validity of MF momentum model We note that the only theoretical assumption in our entire methodology is the validity of MF theory in the momentum distribution wings. We recall from Section 7.2.3 that we assumed a MF approach to be valid for momenta $p^2 > 2mk_\mathrm{B}T\tilde{g}$. If this is invalid, or worse if the MF model is always inappropriate, we should see variation in the fitted variables (μ, T) as this cutoff is varied.

We therefore repeated the extraction of critical parameters for various values of momentum cutoff. Fig. 7.7 shows the dependence of $(\mu_\mathrm{c}, T_\mathrm{c})$ on the fitting momentum cutoff for $\tilde{g} = 0.44$. Reassuringly, a plateau is observed, with the critical parameters being insensitive to cutoff over a reasonable range of values.

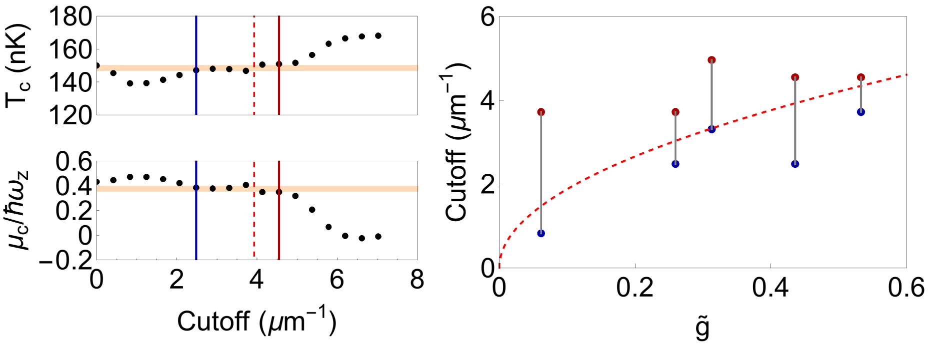

Figure 7.7: *The left plots depict the extracted critical temperature T_c and chemical potential μ_c for interaction strength $\tilde{g} = 0.44$, as a function of the lower bound in fitted momenta. The vertical red dashed line depicts our suggested cutoff $p^2 = 2mk_{\mathrm{B}}T\tilde{g}$ for the validity of a MF fitting model, calculated for $T = 220$ nK, which is greater than any observed temperatures. Reassuringly this lies within a plateau for both quantities, illustrated by oranges bands which represent the mean and standard deviation of T and μ plateau values. The plateau boundaries are estimated as the blue/red solid lines. On the right we show estimated upper (red) and lower (blue) plateau bounds as a function of $\tilde{g}$. The red dashed line is the same MF cutoff, and lies within the plateaux for all $\tilde{g} \lesssim 0.5$.*

The lower plateau boundary is set by beyond-MF effects, which enhances the momentum occupation numbers. This results in a momentum distribution which is more peaky than a pure-MF approach would suggest, increasing the fitted temperature. Such beyond-MF peakiness was experimentally observed in [60]. At extremely small cutoffs this trend reverses due to saturation of the high-OD central region; this reduces the fitted μ and increases the fitted T.

The upper plateau boundary is more confusing. As the fit is restricted further to the momentum distribution wings, it is reasonable to expect that the fit noise would increase but we see a clear systematic trend of increasing fitted temperature. We attribute this effect to the anharmonicity of our momentum focusing trap, due to the Gaussian profile of the ODT beams which provide the focusing potential. Qualitatively, this is a reasonable assumption; the Gaussian potential would lead high-momentum atoms to travel *further* during focusing than an ideal harmonic trap would permit. Our momentum mapping $p = m\omega_{\mathrm{foc}}x$ will then overestimate their momentum, leading to a higher apparent 'local' temperature in the high-momentum wings. More quantitatively, we performed numerical simulations of a cloud evolving in a Gaussian focusing potential rather than harmonic, and observed the same behaviour. This upper bound imposed by our anharmonic focusing potential sets an upper limit of the values of $\tilde{g}$ for which we can reliably extract (μ, T). We therefore restrict our study to $\tilde{g} \lesssim 0.5$.

In Fig. 7.7 we also show the lower and upper plateau bounds for various values of $\tilde{g}$. Reassuringly, our cutoff of $p^2 > 2mk_{\mathrm{B}}T\tilde{g}$ (red dashed line) always lies within the plateau. This gives us good confidence both that our MF model is valid, and our momentum cutoff is appropriate.

7.3 Experimental Results

Having obtained the critical number N_c, chemical potential μ_c and temperature T_c we can proceed to compare them with theoretical predictions for BKT and BEC over a range of interaction strength. As we showed in Section 4.1, in a quasi-two-dimensional system we should expect pure-two-dimensional physics to occur in the axial ground state. We therefore first remove the contribution to N_c from excited axial states. This is straightforwardly accomplished within our MFHF model[1]; using $(\mu_\mathrm{c}, T_\mathrm{c})$ we can calculate the excited state number $N_{j>0}$ by integrating Eq. (7.9) over k, for axial levels $j > 0$. This yields the ground state number $\bar{N}_\mathrm{c} = N_\mathrm{c} - N_{j>0}$.

In the following Sections 7.3.1 and 7.3.2 we present our results for $\bar{N}_\mathrm{c}$ and μ_c as a function of $\tilde{g}$.

7.3.1 Critical Number

In Fig. 7.8, we show $\bar{N}_\mathrm{c}$ for various $\tilde{g}$, scaled to the ideal gas BEC critical number N_c^0 of Eq. (4.13). Our finite momentum resolution means that the BKT transition cannot be reliably identified for $\tilde{g} \lesssim 0.06$; this is denoted by a orange shaded region[2]. This region is wider than the finite crossover region between BKT and BEC ($\tilde{g} \lesssim 0.01$) resulting from the finite size of the system[3], and comparable with the region lacking a sufficiently high thermalisation rate[4], $\tilde{g} \lesssim 0.04$. At higher $\tilde{g} \gtrsim 0.5$, the focusing trap anharmonicity should distort the ratio; when fitting the far wings of the momentum distribution, the apparent temperature rises[5]. This both increases the calculated occupation N_ex of axial excited states, and increases the calculated ideal gas critical number N_c^0; both of these effects reduce the ratio plotted in Fig. 7.8.

Without any adjustable parameters, our data display excellent agreement with the critical point prediction of Eq. (4.21), denoted by the red line. This offers strong support for the validity of modelling the non-perturbative fluctuation region surrounding the BKT critical point using the classical-field approach of [96, 98]. Whilst the classical-field results were anticipated by the authors to be valid for

---

[1] See Section 7.2.3. One might worry about using a MF model, which we have already asserted should fail for low momenta. However, whilst beyond-MF physics affects the distribution of atoms between in-plane momentum states, it should not change the population of each axial level which is dominated by MF physics [99].

[2] This limit can be estimated as when the normal gas correlation length exceeds the distance L over which we probe coherence; this is discussed in Section 6.3.3.

[3] See Section 4.2.3.

[4] See Section 7.1.3.

[5] See Section 7.2.4.

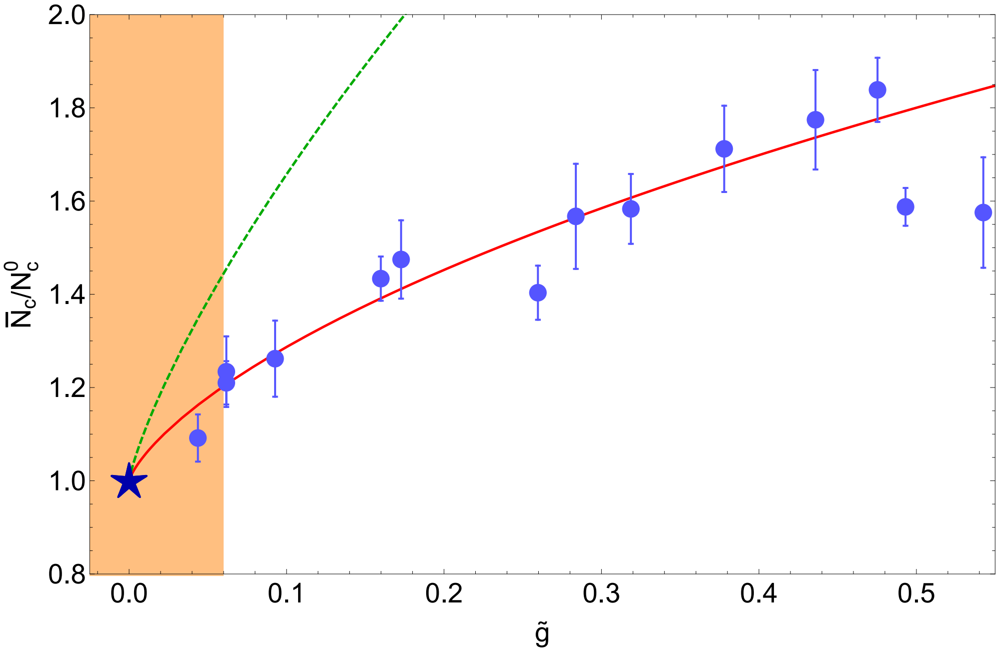

Figure 7.8: *The critical atom number scaled to the ideal gas BEC result* N_c^0*, as a function of interaction strength* $\tilde{g}$*. The solid red line denotes a classical-field prediction for the BKT critical point, without any free parameters, whereas the dashed green line is a MF approximation which neglects suppression of bosonic density fluctuations in the normal state. The star denotes the ideal gas BEC critical point, and the shaded region the values of* $\tilde{g}$ *for which our identification of the onset of coherence is not reliable. Error bars are statistical (see Section 7.4).*

$\tilde{g} \lesssim 0.1$ [98], the critical point prediction describes our data extremely well for all $\tilde{g}$ addressed.

Furthermore, the agreement with Eq. (4.21) over an order of magnitude in $\tilde{g}$, and the proximity of our lowest reliable $\tilde{g}$-values to zero, indicates that the critical atom number smoothly converges onto the ideal gas BEC result as $\tilde{g} \to 0$. This convergence is observed without any free parameters, relying upon an accurate absolute number calibration, and confirms the connection between the BKT and BEC critical point in the ideal gas limit.

It is also interesting to contrast our data with the MF prediction of Eq. (4.18), denoted by the green dashed line. The severe overestimation of N_c provided by this approach emphasises the extent of fluctuation suppression at the critical point.

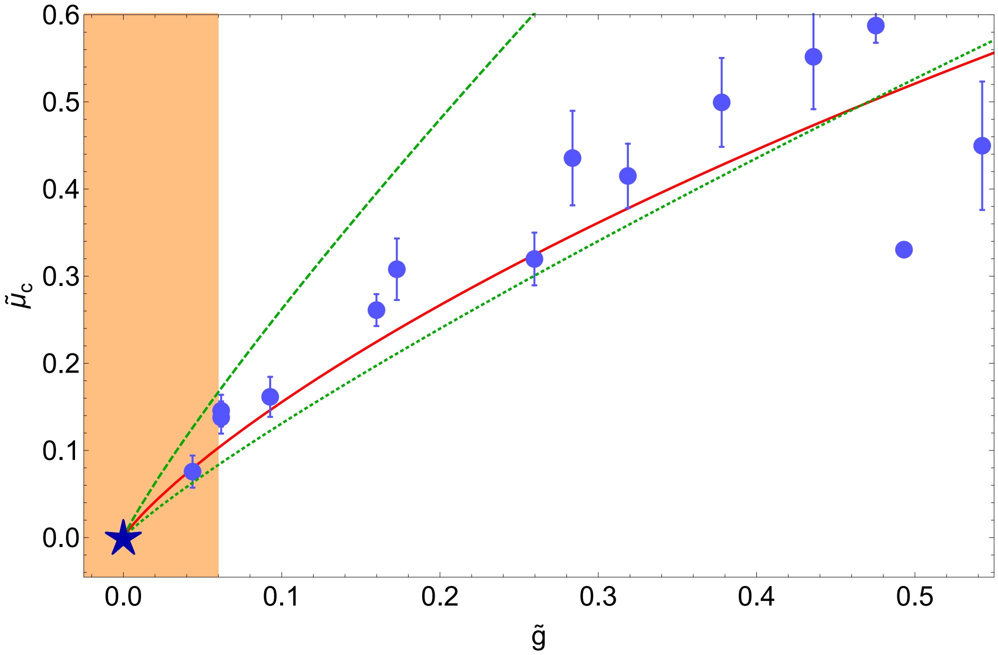

Figure 7.9: *The critical chemical potential as a function of interaction strength $\tilde{g}$. Values are shown scaled to T, in accordance with classical-field predictions and the scale invariance of the two-dimensional Bose gas. The dashed line is a MF result assuming no suppression of density fluctuations, whereas the dotted line assumes full suppression. Error bars are statistical.*

7.3.2 Critical Chemical Potential

For a more direct comparison with the uniform system BKT theory[1] we also consider the critical chemical potential μ_c. As a consequence of the scale invariance of the two-dimensional Bose gas[2] we expect a critical $\tilde{\mu}_c = (\mu/(k_B T))_c$, which is plotted in Fig. 7.9 against $\tilde{g}$. We observe very good agreement with the classical-field prediction of Eq. (3.26), denoted by a red line. Just like the theoretical prediction, our data approach $\tilde{\mu}_c = 0$ as $\tilde{g} \to 0$, which recovers the ideal gas BEC result. The small overall shift between the data and classical-field prediction is comparable with our estimated systematic error[3].

It is illuminating to compare our observed $\tilde{\mu}_c$ with two intuitive MF approximations. We introduce an interaction potential $\gamma g n$, where $\gamma = 2$ corresponds to a fully fluctuating Bose gas and $\gamma = 1$ to full suppression of fluctuations[4]. Although MF theory alone does not predict the BKT transition, we can define a critical chemical potential $\tilde{\mu}_c^\gamma$ such that the density reaches $\mathcal{D}^{\mathrm{BKT}}$. Using the MF

---

[1] See Chapter 3.
[2] See Section 3.2.
[3] See Section 7.4.
[4] See Section 3.2.

	Statistical	Systematics		
		Calibration	*Finite size*	*Anharmonicity*
$\bar{N}_{\mathrm{c}}/N_{\mathrm{c}}^{0}$	± 0.08	± 0.14	+0.04	−0.01
$\tilde{\mu}_c$	± 0.03	± 0.05	+0.005	−0.04

Table 7.1: *Absolute standard uncertainties (68% confidence interval) and estimated systematic shifts affecting the measured $\bar{N}_{\mathrm{c}}/N_{\mathrm{c}}^{0}$ and $\tilde{\mu}_c$. Statistical errors are shown as error bars in the main paper. All values are typical for the experimentally explored range of $\tilde{g}$. The positive (negative) systematic shifts correspond to the measured values being higher (lower) than the true ones.*

equation of state (Eq. (3.1)), this yields

$$\tilde{\mu}_{\mathrm{c}}^{\gamma} = \frac{\gamma \tilde{g} \mathcal{D}^{\mathrm{BKT}}}{2\pi} + \ln\left(1 - e^{-\mathcal{D}^{\mathrm{BKT}}}\right), \tag{7.17}$$

which are plotted as dashed ($\gamma = 2$) and dotted ($\gamma = 1$) lines in Fig. 7.9. Generally the $\gamma = 1$ curve provides a much better approximation to $\tilde{\mu}_{\mathrm{c}}$, highlighting how strong the suppression of fluctuations is at the critical point.

Although it is tempting to consider a fractional $1 < \gamma < 2$ to account for the partial suppression of fluctuations, this approach does not physically make sense; introducing interactions via a potential $V_{\mathrm{int}} \propto n$ is valid only for a density-independent γ. This is only the case for the extremal values $\gamma = 2$ or 1 (see Section 3.5).

Finally, we note that in previous experiments on the *in situ* equation of state [61, 66], $\tilde{\mu}_{\mathrm{c}}$ was deduced by defining it so as to satisfy the theoretical expectation [98] that the phase-space density should be a universal function of $(\tilde{\mu} - \tilde{\mu}_{\mathrm{c}})/\tilde{g}$. Our measurements of $\tilde{\mu}_{\mathrm{c}}$ defined through the emergence of extended coherence show that the two definitions indeed lead to very similar values.

7.4 Error Analysis

Since we are seeking to compare our measured critical points with BKT and BEC predictions without any free parameters, it is important to properly characterise their associated errors. All error bars shown in Figs. (7.8, 7.9) are purely statistical, illustrating how precisely critical parameters can be determined given experimental noise in measured quantities and the finite number of images per critical point sequence. In addition to these statistical errors, there are various sources of systematic error. These can be divided into arising from system calibration uncertainties, finite-size physics, the inhomogeneity of our trapped gas and anharmonicity of our focusing trap. The procedure for estimating statistical and systematic errors is given in Appendix F, with a summary presented in Table 7.1.

Cumulatively, our critical parameter uncertainties are sufficiently small that we may strongly exclude fully fluctuating MF predictions, denoted by green dashed lines in Figs. 7.8 and 7.9. Whilst our critical atom numbers display excellent agreement with classical-field predictions for the BKT critical point, the measured critical chemical potentials are shifted with respect to the classical-field prediction by $0.05 \lesssim \Delta\tilde{\mu} \lesssim 0.1$. This shift is comparable with our combined statistical and systematic errors; within experimental uncertainty we cannot conclude any significant discrepancy.

Chapter 8

Conclusions and Outlook

In this experimental work, we have systematically identified the onset of extended coherence in a harmonically-trapped quasi-two-dimensional gas over a wide range of interaction strengths. Without any free parameters we extracted the critical atom number and chemical potential, comparing them with various predictions for both the BKT and BEC phase transitions. Our central conclusions are two-fold.

First, by identifying the critical point over a wide range of $\tilde{g}$, we showed that the critical point for the normal-superfluid BKT transition does indeed converge onto the ideal gas BEC result. This connection between the interaction-driven BKT and statistically-driven BEC transitions would not be observable in an infinite uniform potential.

Second, we observe excellent agreement of the measured critical atom number and chemical potential with the predictions of a classical-field analysis of the BKT transitions [96, 98, 99]. This agreement is sustained over an order of magnitude in interaction strength $0.05 \lesssim \tilde{g} \lesssim 0.5$; the agreement may persist for higher values of $\tilde{g}$, but we were precluded from addressing these by experimental limitations[1]. This agreement emphasises the crucial importance of beyond-MF behaviour in the vicinity of the BKT transition, and offers support for the validity of using classical-field simulations to model the non-perturbative critical behaviour of interacting bosons. Mean-field predictions for the critical parameters, which assume full bosonic density fluctuations, give a poor description of the critical parameters.

Furthermore, a subtlety worthy of mention is that the classical-field predictions were made for a pure-two-dimensional system, with no excitations or dynamics included in the axial direction. Our measurements were (unavoidably) for the case of quasi-two-dimensional trapping, with $\lesssim 30\%$ of atoms occupying excited axial states. The quality of agreement between the calculated ground state atom number and the pure-two-dimensional classical-field predictions supports

---

[1] Experiments on the equation of state [61, 66] suggested the classical-field results to remain accurate at least up to $\tilde{g} \approx 3$.

the conclusions of Section 4.1 that the axial ground state should display pure-two-dimensional physics, with the caveat that the superfluid be kinematically two-dimensional. In our case the ratio of trap spacing to superfluid interaction energy $\hbar\omega_z/(gn_\mathrm{s}) \approx 3.6$ for our highest interaction strength $\tilde{g} \approx 0.5$, and this condition is well-satisfied.

In future work, it would be very interesting to address the dimensional crossover from two-dimensional to three-dimensional behaviour, and investigate at which point pure-two-dimensional predictions become invalid. In particular, in Section 4.1 we suggested that as collective superfluid excitations become gradually possible in the axial direction, the jump in superfluid fraction at the BKT transition should smoothly disappear.

The recent creation of two-dimensional traps within a uniform planar trapping potential at ENS [105] offer exciting opportunities for studies of non-equilibrium critical phenomena such as the nucleation of phase defects [105]; one could extend recent experiments on the Kibble-Zurek mechanism in the three-dimensional homogenous Bose gas [124] to two dimensions. Another experiment facilitated by a uniform potential would be a conclusive measurement of the predicted algebraic correlation function for a BKT superfluid. Whilst several experiments have addressed the form of the correlation function in harmonic systems [9, 57] measurements were not conclusive; the use of a Ramsey-interferometric method for obtaining correlation functions [57, 124] would offer a quantitative measure of $g^{(1)}$ for a uniform system.

Appendix A

Publications

Connecting Berezinskii-Kosterlitz-Thouless and BEC Phase Transitions by Tuning Interactions in a Trapped Gas

Richard J. Fletcher, Martin Robert-de-Saint-Vincent*, Jay Man, Nir Navon, Robert P. Smith, Konrad G. H. Viebahn, and Zoran Hadzibabic*

Phys. Rev. Lett. **114**, 255302 (2015)

PRL **114,** 255302 (2015) PHYSICAL REVIEW LETTERS week ending 26 JUNE 2015

Connecting Berezinskii-Kosterlitz-Thouless and BEC Phase Transitions by Tuning Interactions in a Trapped Gas

Richard J. Fletcher,* Martin Robert-de-Saint-Vincent,† Jay Man, Nir Navon, Robert P. Smith,
Konrad G. H. Viebahn, and Zoran Hadzibabic
Cavendish Laboratory, University of Cambridge, J. J. Thomson Avenue, Cambridge CB3 0HE, United Kingdom

(Received 12 January 2015; revised manuscript received 22 March 2015; published 26 June 2015)

We study the critical point for the emergence of coherence in a harmonically trapped two-dimensional Bose gas with tunable interactions. Over a wide range of interaction strengths we find excellent agreement with the classical-field predictions for the critical point of the Berezinskii-Kosterlitz-Thouless (BKT) superfluid transition. This allows us to quantitatively show, without any free parameters, that the interaction-driven BKT transition smoothly converges onto the purely quantum-statistical Bose-Einstein condensation transition in the limit of vanishing interactions.

DOI: 10.1103/PhysRevLett.114.255302 PACS numbers: 67.85.-d, 03.75.Hh, 05.30.-d

Reducing the dimensionality of a physical system increases the importance of thermal fluctuations and can profoundly affect the type of order that the system can display at low temperatures [1–4]. In a uniform two-dimensional (2D) Bose gas, the true long-range order associated with Bose-Einstein condensation (BEC) is precluded at any nonzero temperature by the Mermin-Wagner theorem. However, an interacting 2D Bose gas still undergoes the Berezinskii-Kosterlitz-Thouless (BKT) transition to a superfluid state at a critical phase-space density D_{BKT} [5,6]. Quantitatively predicting D_{BKT} requires an accurate description of the nonperturbative behavior of interacting bosons in the fluctuation region near the critical point. Classical-field simulations [7] model this behavior by a turbulent matter-wave field [8], and predict $D_{\mathrm{BKT}} = \ln(380/\tilde{g})$, where $\tilde{g}$ is a dimensionless measure of the interaction strength [9]. This result makes it manifest that the transition is interaction driven; the critical temperature $T_c \propto n/D_{\mathrm{BKT}}$, where n is the gas density, vanishes in the noninteracting limit $\tilde{g} \to 0$ for any noninfinite n. While for phase-space density $D > D_{\mathrm{BKT}}$ true long-range order is still absent, the first order correlation function $g_1(r)$ decays only algebraically at large distance, in contrast to the exponential decay in the normal degenerate gas. Such extended coherence is sufficient for superfluidity [10], and in practice offers a signature of the phase transition [11–14].

In contrast to the infinite uniform system, in a 2D harmonic trap, pertinent to most ultracold-atom experiments on BKT physics [15–29], the modified density of states allows for a BEC transition to occur in the ideal gas ($\tilde{g} = 0$) [30,31] (see also Ref. [32]). In an isotropic trap of frequency ω_r, it should occur at a critical atom number [30,31]

$$N_c^0 = \frac{\pi^2}{6}\left(\frac{k_B T}{\hbar\omega_r}\right)^2. \tag{1}$$

This ideal-gas BEC transition is similar to the familiar condensation in three dimensions; it is purely quantum statistical and follows from Einstein's standard argument of the saturation of the excited states. However, the importance of dimensionality emerges if interactions are introduced. In three dimensions, ideal-gas BEC occurs when in the trap center $D \approx 2.612$; weak interactions slightly shift the critical atom number [33–35], but do not alter the BEC-like nature of the transition. In two dimensions, while N_c^0 is finite, the phase-space density required in the trap center for the excited states to saturate is infinite, just as in a uniform system [14]. For any $\tilde{g} > 0$ this is unattainable and the excited states can accommodate any number of particles [36]. The BEC transition is thus suppressed and one expects it to be replaced by the BKT transition with noninfinite D_{BKT} [10].

These arguments suggest that the two conceptually very different phase transitions, the interaction-driven BKT and the saturation-driven BEC, are in fact continuously connected as $\tilde{g} \to 0$ [10,37]. The harmonic trapping potential offers the opportunity to experimentally observe this unification of BKT and BEC physics. While in an infinite uniform gas no transition occurs for $\tilde{g} = 0$, in a harmonic trap a transition always occurs at a finite N_c and always results in significantly extended coherence of the gas. The nature of this transition is quantitatively encoded in the value of N_c. This picture is supported by the calculations of the critical atom number N_c^{BKT} [10,38], based on the classical-field simulations [7,39], which suggest that N_c^{BKT} smoothly connects to N_c^0 in the limit $\tilde{g} = 0$. In a finite-size system the change from the BKT to the BEC transition is a crossover that spans a nonzero range of $\tilde{g}$ values, but for realistic experimental parameters the width of this crossover region is very small, $\tilde{g} \lesssim 10^{-2}$ [18,40].

Various signatures of a phase transition, including emergence of extended coherence [15,17–19,21] and superfluidity [24], have been observed in trapped 2D gases with different specific $\tilde{g}$ values. On the other hand, systematic studies with a tunable $\tilde{g}$ have focused on *in situ* measurements of the equation of state [22,27], which do not directly reveal any striking signatures of the infinite-order BKT transition.

In this Letter, we systematically study the critical point for the emergence of extended coherence in a harmonically trapped 2D Bose gas over a wide range of interaction strengths, $0.05 < \tilde{g} < 0.5$. We show, without any free parameters, that N_c generally agrees very well with the beyond-mean-field calculation of N_c^{BKT} [38], and converges onto N_c^0 of Eq. (1) as $\tilde{g} \to 0$. The critical chemical potential μ_c, which directly reveals uniform-system conditions for a phase transition to occur in the trap center, also agrees with the BKT theory and converges onto the BEC value, $\mu_c = 0$, for $\tilde{g} \to 0$. Our measurements also reiterate the importance of the suppression of density fluctuations in the normal state near the BKT critical point, previously observed in Refs. [18,19,21–23].

The experiment was carried out using a ^{39}K gas, in the apparatus described in Ref. [41]. For 2D trapping, the tight axial (vertical) confinement is provided by two repulsive "blades" of blue-detuned light, formed by passing a 532-nm Gaussian beam through a 0-π phase plate [20,42], while a red-detuned 1064-nm dipole trap provides the in-plane (horizontal) confinement. The radial and axial trapping frequencies are $(\omega_r, \omega_z) \approx 2\pi \times (38, 4100)$ Hz. For all of our measurements $T \in [140\ \mathrm{nK}, 190\ \mathrm{nK}]$ and $\mu/k_B < 100$ nK, resulting in a small ($< 30\%$) occupation of the excited axial states. The interaction strength $\tilde{g} = \sqrt{8\pi}a/\ell_z$ [14], where a is the s-wave scattering length and $\ell_z = \sqrt{\hbar/(m\omega_z)}$, is controlled via a Feshbach resonance centered at 402.5 G [41,43].

To characterize long-range coherence of a gas we study its (in-plane) momentum distribution $n(k)$ [19]. A change in the functional form of $g_1(r)$ leads to a dramatic change in its values at distances much larger than the thermal wavelength $\lambda = h/\sqrt{2\pi m k_B T}$ [14], and an increase of coherence over some large distance L manifests itself in enhanced population of the low-momentum states $k \lesssim 2\pi/L$. Thus, unlike the in-trap density distribution, which varies very smoothly through the BKT critical point [18,19,22,23], $n(k)$ can provide a dramatic signature of the phase transition [19].

As illustrated in Fig. 1, to identify the critical point for a given $\tilde{g}$, we start with a highly coherent 2D gas and measure $n(k)$ after holding the cloud in the trap for a variable time t. During the hold time, the atom number N slowly decays through various inelastic processes [44], while the elastic-collision rate ($\approx 0.2N\tilde{g}^2\ \mathrm{s}^{-1}$) remains sufficiently high to ensure that the gas is in quasistatic equilibrium. To measure $n(k)$, we employ the "momentum focusing" technique [19,29,45,46]. We turn off just the tight z confinement, so the rapid vertical expansion (predominantly driven by the zero-point motion along z) removes all the interaction energy on a time scale $1/\omega_z \ll 1/\omega_r$. The subsequent horizontal ideal-gas evolution in the remaining in-plane harmonic potential reveals $n(k)$ as the spatial distribution after a quarter of the trap period. We probe this distribution by absorption imaging along z [see Fig. 1(a)].

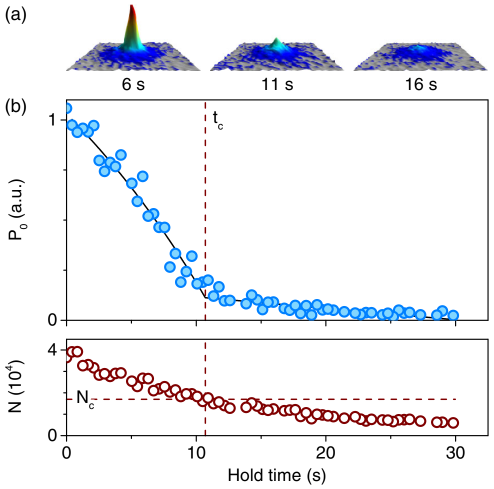

FIG. 1 (color online). Determination of the critical point for the onset of coherence, for $\tilde{g} = 0.28$ and $T \approx 140$ nK. (a) Evolution of the momentum distribution $n(k)$ with the hold time t (see text). Extended coherence is revealed as a sharp peak in $n(k)$. Each image is an average of three experimental realizations. (b) Evolution of the momentum-distribution peak P_0 and the smoothly decaying total atom number N. We associate the thresholdlike behavior of P_0 with the critical time t_c and deduce the corresponding N_c. The solid line is a heuristic piecewise fit function used to determine t_c [47].

Our k-space imaging resolution, $\Delta k \approx 0.4\ \mu\mathrm{m}^{-1}$, sets the largest distance over which we can probe coherence to $L = 2\pi/\Delta k \approx 15\ \mu$m, which is much larger than $\lambda \approx 0.7\ \mu$m. To probe coherence on this length scale, we simply monitor the peak value of the momentum distribution, P_0, without making any theoretical assumptions about the exact shape of $n(k)$ at low k. To get the corresponding atom number N we do a simple summation over the image. Importantly, we eliminate the systematic error due to the uncertainty in the absorption-imaging cross section by independently calibrating our imaging system through measurements of the BEC critical point in a 3D gas [47].

In Fig. 1(b) we show a typical evolution of P_0 and N (here $\tilde{g} = 0.28$). While N decays smoothly, P_0 shows two distinct regimes, which allows us to identify the critical hold time t_c and the corresponding N_c. We note that even for N significantly below N_c the peak of $n(k)$ rises above a Gaussian fitted to the wings of the distribution, indicating some coherence on a length scale $> \lambda$ [18,21]. The smooth evolution of such non-Gaussian "peakiness" of $n(k)$ does not reveal a phase transition [21], and only P_0 corresponding to $L \gg \lambda$ shows a clear change in behavior at a well-defined N_c [51]. Our large L is still small compared to the thermal diameter of the cloud, $2\sqrt{k_B T/(m\omega_r^2)} \approx 50\ \mu$m, so the observed N_c is closely linked to the occurrence of a phase transition in the center of the trap [47].

For comparisons with theory, we also fit μ and T to each $n(k)$ image. Unlike in three dimensions, in two dimensions interactions affect $n(k)$ appreciably even in the normal state, and near the critical point it is in general insufficient to treat them at a mean-field (MF) level. However, beyond-MF correlations primarily affect the highly populated low-k states [38]. We restrict our fits to the high-k wings of the distribution ($\hbar^2 k^2 > 2\tilde{g}mk_BT$), where we expect the beyond-MF effects to be small, and still carefully include the effects of interactions at a MF level [47]. Following Ref. [37], we also account for the residual thermal occupation of the axial excited states and the interaction-induced deformation of the axial eigenstates.

In Fig. 2 we summarize our measurements of the critical atom number for a wide range of interaction strengths. To compare our data with the strictly 2D theoretical calculations, we correct the observed "raw" N_c by subtracting the calculated population of the excited axial states [47]. We scale this corrected critical number $\bar{N}_c$ to the BEC critical atom number N_c^0 of Eq. (1) and plot it versus $\tilde{g}$. Our Δk-limited value of L imposes a lower bound on $\tilde{g}$ for which we can reliably identify the critical point. In the absence of any phase transition, in a weakly interacting degenerate gas $g_1(r) \sim \exp(-r/\ell_0)$, with $\ell_0 = \lambda\exp(D/2)/\sqrt{4\pi}$ [14]. We thus do not expect our measurements to reliably identify N_c if $\ell_0 > L$ for some $D < D_{\rm BKT}$. This occurs for $\tilde{g} < 380\lambda^2/(4\pi L^2) \approx 0.06$, indicated by the shaded area in Fig. 2. Our measurements also stop being reliable for $\tilde{g} \gtrsim 0.5$; in that regime our MF temperature fits are restricted to very high k values, which are affected by the anharmonicity of the optical trap. The error bars in Fig. 2 are statistical, while the systematic uncertainty in $\bar{N}_c/N_c^0$ is $\lesssim 0.2$ [47].

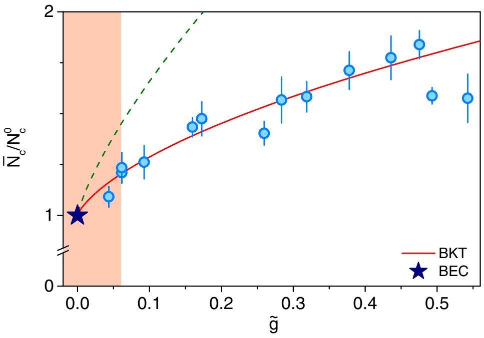

FIG. 2 (color online). Critical atom number as a function of the interaction strength $\tilde{g}$. All numbers are scaled to the ideal-gas BEC critical number N_c^0, defined in Eq. (1). The solid line is the classical-field BKT prediction of Eq. (2), without any free parameters. The dashed line is an approximation that neglects suppression of density fluctuations in the normal state. The star ($\star$) denotes the critical point for BEC, which only occurs in the ideal-gas limit. The shaded region, $\tilde{g} < 0.06$, indicates the regime in which our measurements stop being reliable (see text). The error bars are statistical.

Without any free parameters, we find generally excellent agreement with the prediction of Ref. [38]:

$$\frac{N_c^{\rm BKT}}{N_c^0} \approx 1 + \frac{3\tilde{g}}{\pi^3}\ln^2\left(\frac{\tilde{g}}{16}\right) + \frac{6\tilde{g}}{16\pi^2}\left[15 + \ln\left(\frac{\tilde{g}}{16}\right)\right], \tag{2}$$

which is based on fixing the phase-space density in the trap center to $D_{\rm BKT}$ and integrating a uniform-system equation of state over the trap, using the classical-field results of Ref. [39].

The agreement with Eq. (2) over a very broad range of interaction strengths and the proximity of our lowest reliable $\tilde{g}$ values to zero allow us to conclude that the critical atom number, without any free parameters, indeed smoothly converges onto the BEC result of Eq. (1).

It is instructive to also compare our data with the approximation $N_c^{\rm BKT}/N_c^0 = 1 + 3\tilde{g}D_{\rm BKT}^2/\pi^3$ [10,12], shown by the dashed line in Fig. 2. Here, the critical phase-space density is again set to $D_{\rm BKT}$, but the suppression of bosonic fluctuations in the normal state is neglected; i.e., the density profile is calculated using MF theory with an interaction potential $2gn(r)$, where $g = (\hbar^2/m)\tilde{g}$. Our data strongly exclude this result, confirming the importance of the suppression of density fluctuations near the critical point even for our lowest $\tilde{g}$ values.

For a more direct comparison with the uniform-system theory, we also consider the critical chemical potential for the onset of coherence. Like N_c in Fig. 1, μ_c is experimentally defined via the critical hold time t_c. The classical-field simulations [7] predict $D_{\rm BKT}$ to be reached for $\mu_c^{\rm BKT} = k_BT(\tilde{g}/\pi)\ln(13.2/\tilde{g})$, which reduces to the BEC prediction, $\mu_c = 0$, for $\tilde{g} = 0$.

In Fig. 3 we plot $\tilde{\mu}_c = \mu_c/(k_BT)$ versus $\tilde{g}$, and again observe generally good agreement with the classical-field prediction (solid line), all the way down to $\tilde{g} \approx 0.06$, i.e., very close to the expected BEC limit. The small systematic difference between the data and the theory is comparable to our systematic uncertainty in $\tilde{\mu}_c$ of ~ 0.05 [47].

We also compare our data with two intuitive approximations to $\tilde{\mu}_c$. We consider interaction potentials γgn with $\gamma = 2$, corresponding to a fully fluctuating Bose gas, and $\gamma = 1$, corresponding to a complete suppression of density fluctuations. In both of these extremes one can analytically write $D_\gamma(\tilde{\mu}) = -\ln[1 - \exp(\tilde{\mu} - \gamma gn/(k_BT))]$ [14]. Defining $\tilde{\mu}_c^\gamma$ so that $D_\gamma(\tilde{\mu}_c^\gamma) = D_{\rm BKT}$ we obtain the dashed ($\gamma = 2$) and dotted ($\gamma = 1$) lines in Fig. 3. Generally, $\gamma = 1$ provides a better approximation, highlighting how strong the suppression of density fluctuations in the normal state is.

Finally, we note that in previous experiments [22,27], on the in-trap equation of state, $\tilde{\mu}_c$ was deduced by defining it so as to satisfy the theoretical expectation [7,39] that the

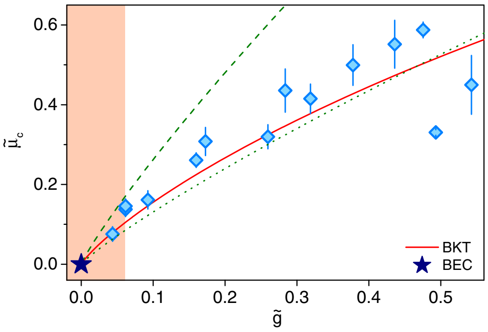

FIG. 3 (color online). Critical chemical potential as a function of the interaction strength $\tilde{g}$. The solid line is the classical-field BKT prediction. The dashed line is derived assuming a fully fluctuating Bose gas, while the dotted line corresponds to a complete suppression of density fluctuations. The error bars are statistical.

phase-space density should be a universal function of $(\tilde{\mu}-\tilde{\mu}_c)/\tilde{g}$. Our measurements of $\tilde{\mu}_c$, defined through the emergence of extended coherence, show that the two definitions indeed lead to very similar values.

In conclusion, by studying the critical point for the emergence of extended coherence in a harmonically trapped 2D gas with tunable interactions, we have quantitatively confirmed the predictions of classical-field theory and observed the expected unification of BKT and BEC transitions in the limit of vanishing interactions. The in-plane harmonic potential enables this observation. However, to quantitatively study the exact functional form of the slowly decaying correlations in a BKT superfluid, in the future it would be very interesting to study coherence of a tunable 2D gas in a uniform potential [52–54]. Just below T_c this should reveal an interaction–strength–independent algebraic decay of the first-order correlation function, corresponding to a universal jump in the superfluid density [55].

We thank Naaman Tammuz and Alex Gaunt for experimental contributions in the early stages of the project, Shannon Whitlock for help with image processing, and Andre Wenz, Markus Holzmann, and Jean Dalibard for useful discussions. This work was supported by AFOSR, ARO, DARPA OLE, and EPSRC [Grant No. EP/K003615/1]. N. N. acknowledges support from Trinity College, Cambridge, R. P. S. from the Royal Society, and K. G. H. V. from DAAD.

R. J. F. and M. R. dS. V. contributed equally to this work.

---

[*] rjf45@cam.ac.uk

[†] martin.rdsv@univ-paris13.fr

[1] R. E. Peierls, *Surprises in Theoretical Physics* (Princeton University Press, Princeton, 1979).
[2] N. N. Bogoliubov, Physica (Amsterdam) **26**, S1 (1960).
[3] P. C. Hohenberg, Phys. Rev. **158**, 383 (1967).
[4] N. D. Mermin and H. Wagner, Phys. Rev. Lett. **17**, 1133 (1966).
[5] V. L. Berezinskii, Soviet Physics JETP **34**, 610 (1971).
[6] J. M. Kosterlitz and D. J. Thouless, J. Phys. C **6**, 1181 (1973).
[7] N. V. Prokof'ev, O. Ruebenacker, and B. V. Svistunov, Phys. Rev. Lett. **87**, 270402 (2001).
[8] N. Berloff and B. V. Svistunov, Physics **2**, 61 (2009).
[9] $\tilde{g}$ is defined so that the strength of contact interactions is $g=\hbar^2\tilde{g}/m$, where m is the atomic mass.
[10] M. Holzmann, G. Baym, J. P. Blaizot, and F. Laloë, Proc. Natl. Acad. Sci. U.S.A. **104**, 1476 (2007).
[11] S. T. Bramwell and P. C. W. Holdsworth, Phys. Rev. B **49**, 8811 (1994).
[12] M. Holzmann and W. Krauth, Phys. Rev. Lett. **100**, 190402 (2008).
[13] R. N. Bisset, M. J. Davis, T. P. Simula, and P. B. Blakie, Phys. Rev. A **79**, 033626 (2009).
[14] Z. Hadzibabic and J. Dalibard, Riv. Nuovo Cimento Soc. Ital. Fis. **34**, 389 (2011).
[15] Z. Hadzibabic, P. Krüger, M. Cheneau, B. Battelier, and J. Dalibard, Nature (London) **441**, 1118 (2006).
[16] V. Schweikhard, S. Tung, and E. A. Cornell, Phys. Rev. Lett. **99**, 030401 (2007).
[17] P. Krüger, Z. Hadzibabic, and J. Dalibard, Phys. Rev. Lett. **99**, 040402 (2007).
[18] P. Cladé, C. Ryu, A. Ramanathan, K. Helmerson, and W. D. Phillips, Phys. Rev. Lett. **102**, 170401 (2009).
[19] S. Tung, G. Lamporesi, D. Lobser, L. Xia, and E. A. Cornell, Phys. Rev. Lett. **105**, 230408 (2010).
[20] S. P. Rath, T. Yefsah, K. J. Günter, M. Cheneau, R. Desbuquois, M. Holzmann, W. Krauth, and J. Dalibard, Phys. Rev. A **82**, 013609 (2010).
[21] T. Plisson, B. Allard, M. Holzmann, G. Salomon, A. Aspect, P. Bouyer, and T. Bourdel, Phys. Rev. A **84**, 061606 (2011).
[22] C.-L. Hung, X. Zhang, N. Gemelke, and C. Chin, Nature (London) **470**, 236 (2011).
[23] T. Yefsah, R. Desbuquois, L. Chomaz, K. J. Günter, and J. Dalibard, Phys. Rev. Lett. **107**, 130401 (2011).
[24] R. Desbuquois, L. Chomaz, T. Yefsah, J. Leonard, J. Beugnon, C. Weitenberg, and J. Dalibard, Nat. Phys. **8**, 645 (2012).
[25] J. Y. Choi, S. W. Seo, W. J. Kwon, and Y. I. Shin, Phys. Rev. Lett. **109**, 125301 (2012).
[26] J. Y. Choi, S. W. Seo, and Y. I. Shin, Phys. Rev. Lett. **110**, 175302 (2013).
[27] L.-C. Ha, C.-L. Hung, X. Zhang, U. Eismann, S.-K. Tung, and C. Chin, Phys. Rev. Lett. **110**, 145302 (2013).
[28] R. Desbuquois, T. Yefsah, L. Chomaz, C. Weitenberg, L. Corman, S. Nascimbène, and J. Dalibard, Phys. Rev. Lett. **113**, 020404 (2014).
[29] M. G. Ries, A. N. Wenz, G. Zürn, L. Bayha, I. Boettcher, D. Kedar, P. A. Murthy, M. Neidig, T. Lompe, and S. Jochim, Phys. Rev. Lett. **114**, 230401 (2015).
[30] R. Masut and W. J. Mullin, Am. J. Phys. **47**, 493 (1979).
[31] V. S. Bagnato and D. Kleppner, Phys. Rev. A **44**, 7439 (1991).
[32] U. R. Fischer, Phys. Rev. Lett. **89**, 280402 (2002).

[33] F. Dalfovo, S. Giorgini, L. P. Pitaevskii, and S. Stringari, Rev. Mod. Phys. **71**, 463 (1999).

[34] F. Gerbier, J. H. Thywissen, S. Richard, M. Hugbart, P. Bouyer, and A. Aspect, Phys. Rev. Lett. **92**, 030405 (2004).

[35] R. P. Smith, R. L. D. Campbell, N. Tammuz, and Z. Hadzibabic, Phys. Rev. Lett. **106**, 250403 (2011).

[36] Here, we neglect the effects of the finite system size. Because of the nonzero spacing of the trap energy levels, $\hbar\omega_r$, the infinite D_{BEC} is replaced by a very large nonuniversal value and the saturation-driven BEC can occur for a range of extremely small $\tilde{g}$ values; in our case $\tilde{g} \ll 10^{-2}$ [14].

[37] Z. Hadzibabic, P. Krüger, M. Cheneau, S. P. Rath, and J. Dalibard, New J. Phys. **10**, 045006 (2008).

[38] M. Holzmann, M. Chevallier, and W. Krauth, Phys. Rev. A **81**, 043622 (2010).

[39] N. V. Prokof'ev and B. V. Svistunov, Phys. Rev. A **66**, 043608 (2002).

[40] We estimate the width of the crossover region by noting that to observe interaction physics the interaction energy must be larger than $\hbar\omega_r$.

[41] R. L. D. Campbell, R. P. Smith, N. Tammuz, S. Beattie, S. Moulder, and Z. Hadzibabic, Phys. Rev. A **82**, 063611 (2010).

[42] N. L. Smith, W. H. Heathcote, G. Hechenblaikner, E. Nugent, and C. J. Foot, J. Phys. B **38**, 223 (2005).

[43] G. Roati, M. Zaccanti, C. D'Errico, J. Catani, M. Modugno, A. Simoni, M. Inguscio, and G. Modugno, Phys. Rev. Lett. **99**, 010403 (2007).

[44] These include collisions with the background gas in the vacuum chamber, three-body recombination, and scattering of photons from the trapping beams.

[45] I. Shvarchuck, C. Buggle, D. S. Petrov, K. Dieckmann, M. Zielonkowski, M. Kemmann, T. G. Tiecke, W. von Klitzing, G. V. Shlyapnikov, and J. T. M. Walraven, Phys. Rev. Lett. **89**, 270404 (2002).

[46] P. A. Murthy, D. Kedar, T. Lompe, M. Neidig, M. G. Ries, A. N. Wenz, G. Zürn, and S. Jochim, Phys. Rev. A **90**, 043611 (2014).

[47] See Supplemental Material at http://link.aps.org/supplemental/10.1103/PhysRevLett.114.255302, which includes Refs. [48–50], for details of image analysis, absolute atom-number calibration, fitting procedures, k-space resolution, and systematic errors.

[48] C. F. Ockeloen, A. F. Tauschinsky, R. J. C. Spreeuw, and S. Whitlock, Phys. Rev. A **82**, 061606 (2010).

[49] T. Haugset, H. Haugerud, and J. O. Andersen, Phys. Rev. A **55**, 2922 (1997).

[50] R. N. Bisset, D. Baillie, and P. B. Blakie, Phys. Rev. A **79**, 013602 (2009).

[51] If we probe coherence on a length scale $L' < L$, obtaining P_0' by summing $n(k)$ up to $k' > \Delta k$, the change in the slope of P_0' at t_c progressively gets washed out for decreasing L'.

[52] A. L. Gaunt, T. F. Schmidutz, I. Gotlibovych, R. P. Smith, and Z. Hadzibabic, Phys. Rev. Lett. **110**, 200406 (2013).

[53] L. Corman, L. Chomaz, T. Bienaimé, R. Desbuquois, C. Weitenberg, S. Nascimbène, J. Dalibard, and J. Beugnon, Phys. Rev. Lett. **113**, 135302 (2014).

[54] L. Chomaz, L. Corman, T. Bienaimé, R. Desbuquois, C. Weitenberg, S. Nascimbène, J. Beugnon, and J. Dalibard, Nat. Commun. **6**, 6162 (2015).

[55] D. R. Nelson and J. M. Kosterlitz, Phys. Rev. Lett. **39**, 1201 (1977).

Connecting Berezinskii-Kosterlitz-Thouless and BEC phase transitions by tuning interactions in a trapped gas

Supplemental Information

Richard J. Fletcher*, Martin Robert-de-Saint-Vincent*,
Jay Man, Nir Navon, Robert P. Smith, Konrad G. H. Viebahn, and Zoran Hadzibabic
Cavendish Laboratory, University of Cambridge, J. J. Thomson Avenue, Cambridge CB3 0HE, United Kingdom

Absorption image analysis

Fringe removal: Optical density (OD) images are usually affected by fringes due to the temporal variations in the probe beam. We eliminate this effect using the fringe-removal algorithm of Ockeloen *et al.* [1].

Imaging at high magnetic field: Near the Feshbach resonance our atoms are in the electronic ground state approximately described by $|4S_{1/2}, m_J = -1/2, I = 3/2, m_I = 3/2\rangle$, and are imaged on the transition to the excited state $|4P_{3/2}, m_J = -3/2, I = 3/2, m_I = 3/2\rangle$. However, due to the residual hyperfine mixing in the ground state manifold, the imaging transition is not perfectly cycling, and the probability of optical pumping into other ground states is $\approx 3\%$ per cycle. Consequently, the relation between the observed OD and the atomic column density depends on the number of photons scattered per atom, which in turn varies with the inhomogeneities of the probe beam.

To correct for this effect, we experimentally calibrate the relative variation of the observed $\mathrm{OD}(\vec{r})$ with the camera counts, $C(\vec{r})$, in the reference image taken without atoms. For this, we image a 3d thermal cloud after expansion from a dipole trap. Assuming cylindrical symmetry of the cloud, any variations in OD observed along a ring concentric with the cloud centre we attribute to the variations in the probe intensity. Averaging over several images, we build, pixel by pixel, a correlation plot of $\mathrm{OD}/\mathrm{OD}_0$ versus C/C_0, where C_0 is a fixed reference value and OD_0 the corresponding optical density. We construct such plots for various ring radii (i.e. various atomic column densities) and various (mean) probe intensities, and find that to a very good approximation the scaling of the optical density due to the optical pumping depends only on the light intensity and not on the atomic column density. We thus finally create an interpolated rescaling function $F(C/C_0) = \mathrm{OD}_0/\mathrm{OD}$, and correct our images according to $\mathrm{OD}_{\mathrm{scaled}}(\vec{r}) = \mathrm{OD}(\vec{r}) \cdot F\left(C(\vec{r})/C_0\right)$. This relative calibration corrects for both the optical pumping and for the Doppler shifting of atoms with increasing number of scattering events.

Imaging-intensity optimisation: In our main experimental sequences we take two sets of interlaced images, under identical conditions, but with two different (mean) imaging-beam intensities: a "low" intensity $I_0 \approx 0.08\,\mathrm{mW/cm^2}$ and a "high" intensity $I_1 \approx 0.3\,\mathrm{mW/cm^2}$ (which is still well below the saturation intensity $I_{\mathrm{sat}} \approx 1.8\,\mathrm{mW/cm^2}$), for which the scaling function F is larger by a factor of 2.7. The low-intensity images are used for determining N, T and μ, while the high-intensity images are used just to determine, with a larger dynamic range, the high-OD momentum peak P_0.

Absolute atom-number calibration

To calibrate our absolute imaging detectivity, we measure the BEC critical point in a 3d gas [2], prepared in an optical dipole trap of frequencies $(\omega_x, \omega_y, \omega_z) = 2\pi \times (64.3(1.0), 54.0(6), 93.9(2))$ Hz. We calibrate the observed critical atom number on the theoretical value:

$$N_c = A \frac{N_c^{\mathrm{ideal}}}{\left[1 - 3.426(a/\lambda) + 42(a/\lambda)^2\right]^3} + \delta N_c^{\mathrm{fs}}. \qquad (1)$$

Here, $N_c^{\mathrm{ideal}} = \zeta(3)(k_{\mathrm{B}}T)^3/(\hbar^3\omega_x\omega_y\omega_z)$, where ζ is the Riemann function, the denominator in Eq. (1) corresponds to mean-field (MF) and beyond-MF corrections [2], $A \approx 1.1$ is the trap-anharmonicity correction for our Gaussian potential, and δN_c^{fs} is the finite size-correction [3]. For probe intensity I_0 and image-pulse duration of 80 μs we obtain an effective absorption cross section $\sigma_{\mathrm{eff}} = 0.25(1) \times 3\lambda_0^2/(2\pi)$, where $\lambda_0 \approx 767$ nm is the imaging wavelength.

Extraction of thermodynamic parameters

Model functions: To extract μ and T from our images, we fit a model to the azimuthally-averaged momentum distributions. By constraining the fit to the wings where $\hbar^2 k^2 > 2mk_{\mathrm{B}}T\tilde{g}$, we ensure that interaction effects are described well within a mean-field (MF) framework [4].

The model we use includes the thermal occupation of the excited axial states and the interactions between atoms in all axial states, as in [5, 6], and also the axial deconfinement of the cloud due to the repulsive interactions, as in [7].

We construct the model 2d momentum distribution for an in-plane potential $V(x, y)$ within the 2d local density approximation. Defining the local chemical potential $\mu_{\mathrm{L}}(x, y) = \mu - V(x, y)$, and writing $\vec{r} = (x, y)$, we have

$$n(\vec{k}) = \sum_j \int \mathrm{d}^2 r \left[\exp\left(\frac{\frac{\hbar^2 k^2}{2m} + \varepsilon_j(\vec{r}) - \mu_{\mathrm{L}}(\vec{r})}{k_{\mathrm{B}}T}\right) - 1\right]^{-1}, \qquad (2)$$

	Statistical	Systematics		
		Calibration	*Finite size*	*Anharmonicity*
$\bar{N}_c/N_c^0$	± 0.08	± 0.14	+0.04	−0.01
$\tilde{\mu}_c$	± 0.03	± 0.05	+0.005	−0.04

TABLE I. Absolute standard uncertainties (68% confidence interval) and estimated systematic shifts affecting the measured $\bar{N}_c/N_c^0$ and $\tilde{\mu}_c$. Statistical errors are shown as error bars in the main paper. All values are typical for the experimentally explored range of $\tilde{g}$. The positive (negative) systematic shifts correspond to the measured values being higher (lower) than the true ones.

where $\{\varepsilon_j\}(\vec{r})$ are the eigenenergies of the axial states of motion, $\{|\phi_j(z)\rangle\}(\vec{r})$, measured from the zero-point energy $\hbar\omega_z/2$. Due to interactions, they are not simply $j\hbar\omega_z$, but depend on $\mu_L(\vec{r})$.

To evaluate the set $\{\varepsilon_j\}(\mu_L)$ we solve the 1d axial problem defined by two coupled equations:

$$n_3(z) = -\frac{1}{\lambda^2}\sum_j \ln\left[1-\exp\left(\frac{\mu_L-\varepsilon_j}{k_B T}\right)\right]|\phi_j(z)|^2, \quad (3)$$

where n_3 is 3d density, and

$$\left[\frac{-\hbar^2}{2m}\frac{d^2}{dz^2}+\frac{m\omega_z^2 z^2}{2}-\frac{\hbar\omega_z}{2}+2g_3\,n_3(z)\right]\phi_j(z)=\varepsilon_j\phi_j(z), \quad (4)$$

where $g_3 = 4\pi\hbar^2 a/m$. We iteratively find a self-consistent solution to Eqs. (3-4), and then compute $n(\vec{k})$ in Eq. (2).

Critical parameters: To identify the critical time t_c, we fit the following heuristic function to $P_0(t)$:

$$\begin{aligned} P_0(t) = P_c &+ \Theta(t-t_c)\cdot c\cdot|t-t_c| \quad (5)\\ &+ \Theta(t_c-t)\cdot a\,[1-\exp(-b|t-t_c|)]\,, \end{aligned}$$

where $\Theta(t)$ is the Heaviside function. In the limit $b \ll 1/|t-t_c|$, this is simply a piecewise linear function, while the non-zero b allows for the saturation of the peak OD at short t.

To determine $N(t_c)$, $T(t_c)$ and $\mu(t_c)$ we fit the smooth time evolutions of N, T and μ by third-order polynomials.

Finally, we use the above MF model to compute the occupations of the $j > 0$ axial states for $(T(t_c), \mu(t_c))$, and correct N_c to get $\bar{N}_c$. This operation assumes that beyond-MF effects affect only the axial ground state. This approximation is justified by the fact that $\hbar\omega_z/k_B T > \tilde{g}$ [4].

Momentum-space resolution

Our k-space resolution is limited by the camera pixel size and by the slight anisotropy of the in-plane harmonic potential in which we perform the momentum focusing. After removing the green "blade" beams, we have $\omega_{x,y} = \bar{\omega} \pm \Delta\omega$, with $\bar{\omega}/(2\pi) = 36.3(1)$ Hz and $\Delta\omega/(2\pi) = 2.5(1)$ Hz. This means that the focusing is not obtained simultaneously in both directions, but at the focusing time $t_f = \pi/(2\bar{\omega}) \approx 7$ ms the blurring of the momentum distribution is isotropic, with $\Delta k \approx \sqrt{m k_B T/\hbar^2}\sin(\Delta\omega\, t_f) \approx 0.4\,\mu\text{m}^{-1}$. This happens to closely coincide with the resolution set by the pixel size. To determine the height of the momentum peak, P_0, we average the image within one pixel of the fitted cloud centre.

Confidence intervals

In Table I, we summarise the main uncertainties in the critical parameters $\bar{N}_c/N_c^0$ and $\tilde{\mu}_c$ in Figs. 2-3 in the main paper.

The statistical errors, defined as 68% confidence interval and arising from experimental noise and fitting errors, are shown by the error bars in the main paper. Here they are averaged over the experimental points.

Systematic uncertainties in Table I fall into three categories: (i) calibration errors and drifts in the trapping frequencies, imaging magnification and absolute detectivity, (ii) finite-size (non-zero ω_r) effects, and (iii) anharmonicity of the optical trapping potentials. These affect the calculated N_c^0 and also the model functions used for extracting μ and T. The calibration errors we calculate by propagating errors, the finite-size effects are calculated following [3], and we assess the typical magnitude of the anharmonicity shifts by numerical simulations in the ideal-gas limit.

Additionally, two more fundamental systematic effects could shift the apparent critical point. If we assume that the emergence of coherence over lengthscale L requires the whole region near the cloud centre, of radius $L/2$, to be superfluid, then the trap inhomogeneity leads to apparent positive shifts of $\bar{N}_c/N_c^0$ and $\tilde{\mu}_c$, of $\lesssim 0.2$ and ≈ 0.05, respectively. On the other hand, the critical divergence of the correlation length above T_c has an opposite effect, which we estimate to be of comparable absolute size [8]. We thus expect these two effects to partially cancel, and lead to overall shifts that do not exceed our statistical and systematic errors (see also [9]).

[1] C. F. Ockeloen, A. F. Tauschinsky, R. J. C. Spreeuw, and S. Whitlock, Phys. Rev. A **82**, 061606 (2010).

[2] R. P. Smith, R. L. D. Campbell, N. Tammuz, and Z. Hadzibabic, Phys. Rev. Lett. **106**, 250403 (2011).

[3] T. Haugset, H. Haugerud, and J. O. Andersen, Phys. Rev. A **55**, 2922 (1997).

[4] M. Holzmann, M. Chevallier, and W. Krauth, Phys. Rev. A **81**, 043622 (2010).

[5] R. N. Bisset, D. Baillie, and P. B. Blakie, Phys. Rev. A **79**, 013602 (2009).

[6] S. Tung *et al.*, Phys. Rev. Lett. **105**, 230408 (2010).

[7] Z. Hadzibabic *et al.*, New J. Phys. **10**, 045006 (2008).

[8] Z. Hadzibabic and J. Dalibard, Rivista del Nuovo Cimento **34**, 389 (2011).

[9] R. N. Bisset, M. J. Davis, T. P. Simula, and P. B. Blakie, Phys. Rev. A **79**, 033626 (2009).

Stability of a Unitary Bose Gas

Richard J. Fletcher, Alexander L. Gaunt, Nir Navon, Robert P. Smith, and Zoran Hadzibabic

Phys. Rev. Lett. **111**, 125303 (2013)

Stability of a Unitary Bose Gas

Richard J. Fletcher, Alexander L. Gaunt, Nir Navon, Robert P. Smith,* and Zoran Hadzibabic
Cavendish Laboratory, University of Cambridge, J. J. Thomson Avenue, Cambridge CB3 0HE, United Kingdom

(Received 10 July 2013; published 20 September 2013)

We study the stability of a thermal ^{39}K Bose gas across a broad Feshbach resonance, focusing on the unitary regime, where the scattering length a exceeds the thermal wavelength λ. We measure the general scaling laws relating the particle-loss and heating rates to the temperature, scattering length, and atom number. Both at unitarity and for positive $a \ll \lambda$ we find agreement with three-body theory. However, for $a < 0$ and away from unitarity, we observe significant four-body decay. At unitarity, the three-body loss coefficient, $L_3 \propto \lambda^4$, is 3 times lower than the universal theoretical upper bound. This reduction is a consequence of species-specific Efimov physics and makes ^{39}K particularly promising for studies of many-body physics in a unitary Bose gas.

DOI: 10.1103/PhysRevLett.111.125303 PACS numbers: 67.85.−d

The control of interactions provided by Feshbach resonances makes ultracold atomic gases appealing for studies of both few- and many-body physics. On resonance, the s-wave scattering length a, which characterizes two-body interactions, diverges. At and near the resonance a gas is in the unitary regime, where the interactions do not explicitly depend on the diverging a. Instead, a is replaced by another natural length scale. In a degenerate gas this length scale is set by the interparticle spacing; in a thermal gas it is set by the thermal wavelength $\lambda = h/\sqrt{2\pi m k_B T}$, where m is the particle mass and T is the temperature.

Over the past decade, there have been many studies of the unitary Fermi gas [1]. More recently, there has been an increasing interest in both universal and species-specific properties of a unitary Bose gas [2–15]. It is however an open question to what extent this state can be studied in (quasi-)equilibrium, since at unitarity three-body recombination leads to significant particle loss and heating [16]. The severity of this instability is not universal [10], as it depends on the species-specific few-body Efimov physics [8,18–28]. Characterizing and understanding the stability of a unitary Bose gas is thus important both from the perspective of Efimov physics and for identifying suitable atomic species for many-body experiments.

The per-particle loss rate due to three-body recombination is given by

$$\gamma_3 \equiv -\dot{N}/N = L_3\langle n^2\rangle, \tag{1}$$

where N is the atom number, L_3 is the three-body loss coefficient, n is the density, and $\langle\cdots\rangle$ denotes an average over the density distribution in a trapped gas. Away from unitarity, $L_3 \sim \hbar a^4/m$ [29,30], with a dimensionless prefactor exhibiting additional variation with a due to Efimov physics [19,27]. At unitarity L_3 should saturate at $\sim\hbar\lambda^4/m \propto 1/T^2$. Experimental evidence for such saturation was observed in [8,10,18]. More quantitatively, at unitarity we expect

$$L_3 \approx \zeta\frac{9\sqrt{3}\hbar}{m}\lambda^4 = \zeta\frac{36\sqrt{3}\pi^2\hbar^5}{m^3(k_B T)^2}, \tag{2}$$

where $\zeta \leq 1$ is a species-dependent, nonuniversal dimensionless constant [10] (see also Refs. [31–33]).

Similar scaling arguments apply to the two-body elastic scattering rate, γ_2, which drives continuous re-equilibration of the gas during loss and heating. Away from unitarity $\gamma_2 \propto \langle n\rangle\hbar a^2/(m\lambda)$; hence, at unitarity $\gamma_2 \propto \langle n\rangle\hbar\lambda/m$. The possibility to experimentally explore many-body physics of a quasiequilibrium unitary Bose gas depends on the ratio γ_3/γ_2. Remarkably, at a given phase-space density, $n\lambda^3$, this ratio depends only on the species-specific ζ.

Recently, $\zeta \approx 0.9$ was measured for ^{7}Li [10]. The gas was held in a relatively shallow trap, so that continuous evaporation converted heating into an additional particle loss, and the extraction of ζ relied on theoretically modeling this conversion and assuming the $1/T^2$ scaling of Eq. (2).

In this Letter, we study the stability of the ^{39}K Bose gas in the $|F, m_F\rangle = |1, 1\rangle$ hyperfine ground state, across a broad Feshbach resonance centered at 402.5 G [25]. We perform experiments in a deep trap and verify the predicted recombination-heating rate both at unitarity and for positive $a \ll \lambda$ [10,30]. At unitarity we measure $L_3 \propto T^{-1.7\pm0.3}$ and $\zeta \approx 0.3$, a value that makes ^{39}K particularly promising for studies of an equilibrium unitary gas. Additional measurements at $a < 0$, away from unitarity, reveal the importance of four-body processes [20,23], consistent with previous studies in ^{133}Cs [22], ^{39}K [25], and ^{7}Li [26].

Our experimental setup is described in Ref. [34]. We start by preparing a weakly interacting ($\lambda/a \approx 35$) thermal gas in a harmonic optical trap. The trap has a depth of $U \approx k_B \times 30$ μK and is nearly isotropic, with the geometric mean of the trapping frequencies $\omega = 2\pi \times 185$ Hz. We then tune a close to a Feshbach resonance, by ramping an external magnetic field over 10 ms. At this point we have $N \approx 10^5$ atoms at $T \approx 1$ μK, corresponding to

$\lambda \approx 5 \times 10^3 a_0$, where a_0 is the Bohr radius. At the trap center $n \approx 3 \times 10^{12}$ cm^{-3} and $n\lambda^3 < 0.1$, so even at unitarity and assuming $\zeta = 1$, we still always have $\gamma_2 \gg \gamma_3$. We let the cloud evolve for a variable hold time, t, of up to 4 s, and then simultaneously switch off the trap and the Feshbach field (within ~100 μs [35]). Finally, we image the cloud after 5 ms of time-of-flight expansion.

Figure 1 shows the particle loss and heating in a resonantly interacting gas ($\lambda/a = 0$). Restricting our measurements to $T < 2$ μK ensures that evaporative losses and cooling are negligible. We have taken 19 similar data series, each at a fixed a, spanning the range $-12 < \lambda/a < 12$.

We first study the relationship between T and N during the evolution of the cloud. One expects three sources of heating related to three-body recombination [10,30]. (i) For any a, losses preferentially occur near the center of the cloud, where the atoms have lower potential energy. (ii) For $a > 0$, recombination results in a shallow dimer with binding energy $\varepsilon = \hbar^2/(ma^2)$, and the third atom carries away $(2/3)\varepsilon$ as kinetic energy. In all our experiments $\varepsilon < U$, so this atom remains trapped and increases the energy of the cloud. (iii) At unitarity, three-body recombination preferentially involves atoms that also have lower kinetic energy.

To a good approximation, in our experiments we can capture all these effects by a simple scaling law:

$$NT^{\beta} = \text{const}, \tag{3}$$

with the exponent β varying across the resonance. Ignoring unitarity effects, $\beta = 3$ for $a \leq 0$, and $\beta = 3/[1 + \lambda^2/(9\pi a^2)]$ for $a > 0$ (see also [30]). In the latter case β changes as the cloud heats, but in our measurements this variation is small enough that a constant $\beta = -d[\ln(N)]/d[\ln(T)]$ describes the data well (see inset of Fig. 2). At unitarity, a universal value of $\beta = 1.8$ was predicted in Ref. [10].

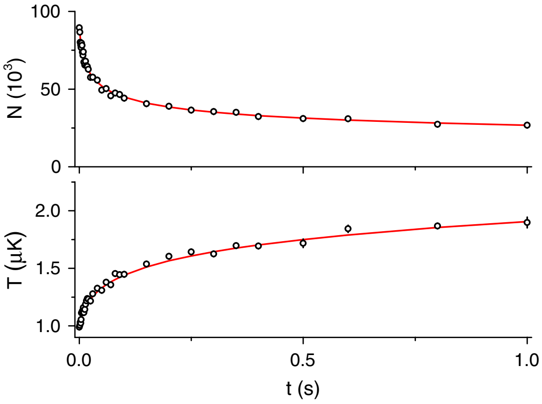

FIG. 1 (color online). Particle loss and heating in a resonantly interacting Bose gas ($\lambda/a = 0$). Each point is an average of 5 measurements and error bars show standard statistical errors. Solid red lines are fits based on Eqs. (5) and (3).

In Fig. 2 we show our measured values of β. For $\lambda/a \gg 1$ we find agreement with the nonunitary prediction shown by the red dashed line. However, approaching unitarity we see gradual deviation from this theory. On resonance, we measure $\beta = 1.94 \pm 0.09$, close to the unitary prediction of $\beta = 1.8$ (indicated by the red star), and far from the nonunitary $\beta = 3$.

Moving away from unitarity into the $a < 0$ region (open symbols in Fig. 2, corresponding to $-2000 < a/a_0 < -400$), β rises further, but does not reach the expected nonunitary limit. By analyzing the dynamics of the particle loss, $N(t)$, we find that in this region four-body decay is also significant (see Fig. 3); in this case our prediction for β is not applicable. Previously, indirect evidence for four-body decay in this region was seen in Ref. [25], but not in Ref. [28], where the initial cloud density was significantly lower.

We fit the $N(t)$ data by numerically evolving a loss equation featuring both three- and four-body decay [22],

$$\dot{N} = -L_3\langle n^2\rangle N - L_4\langle n^3\rangle N, \tag{4}$$

where L_3 and L_4 are fitting parameters and we use the measured $T(t)$ to evaluate the thermal density averages. To obtain purely three- (four-) body fits we fix L_4 (L_3) to zero.

In Fig. 3 we show $N(t)$ for $a = -850a_0$. The model including both L_3 and L_4 provides an excellent fit to the data, with $\chi^2 \approx 1$. In comparison, pure four- and three-body fits have $\chi^2 \approx 5$ and 7, respectively. We observe four-body effects for all our data with $-2000 < a/a_0 < -400$. However, we find that they are relevant only at densities $\gtrsim 10^{12}$ cm^{-3}, which reconciles the observations of

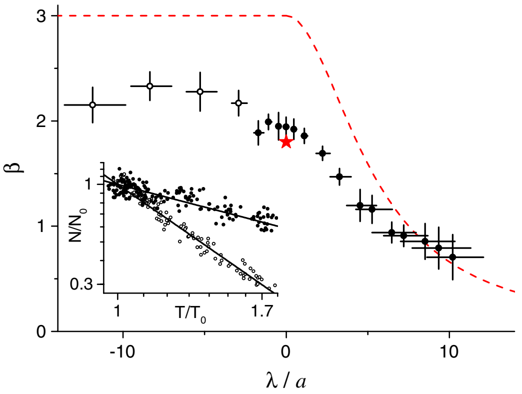

FIG. 2 (color online). Heating exponent β, as defined in Eq. (3). The red dashed line is a result of nonunitary three-body theory, while the red star indicates the predicted value of 1.8 at unitarity. Open symbols indicate the region where four-body decay is significant (see text and Fig 3). Note that $\lambda \approx 5 \times 10^3 a_0$ and horizontal error bars reflect its variation during a measurement sequence at a fixed a. Vertical error bars show fitting uncertainties. Inset: Log-log plots of N vs T (scaled to their values at $t = 0$) for the data series at $\lambda/a \approx -5.3$ (open) and 8.5 (solid).

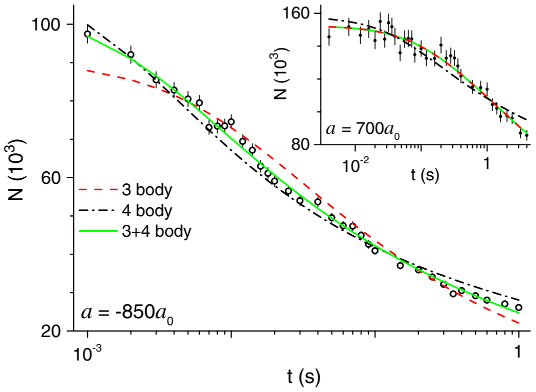

FIG. 3 (color online). Three- vs four-body decay for $a < 0$ (away from unitarity). N decay at $a = -850a_0$ is fitted to a model including both three- and four-body losses (green solid line), as well as to pure three- and four-body models (red dashed and black dot-dashed line, respectively). Inset: For comparison, at $a = 700a_0$, the solid green and the dashed red lines are indistinguishable, showing that four-body decay does not play a detectable role.

Refs. [25,28]. A more detailed study of this region, including any four-body resonances [22], is outside the scope of this Letter.

For $a > 0$ the same analysis does not reveal any four-body decay (see inset of Fig. 3). In this case the pure three-body fit and the fit including both L_3 and L_4 are indistinguishable, with $\chi^2 \approx 1$, and give the same L_3 (within the 10% fitting errors), while the pure four-body fit has $\chi^2 \approx 2$. This strongly excludes L_4 as a relevant fit parameter. Using a similar procedure, we have also checked that for both positive and negative a we do not detect any five-body decay.

We henceforth focus on the three-body decay dynamics at unitarity, using the $a > 0$ nonunitary regime for comparison. Invoking Eq. (3), in both regimes the particle loss should be described by:

$$\dot{N} = -AN^{\nu}, \tag{5}$$

where A and ν are constants. Here, ν absorbs all the N and T dependence of L_3 and $\langle n^2 \rangle$. Integration gives a fitting function $N(t) = [A(\nu - 1)t + N(0)^{1-\nu}]^{1/(1-\nu)}$. For $a \ll \lambda$ we expect $\nu = 3 + 3/\beta$, whereas at unitarity $L_3 \propto 1/T^2$ implies $\nu = 3 + 5/\beta$. To test this hypothesis in an unbiased way, we analyze our data using ν as a free parameter.

Note that here we invoke Eq. (3) merely to anticipate the validity of Eq. (5) and the ν values; experimentally, our analysis of $N(t)$ and ν is decoupled from the measurements of $T(t)$ and β. The validity of our approach is seen in Fig. 1, where the fit of $N(t)$ is based on Eq. (5). The fit of $T(t)$ is then obtained by inserting the fitted $N(t)$ and β into Eq. (3).

Our fitted values of ν are summarized in Fig. 4. We see a crossover from nonunitary to unitary behavior as the resonance is approached, confirming the appearance of a temperature-dependent L_3. Now combining our measurements of β and ν, at unitarity we get $L_3 \propto T^{-1.7\pm0.3}$, in agreement with the expected $1/T^2$ scaling.

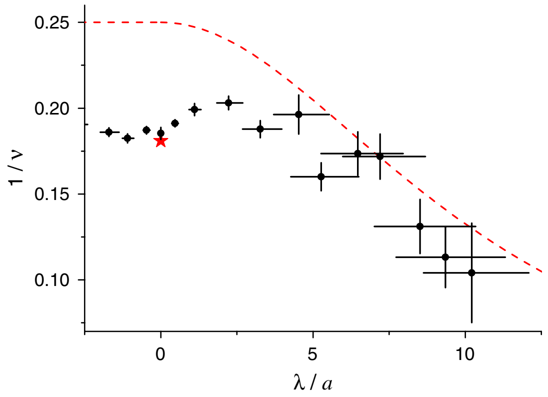

FIG. 4 (color online). Particle-loss exponent ν, as defined in Eq. (5). The red dashed line shows the nonunitary theory, $\nu = 3 + 3/\beta$, assuming nonunitary β values. The red star shows the unitary prediction, $\nu = 3 + 5/\beta$, corresponding to $L_3 \propto 1/T^2$ and the measured β. Error bars are analogous to those in Fig. 2.

Next, using the fitted A and ν, for each data series at a particular a, and for any evolution time t, we extract

$$L_3(t) = 3\sqrt{3}\left(\frac{2\pi k_B T(t)}{m\omega^2}\right)^3 N(t)^{\nu-3}A. \tag{6}$$

Combining all our data series, we reconstruct $L_3(a, T)$.

In Fig. 5 (main panel) we show L_3 at a fixed $T = 1.1\ \mu$K, scaled to the theoretical upper bound $L_3^{\mathrm{M}}(T)$,

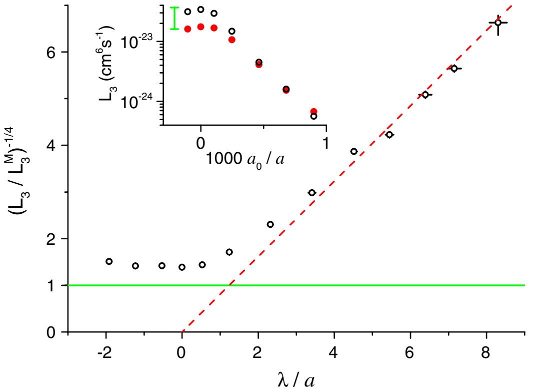

FIG. 5 (color online). Three-body loss coefficient. Main panel: $(L_3/L_3^{\mathrm{M}})^{-1/4}$ (see text) at $T = 1.1\ \mu$K. Horizontal green line marks the theoretical upper bound on L_3, while the red dashed line is a guide to the eye showing the $L_3 \propto a^4$ nonunitary scaling. At unitarity, $L_3/L_3^{\mathrm{M}} \approx 0.27$. Inset: L_3 at 1.1 μK (open symbols) and 1.7 μK (solid symbols). The expected ratio between the two unitary plateaux is indicated by the green vertical bar.

obtained by setting $\zeta = 1$ in Eq. (2). Plotting $(L_3/L_3^{\rm M})^{-1/4}$ versus λ/a clearly reveals two key effects. First, for $\lambda/a \gtrsim 3$, we see the nonunitary scaling $L_3 \propto a^4$ [37]. Second, close to the resonance, L_3 saturates at $\approx 0.27 L_3^{\rm M}$.

In the inset of Fig. 5 we focus on the region close to the resonance and compare L_3 for two different temperatures, $T = 1.1\ \mu$K and $1.7\ \mu$K. Away from the resonance, L_3 does not show any T dependence. At unitarity, the ratio of the two saturated L_3 values is close to the expected $1/T^2$ scaling.

Finally, to refine our estimate of ζ, we fix $\nu = 3 + 5/\beta$ (i.e., $L_3 \propto 1/T^2$) and reanalyze the three data series taken closest to the resonance, for which $|\lambda/a| < 0.6$ at all times. This gives us a combined estimate of $\zeta = 0.29 \pm 0.03$, while the systematic uncertainty in ζ due to our absolute atom-number calibration [38,39] is about 30%. Writing $L_3 = \lambda_3/T^2$, this corresponds to $\lambda_3 \approx 4.5 \times 10^{-23}\ (\mu\mathrm{K})^2\,\mathrm{cm}^6\,\mathrm{s}^{-1}$. In the context of Efimov physics, $\zeta = 1 - e^{-4\eta}$ [10], where η is the Efimov width parameter [40]. We deduce $\eta = 0.09 \pm 0.04$ (see also [25]).

In conclusion, we have fully characterized the stability of a ^{39}K gas at and near unitarity. We have experimentally verified the theoretically predicted general scaling laws characterizing particle loss and heating in the unitary regime, confirmed the relevance of four-body decay on the negative side of the Feshbach resonance, and measured the species-specific unitarity-limited three-body loss coefficient, $L_3 \propto 1/T^2$. The unitary value of L_3, 3 times lower than the universal theoretical upper bound, makes ^{39}K a promising candidate for experimental studies of many-body physics in a unitary Bose gas.

We thank F. Chevy, J. Dalibard, A. Grier, P. Massignan, B. Rem, and F. Werner for useful discussions and comments on the Letter. This work was supported by EPSRC (Grant No. EP/K003615/1), the Royal Society, AFOSR, ARO and DARPA OLE.

Note added.—Recently, a study of a degenerate unitary ^{85}Rb gas was reported [41].

---

*rps24@cam.ac.uk

[1] *BCS-BEC Crossover and the Unitary Fermi Gas*, edited by W. Zwerger, Lecture Notes in Physics Vol. 836 (Springer, Berlin, 2011).

[2] S. Cowell, H. Heiselberg, I. E. Mazets, J. Morales, V. R. Pandharipande, and C. J. Pethick, Phys. Rev. Lett. **88**, 210403 (2002).

[3] J. L. Song and F. Zhou, Phys. Rev. Lett. **103**, 025302 (2009).

[4] Y.-L. Lee and Y.-W. Lee, Phys. Rev. A **81**, 063613 (2010).

[5] N. Navon, S. Piatecki, K. Günter, B. Rem, T. C. Nguyen, F. Chevy, W. Krauth, and C. Salomon, Phys. Rev. Lett. **107**, 135301 (2011).

[6] D. Borzov, M. S. Mashayekhi, S. Zhang, J.-L. Song, and F. Zhou, Phys. Rev. A **85**, 023620 (2012).

[7] W. Li and T.-L. Ho, Phys. Rev. Lett. **108**, 195301 (2012).

[8] R. J. Wild, P. Makotyn, J. M. Pino, E. A. Cornell, and D. S. Jin, Phys. Rev. Lett. **108**, 145305 (2012).

[9] F. Werner and Y. Castin, Phys. Rev. A **86**, 053633 (2012).

[10] B. S. Rem, A. T. Grier, I. Ferrier-Barbut, U. Eismann, T. Langen, N. Navon, L. Khaykovich, F. Werner, D. S. Petrov, F. Chevy, and C. Salomon, Phys. Rev. Lett. **110**, 163202 (2013).

[11] L. Pricoupenko, Phys. Rev. Lett. **110**, 180402 (2013).

[12] Y. Castin and F. Werner, Can. J. Phys. **91**, 382 (2013).

[13] J. J. R. M. van Heugten and H. T. C. Stoof, arXiv:1302.1792.

[14] J. J. R. M. van Heugten and H. T. C. Stoof, arXiv:1306.1104.

[15] S. Piatecki and W. Krauth, arXiv:1307.4671.

[16] This is in contrast to a two-component Fermi gas, where three-body effects are suppressed by Pauli exclusion [17].

[17] D. S. Petrov, C. Salomon, and G. V. Shlyapnikov, Phys. Rev. Lett. **93**, 090404 (2004).

[18] T. Kraemer, M. Mark, P. Waldburger, J. G. Danzl, C. Chin, B. Engeser, A. D. Lange, K. Pilch, A. Jaakkola, H. C. Nägerl, and R. Grimm, Nature (London) **440**, 315 (2006).

[19] E. Braaten and H.-W. Hammer, Ann. Phys. (Amsterdam) **322**, 120 (2007).

[20] H.-W. Hammer and L. Platter, Eur. Phys. J. A **32**, 113 (2007).

[21] E. Braaten, H.-W. Hammer, D. Kang, and L. Platter, Phys. Rev. A **78**, 043605 (2008).

[22] F. Ferlaino, S. Knoop, M. Berninger, W. Harm, J. P. D'Incao, H.-C. Nägerl, and R. Grimm, Phys. Rev. Lett. **102**, 140401 (2009).

[23] J. von Stecher, J. P. D'Incao, and C. H. Greene, Nat. Phys. **5**, 417 (2009).

[24] N. Gross, Z. Shotan, S. Kokkelmans, and L. Khaykovich, Phys. Rev. Lett. **103**, 163202 (2009).

[25] M. Zaccanti, B. Deissler, C. D'Errico, M. Fattori, M. Jona-Lasinio, S. Mueller, G. Roati, M. Inguscio, and G. Modugno, Nat. Phys. **5**, 586 (2009).

[26] S. E. Pollack, D. Dries, and R. G. Hulet, Science **326**, 1683 (2009).

[27] F. Ferlaino, A. Zenesini, M. Berninger, B. Huang, H.-C. Nägerl, and R. Grimm, Few-Body Syst. **51**, 113 (2011).

[28] S. Roy, M. Landini, A. Trenkwalder, G. Semeghini, G. Spagnolli, A. Simoni, M. Fattori, M. Inguscio, and G. Modugno, Phys. Rev. Lett. **111**, 053202 (2013).

[29] P. O. Fedichev, M. W. Reynolds, and G. V. Shlyapnikov, Phys. Rev. Lett. **77**, 2921 (1996).

[30] T. Weber, J. Herbig, M. Mark, H.-C. Nägerl, and R. Grimm, Phys. Rev. Lett. **91**, 123201 (2003).

[31] C. H. Greene, B. Esry, and H. Suno, Nucl. Phys. **A737**, 119 (2004).

[32] J. P. D'Incao, H. Suno, and B. D. Esry, Phys. Rev. Lett. **93**, 123201 (2004).

[33] N. P. Mehta, S. T. Rittenhouse, J. P. D'Incao, J. von Stecher, and C. H. Greene, Phys. Rev. Lett. **103**, 153201 (2009).

[34] R. L. D. Campbell, R. P. Smith, N. Tammuz, S. Beattie, S. Moulder, and Z. Hadzibabic, Phys. Rev. A **82**, 063611 (2010).

[35] The rapid switch-off ensures that no atoms are converted into molecules when starting on the $a < 0$ side of the resonance [36].

[36] T. Köhler, K. Góral, and P. S. Julienne, Rev. Mod. Phys. **78**, 1311 (2006).

[37] For the range of a values relevant here, Efimov physics is not expected to significantly modify this simple scaling [25].

[38] R. P. Smith, R. L. D. Campbell, N. Tammuz, and Z. Hadzibabic, Phys. Rev. Lett. **106**, 250403 (2011).

[39] R. P. Smith, N. Tammuz, R. L. D. Campbell, M. Holzmann, and Z. Hadzibabic, Phys. Rev. Lett. **107**, 190403 (2011).

[40] E. Braaten, H.-W. Hammer, and M. Kusunoki, Phys. Rev. A **67**, 022505 (2003).

[41] P. Makotyn, C. E. Klauss, D. L. Goldberger, E. A. Cornell, and D. S. Jin, arXiv:1308.3696.

A Superheated Bose-Condensed Gas

Alexander L. Gaunt, Richard J. Fletcher*, Robert P. Smith, and Zoran Hadzibabic*

Nature Phys. **9**, 271-274 (2013)

nature physics

LETTERS

PUBLISHED ONLINE: 24 MARCH 2013 | DOI: 10.1038/NPHYS2587

A superheated Bose-condensed gas

Alexander L. Gaunt†, Richard J. Fletcher†, Robert P. Smith★ and Zoran Hadzibabic

Our understanding of various states of matter usually relies on the assumption of thermodynamic equilibrium. However, the transitions between different phases of matter can be strongly affected by non-equilibrium phenomena. Here we demonstrate and explain an example of non-equilibrium stalling of a continuous, second-order phase transition. We create a superheated atomic Bose gas, in which a Bose–Einstein condensate (BEC) persists above the equilibrium critical temperature[1,2], T_c, if its coupling to the surrounding thermal bath is reduced by tuning interatomic interactions. For vanishing interactions the BEC persists in the superheated regime for a minute. However, if strong interactions are suddenly turned on, it rapidly boils away. Our observations can be understood within a two-fluid picture, treating the condensed and thermal components of the gas as separate equilibrium systems with a tunable inter-component coupling. We experimentally reconstruct a non-equilibrium phase diagram of our gas, and theoretically reproduce its main features.

Non-equilibrium many-body states can persist for a very long time if, for example, a system is integrable, the transition to the lower free-energy state is inhibited by an energy barrier, or the target equilibrium state is continuously evolving owing to dissipation. Ultracold atomic gases offer excellent possibilities for fundamental studies of non-equilibrium phenomena[3–14] and have been used to create counter-intuitive states such as repulsively bound atom pairs[5] and Mott insulators with attractive inter-particle interactions[12].

Our superheated Bose gas is reminiscent of superheated distilled water, which remains liquid above 100 °C. Specifically, as the temperature characterizing the average energy per particle and the populations of the excited states rises above T_c, the cloud remains in the partially condensed phase, which in true equilibrium should exist only below T_c. However, there are also important differences. Boiling of water is a first-order phase transition and is stalled in clean samples by the absence of nucleation centres. In that case the transition is inhibited by an energy barrier. For a second-order phase transition such a barrier does not exist and the superheating we observe is a purely dynamical non-equilibrium effect, which arises because different properties of the system evolve at different rates. In this respect our gas also bears resemblance to the long-lived non-equilibrium spin structures observed in spinor condensates[6,9], pre-thermalized states in quenched one-dimensional Bose gases[14] and supercritical superfluids predicted to occur in quenched two-dimensional gases[15]. In all of those cases, however, non-equilibrium states are observed owing to the system's slow approach to true equilibrium. Here, the system actually evolves away from equilibrium.

In Fig. 1 we summarize the basic idea of our experiments and the key concepts needed to understand them. In an equilibrium gas, a BEC is present only if $T < T_c$, where T_c depends on the total particle number N, or equivalently if the chemical potential $\mu > \mu_c$. In a standard experiment, after a BEC is produced, it gradually decays because T rises, owing to technical heating, and/or T_c decreases, because N decays through various inelastic processes. As T/T_c increases, elastic collisions redistribute the atoms between the thermal and condensed components, aiming to ensure the equilibrium particle distribution. The BEC atom number, N_0, can therefore decay in two ways: by direct inelastic loss, and through elastic transfer of atoms into the thermal component. Here we reduce the rate of the elastic particle transfer by tuning the strength of inter-particle interactions, characterized by the s-wave scattering length a. This protects the BEC deep into the superheated regime, where $N_0 > 0$ even though $T > T_c$.

We can understand our observations within the two-fluid picture outlined in Fig. 1b. Here we treat the thermal and condensed components as two coupled subsystems with atom numbers N' and N_0, chemical potentials μ' and μ_0, and instantaneous per-particle inelastic decay rates Γ' and Γ_0, respectively. In equilibrium $\mu' = \mu_0$; note that μ_0 is defined only if $N_0 > 0$, so $\mu_0 > \mu_c$.

The two components are coupled in two ways, both dependent on the scattering length a. First, the local kinetic thermal equilibrium between the collective excitations in the BEC (phonons) and the thermal bath is ensured by Landau damping, the rate of which is $\propto \sqrt{a}$ (refs 16,17). Second, the global phase equilibrium (that is, the equilibrium condensed fraction N_0/N) is ensured by the elastic scattering with a rate $\propto a^2$. Crucially, owing to the different scalings with a, we find a large parameter space where the two components can be considered to be in kinetic equilibrium while the system is not in global phase equilibrium. In other words, the two components are at the same temperature, but have different chemical potentials.

In our optically trapped ^{39}K gas[18], we control a by an external magnetic field tuned close to a Feshbach resonance at 402 G (ref. 19), the dominant source of Γ' and Γ_0 is spontaneous scattering of photons from the trapping laser beams, and Γ_0 has an additional contribution from three-body recombination.

The key steps in our experimental sequence are summarized in Fig. 1c. We start by preparing a partially condensed gas in the $|F, m_F\rangle = |1, 1\rangle$ hyperfine ground state by evaporative cooling at $a = 135a_0$, where a_0 is the Bohr radius[18]. We then reduce a (over 50 ms) and follow the subsequent evolution of the cloud, probing the atomic momentum distribution by absorption imaging in time-of-flight expansion. Reducing a (at constant N_0) initially reduces μ_0 below μ' (ref. 13), but subsequently μ_0 decays slower.

In Fig. 2 we quantitatively contrast the equilibrium evolution of a cloud at $a = 83a_0$ and the non-equilibrium evolution at $5a_0$. In both cases we start at time $t = 0$ (Fig. 1c) with $N_0 \approx 2 \times 10^4$ and $N \approx 2 \times 10^5$ at $T \approx 160$ nK. In both cases T_c decreases at a similar rate owing to similar N decay. At $5a_0$, the temperature rises faster owing to less effective evaporative cooling at a fixed optical trap depth.

Whether the gas is in equilibrium or not, it can always be characterized by two extensive variables, the total particle number N and energy E. We measure these quantities by direct summation

---

Cavendish Laboratory, University of Cambridge, J. J. Thomson Avenue, Cambridge CB3 0HE, UK. †These authors contributed equally to this work. *e-mail: rps24@cam.ac.uk.

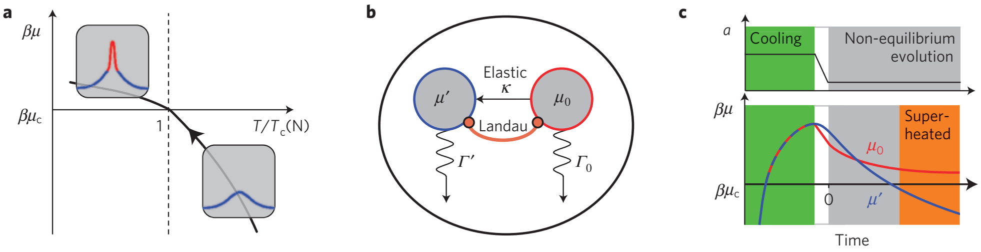

Figure 1 | Creating and understanding a superheated Bose-condensed gas. a, In equilibrium, a BEC is present if $T < T_c$ or equivalently $\mu > \mu_c$ (here, $\beta = 1/(k_B T)$). The arrow indicates the cooling trajectory along which a BEC is produced. The insets show measured momentum distributions, with the condensed component indicated in red. **b**, Two-component picture. The thermal and condensed components have chemical potentials μ' and μ_0, and inelastic decay rates Γ' and Γ_0, respectively. The net flow of particles between the two components, κ, depends on μ', μ_0 and the scattering rate $\propto a^2$. In equilibrium $\mu' = \mu_0 = \mu^{\rm eq}$. The Landau damping of the collective modes in the BEC has a rate $\propto \sqrt{a}$. **c**, Time sequence of the experiment. Reducing a after preparing a BEC reduces the coupling between the two components and extends the condensate lifetime. In the superheated regime $\mu' < \mu^{\rm eq} < \mu_c$ but $\mu_0 > \mu_c$.

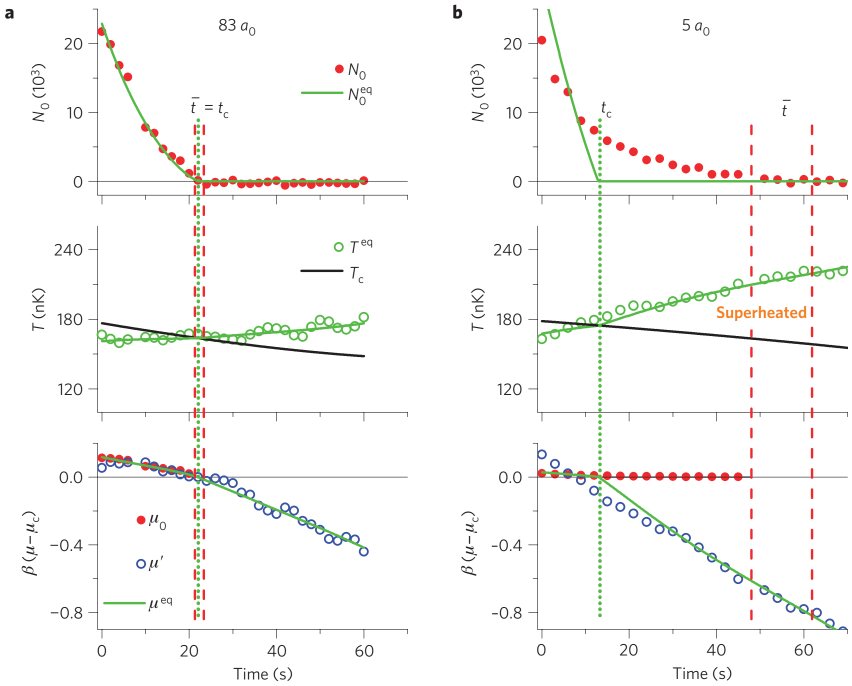

Figure 2 | Equilibrium versus non-equilibrium BEC decay. a, At $a = 83a_0$ the cloud is always in quasi-static equilibrium. The measured N_0 is in excellent agreement with the predicted $N_0^{\rm eq}$ and vanishes when $T^{\rm eq} = T_c$; the three separately calculated chemical potentials, μ_0, μ' and $\mu^{\rm eq}$, all agree with each other. The dotted green line marks the equilibrium critical time, t_c, and the dashed red lines show the experimental bounds on the time $\bar{t}$ when the BEC actually vanishes. **b**, At $5a_0$, the BEC persists in the superheated regime ($T^{\rm eq} > T_c$) for $\bar{t} - t_c \approx 40$ s.

of the momentum distribution and its second moment. To measure N_0 we count the atoms within the central peak rising above the smooth thermal distribution.

From the measured $N(t)$ alone we calculate the equilibrium $T_c(t)$ (ref. 2). From $N(t)$ and $E(t)$ we calculate the equilibrium intensive thermodynamic variables $\mu^{\rm eq}(t)$ and $T^{\rm eq}(t)$, and the equilibrium number of condensed atoms, $N_0^{\rm eq}(t)$ (refs 2,20,21); in these calculations $N_0^{\rm eq} > 0$ if and only if $T^{\rm eq} < T_c$. For comparison, we also directly fit a temperature T^f to the wings of the momentum distribution. In addition, supposing only that the two components are separately in equilibrium, from the measured N_0 and N' we calculate μ_0 and μ'. (For theoretical details see Supplementary Information.)

At $83a_0$ (Fig. 2a) we find excellent agreement between the measured N_0 and the $N_0^{\rm eq}$ predicted without any free parameters. The BEC vanishes exactly at the equilibrium critical time t_c (dotted green line), at which $T^{\rm eq} = T_c$. Note that the dashed red lines show the experimental bounds on the time $\bar{t}$ when the BEC vanishes. The separately calculated μ_0, μ' and $\mu^{\rm eq}$ are all consistent and we have also checked that the fitted T^f coincides with the calculated $T^{\rm eq}$. All this gives us full confidence in our equilibrium calculations.

At $5a_0$ (Fig. 2b) we observe strikingly different behaviour. The BEC now survives much longer than it would in true equilibrium; $\bar{t} - t_c \approx 40$ s. We also see that μ_0 and μ' diverge from each other for $t > t_c$, so the system is moving away from the global phase equilibrium rather than towards it. The observed superheating can

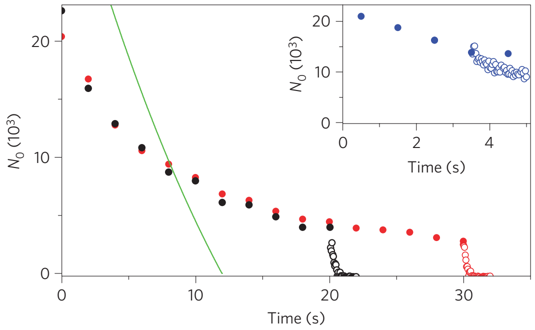

Figure 3 | Quenching the superheated Bose-condensed gas. Filled symbols show the evolution of N_0 at $a = 3a_0$, the green solid line shows $N_0^{\rm eq}$ and orange shading indicates the superheated regime. Open symbols show the rapid decay of the BEC after it is strongly coupled to the thermal bath by an interaction quench to $a = 62a_0$ at time t_q. We show two experimental series in which $t_q = 20$ s (black) and 30 s (red). Inset: an interaction quench at a time when $T < T_c$ and $N_0^{\rm eq} > 0$ does not kill the BEC. (Note that here we make an even stronger quench, to $100a_0$.)

thus not be understood as just a transient effect. (Note that $\mu_0 – \mu_c$ is always very small owing to weak interactions.)

At $5a_0$ the gas is not in global phase equilibrium, but it is still a good approximation to view its two components as two equilibrium subsystems at the same (kinetic) temperature, as in Fig. 1b. We have checked that the momentum distribution in the non-condensed component is still fitted well by a thermal distribution, with T^f always within 10% of the calculated $T^{\rm eq}(N, E)$ (see Supplementary Information). For the BEC, in a weakly interacting gas the equilibrium relation $\mu_0(N_0)$ relies on the macroscopic occupation of a single quantum state[1], rather than on global equilibrium. Moreover, even for the lowest-energy collective modes we estimate the Landau damping time to be <1 s (refs 16,17; see Supplementary Information), that is, much shorter than the characteristic timescale of our experiments. Thus, although this distribution is not directly measurable, we expect the distribution of collective excitations in the BEC to be characterized by a temperature T_0 that is also close to $T^{\rm eq} \approx T^f$.

These conclusions hold for any $a \gtrsim 1a_0$ (see Supplementary Information). Exactly at $a = 0$ our theoretical picture does break down, because the Landau damping rate vanishes and the BEC has no equilibrium features; the two components are simply completely decoupled. Bearing this small caveat in mind, from here on we refer to $T_0 \approx T^f \approx T^{\rm eq}$ simply as the temperature of the system T.

A way to directly see that the gas is superheated is to suddenly increase the coupling of the BEC to the thermal bath. In Fig. 3 we show the results of two experimental series in which a is quenched (within 10 ms) from $3a_0$ to $62a_0$ at different times in the superheated regime. The filled (open) symbols show N_0 measured before (after) the quench. The small Γ_0 is almost unaffected by the change in a, and the sudden N_0 decay is due to the increase in κ (Fig. 1b). For reference, the green line shows the calculated $N_0^{\rm eq}$ at $3a_0$ and orange shading indicates the superheated regime. As shown in the inset of Fig. 3, we have checked that an interaction quench at $t < t_c$ (that is, when $T < T_c$ and $N_0^{\rm eq} > 0$) does not kill the BEC.

As shown in Fig. 4, we have explored the limits of superheating for a range of interaction strengths, including small negative values of a. For $a < 0$, a BEC is stable against collapse only for $N_0 < -C/a$, with $C \approx 2 \times 10^4 a_0$ for our trap parameters[22–24]. However, after N_0 drops below this critical value, at small $|a|$ it decays slowly.

In Fig. 4a we plot the highest temperature at which we still observe a BEC, $\bar{T} \equiv T(t = \bar{t})$, scaled to the equilibrium T_c at the same N. For $a \to 0$, the BEC survives up to $T \approx 1.5T_c$. (For comparison, this is analogous to superheated water at 280 °C.)

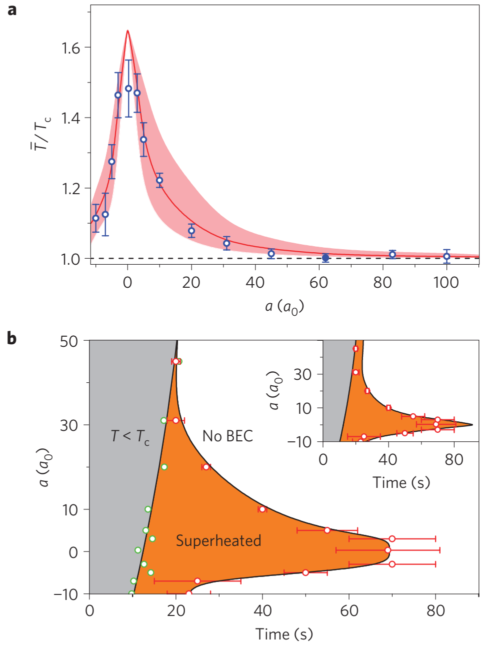

Figure 4 | Limits of superheating. a, The highest temperature at which we observe a BEC, $\bar{T}$, scaled to the equilibrium T_c. Close to $a = 0$ the BEC survives up to $\approx 1.5T_c$. The red line shows the results of our numerical calculations, with the shaded area indicating the theoretical uncertainty. Experimental error bars are statistical. The point at $62a_0$ is fixed to unity by the absolute atom number calibration[2,27]. **b**, Temporal phase diagram. For each value of a we plot the equilibrium t_c (green points) and the time $\bar{t}$ at which the BEC actually vanishes (red points). The $\bar{t}$ errors correspond to dashed lines in Fig. 2 and the uncertainty in t_c is indicated by the scatter of points. Solid curves are spline fits to the data. For $a \approx 0$ the BEC survives in the superheated regime for a whole minute. Inset: numerically calculated phase diagram, with $\bar{t}$ data overlaid.

In Fig. 4b we reconstruct the temporal phase diagram of our non-equilibrium gas. Here, a horizontal cut through the graph corresponds to a time series such as shown in Fig. 2. For each a, we plot the measured $\bar{t}$ (red points) and the equilibrium t_c (green points). The solid curves are spline fits to the data. The width of the orange-shaded region corresponds to the time that the BEC survives in the superheated regime. For $a \approx 0$ this region spans a whole minute.

The phase diagram in Fig. 4b is measured by always starting with $N_0 \approx 2 \times 10^4$. In general, non-equilibrium behaviour can strongly depend on the initial conditions. However, we find that $\bar{t}$ is essentially constant (within experimental errors) for initial N_0 in the range $(1–5) \times 10^4$. The primary reason for this is that the three-body contribution to Γ_0 grows with N_0; this leads to self-stabilization of the condensed atom number on timescales much shorter than $\bar{t}$.

We theoretically reproduce our non-equilibrium observations using a two-component model directly corresponding to Fig. 1b. Starting with the measured initial N_0, we numerically simulate the evolution of a BEC coupled to a thermal bath characterized by $\mu'(t)$. To do this we calculate Γ_0 from our experimental parameters, and for κ we use the form[25]

$$\kappa = A\gamma_{\rm el} N_0 \left[e^{\beta(\mu_0 - \mu_c)} - e^{\beta(\mu' - \mu_c)} \right] \tag{1}$$

Here $\gamma_{\mathrm{el}} \propto a^2$ is the elastic collision rate and A is a dimensionless coefficient. The largest uncertainty in our calculations comes from the theoretical uncertainty in $A \approx 1$–10 (ref. 26). (For details see Supplementary Information.)

In Fig. 4a we show the calculated $\bar{T}/T_c$. The red line corresponds to $A = 3$ and the shaded area to the range $A = 1$–10. The calculation generally captures our experimental observations well. With $A = 3$ we obtain quantitative agreement with the data, except exactly at $a = 0$, where the model is not valid. In the inset of Fig. 4b we show the calculated temporal phase diagram, with $A = 3$, together with the experimental $\bar{t}$ data. Again the general features of the diagram are captured well for $a \neq 0$.

The success of our calculations supports a conceptually simple way to think about dynamical non-equilibrium effects near a continuous phase transition. Extending the BEC lifetime by tuning interactions could also have practical benefits for precision measurements and quantum information processing.

Received 3 September 2012; accepted 14 February 2013;

References

1. Dalfovo, F., Giorgini, S., Pitaevskii, L. P. & Stringari, S. Theory of Bose–Einstein condensation in trapped gases. *Rev. Mod. Phys.* **71,** 463–512 (1999).
2. Smith, R. P., Campbell, R. L. D., Tammuz, N. & Hadzibabic, Z. Effects of interactions on the critical temperature of a trapped Bose gas. *Phys. Rev. Lett.* **106,** 250403 (2011).
3. Polkovnikov, A., Sengupta, K., Silva, A. & Vengalattore, M. Colloquium: Nonequilibrium dynamics of closed interacting quantum systems. *Rev. Mod. Phys.* **83,** 863–883 (2011).
4. Kinoshita, T., Wenger, T. & Weiss, D. S. A quantum Newton's cradle. *Nature* **440,** 900–903 (2006).
5. Winkler, K. *et al.* Repulsively bound atom pairs in an optical lattice. *Nature* **441,** 853–856 (2006).
6. Sadler, L. E., Higbie, J. M., Leslie, S. R., Vengalattore, M. & Stamper-Kurn, D. M. Spontaneous symmetry breaking in a quenched ferromagnetic spinor Bose–Einstein condensate. *Nature* **443,** 312–315 (2006).
7. Hofferberth, S., Lesanovsky, I., Fischer, B., Schumm, T. & Schmiedmayer, J. Non-equilibrium coherence dynamics in one-dimensional Bose gases. *Nature* **449,** 324–327 (2007).
8. Haller, E. *et al.* Realization of an excited, strongly correlated quantum gas phase. *Science* **325,** 1224–1227 (2009).
9. Guzman, J. *et al.* Long-time-scale dynamics of spin textures in a degenerate $F = 1$ ^{87}Rb spinor Bose gas. *Phys. Rev. A* **84,** 063625 (2011).
10. Cheneau, M. *et al.* Light-cone-like spreading of correlations in a quantum many-body system. *Nature* **481,** 484–487 (2012).
11. Trotzky, S. *et al.* Probing the relaxation towards equilibrium in an isolated strongly correlated one-dimensional Bose gas. *Nature Phys.* **8,** 325–330 (2012).
12. Mark, M. J. *et al.* Preparation and spectroscopy of a metastable Mott-insulator state with attractive interactions. *Phys. Rev. Lett.* **108,** 215302 (2012).
13. Smith, R. P., Beattie, S., Moulder, S., Campbell, R. L. D. & Hadzibabic, Z. Condensation dynamics in a quantum-quenched Bose gas. *Phys. Rev. Lett.* **109,** 105301 (2012).
14. Gring, M. *et al.* Relaxation and pre-thermalization in an isolated quantum system. *Science* **337,** 1318–1322 (2012).
15. Mathey, L. & Polkovnikov, A. Light cone dynamics and reverse Kibble–Zurek mechanism in two-dimensional superfluids following a quantum quench. *Phys. Rev. A* **81,** 033605 (2010).
16. Fedichev, P. O., Shlyapnikov, G. V. & Walraven, J. T. M. Damping of low-energy excitations of a trapped Bose–Einstein condensate at finite temperatures. *Phys. Rev. Lett.* **80,** 2269–2272 (1998).
17. Pethick, C. & Smith, H. *Bose–Einstein Condensation in Dilute Gases* (Cambridge Univ. Press, 2002).
18. Campbell, R. L. D. *et al.* Efficient production of large ^{39}K Bose–Einstein condensates. *Phys. Rev. A* **82,** 063611 (2010).
19. Roati, G. *et al.* ^{39}K Bose–Einstein condensate with tunable interactions. *Phys. Rev. Lett.* **99,** 010403 (2007).
20. Tammuz, N. *et al.* Can a Bose gas be saturated? *Phys. Rev. Lett.* **106,** 230401 (2011).
21. Smith, R. P. & Hadzibabic, Z. Effects of interactions on Bose–Einstein condensation of an atomic gas. Preprint at http://arxiv.org/abs/1203.2063 (2012).
22. Ruprecht, P. A., Holland, M. J., Burnett, K. & Edwards, M. Time-dependent solution of the nonlinear Schrödinger equation for Bose-condensed trapped neutral atoms. *Phys. Rev. A* **51,** 4704–4711 (1995).
23. Gerton, J. M., Strekalov, D., Prodan, I. & Hulet, R. G. Direct observation of growth and collapse of a Bose–Einstein condensate with attractive interactions. *Nature* **408,** 692–695 (2000).
24. Donley, E. A. *et al.* Dynamics of collapsing and exploding Bose–Einstein condensates. *Nature* **412,** 295–299 (2001).
25. Gardiner, C. W., Zoller, P., Ballagh, R. J. & Davis, M. J. Kinetics of Bose–Einstein condensation in a trap. *Phys. Rev. Lett.* **79,** 1793–1796 (1997).
26. Gardiner, C. W., Lee, M. D., Ballagh, R. J., Davis, M. J. & Zoller, P. Quantum kinetic theory of condensate growth: Comparison of experiment and theory. *Phys. Rev. Lett.* **81,** 5266–5269 (1998).
27. Smith, R. P., Tammuz, N., Campbell, R. L. D., Holzmann, M. & Hadzibabic, Z. Condensed fraction of an atomic Bose gas induced by critical correlations. *Phys. Rev. Lett.* **107,** 190403 (2011).

Acknowledgements

We thank S. Beattie and S. Moulder for experimental assistance. This work was supported by EPSRC (Grant No. EP/K003615/1), the Royal Society, AFOSR, ARO and DARPA OLE.

Author contributions

All authors contributed extensively to this work.

Additional information

Supplementary information is available in the online version of the paper. Reprints and permissions information is available online at www.nature.com/reprints. Correspondence and requests for materials should be addressed to R.P.S.

Competing financial interests

The authors declare no competing financial interests.

nature physics
SUPPLEMENTARY INFORMATION
DOI: 10.1038/NPHYS2587

A superheated Bose-condensed gas

Alexander L. Gaunt, Richard J. Fletcher, Robert P. Smith, and Zoran Hadzibabic
Cavendish Laboratory, University of Cambridge, J. J. Thomson Ave., Cambridge CB3 0HE, United Kingdom

(Dated: February 8, 2013)

Determination of N, E and N_0

We take an absorption image of the atom cloud after $\tau = 18$ ms of time-of-flight (TOF) expansion from a nearly isotropic trap with a geometric mean of trapping frequencies $\bar{\omega}/2\pi \approx 70\,\text{Hz}$.

For absolute calibration of our atom numbers we use a T_c measurement at $a = 62\,a_0$, assuming that at this a the cloud is in equilibrium [1, 2].

For $a < 100\,a_0$ we assess the interaction-energy contribution to the total energy E to be $\lesssim 1\%$ and thus $E \approx 2E_k$, where E_k is the kinetic energy. We obtain E_k from the second moment of the atom distribution after TOF, and correct it for the small effect of the initial in-trap cloud size. This amounts to rescaling the energy by a factor $\bar{\omega}^2\tau^2/(1+\bar{\omega}^2\tau^2)$.

In Fig. S1 we show N and E_k for the same two experimental series shown in Fig. 2 in the main text.

To improve the detection of small N_0 values we always switch a to zero at the start of TOF [1].

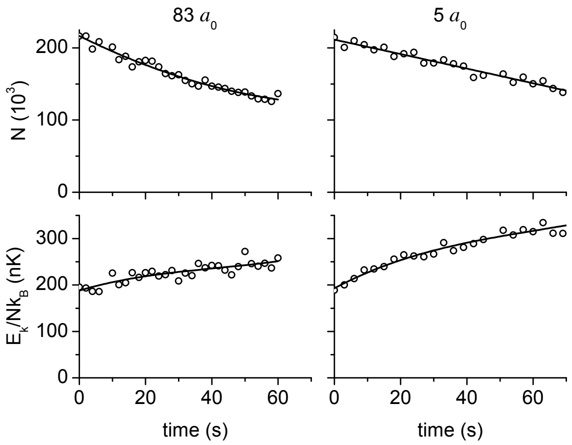

Fig. S1: **Parametrization of N and E_k.** The total atom number N and kinetic energy per particle E_k/N for two experimental series at $83\,a_0$ and $5\,a_0$. The experimental data are fitted with polynomial forms to obtain smooth functions $N(t)$ and $E_k(t)$.

Equilibrium calculations

For an equilibrium ideal Bose gas in a spherically symmetric harmonic trap of frequency ω, the thermal component satisfies:

$$N'(\mu',T) = \frac{N_c^0}{\zeta(3)} \int_0^\infty \mathrm{g}_2\left(\exp\left(\frac{\mu'-\mu_c^0}{k_\mathrm{B}T} - \frac{u^2}{2}\right)\right) u\,\mathrm{d}u, \tag{1}$$

$$\frac{E_k(\mu',T)}{N'(\mu',T)} = \frac{3}{2} k_\mathrm{B}T \frac{\int_0^\infty \mathrm{g}_2\left(\exp(\frac{\mu'-\mu_c^0}{k_\mathrm{B}T} - \frac{u^2}{2})\right) \frac{u^2}{2} u\,\mathrm{d}u}{\int_0^\infty \mathrm{g}_2\left(\exp(\frac{\mu'-\mu_c^0}{k_\mathrm{B}T} - \frac{u^2}{2})\right) u\,\mathrm{d}u}, \tag{2}$$

where $N_c^0 = \zeta(3)\left(\frac{k_\mathrm{B}T}{\hbar\omega}\right)^3 \left(1 - \frac{\zeta(2)}{2\zeta(3)}\frac{\hbar\omega}{k_\mathrm{B}T}\right)^{-3}$ includes the finite size correction, $\mu_c^0 = \frac{3}{2}\hbar\omega$, and $\mathrm{g}_2(z)$ is the dilogarithm function. Note that Eqs. (1) and (2) are obtained by integrating the three-dimensional momentum distribution in a harmonically trapped Bose gas, described by the polylogarithm function $g_{3/2}$ [3], along one direction. For $N > N_c^0$, the chemical potential is capped at $\mu' = \mu_c^0$ and also $\mu_0 = \mu_c^0$. The thermal atom number is saturated, $N' = N_c^0$, and any additional particles must go into the condensate, $N_0 = N - N_c^0$.

Interactions modify this picture in two ways:

(i) The critical point is shifted. At mean-field (MF) level $\mu_c = \mu_c^0 + 4\zeta(3/2)a/\lambda$, where $\lambda = \sqrt{\frac{2\pi\hbar^2}{mk_B T}}$ is the thermal wavelength. A small beyond-MF correction is quadratic in a/λ and has an additional logarithmic correction. Experimentally, the corresponding N_c is [1, 2]

$$N_c = N_c^0 \left(1 - 3.426\frac{a}{\lambda} + 42\left(\frac{a}{\lambda}\right)^2\right)^{-3} . \tag{3}$$

(ii) Due to interactions, in the presence of a BEC, N' is no longer saturated at N_c. Empirically,

$$N' = N_c + S_0(N_0)^{2/5} + S_2(N_0)^{4/5}, \tag{4}$$

where the non-saturation parameters S_0 and S_2 depend on a and T [4, 5]. The excess number of thermal atoms, $N' - N_c$, can be directly attributed to the shift of the chemical potential above μ_c; for an interacting BEC $\mu_0 > \mu_c$ and in equilibrium $\mu' = \mu_0$.

For μ_0 we use a modified Thomas-Fermi law [8]:

$$\mu_0 - \mu_c = \frac{\hbar\omega}{2}\left\{\left(15\frac{N_0 a}{a_{\rm osc}} + 3^{5/2}\right)^{2/5} - 3\right\}, \tag{5}$$

where $a_{\rm osc} = \sqrt{\hbar/m\omega}$ is the harmonic oscillator length.

Eq. (5) and Eqs. (1) and (2) modified to include interaction effects ($N_c^0 \to N_c$ and $\mu_c^0 \to \mu_c$) form a complete set needed for our calculations [6]. We proceed in two ways:

(1) Assuming that the system is in global equilibrium, $\mu' = \mu_0 = \mu^{\rm eq}$, we use *only* $N(t)$ and $E(t)$ to calculate $\mu^{\rm eq}(t)$, $N_0^{\rm eq}(t)$ and $T^{\rm eq}(t)$ (green lines in main-text Fig. 2).

(2) Additionally, from N, E and the *measured* N_0 we calculate μ_0 and μ' without assuming $\mu' = \mu_0$ (red and blue points in the bottom panel of main-text Fig. 2).

Justification of the two-fluid picture for a gas out of global phase equilibrium

In our theoretical picture (Fig. 1(b) in the paper), we assume that in the superheated regime the thermal and condensed components can still to a good approximation be assumed to be separately in equilibrium. Moreover, we assume that they are at the same temperature, but just have different chemical potentials.

Here we provide a more detailed justification of these assumptions.

First, for the thermal component we show in Fig. S2 that the radial velocity distribution still looks like a thermal distribution at a temperature very close to the calculated $T^{\rm eq}(N, E)$. Here we show data for the same 5 a_0 series as shown in Fig. 2(b) in the main paper. In Fig. S2(a) we show the distribution measured at $t = 45$ s, i.e. deep in the superheated regime. The data (red) is fitted almost perfectly by an equilibrium thermal distribution (green) constrained to be characterised by N, E and $T^{\rm eq}$. An unconstrained fit (blue) gives only a very slightly different shape with T^f within few % of $T^{\rm eq}$. Note that full thermalisation of the thermal component, in the sense that occupations of all the individual momentum states acquire their equilibrium values, should have a rate $\propto a^2$. Still, experimentally, the overall "coarse-grained" shape of the distribution is essentially thermal. In Fig. S2(b) we compare the calculated $T^{\rm eq}$ (green) and the fitted T^f (blue) for the whole 5 a_0 series. For comparison we also show the equilibrium T_c (black line). Note that this is the same plot as in Fig. 2(b) in the main paper, with just the T^f points added.

Second, for the collective excitations in the BEC to be in equilibrium with the thermal bath, the Landau-damping time τ_L [3, 7] must be short compared to the characteristic time scale of the experiment. For a uniform system at a temperature higher than the interaction energy per particle [3]:

$$\frac{\tau_L \omega}{2\pi} \approx \frac{n_0^{1/2}\lambda^2}{4\pi a^{1/2}} , \tag{6}$$

where ω is the excitation frequency, n_0 is the condensate density, and λ is the thermal wavelength. For our assessment we use this uniform-system result with our peak n_0; this only overestimates τ_L for our harmonically trapped gas [7].

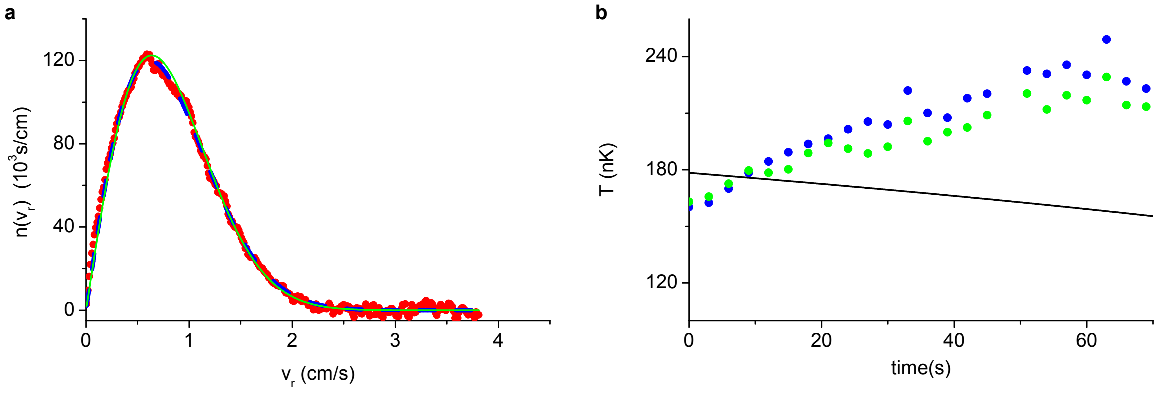

Fig. S2: **Thermal distribution in a gas out of global phase equilibrium**. (a) For a gas at 5 a_0 in the superheated regime we show the radial velocity distribution (red), the distribution corresponding to N, E and $T^{\rm eq}$ (green) and the unconstrained fit (blue) giving T^f. Even though the gas is not in true equilibrium the distribution still looks thermal and T^f and $T^{\rm eq}$ agree to within few %. (b) Comparison of T^f (blue) and $T^{\rm eq}$ (green) for the whole 5 a_0 data series shown in Fig. 2(b) of the main paper. The solid black line shows the equilibrium T_c.

Exactly at $a = 0$ the damping time diverges and our theoretical picture breaks down. However, already for $a = 1\ a_0$, for all our experimental parameters the RHS of Eq. (6) is < 100. Then, even for our lowest-energy modes, with $\omega/2\pi \sim 100$ Hz, we get $\tau_L < 1$ s.

Non-equilibrium evolution of N_0

The non-equilibrium evolution of N_0 is described by the differential equation

$$\dot{N}_0 = -\kappa - \Gamma_0 N_0\,, \tag{7}$$

where κ is the coupling to the thermal bath due to elastic collisions and Γ_0 is the instantaneous inelastic loss rate per particle. Following [9] we use

$$\kappa = A\frac{8m(ak_{\rm B}T)^2}{\pi\hbar^3}e^{2\beta(\mu'-\mu_c)}\left[e^{\beta(\mu_0-\mu')}-1\right]N_0 = A\gamma_{\rm el}N_0\left[e^{\beta(\mu_0-\mu_c)}-e^{\beta(\mu'-\mu_c)}\right]\,, \tag{8}$$

where $\gamma_{\rm el} = \frac{8m(ak_{\rm B}T)^2}{\pi\hbar^3}e^{\beta(\mu'-\mu_c)}$ is essentially the elastic scattering rate for a thermal cloud at μ' and $A \approx 1-10$ is a theoretically uncertain prefactor [8].

In the inelastic loss term we include contributions from one-body scattering and three-body recombination, $\Gamma_0 = \Gamma_0^{(1)} + \Gamma_0^{(3)}$. In our system, one-body loss is dominated by spontaneous scattering of photons from the trapping laser beams. We calculate it from the known wavelength and intensity of the beams. For all the reported experiments

$$\Gamma_0^{(1)} \approx \frac{1}{35}\text{s}^{-1}\,. \tag{9}$$

The loss rate of condensate atoms due to three-body recombination in the presence of a thermal cloud is given by [10]

$$\Gamma_0^{(3)} = \frac{K_3(a)}{6}\left(\langle n_0^2\rangle + 6\langle n_0 n'\rangle + 6\langle n'^2\rangle\right)\,, \tag{10}$$

where n_0 is the condensate density, n' the thermal density, $K_3(a)$ the known a-dependant three-body coefficient [11, 12], and $\langle\ldots\rangle$ stands for an average over the density distribution. We set n' to its value in the centre of the trap and for the condensate we again use a modified Thomas-Fermi approach:

$$\langle n_0\rangle = \frac{\langle n_0\rangle_{\rm GS}}{\left[1+\left(\langle n_0\rangle_{\rm GS}/\langle n_0\rangle_{\rm TF}\right)^{5/3}\right]^{3/5}}\,, \tag{11}$$

$$\langle n_0^2 \rangle = \frac{\langle n_0^2 \rangle_{\mathrm{GS}}}{\left[1 + \left(\langle n_0^2 \rangle_{\mathrm{GS}} / \langle n_0^2 \rangle_{\mathrm{TF}}\right)^{5/6}\right]^{6/5}} . \tag{12}$$

Here GS refers to the non-interacting Gaussian ground state and TF to the Thomas-Fermi approximation, $\langle n_0 \rangle_{\mathrm{TF}} = \sqrt{2\pi}(15/7)(15 N_0 a/a_{\mathrm{osc}})^{-3/5} \langle n_0 \rangle_{\mathrm{GS}}$ and $\langle n_0^2 \rangle_{\mathrm{TF}} = \sqrt{3}\pi(15^2/56)(15 N_0 a/a_{\mathrm{osc}})^{-6/5} \langle n_0^2 \rangle_{\mathrm{GS}}$, where $\langle n_0 \rangle_{\mathrm{GS}} = N_0/(2\pi a_{\mathrm{osc}}^2)^{3/2}$ and $\langle n_0^2 \rangle_{\mathrm{GS}} = N_0^2/(3\pi^2 a_{\mathrm{osc}}^4)^{3/2}$. Eqs. (11) and (12) smoothly interpolate between the ground state result (for $N_0 a/a_{\mathrm{osc}} \ll 1$) and the Thomas-Fermi approximation (for $N_0 a/a_{\mathrm{osc}} \gg 1$). Note that other forms which smoothly interpolate between these two limits give essentially the same results.

Using Eqs. (7) - (12) we simulate the evolution of the condensate atom number, $N_0(t)$, from its initial value $N_0(t = 0)$. We use the measured $N(t)$ and $E(t)$ and the numerically evolved $N_0(t)$ to obtain $\mu'(t)$ for use in Eq. (8). To determine $\bar{t}$ from our calculations we define the condensate to be present if N_0 is larger than $N_0^{\mathrm{min}} = 3k_{\mathrm{B}}T/(\hbar\omega)$, the thermal occupation of the first excited state.

In the main text we show the results of our calculations for $\bar{T}$ and $\bar{t}$ (Fig. 4), with $A = 3$. In Fig. S3 we show that our calculations (with the same value of A) also describe well the full dynamics $N_0(t)$.

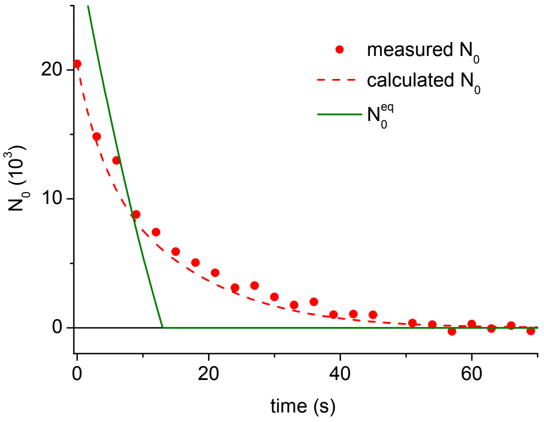

Fig. S3: **Non-equilibrium N_0 dynamics**. We plot the calculated $N_0(t)$ (dashed red line) together with the measured N_0 (red points) for the same 5 a_0 data series as in Fig. 2(b) in the main text. For comparison we also show the calculated $N_0^{\mathrm{eq}}(t)$ (solid green line).

[1] Smith, R. P., Campbell, R. L. D., Tammuz, N. & Hadzibabic, Z. Effects of interactions on the critical temperature of a trapped Bose gas. *Phys. Rev. Lett.* **106**, 250403 (2011).

[2] Smith, R. P., Tammuz, N., Campbell, R. L. D., Holzmann, M. & Hadzibabic, Z. Condensed fraction of an atomic Bose gas induced by critical correlations. *Phys. Rev. Lett.* **107**, 190403 (2011).

[3] Pethick, C. & Smith, H. *Bose–Einstein Condensation in Dilute Gases* (Cambridge University Press, Cambridge, 2002).

[4] Tammuz, N. *et al.* Can a Bose gas be saturated? *Phys. Rev. Lett.* **106**, 230401 (2011).

[5] Smith, R. P. & Hadzibabic, Z. Effects of interactions on Bose-Einstein condensation of an atomic gas. *arXiv:1203.2063* (2012).

[6] In Eqs. (1) and (2) we also replace the function g_2 with a slightly modified dilogarithm function $\tilde{\mathrm{g}}(z) = (3/4)|\mathrm{g}_2(z)| + (1/4)\mathrm{Re}\{\mathrm{g}_2(z)\}$, which remains real for $z > 1$. This is done just for mathematical convenience and does not affect our results since the integrals are strongly dominated by the region where $x^2/2 > (\mu' - \mu_c)/k_{\mathrm{B}}T$ and $\tilde{\mathrm{g}} = \mathrm{g}_2$.

[7] Fedichev, P. O., Shlyapnikov, G. V. & Walraven, J. T. M. Damping of low-energy excitations of a trapped Bose–Einstein condensate at finite temperatures. *Phys. Rev. Lett.* **80**, 2269 (1998).

[8] Gardiner, C. W., Lee, M. D., Ballagh, R. J., Davis, M. J. & Zoller, P. Quantum kinetic theory of condensate growth: comparison of experiment and theory. *Phys. Rev. Lett.* **81**, 5266–5269 (1998).

[9] Gardiner, C. W., Zoller, P., Ballagh, R. J. & Davis, M. J. Kinetics of Bose–Einstein condensation in a trap. *Phys. Rev. Lett.* **79**, 1793–1796 (1997).

[10] Söding, J. *et al.* Three-body decay of a rubidium Bose–Einstein condensate. *Appl. Phys. B* **69**, 257 (1999).

[11] Zaccanti, M. *et al.* Observation of an Efimov spectrum in an atomic system. *Nature Physics* **5**, 586–591 (2009).

[12] Zaccanti, M. *Tuning of the interactions in ultracold K-Rb quantum gases*. Ph.D. thesis, University of Florence (2007).

Persistent Currents in Spinor Condensates

Scott Beattie, Stuart Moulder, Richard J. Fletcher, and Zoran Hadzibabic

Phys. Rev. Lett. **110**, 025301 (2013)

Persistent Currents in Spinor Condensates

Scott Beattie, Stuart Moulder, Richard J. Fletcher, and Zoran Hadzibabic
Cavendish Laboratory, University of Cambridge, J. J. Thomson Avenue, Cambridge CB3 0HE, United Kingdom

(Received 18 October 2012; published 9 January 2013)

We create and study persistent currents in a toroidal two-component Bose gas, consisting of ^{87}Rb atoms in two different spin states. For a large spin-population imbalance we observe supercurrents persisting for over two minutes. However, we find that the supercurrent is unstable for spin polarization below a well-defined critical value. We also investigate the role of phase coherence between the two spin components and show that only the magnitude of the spin-polarization vector, rather than its orientation in spin space, is relevant for supercurrent stability.

DOI: 10.1103/PhysRevLett.110.025301 PACS numbers: 67.85.−d, 03.75.Kk

Persistent currents are a hallmark of superfluidity and superconductivity, and have been studied in liquid helium and solid state systems for decades. More recently, it has become possible to trap an atomic Bose-Einstein condensate (BEC) in a ring geometry [1–8] and induce rotational superflow in this system [3,5,7,8]. This offers new possibilities for fundamental studies of superfluidity in a flexible experimental setting. Both long-lived superflow [5,7] and quantized phase slips corresponding to singly charged vortices crossing the superfluid annulus have been observed [7,8].

So far experiments on persistent currents in atomic BECs were limited to spinless, single-component condensates. Extending such studies to multicomponent systems, in particular those involving two or more spin states [9–11], is essential for understanding superfluids with a vectorial order parameter and for applications in atom interferometry [12,13]. Persistent flow in a two-component Bose gas has been studied theoretically [14–17] but many issues remain open. Even the central question of whether, and under what conditions, this system supports persistent currents has not been settled.

In this Letter, we study the stability of supercurrents in a toroidal two-component gas consisting of ^{87}Rb atoms in two different spin states. For a large spin-population imbalance we observe superflow persisting for over two minutes and limited only by the atom-number decay. However at a small population imbalance the onset of supercurrent decay occurs within a few seconds. We demonstrate the existence of a well-defined critical spin polarization separating the stable- and unstable-current regimes. We also study the connection between spin coherence and superflow stability, and show that in our system only the modulus of the spin-polarization vector is relevant for the stability of the supercurrent. The existence of a critical population imbalance was anticipated in Refs. [15–17], but quantitative comparison with our measurements will require further theoretical work.

Our setup is outlined in Fig. 1(a). We load a BEC of $N \approx 10^5$ atoms into an optical ring trap of radius 12 μm, created by intersecting a 1070 nm "sheet" laser beam and an 805 nm "tube" beam [7]. The sheet beam confines the atoms to the horizontal plane with a trapping frequency of 350 Hz. In plane, the tube beam confines the atoms to the ring with a trapping frequency of 50 Hz. The trap depth is about twice the BEC chemical potential, $\mu_0/h \approx 0.6$ kHz, and varies azimuthally by $<10\%$.

Our tube trapping beam is a Laguerre-Gauss LG^3 laser mode in which each photon carries orbital angular

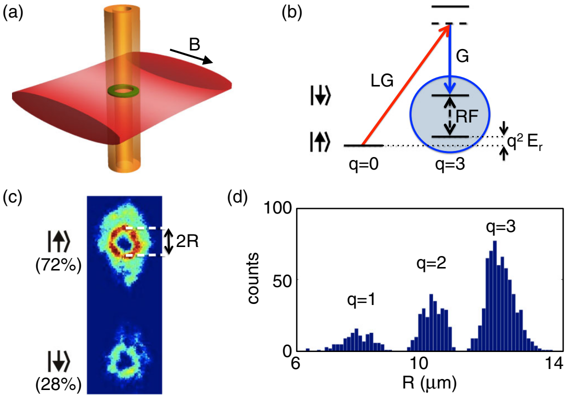

FIG. 1 (color online). Preparation and detection of supercurrent in a two-component gas. (a) The ring trap is formed by a horizontal "sheet" beam and a vertical Laguerre-Gauss (LG) "tube" beam. B is the external magnetic field. (b) Supercurrent is induced by a Raman transfer of atoms between two spin states, $|\uparrow\rangle$ and $|\downarrow\rangle$, using the LG beam and an auxiliary Gaussian (G) beam. During the transfer each atom absorbs $3\hbar$ of angular momentum from the LG beam. Two-component gas is created by coupling $|\uparrow\rangle$ and $|\downarrow\rangle$ states with an rf field. The characteristic rotational energy is $E_r/h \approx 0.4$ Hz. (c) Time-of-flight image of the atoms, with spin states separated using a Stern-Gerlach gradient. The rotational state q is deduced from the radius R characterizing the central hole in the density distribution. The image shown was taken after $t = 4$ s of rotation; the longitudinal spin polarization is $P_z = 0.44$ and $q = 3$ for both spin states. (d) Histogram of $\approx$900 measurements of R at various P_z and t.

momentum $3\hbar$. We use the same beam to induce a supercurrent via a two-photon Raman process [3,7,18]. We briefly (200 μs) pulse on an auxiliary TEM$_{00}$ Gaussian beam, copropagating with the LG beam, to transfer all atoms between two spin states, $|\uparrow\rangle$ and $|\downarrow\rangle$ [Fig. 1(b)]. Each atom absorbs angular momentum $3\hbar$ from the LG beam and we thus create a (single-component) current corresponding to a vortex of charge $q = 3$ trapped at the ring centre. Such current can persist for over a minute and decays in quantized $q \rightarrow q - 1$ steps, corresponding to 2π phase slips in the BEC wave function [7].

The $|\uparrow\rangle$ and $|\downarrow\rangle$ states also define the spin space for our two-component experiments. To create a two-component current we prepare a pure $|q = 3, \downarrow\rangle$ state and then couple $|\uparrow\rangle$ and $|\downarrow\rangle$ by a radio frequency (rf) field, which carries no orbital angular momentum and does not affect the motional state of the atoms. The $|\uparrow\rangle$ and $|\downarrow\rangle$ are two $F = 1$ hyperfine ground states, $m_F = 1$ and 0, respectively. The $m_F = -1$ state is detuned from Raman and rf resonances by the quadratic Zeeman shift in an external magnetic field B of 10 G.

After preparing a rotating ($q = 3$) cloud in a specific spin state, we let it evolve in the ring trap for a time t and then probe it by absorption imaging after 29 ms of time-of-flight expansion. We separate the two spin components with a Stern-Gerlach gradient and directly measure the longitudinal spin-polarization $P_z = (N_\uparrow - N_\downarrow)/(N_\uparrow + N_\downarrow)$, where $N_\uparrow$ ($N_\downarrow$) is the number of atoms in the $|\uparrow\rangle$ ($|\downarrow\rangle$) state [Fig. 1(c)]. The rotational state, $0 \leq q \leq 3$, is seen in the size R of the central hole in the atomic distribution [7], arising due to a centrifugal barrier [3]. As shown in Fig. 1(d), the R values are clearly quantized [7,8], allowing us to determine q with >99% fidelity [19].

In Fig. 2 we illustrate the dramatic difference between superflow stability in a $P_z = 1$ single-component gas and a $P_z = 0$ two-component system. The two different P_z states are created, respectively, by a (140 μs) π and a (70 μs) $\pi/2$ rf pulse at $t = 0$. In the pure $|\uparrow\rangle$ state [Fig. 2(a)] the current persists for over two minutes, with the BEC always remaining in the $q = 3$ state for $\approx$90 s. In contrast, at $P_z = 0$ [Fig. 2(b)] the first phase slip occurs within 5 s and the current completely decays within 20 s. During the decay we always observe the two spin components to be in the same q state.

Supercurrent stability generally depends on the number of condensed atoms [5,7] and at $P_z = 0$ the atom number per spin state is halved. However, from the N-decay curves in Fig. 2(c) we see that this alone cannot explain the difference in superflow stability. At $P_z = 1$ rotation still persists for $N \approx 10^4$ while at $P_z = 0$ it stops already at $N > 4 \times 10^4$. Moreover, if we apply a $\pi/2$ rf pulse at $t = 0$ but then immediately remove all the $|\uparrow\rangle$ atoms from the trap with a resonant light pulse, the current again persists for over a minute. This unambiguously confirms that in Fig. 2(b) the superflow is inhibited by the presence of *both* spin components.

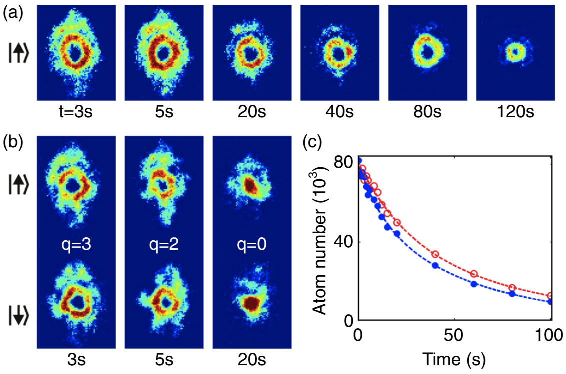

FIG. 2 (color online). Single- versus two-component supercurrent. (a) In a pure $|\uparrow\rangle$ state ($P_z = 1$) supercurrent persists for over 2 min, with no phase slips occurring for $\approx$90 s. (b) At $P_z = 0$ the first phase slip occurs within 5 s and we observe no rotation beyond 20 s. (c) Total atom number decay for $P_z = 1$ (open symbols) and $P_z = 0$ (solid symbols). Dashed lines are double-exponential fits.

We now turn to a quantitative study of the supercurrent stability as a function of the spin-population imbalance (Fig. 3). We tune P_z by varying the length Δt of the rf pulse applied at $t = 0$, and measure the q state of the majority ($|\uparrow\rangle$) spin component as a function of t. Whenever the radius R is fittable for the minority component we get the same q for both spin components in >99% of cases. However, for $N_\downarrow < 10^4$ we cannot determine q for the minority component.

Based on $\approx$1600 measurements of $q(P_z, t)$, in Fig. 3 we reconstruct the complete current stability diagram for $0 \leq P_z \leq 1$ [20]. The contour plot of $\langle q(P_z, t)\rangle$ is obtained by spline interpolation through a 3D mesh of data points

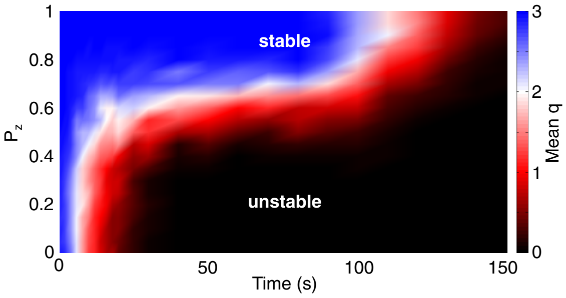

FIG. 3 (color online). Supercurrent stability in a partially spin-polarized gas. The statistically averaged supercurrent state, $\langle q\rangle$, of the majority spin component is shown as a function of P_z and the evolution time t. The contour plot is based on $\approx$1600 measurements of $q(P_z, t)$. The transition between stable- and unstable-current regimes occurs at $0.6 < P_z < 0.7$. In the stable regime the current eventually decays due to the atom-number decay.

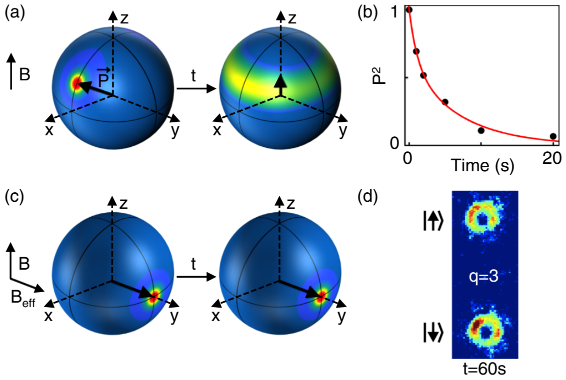

FIG. 4 (color online). The role of spin-coherence in superflow stability. (a) An rf pulse at $t = 0$ creates a spin-superposition state in which $P_z < 1$ but $P = 1$. As the superposition decoheres, transverse spin-polarization decays and $P \rightarrow P_z$. (b) Transverse-polarization decay (see text). Double-exponential fit (solid red line) gives the decay function $f(t)$. (c) Adiabatic dressing of the spin state. In presence of a resonant rf field $\vec{B}_{\mathrm{eff}} \propto \hat{y}$ and the dressed $P_z = 0$ state $|y\rangle$ is stable against decoherence. (d) In the dressed $|y\rangle$ state the supercurrent is also stable.

with integer q values. The blue-shaded region corresponds to rotation times for which no phase slips occur. We clearly distinguish two qualitatively different regimes. For large P_z the superflow is fundamentally stable and limited only by the atom-number decay; for low P_z the current starts to decay within a few seconds. A sharp transition between the two regimes occurs at $0.6 < P_z < 0.7$.

To fully understand these observations, we need to distinguish a coherent superposition of $|\uparrow\rangle$ and $|\downarrow\rangle$ states from an incoherent mixture. The rf pulse at $t = 0$ corresponds to rotation around the y axis on a Bloch sphere and puts the BEC in a superposition state $|\theta\rangle = \sin(\theta/2)|\uparrow\rangle + \cos(\theta/2)|\downarrow\rangle$. Here, $\theta = \Omega_R \Delta t$, where Ω_R is the rf Rabi frequency. In this state $P_z = -\cos(\theta)$ but the gas is still fully spin polarized; the polarization vector is $\vec{P} = [\sin(\theta), 0, -\cos(\theta)]$ and $P \equiv |\vec{P}| = 1$. Subsequently the spin superposition decoheres, due to both intrinsic spin diffusion [21] and small magnetic field inhomogeneities [22]. P_z is a constant of motion but the transverse polarization decays and $P \rightarrow P_z$ [Fig. 4(a)].

We study the transverse-polarization decay in a Ramsey-type experiment. Starting in the $|\downarrow\rangle$ state we apply two $\pi/2$ rf pulses separated by time t and then measure P_z. The first pulse creates a purely transverse $\vec{P} = (1, 0, 0)$ and the second one maps the decaying P into P_z [23]. As seen in Fig. 4(b), we observe a very long spin-coherence time, $t_{\mathrm{coh}} \sim 10$ s. This means that in the unstable regime in Fig. 3 phase slips occur already at $t \lesssim t_{\mathrm{coh}}$, when we cannot equate P and P_z.

We also perform a complementary experiment in which we adiabatically dress the rotating BEC with the rf field. In presence of the rf field of frequency ω, the effective magnetic field is $\vec{B}_{\mathrm{eff}} = (2\hbar/\mu_B)(0, \Omega_R, -\delta)$, where μ_B is the Bohr magneton and $\delta = \omega - \mu_B B/(2\hbar)$ is the detuning from resonance. On resonance, $\vec{B}_{\mathrm{eff}} \propto \hat{y}$. At $t = 0$ we adiabatically (in 100 ms) sweep δ from a large value ($\gg \Omega_R$) to zero, thus preparing a $P_z = 0$ superposition state $|y\rangle = (|\uparrow\rangle + i|\downarrow\rangle)/\sqrt{2}$ [Fig. 4(c)]. At this point, $|y\rangle$ is equivalent to the $|\pi/2\rangle$ state prepared by an rf pulse, which does not show long-term current stability [Fig. 2(b)]. However, if we leave the rf field on during the in-trap evolution, $|y\rangle$ is an eigenstate of the Hamiltonian and the coherence between $|\uparrow\rangle$ and $|\downarrow\rangle$ components does not decay [24]. In this case $P_z = 0$ supercurrent is stable and persists for more than a minute [Fig. 4(d)].

These experiments clearly show that for analyzing current stability in a partially polarized gas we must distinguish P_z and $|\vec{P}|$. With this understanding, we now quantitatively characterize the onset of the supercurrent decay in Fig. 3 by the time τ at which the probability that the first phase slip ($q = 3 \rightarrow 2$) has occurred is 50%; this closely corresponds to the border of blue- and white-shaded regions.

In Fig. 5(a) we see that τ rapidly increases for $P_z \gtrsim 0.64$, saturating at 100 s due to the N decay. We now combine our measurements of τ and the transverse-polarization decay $f(t)$ [Fig. 4(b)] to calculate $|\vec{P}|$ at the onset of supercurrent decay:

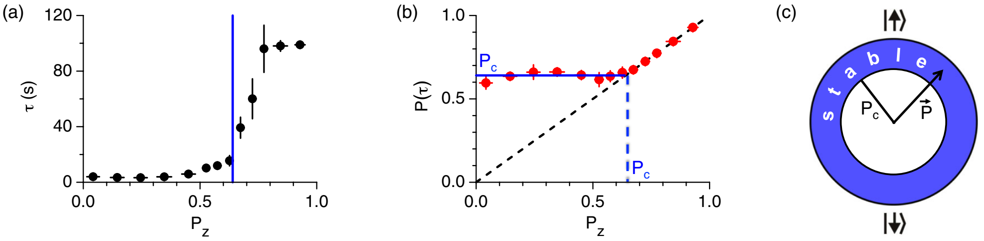

FIG. 5 (color online). Critical spin polarization P_c. (a) Characteristic time of the first phase slip, τ, versus P_z. Vertical blue line marks P_c, accurately determined in (b). (b) $|\vec{P}|$ at the onset of the supercurrent decay. Fit to the points with $P(\tau) > P_z$ (horizontal blue line) gives $P_c = 0.64(1)$. (c) Stability diagram on the Bloch sphere. The blue-shaded region in Fig. 3 maps into the outer shell $|\vec{P}| > P_c$.

$$P(\tau) = \sqrt{P_z^2 + (1 - P_z^2) f(\tau)}. \tag{1}$$

In Fig. 5(b) we clearly distinguish two regimes: one where $P(\tau)$ is constant (within errors) and one where $P(\tau) = P_z$. We thus complete our physical picture and accurately determine the critical spin polarization P_c. (1) If $P_z > P_c$, then $|\vec{P}|$ *never* drops below P_c; the supercurrent is fundamentally stable, $\tau \gg t_{\mathrm{coh}}$ and $P(\tau) = P_z$. (2) If $P_z < P_c$, supercurrent decay starts at $\tau \lesssim t_{\mathrm{coh}}$, when the decaying P becomes equal to P_c. From all the data in this regime we get $P_c = 0.64(1)$.

For $0 \leq P_z \leq P_c$ the value of τ varies from 4 to 15 s and the orientation of $\vec{P}(\tau) = (\sqrt{P_c^2 - P_z^2}, 0, P_z)$ in spin space varies from purely transverse to purely longitudinal, but the onset of the supercurrent decay always occurs at the same $|\vec{P}|$. We thus conclude that the region of supercurrent stability is in fact the outer shell of the Bloch sphere where $|\vec{P}| > P_c$ [Fig. 5(c)]. This spin-rotational symmetry is intuitive but we note that it need not be universal. In our ^{87}Rb gas the strengths of intra- and intercomponent interactions are almost identical, so the Hamiltonian is almost invariant under rotations in spin space. In the future it would be very interesting to study supercurrent stability as a function of both intra- and intercomponent coupling strengths.

The existence of a critical population imbalance for superflow stability was predicted in Refs. [15–17], assuming equal intra- and intercomponent interactions and no intercomponent coherence. The current instability was associated with out-of-phase density fluctuations in the two components. However, the agreement on the value of P_c has not been reached. In Refs. [15,16] it was predicted that any $q > 1$ flow is unstable for essentially any $P < 1$, but according to Ref. [17] such current is stable above some nontrivial interaction-dependent P_c. The latter conclusion qualitatively agrees with our observations. However, none of the existing theories is quantitatively applicable to our experiments, since they are limited to the simplified cases of reduced dimensionality and very weak interactions. Moreover, the interplay of the spin and rotational degrees of freedom may involve new physical effects. Specifically, the dynamics of the local spin vector on the Bloch sphere can result in a Berry phase and unwind the "scalar" phase describing the rotational flow; the time scale for this process would be the same as the spin decoherence seen in a Ramsey experiment [25].

In summary, we have observed persistent currents in multiply connected spinor condensates, demonstrated the existence of a critical spin polarization for stable superflow, and elucidated the role of spin coherence in supercurrent stability. Our results should stimulate further theoretical work on this fascinating many-body problem and are also relevant for applications in trapped-atom interferometry. An important next step would be to study supercurrents in a two-species system with significantly different intra- and intercomponent interactions.

We thank A. Gaunt and R. Smith for experimental assistance and N. Cooper, S. Baur, E. Demler, T. Kitagawa, G. Kavoulakis, J. Smyrnakis, J. Dalibard, and J. Thywissen for discussions. This work was supported by EPSRC (Grants No. EP/G026823/1 and No. EP/I010580/1).

[1] S. Gupta, K. W. Murch, K. L. Moore, T. P. Purdy, and D. M. Stamper-Kurn, Phys. Rev. Lett. **95**, 143201 (2005).
[2] A. S. Arnold, C. S. Garvie, and E. Riis, Phys. Rev. A **73**, 041606 (2006).
[3] C. Ryu, M. F. Andersen, P. Cladé, V. Natarajan, K. Helmerson, and W. D. Phillips, Phys. Rev. Lett. **99**, 260401 (2007).
[4] K. Henderson, C. Ryu, C. MacCormick, and M. G. Boshier, New J. Phys. **11**, 043030 (2009).
[5] A. Ramanathan, K. C. Wright, S. R. Muniz, M. Zelan, W. T. Hill III, C. J. Lobb, K. Helmerson, W. D. Phillips, and G. K. Campbell, Phys. Rev. Lett. **106**, 130401 (2011).
[6] B. E. Sherlock, M. Gildemeister, E. Owen, E. Nugent, and C. J. Foot, Phys. Rev. A **83**, 043408 (2011).
[7] S. Moulder, S. Beattie, R. P. Smith, N. Tammuz, and Z. Hadzibabic, Phys. Rev. A **86**, 013629 (2012).
[8] K. C. Wright *et al.*, arXiv:1208.3608.
[9] T.-L. Ho, Phys. Rev. Lett. **81**, 742 (1998).
[10] T. Ohmi and K. Machida, J. Phys. Soc. Jpn. **67**, 1822 (1998).
[11] J. Stenger, S. Inouye, D. M. Stamper-Kurn, H.-J. Miesner, A. P. Chikkatur, and W. Ketterle, Nature (London) **396**, 345 (1998).
[12] T. L. Gustavson, P. Bouyer, and M. A. Kasevich, Phys. Rev. Lett. **78**, 2046 (1997).
[13] P. L. Halkyard, M. P. A. Jones, and S. A. Gardiner, Phys. Rev. A **81**, 061602 (2010).
[14] T.-L. Ho, Phys. Rev. Lett. **49**, 1837 (1982).
[15] J. Smyrnakis, S. Bargi, G. M. Kavoulakis, M. Magiropoulos, K. Kärkkäinen, and S. M. Reimann, Phys. Rev. Lett. **103**, 100404 (2009).
[16] S. Bargi, F. Malet, G. M. Kavoulakis, and S. M. Reimann, Phys. Rev. A **82**, 043631 (2010).
[17] K. Anoshkin, Z. Wu, and E. Zaremba, arXiv:1207.3449.
[18] M. F. Andersen, C. Ryu, P. Cladé, V. Natarajan, A. Vaziri, K. Helmerson, and W. D. Phillips, Phys. Rev. Lett. **97**, 170406 (2006).
[19] The histogram in Fig. 1(d) was obtained for $t < 20$ s. At longer t the characteristic value $R(q)$ slowly decreases [7]. We take this into account when determining q.
[20] Based on ≈ 500 measurements we find essentially symmetric behavior for negative P_z. One small difference is that no phase slips occur for about 70 s for $P_z \to -1$ and 90 s for $P_z \to 1$.
[21] A. Widera, S. Trotzky, P. Cheinet, S. Fölling, F. Gerbier, I. Bloch, V. Gritsev, M. D. Lukin, and E. Demler, Phys. Rev. Lett. **100**, 140401 (2008).
[22] In the presence of in-plane field gradients the two-component gas is extremely susceptible to phase

separation. By balancing $|\uparrow\rangle$ and $|\downarrow\rangle$ in-trap density distributions we minimized such gradients to $<5 \times 10^{-5}$ G/cm.

[23] Because of long separation the two rf pulses have a random relative phase φ. After the second pulse $P_z = P\cos(\varphi)$ and $\langle P_z^2\rangle = P^2/2$. For each t we get $\langle P_z^2\rangle$ from about 40 measurements.

[24] We checked for t up to 100 s that we can always convert $|y\rangle$ into pure $|\downarrow\rangle$ by sweeping ω away from resonance.

[25] S. Baur (private communication).

Appendix B

Light Potentials

In this Appendix, we first overview the relationship between light intensity and the potential experienced by a ^{39}K atom in the relevant hyperfine state for the experiments in this thesis. Next, we introduce the concept of using Fourier optics to craft atomic potentials.

B.1 Light Potentials

If far-detuned light of frequency ω and intensity I illuminates a two-level quantum system $\{|1\rangle, |2\rangle\}$ with resonant frequency ω_0, a potential is induced via the AC Stark effect [12]:

$$V(I) = |\langle 1|e\mathbf{r}|2\rangle|^2 \frac{1}{2\epsilon_0\hbar}\left[\frac{1}{\omega_0-\omega}+\frac{1}{\omega_0+\omega}\right] I, \tag{B.1}$$

where $e\mathbf{r}$ is the dipole operator. The coupling matrix element can be related to the decay linewidth $\Gamma = \text{lifetime}^{-1}$ via $|\langle 1|e\mathbf{r}|2\rangle|^2 = 3\pi\epsilon_0\hbar c^3\Gamma/\omega_0^3$ [125].

In the case of a real atom, transitions are generally between two manifolds of many spin states. For two levels with angular momentum numbers $|J, F, m_F\rangle$ and $|J', F', m'_F\rangle$ the appropriate matrix element is [126],

$$|\langle J, F, m_F|e\mathbf{r}|J', F', m'_F\rangle|^2 = \underbrace{\frac{3\pi\epsilon_0\hbar c^3\Gamma}{\omega_0^3}}_{\substack{\text{Matrix element}\\ \text{for two-level}\\ \text{system}}} \underbrace{\frac{2J'+1}{2J+1}}_{\substack{\text{Accounts for}\\ \text{degeneracy of}\\ \text{each } J \text{ state}}} \underbrace{\Lambda^2(J, F, m_F, J', F', m'_F)}_{\substack{\text{Clebsch-Gordon}\\ \text{coefficient, gives}\\ \text{spin-state overlap}}}. \tag{B.2}$$

In our experiment, axial confinement is produced by π-polarised light at 532 nm. Labelling atomic states in the low-field basis, experiments are performed in $|4\,^2S_{1/2}, F = 1, m_F = 1\rangle$; this is coupled to excited states $\{|F = 1, m_F = 1\rangle, |F = 2, m_F = 1\rangle\}$ in both D1 ($J = 1/2$) and D2 ($J = 3/2$) upper manifolds. Inserting the generalised matrix element of Eq. (B.2), the two-level potential of Eq. (B.1) is modified

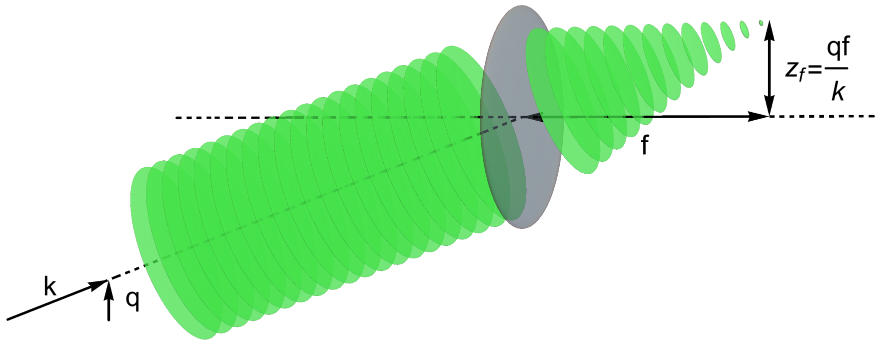

Figure B.1: *The effect of a lens on an incident plane wave, with wavevector component q normal to the optic axis. The plane wave is brought to a point at a position $z_f = qf/k$ on the focal plane.*

---

to:

$$V(I) = \left(\frac{1}{3} \frac{3\pi c^2}{\omega_{\mathrm{D1}}^3} \left[\frac{\Gamma_{\mathrm{D1}}}{\omega_{\mathrm{D1}} - \omega} + \frac{\Gamma_{\mathrm{D1}}}{\omega_{\mathrm{D1}} + \omega} \right] + \frac{2}{3} \frac{3\pi c^2}{\omega_{\mathrm{D2}}^3} \left[\frac{\Gamma_{\mathrm{D2}}}{\omega_{\mathrm{D2}} - \omega} + \frac{\Gamma_{\mathrm{D2}}}{\omega_{\mathrm{D2}} + \omega} \right] \right) I. \tag{B.3}$$

The detuning of our axial light is much larger than the fine-structure splitting, and so the above expression effectively reduces to the simple two-level result. Specific transition parameters for ^{39}K are tabulated in [121].

B.2 Sculpting Potentials via Fourier Optics

If one can shape light into a desired geometry, then the light potential of Eq. (B.3) induces a corresponding atomic potential. One particularly useful phenomenon for crafting intricate optical patterns is the ability of a lens to project the Fourier transform of an incident optical field onto its focal plane. For monochromatic light of wavenumber k, the wavevector component parallel to the plane of the lens, q, is mapped onto spatial position z_f at the focal plane.

This can straightforwardly be seen by considering a plane wave incident on a lens, illustrated in Fig. B.1. For simplicity we work in 1D. The incident amplitude pattern on the lens is $\sim e^{iqz}$; the effect of the lens is to impart a phase change $-kz^2/(2f)$. To obtain the amplitude $E_f(z_f)$ at some point z_f on the focal plane, one integrates over all possible paths taken from the lens plane to z_f.

$$E_f(z_f) \sim \underbrace{\int \mathrm{d}z}_{\text{Integrate over lens plane}} \underbrace{e^{iqz}}_{\text{Incident amplitude}} \underbrace{e^{-ikz^2/(2f)}}_{\text{Lens}} \underbrace{e^{ik\sqrt{f^2+(z_f-z)^2}}}_{\text{Propagate phase to focal plane}} \underbrace{\frac{1}{\sqrt{f^2+(z_f-z)^2}}}_{\text{Decay of amplitude}} . \tag{B.4}$$

Making the assumption that $|z_f - z| \ll f$, the path length can be expanded as,

$$\sqrt{f^2 + (z_f - z)^2} \approx f + \frac{z_f^2}{2f^2} + \frac{z^2}{2f^2} - \frac{z_f}{f} z. \tag{B.5}$$

The first two terms are independent of z and can be taken outside of the integral. The third term is exactly cancelled by the lens, leaving only the linear fourth term. Our amplitude integral therefore simplifies considerably, to

$$\begin{aligned} E(z_f) &\sim \int \mathrm{d}z \; e^{iqz} \; e^{-ikz_f z/f}, \\ &= \int \mathrm{d}z \; e^{iz(q - z_f z/f)}, \\ &\sim \delta\left(q - \frac{z_f}{f} y\right). \end{aligned} \tag{B.6}$$

For some incident collection of plane waves, each is mapped onto position in the focal plane according to,

$$q \rightarrow \frac{z_f k}{f}. \tag{B.7}$$

This reciprocal relationship allows intricate, micron-scale patterns of light to be constructed from their macroscopic counterparts in Fourier space[1].

One trivial example is focusing a Gaussian beam; an incoming amplitude profile $E(r) \sim e^{-r^2/w^2}$ has a Fourier spectrum $\tilde{E}(q) \sim e^{-q^2 w^2/4}$. Making use of the lens mapping of Eq. (B.7), in the focal plane of the lens $E_f(r_f) \sim e^{-r_f^2/W^2}$, where the focused waist $W = \lambda f/(\pi w)$.

---

[1] In terms of amplitude, the pattern on one focal plane of a lens is the Fourier transform of the pattern on the opposing focal plane. In the case of an object being some arbitrary distance from a lens, the *intensity* pattern on the focal plane still corresponds to the square modulus of the object's Fourier transform. However, the amplitude itself will in general differ by some phase from the exact Fourier transform. This means that the distance from object to lens can be freely varied, whilst leaving the focal intensity pattern unchanged.

Appendix C

Trap Characterisation

This Appendix provides the experimental procedure for measurement of trapping frequencies in both the axial and planar direction, and the appropriate focusing time for the momentum focusing of our two-dimensional gas.

C.1 Axial Frequency

The axial trap frequency was obtained from observing the axial breathing mode of an ideal gas BEC. For a gas of non-interacting particles oscillating symmetrically in a harmonic potential, the cloud distribution repeats every half trap-period. The observed breathing mode frequency is therefore $2\omega_z$, and provides a clean measure of trapping frequency. This mode was excited as follows:

1. Prepare an almost-pure BEC in the two-dimensional trap (see Section 7.1).
2. Switch interactions to zero, by ramping the Feshbach field slowly to its zero crossing.
3. Flash the axial trapping light off for 17 μs, corresponding to 7% of a trap period.
4. Wait for a variable hold time.
5. Release the BEC from the trapping beams, and observe horizontally after 17 ms ToF to access the momentum distribution of the breathing BEC.

The evolution of the BEC vertical extent with hold time then reveals the frequency of the breathing mode, and is illustrated in Fig. 6.4.

C.2 Planar Frequency

To determine the in-plane frequencies, we again prepare an almost-pure BEC identically to the axial frequency sequence of Section C.1. The BEC is then displaced in-plane using a red-detuned ‘tweezer’ beam propagating in the axial direction, of wavelength 820 nm and waist $W_{\mathrm{tw}} = 240\ \mu$m. The optical setup for this beam is described in [21]. The following sequence is used to determine the planar frequencies:

1. Prepare an almost-pure BEC, identically to the axial frequency sequence.
2. Slowly ramp up the tweezer beam, centred $W_{\mathrm{tw}}/2 = 120\ \mu$m away from the ODT centre. At this displacement, the maximum in-plane force is exerted at a given tweezer power.
3. Rapidly ($< 1\ \mu$s) switch off the tweezer beam.
4. Hold the BEC in-trap for a variable wait time, t_{hold}.
5. Take an *in situ* image on the vertical imaging system.

From the resulting evolution of the in-plane position of the cloud, we obtain both the trap eigenfrequencies and the orientation of the trap eigenaxes; these are given in Eqs. (6.13) and (6.14).

C.3 Focusing Time

The momentum distribution of our two-dimensional gas is obtained using momentum focusing, outlined in Section 6.3, in which free particle evolution in a harmonic trap maps a particle’s momentum onto position over a quarter-oscillation. We empirically determine the focusing time at which the momentum distribution is revealed, by preparing a degenerate cloud and monitoring the width of the sharp low-momentum peak as a function of focusing time. The experimental sequence is as follows:

1. Prepare a degenerate two-dimensional cloud; see Section 7.1.
2. Switch off the axial trapping.
3. Wait some variable hold time, before taking a vertical absorption image.

When taking critical point data (Section 7.1.4), the Feshbach field is jumped to its zero-crossing value before taking the image, ensuring an identical spin state composition for imaging regardless of the in-trap interaction strength. This step is omitted for determining focusing time; the field takes several ms to stablise to some new strength, and we wish to avoid the risk of any inadvertent variable detuning as the focusing time is scanned. We therefore hold the scattering length fixed throughout both trapping and focusing at a low value $a = 10\ a_0$, (equivalently $\tilde{g} = 0.01$), and image with a frequency resonant at this field. The absolute imaging efficiency is unknown, but we are interested solely in the variation of peak width with hold time.

Our focusing trap is anisotropic, with the eigenaxes at an angle of $\theta = 37^\circ$ to the camera axes[1]. We therefore rotate our cloud images by θ, such that the fitted x and y widths on an image correspond to those along trap eigenaxes. Finally, we fit the rotated image with some heuristic two-curve model, for example two Gaussians, to account for the low-momentum peak and broad thermal wings. Evolution of the peak width with focusing time is plotted in Fig. 6.9, and we take the appropriate focusing times as the location of a width minimum.

---

[1] See Eq. (6.14).

Appendix D

Absorption Imaging and Calibration

D.1 Absorption Imaging

We probe our cloud using absorption imaging, in which a beam of resonant light of wavelength λ is directed through the atoms, which are at the focal plane of a CCD camera. As the resonant imaging light passes through a cloud, it drives transitions from the initial ground state to some excited state. The atom subsequently decays over a timescale Γ^{-1}, emitting a photon isotropically, and reducing the net flux of imaging light through the cloud. From the amount of transmitted light as a function of position over the cloud, the column density can be mapped.

For an atomic transition of saturation intensity[1] I_s, the intensity I of the imaging light decays with propagation distance z through the sample [119], according to,

$$\frac{\mathrm{d}I}{\mathrm{d}z} = -n_{3\mathrm{D}}\frac{\sigma_0}{1+\frac{I}{I_\mathrm{s}}}I \tag{D.1}$$

where the zero-intensity cross section $\sigma_0 = 3\lambda^2/(2\pi)$ for a closed cycling transition [119]. This equation can be integrated to yield

$$\mathrm{OD} = -\ln\frac{I}{I_0} + \frac{I_0 - I}{I_\mathrm{s}}, \tag{D.2}$$

where I_0 is the incident imaging intensity, and the optical density OD is defined in terms of the column density n as $\mathrm{OD} = \sigma_0 n$.

Typically cold atoms experiments make use of two limits. For low intensities $(I/I_\mathrm{s}) \ll 1$, the log term dominates and the linear term can be neglected. At high intensities the opposite situation arises, and the transmitted intensity varies

---

[1] Defined as $\frac{\pi h c \Gamma}{3\lambda^3}$, this is the intensity for which the Rabi frequency of transfer from the ground to excited state equals the spontaneous decay rate Γ.

linearly with OD. Practically, photon shot noise provides an experimental limitation to which method is used, giving an upper bound to the OD which can be reliably resolved by low-intensity imaging, and a lower bound to high-intensity imaging. For extraction of (μ, T) from a cloud image good accuracy is required in the low-OD wings of the distribution, and so we make use of low-intensity imaging.

Practically, for a single atomic sample we take three images:

1. An initial image with atoms present, whose shadow is projected onto the CCD. This takes the form of a map of detected photon counts $C_{\text{atom}}(\mathbf{r}) + C_{\text{back}}(\mathbf{r})$ over the cloud.
2. A reference image $C_{\text{ref}}(\mathbf{r}) + C_{\text{back}}(\mathbf{r})$, with an identical pulse of imaging light but no atoms present.
3. A background image $C_{\text{back}}(\mathbf{r})$, with no imaging light but all other experimental settings identical. This accounts for any contribution to camera counts from sources other than imaging light.

The optical density is then obtained as,

$$\text{OD} \approx -\ln\left(\frac{C_{\text{atom}}(\mathbf{r})}{C_{\text{ref}}(\mathbf{r})}\right). \tag{D.3}$$

It is worth estimating our upper bound to measurable OD; for a total number of detected imaging photons γ on a camera pixel (in the absence of atoms), the maximum OD that can be reliably measured is found by equating the corresponding detected photon count to the shot noise $\sqrt{\gamma}$. Thus,

$$\text{OD}_{\text{max}} = -\ln\frac{\sqrt{\gamma}}{\gamma}. \tag{D.4}$$

For an imaging intensity I, pulse duration τ, imaging wavelength λ, pixelsize Δx, and CCD quantum efficiency q, one has $\gamma = Iq\tau\Delta x^2\lambda/(hc)$. This results in a maximum observable OD of,

$$\text{OD}_{\text{max}} = \frac{1}{2}\ln\frac{Iq\tau\Delta x^2\lambda}{hc}. \tag{D.5}$$

D.2 Magnification of Imaging Systems

The magnification of our *horizontal* imaging setup is obtained by observing a free-falling cloud at various times; it accelerates at a known $g = 9.81\ \text{ms}^{-2}$ downwards. The pixelsize Δx is the in-trap length which maps to a single CCD pixel on our camera. We find a small spatial variation in Δx, summarised in Table D.1. We do not attribute this variation to a particular source; possibilities are some residual curvature of the CCD, or aberrations of our imaging system. We heuristically

ToF (ms)	**M**	**Pixelsize $\boldsymbol{\Delta x}$ (μm)**
2	2.65	2.43
4.5	2.71	2.38
7.5	2.71	2.38
10.5	2.72	2.37
12.5	2.73	2.36

Table D.1: *Magnification M and pixelsize for the horizontal imaging system at various free-fall times, determined from free-fall under gravity.*

account for it via a linear fit, giving a pixelsize $\Delta x = 2.43 - 0.0056 \times \mathrm{ToF}$, where Δx is in μm and ToF in ms.

Having calibrated the horizontal pixelsize against gravity, the magnification of the vertical imaging system can now be obtained by relation. We prepare an almost-pure BEC in the ODT [16], and compare images taken on both the horizontal and vertical imaging systems. The Thomas-Fermi density profile [12] of an interacting BEC has a sharp-edge, giving a robust cloud lengthscale. The absorption image is taken along the horizontal direction only, and the resulting fluorescence is observed on the vertical camera; this ensures that precisely the same object is observed on each camera. We take several cautionary steps to improve accuracy:

- For imaging intensity I and imaging pulse duration τ, the acceleration of an atom during a pulse scales as I, displacement as $I\tau^2$ and fluorescence signal as $I\tau$. The cloud distortion in the vertical image at a fixed signal is therefore minimised by decreasing the pulse duration whilst preserving the product $I\tau$.

  We therefore shorten our imaging pulse from our typical value of 80 μs to 40 μs, whilst increasing our imaging beam intensity to $\approx 0.6 I_\mathrm{s}$ from our typical value of $\approx 0.3 I_\mathrm{s}$.

- We desire as large a BEC as possible, to reduce the fractional error in radius measurements. However, the resultant peak OD is high enough to saturate absorption images, leading to a distortion in the fitted TF profile. For our imaging intensity, pulse duration and horizontal camera parameters[1] Eq. (D.5) gives a maximum observable $\mathrm{OD}_\mathrm{max} \approx 4$, much less than typical BEC densities.

  To circumvent this problem, we selectively prepare only a small atomic fraction in a visible state. Experiments are performed with ^{39}K in the state $|F = 1, m_F = 1\rangle$ and horizontal imaging is on the cooling transition, with ground state $|F = 2, m_F = 2\rangle$. Exposure to repump light could be used to controllably transfer atoms to the visible state before imaging; however, for optically thick samples the non-uniform repumping would lead to a distorted transferred cloud. Instead we employ a microwave (MW) pulse of duration 200 μs immediately prior to imaging, approximately resonant with

---

[1] Quantum efficiency ≈ 0.25, $\Delta x = 2.43$ μm from Table D.1.

the $|F=1, m_F=1\rangle \to |F=2, m_F=2\rangle$ transition. We empirically tune the MW frequency to 468.4 MHz, such that the horizontal image OD is just below saturation.

The horizontal and vertical images are each integrated along one direction (vertically on the horizontal image, and along the imaging beam on the vertical image). The two resulting 1D profiles $n(x)$ should correspond to exactly the same doubly-integrated cloud density profile, and are each fitted with a doubly integrated Thomas-Fermi profile,

$$n(x) = A\left(1 - \frac{x^2}{R_x^2}\right)^2 . \tag{D.6}$$

Averaging over 23 images, we find a size ratio of 1.21 ± 0.01, giving a vertical magnification of 4.41 and pixelsize $\Delta x = 2.95\ \mu$m.

D.3 Rescaling Function

As discussed in Section 6.4.1, on each absorption imaging cycle there is a small ($\approx 2.5\%$) probability than an atom relaxes into a dark state. We empirically account for this via a rescaling function $\mathcal{F}$, scaling the OD on each image pixel by a photon-count-dependent factor. This mapping is obtained as follows:

1. Prepare a thermal cloud of ^{39}K in our ODT [16] at $T \approx 600$ nK, in the presence of an anti-gravity gradient.
2. Release the cloud for 10 ms ToF in total.
3. Jump the Feshbach field to its zero crossing value $t_{\text{foc}} = 6.96$ ms (see Eq. (6.27)) before the image is taken. This ensures magnetic conditions are identical to those after momentum focusing of a two-dimensional cloud.
4. Repeat for a wide range of imaging intensities.
5. For each image, obtain an optimal reference pattern[1] of imaging photon counts $C^{\text{opt}}_{\text{ref}}(\mathbf{r})$.
6. Assume that on each ring of pixels, concentric with the cloud centre, the variation in OD is due to the variation in the incident imaging photon count. For a single ring-radius, from all images construct a plot of (OD_0/OD) vs (C/C_0), where C_0 is a fixed reference count and OD_0 the corresponding optical density. In our case we choose $C_0 = 1300$, equivalent to $(I/I_\text{s}) \approx 0.028$.
7. Repeat the previous step for a range of ring radii; the lower bound should be set so as to avoid any regions of saturated OD, and the upper bound set to lie within the atomic cloud.

---

[1] See Section 6.4.

8. Finally, construct a numerical interpolating function $(\mathrm{OD}_0/\mathrm{OD}) = \mathcal{F}(C/C_0)$ from the compiled correlation plots from all radii.

In principle the function $\mathcal{F}(C/C_0)$ could be obtained from a single ring radius; reassuringly, we find that the functions from each radius overlap extremely well, which is illustrated in Fig. 6.15. This implies that the true rescaling function is a separable function of actual atomic density and imaging count.

The rescaling function, along with an analytic toy model which explains its behaviour well, is given in Fig. 6.16.

D.4 Imaging Efficiency

The absolute imaging efficiency is determined by comparison of the observed BEC critical number with its theoretical value. In a harmonic trap of frequencies $(\omega_x, \omega_y, \omega_z)$, this critical number is

$$N_{\mathrm{c}}^{\mathrm{3D}} = A\,\zeta(3)\left(\frac{k_{\mathrm{B}}T}{\hbar(\omega_x\omega_y\omega_z)^{1/3}}\right)^3 \frac{1}{(1-3.426(a/\lambda_{\mathrm{th}})+42(a/\lambda_{\mathrm{th}})^2)^3} + \delta N_{\mathrm{c}}^{\mathrm{fs}}. \quad \text{(D.7)}$$

Here A is a correction due to anharmonicity of the Gaussian trapping beams, and $\delta N_{\mathrm{c}}^{\mathrm{fs}}$ the finite-size shift of the critical point [127]. We also take into account the interaction-induced shift of the critical point [79].

The critical point is extracted in the following manner. An anti-gravity gradient is present for all stages, to ensure identical magnetic conditions to experiments with two-dimensional gases.

1. Evaporatively cool a thermal cloud in the ODT [16], until a small BEC is produced.
2. Wait a variable hold time at a scattering length of 59 a_0. During this hold atoms are lost via background gas collisions and scattering from trapping beams.
3. Release the cloud for 10 ms ToF in total.
4. Jump the Feshbach field to its zero crossing value $t_{\mathrm{foc}} = 6.96$ ms (see Eq. (6.27)) before the image is taken. This ensures magnetic conditions are identical to those after momentum focusing of a two-dimensional cloud.
5. Take an absorption image of the cloud. Optimal reference images are calculated[1], and the OD rescaling of Eq. (6.39) applied.
6. Extract the thermal number N, temperature T, and condensed number N_0.
7. Plot N vs $N_0^{2/5}$, and T vs N_0. The critical point (N_c^{3D}, T_c) is found as the corresponding intercepts.

---

[1] See Section 6.4.

The $N_0^{2/5}$ x-axis of the number plot ensures that total number N varies linearly with the x-coordinate [78], making extrapolation to the intercept more reliable.

The anharmonicity factor A is found by numerical integration of the Bose distribution at $\mu = 0$ over our true trapping potential, which is the sum of crossed attractive Gaussian beams. This method is outlined in [114], and yields $A \approx 1.09$.

Our trap frequencies at the ODT power used are $(\omega_x, \omega_y, \omega_z) = 2\pi \times (53.2, 63.1, 89.5)$ Hz. The planar frequencies are obtained identically to Section 6.1.2, and the vertical frequency by displacing the cloud using an Ioffe coil [113, 114] and observing the subsequent vertical oscillation on the horizontal imaging system.

We find a ratio of theoretical to observed critical number of 4.3 ± 0.2. The error is estimated from taking five similar critical points over the course of one month. We also repeated the above sequence for various in-trap interaction strengths ranging $59 - 242\ a_0$, which led to a similar spread.

Appendix E

Anti-Gravity Field

During the momentum focusing, it is essential that atoms experience minimal vertical displacement so that they remain within the harmonic region of the ODT. During focusing, the ODT is insufficient to support the atoms against gravity. We therefore perform our experiments within a vertical magnetic field gradient, which compensates the gravitational potential gradient.

This is provided by an anti-Helmholtz coil pair, which provides a quadrupole magnetic field at the atoms. This coil pair is also used for our MOT field, magnetic transport, and provides the quadrupole component of our magnetic QUIC trap. Extensive details of the coil setup can be found in [113, 114].

The atoms experience a superposition of the uniform Feshbach field $(0, 0, B_\mathrm{F})$, and a quadrupole field $(Ax, Ay, -2Az)$, where B_F and A are functions of the current in the Feshbach and quadrupole coils respectively. The total field, and its magnitude, are then given by

$$\mathbf{B} = \begin{pmatrix} Ax \\ Ay \\ B_\mathrm{F} - 2Az \end{pmatrix} \quad , \quad |\mathbf{B}| = B_\mathrm{F}\sqrt{1 - \frac{4Az}{B_\mathrm{F}} + \frac{A^2}{B_\mathrm{F}^2}\left(x^2 + y^2 + 4z^2\right)}. \tag{E.1}$$

Knowing from dimensional analysis that we require $\mu_\mathrm{B} A \sim mg$, where g is the gravitational acceleration and μ_B the Bohr magneton, for typical cloud radii $R \sim 100\ \mu\mathrm{m}$ the quadrupole field varies by $\sim AR \sim mgR/\mu_\mathrm{B} = 0.07$ G. This is extremely small compared with the Feshbach field $B_\mathrm{F} \approx 400$ G, and keeping first order terms in A

$$|\mathbf{B}| = B_\mathrm{F} - 2Az. \tag{E.2}$$

The atoms are located at the quadrupole centre ($z = 0$) where the field strength is set solely by the Feshbach coils. However, $|\mathbf{B}|$ now varies linearly with vertical displacement z; empirically, we find the necessary quadrupole current by creating a BEC in our ODT [16], releasing it in the presence of our anti-gravity field, and imaging along the horizontal direction. Tuning the current such that vertical displacement over very long (30 ms) ToF is less than 1 pixel ($= 2.43\ \mu$m) ensures that the residual vertical acceleration is $\lesssim 10^{-3}g$. This would induce a vertical displacement $\lesssim 0.2$ μm during our focusing time of ≈ 7 ms, which is negligible compared with the ODT waist of 140 μm.

As expected from Eq. (E.2) the necessary quadrupole current is independent of B_{F}. To confirm that the quadrupole field does not shift the field strength at the atoms, we measured the resonant imaging frequency of a thermal cloud in the ODT, both with and without the anti-gravity field. Imaging was along the Feshbach field (axial) direction, between the ground state $|4S_{1/2}, I = 3/2, m_I = 3/2, m_J = -1/2\rangle$ and excited state $|4P_{3/2}, I = 3/2, m_I = 3/2, m_J = -3/2\rangle$; the details of this 'high-field' imaging is discussed in Section 6.4. The field strength used was 305.5 G.

The resonant imaging frequency in the presence of the anti-gravity field was shifted by -0.1 ± 0.1 MHz compared to its absence. The energy splitting of our imaging two-level system varies as $-\mu_{\mathrm{B}} B$ (see Section 6.4.1), which implies a shift in magnetic field of 0.07 ± 0.07 G, less than our Feshbach field resolution of ≈ 0.1 G. At our highest $\tilde{g} \approx 0.5$, using Eq. (1.6) this field shift would correspond to an error of $\Delta\tilde{g} \approx 0.01$; this source of error was subsequently neglected.

Appendix F

Error Analysis

The errors on our measured critical atom number and chemical potential for the BKT transition can be divided into two categories: statistical, and systematic. Statistical errors are a measure of how well we can determine critical parameters given the scatter in experimental data. In addition to these statistical errors, there are various sources of systematic error. These can be divided into arising from system calibration uncertainties, finite-size physics, the inhomogeneity of our trapped gas and anharmonicity of our focusing trap. In this Appendix we outline our estimates of both categories of error, and a summary of their values is given in Table 7.1.

F.1 Statistical

Each critical point measurement consists of $M \approx 72$ images of a gas crossing the BKT point; we estimate the statistical error in critical parameters via the following 'bootstrapping' approach.

1. Randomly select M images from the entire critical point measurement; some images may be selected multiple times, others not at all.
2. Apply the analysis of Section 7.2.4 to obtain N_c, T_c and μ_c for this selected image set.
3. Repeat a large number of times, in our case 1000.
4. Take the standard deviation of the critical values to be representative of the statistical uncertainty in their determination.

This method avoids the use of fit uncertainties; our fit functions for $P_0(t)$, $\mu(t)$, $T(t)$ and $N(t)$ are somewhat arbitrary.

F.2 Systematic

Calibration uncertainty The accurate extraction of atom numbers and temperatures require good knowledge of our trap and imaging parameters. Uncertainties in trap frequencies, imaging magnification and absolute imaging efficiency all contribute to uncertainty in critical parameters $\bar{N}_\mathrm{c}/N_\mathrm{c}^0$ and $\tilde{\mu}_\mathrm{c}$. These uncertainties are given at appropriate points within Chapter 6 but are tabulated in Table F.1 for convenience. They are propagated to our final critical parameters $\bar{N}_\mathrm{c}/N_\mathrm{c}^0$ and $\tilde{\mu}_\mathrm{c}$, assuming an ideal gas result for the number of atoms in excited states.

Parameter	**Nominal Value**	**Uncertainty**
Planar trap frequency ω_r	37.7 Hz	±0.3 Hz
Axial trap frequency ω_z	4040 Hz	±6 Hz
Focusing trap frequency ω_foc	36.2 Hz	±0.1 Hz
Imaging pixelsize Δx	2.95 μm	±0.02 μm
Imaging efficiency	0.23	±0.01

Table F.1: *Calibrated system parameters and their uncertainties.*

The end result is a symmetric systematic error of $\Delta\tilde{\mu}_\mathrm{c} \approx \pm 0.05$ and $\Delta(\bar{N}_\mathrm{c}/N_\mathrm{c}^0) \approx \pm 0.14$

Finite size The ideal gas critical number N_c^0 of Eq. (4.13) is exact in the thermodynamic limit [128], in which $N \to \infty$ and $\omega_r \to 0$ with $N\omega_r^2$ held constant. For a finite size system, this critical number is slightly shifted. This effect can be understood as μ needing to reach the lowest trap energy $\hbar\omega_r/2$ for BEC to occur, rather than zero, and increases the critical atom number with respect to the infinite system result.

This can be estimated straightforwardly, since the shift in $\tilde{\mu}_\mathrm{c}$ for the ideal gas is simply $\Delta\tilde{\mu}_\mathrm{c} \approx \hbar\omega_r/(2k_\mathrm{B}T)$. Evaluating this for a characteristic $T = 170$ nK gives $\Delta\tilde{\mu}_\mathrm{c} \approx +0.005$. The corresponding shift in critical number is calculated following [127], giving $\Delta(\bar{N}_\mathrm{c}/N_\mathrm{c}^0) \approx +0.04$.

Inhomogeneity Exactly at the critical point of a harmonically-trapped two-dimensional gas, the gas becomes critical at the trap centre only, over a vanishingly small area. Since we are probing coherence over a finite distance $L \approx 15$ μm, at the critical point coherence cannot exist over this length. One expects that the momentum distribution peak P_0 should grow rapidly once a region of diameter L has become superfluid. This results in a shift $\Delta\tilde{\mu}$ in the apparent critical chemical potential:

$$\Delta\tilde{\mu} = \frac{1}{2k_\mathrm{B}T} m\omega_r^2 \left(\frac{L}{2}\right)^2. \tag{F.1}$$

For our trap parameters, this evaluates to $\Delta\tilde{\mu} \approx +0.05$.

In terms of the critical number ratio $\bar{N}_{\mathrm{c}}/N_{\mathrm{c}}^{0}$, a rough estimate comes from assuming that the shift in atom number associated with some chemical potential shift $\Delta\tilde{\mu}$ is dominated by atoms in the distribution wings, which are well-described by MF theory. We can then use the MF critical number expression of Eq. (4.17), evaluated at $\tilde{\mu} = \tilde{\mu}_{\mathrm{c}}$ and $\tilde{\mu} = \tilde{\mu}_{\mathrm{c}} + \Delta\tilde{\mu}$. This yields a positive shift in the critical number ratio of $\lesssim 0.2$.

Critical divergence of ξ As a normal gas approaches the BKT transition, the correlation length ξ diverges exponentially [51, 95],

$$\xi = \lambda_{\mathrm{th}} \exp\left(\sqrt{\frac{aT_{\mathrm{BKT}}}{T - T_{\mathrm{BKT}}}}\right), \tag{F.2}$$

where T_{BKT} is the critical BKT transition temperature, and a is a model-dependent dimensionless parameter. In our experiment this divergence corresponds to a sharp growth in P_0 as the transition is approached; in principle P_0 should still exhibit a discontinuous gradient at the BKT transition, but experimentally the diverging ξ makes detection of this change difficult and will shift the apparent critical temperature by ΔT.

It is worth pointing out that this critical divergence in ξ is entirely distinct from the rapid growth in a normal gas as phase-space density is increased[1]. The former divergence is 'pinned' to the BKT transition temperature, and would shift the apparent onset of coherence regardless of the phase-space density or $\tilde{g}$ in question. The latter represents a growth in ξ independent of any transition, and precludes reliable measurement of the transition if $\xi \gg L$ before the system is even close to criticality[2]. The two separate phenomena are illustrated in Fig. F.1.

We can estimate the criticality-induced shift by setting $a = 1$ and asking when $\xi = L$. This yields a fractional temperature shift $\Delta T/T_{\mathrm{BKT}} \approx 0.1$. The weak logarithmic dependence of ΔT upon L means that decreasing this criticality-induced shift to 1% would requires us to increase $(L/\lambda_{\mathrm{th}})$ by a factor of 10^3!

A positive fractional temperature shift of 0.1 corresponds to a negative shift in the critical phase-space density $\Delta\mathcal{D} \approx -0.1\mathcal{D}^{\mathrm{BKT}}$. Noting that the critical chemical potential is dominated by interaction energy and assuming fully suppressed fluctuations at the critical point, we can deduce a corresponding shift in $\tilde{\mu}_{\mathrm{c}}$:

$$\begin{aligned} \tilde{\mu}_{\mathrm{c}} &\approx \frac{\tilde{g}\mathcal{D}^{\mathrm{BKT}}}{2\pi}, \\ \implies \Delta\tilde{\mu}_{\mathrm{c}} &\approx -\frac{\tilde{g}}{2\pi} 0.1\mathcal{D}^{\mathrm{BKT}}, \end{aligned} \tag{F.3}$$

giving a shift of $\Delta\tilde{\mu}_{\mathrm{c}} \approx -0.05$ at our maximal $\tilde{g} = 0.5$. Fortuitously, this is comparable in magnitude and of opposite sign to our shift due to trap inhomogeneity, and so we expect these systematic shifts to approximately cancel each other.

---

[1] See Eq. (6.31).

[2] See Section 6.3.3.

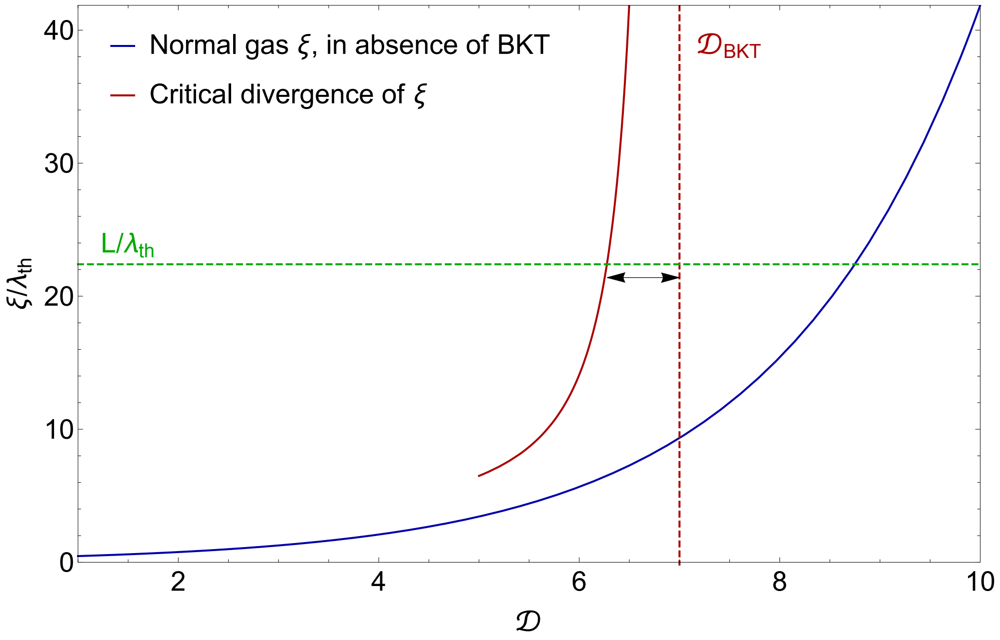

Figure F.1: *The behaviour of the correlation length* ξ *in the vicinity of the BKT transition, which occurs at phase-space density* $\mathcal{D}^{BKT}$ *(red dashed line). In the absence of any transition, the normal gas* ξ *grows exponentially with phase-space density* $\mathcal{D}$*. If* ξ *exceeds our experimentally-probed coherence lengthscale* L *(green dashed line) for* $\mathcal{D} < \mathcal{D}^{BKT}$*, reliable identification of the transition is precluded. However, regardless of the normal gas behaviour, in the vicinity of the BKT point* ξ *diverges and will always lead to an apparent shift in the critical point; this shift is illustrated by an arrow.*

Anharmonicity of planar potential The planar potential for both in-plane trapping and momentum focusing is provided by our ODT. The beam waist is 140 μm; in comparison the thermal diameter of a 170 nK cloud in a 38 Hz planar potential is 50 μm. The atoms therefore experience a small deviation from perfect harmonic trapping; there are two principle consequences to consider:

1. The atom number required for the central density to become critical is shifted relative to harmonic trapping.
2. The momentum focusing no longer provides a perfect mapping between initial momentum and final position.

We are interested in the order of magnitude of these shifts, and so consider an ideal gas case for simplicity. The critical atom number shift is calculated by numerically integrating the Bose distribution over our true ODT potential of crossed Gaussian beams at $\mu = 0$, and comparing the obtained atom number with the harmonic trap result; this method is outlined in [114], and gives a positive shift to the critical atom number of $\sim 10\%$.

Our fit functions for extraction of T and μ assume a harmonic focusing trap; the anharmonicity therefore leads to a shift in the measured values with respect to their true values. An ideal gas is invariant under momentum focusing; there are no interaction effects, and so switching off the axial trapping has no effect upon the planar distribution. We therefore simply populate our true ODT potential at $\mu = 0$ and a typical $T \approx 170$ nK, according to the Bose distribution for an ideal gas; this gives the atom distribution that would be obtained in an image. We then fit the distribution with an ideal gas model for a perfect harmonic trap, and compare the fitted μ and T with their true values.

Fortuitously, the two effects oppose each other; the actual critical number is increased, but the fitted temperature is higher than the true and so we normalise to an increased N_c^0. Overall, we obtain a shift in the critical chemical potential $\Delta\tilde{\mu}_\mathrm{c} \approx -0.04$, and atom number $\Delta(\bar{N}_\mathrm{c}/N_\mathrm{c}^0) \approx -0.01$.

Bibliography

[1] I. Bloch, J. Dalibard, and S. Nascimbene, Nature Physics **8**, 267 (2012).

[2] C. Chin, R. Grimm, P. Julienne, and E. Tiesinga, Rev. Mod. Phys. **82**, 1225 (2010).

[3] J. Dalibard, F. Gerbier, G. Juzeliūnas, and P. Öhberg, Rev. Mod. Phys. **83**, 1523 (2011).

[4] R. P. Feynman, International Journal of Theoretical Physics **21**, 467 (1982).

[5] M. H. Anderson *et al.*, Science **269**, 198 (1995).

[6] M. Greiner *et al.*, Nature **415**, 39 (2002).

[7] M. R. Matthews *et al.*, Phys. Rev. Lett. **83**, 2498 (1999).

[8] K. W. Madison, F. Chevy, W. Wohlleben, and J. Dalibard, Phys. Rev. Lett. **84**, 806 (2000).

[9] Z. Hadzibabic *et al.*, Nature **441**, 1118 (2006).

[10] J. Billy *et al.*, Nature **453**, 891 (2008).

[11] K. Baumann, C. Guerlin, F. Brennecke, and T. Esslinger, Nature **464**, 1301 (2010).

[12] C. Pethick and H. Smith, *Bose–Einstein Condensation in Dilute Gases* (Cambridge University Press, Cambridge, 2002).

[13] M. Zaccanti *et al.*, Nature Physics **5**, 586 (2009).

[14] D. J. Griffiths, *Introduction to Quantum Mechanics* (Prentice Hall, Englewood Cliffs, 1995).

[15] G. Roati *et al.*, Phys. Rev. Lett. **99**, 010403 (2007).

[16] R. L. D. Campbell *et al.*, Phys. Rev. A **82**, 063611 (2010).

[17] A. L. Gaunt, R. J. Fletcher, R. P. Smith, and Z. Hadzibabic, Nature Physics **9**, 271 (2013).

[18] R. J. Fletcher *et al.*, Phys. Rev. Lett. **111**, 125303 (2013).

[19] R. J. Fletcher *et al.*, Phys. Rev. Lett. **114**, 255302 (2015).

[20] S. Beattie, S. Moulder, R. J. Fletcher, and Z. Hadzibabic, Phys. Rev. Lett. **110**, 025301 (2013).

[21] S. Moulder, Ph.D. thesis, Cambridge, UK, 2013.

[22] J. P. D'Incao, H. Suno, and B. D. Esry, Phys. Rev. Lett. **93**, 123201 (2004).

[23] J. P. D'Incao, C. H. Greene, and B. D. Esry, Journal of Physics B: Atomic, Molecular and Optical Physics **42**, 044016 (2009).

[24] W. Li and T.-L. Ho, Phys. Rev. Lett. **108**, 195301 (2012).

[25] B. S. Rem *et al.*, Phys. Rev. Lett. **110**, 163202 (2013).

[26] S. Cowell *et al.*, Phys. Rev. Lett. **88**, 210403 (2002).

[27] J. L. Song and F. Zhou, Phys. Rev. Lett. **103**, 025302 (2009).

[28] Y.-L. Lee and Y.-W. Lee, Phys. Rev. A **81**, 063613 (2010).

[29] P. Makotyn *et al.*, Nature Physics **10**, 116 (2014).

[30] N. Navon *et al.*, Phys. Rev. Lett. **107**, 135301 (2011).

[31] *BCS-BEC Crossover and the Unitary Fermi Gas*, Vol. 836 of *Lecture Notes in Physics*, edited by W. Zwerger (Springer, Berlin, 2011).

[32] L. Yin, Phys. Rev. A **77**, 043630 (2008).

[33] S. K. Adhikari and L. Salasnich, Phys. Rev. A **77**, 033618 (2008).

[34] J. M. Diederix, T. C. F. van Heijst, and H. T. C. Stoof, Phys. Rev. A **84**, 033618 (2011).

[35] D. Borzov *et al.*, Phys. Rev. A **85**, 023620 (2012).

[36] F. Werner and Y. Castin, Phys. Rev. A **86**, 053633 (2012).

[37] L. Pricoupenko, Phys. Rev. Lett. **110**, 180402 (2013).

[38] Y. Castin and F. Werner, Canadian Journal of Physics **91**, 382 (2013).

[39] J. J. R. M. van Heugten and H. T. C. Stoof, arXiv:1302.1792 (2013).

[40] J. J. R. M. van Heugten and H. T. C. Stoof, arXiv:1306.1104 (2013).

[41] S. Piatecki and W. Krauth, Nature Communications **5**, (2014).

[42] S. B. Papp *et al.*, Phys. Rev. Lett. **101**, 135301 (2008).

[43] S. E. Pollack, D. Dries, and R. G. Hulet, Science **326**, 1683 (2009).

[44] R. J. Wild *et al.*, Phys. Rev. Lett. **108**, 145305 (2012).

[45] P. O. Fedichev, M. W. Reynolds, and G. V. Shlyapnikov, Phys. Rev. Lett. **77**, 2921 (1996).

[46] P. O. Fedichev, G. V. Shlyapnikov, and J. T. M. Walraven, Phys. Rev. Lett. **80**, 2269 (1998).

[47] H. Wu, E. Arimondo, and C. J. Foot, Phys. Rev. A **56**, 560 (1997).

[48] R. E. Peierls, Helv. Phys. Acta **7**, 81 (1934).

[49] N. D. Mermin and H. Wagner, Phys. Rev. Lett. **17**, 1133 (1966).

[50] J. M. Kosterlitz and D. J. Thouless, J. Phys. C: Solid State Physics **6**, 1181 (1973).

[51] Z. Hadzibabic and J. Dalibard, Rivista del Nuovo Cimento **34**, 389 (2011).

[52] J. V. Jose, *40 Years of Berezinskii-Kosterlitz-Thouless Theory* (World Scientific, Singapore, 2013).

[53] D. J. Bishop and J. D. Reppy, Phys. Rev. Lett. **40**, 1727 (1978).

[54] W. H. Nitsche *et al.*, Phys. Rev. B **90**, 205430 (2014).

[55] V. Schweikhard, S. Tung, and E. A. Cornell, Phys. Rev. Lett. **99**, 030401 (2007).

[56] P. Krüger, Z. Hadzibabic, and J. Dalibard, Phys. Rev. Lett. **99**, 040402 (2007).

[57] P. Cladé *et al.*, Phys. Rev. Lett. **102**, 170401 (2009).

[58] S. Tung *et al.*, Phys. Rev. Lett. **105**, 230408 (2010).

[59] S. P. Rath *et al.*, Phys. Rev. A **82**, 013609 (2010).

[60] T. Plisson *et al.*, Phys. Rev. A **84**, 061606 (2011).

[61] C.-L. Hung, X. Zhang, N. Gemelke, and C. Chin, Nature **470**, 236 (2011).

[62] T. Yefsah *et al.*, Phys. Rev. Lett. **107**, 130401 (2011).

[63] R. Desbuquois *et al.*, Nature Physics **8**, 645 (2012).

[64] J.-y. Choi, S. W. Seo, W. J. Kwon, and Y.-i. Shin, Physical Review Letters **109**, 125301 (2012).

[65] J.-y. Choi, S. W. Seo, and Y.-i. Shin, Physical Review Letters **110**, 175302 (2013).

[66] L.-C. Ha *et al.*, Phys. Rev. Lett. **110**, 145302 (2013).

[67] R. Desbuquois *et al.*, Phys. Rev. Lett. **113**, 020404 (2014).

[68] M. G. Ries *et al.*, Phys. Rev. Lett. **114**, 230401 (2015).

[69] O. Penrose and L. Onsager, Phys. Rev. **104**, 576 (1956).

[70] B. W. Anderson, Rev. Mod. Phys. **38**, 298 (1966).

[71] P. Kapitza, Nature **141**, 74 (1938).

[72] J. F. Allen and A. D. Misener, Nature **141**, 75 (1938).

[73] F. London, Nature **141**, 643 (1938).

[74] L. D. Landau, J. Phys. (USSR) **5**, 71 (1941).

[75] A. L. Fetter, Rev. Mod. Phys. **81**, 647 (2009).

[76] A. Griffin, D. W. Snoke, and S. Stringari, *Bose–Einstein Condensation* (Cambridge University Press, Cambridge, 1995).

[77] A. Einstein, Sitzungsberichte/Physikalische Klasse, Preussische Akademie der Wissenschaften **1**, 3 (1925).

[78] N. Tammuz *et al.*, Phys. Rev. Lett. **106**, 230401 (2011).

[79] R. P. Smith, R. L. D. Campbell, N. Tammuz, and Z. Hadzibabic, Phys. Rev. Lett. **106**, 250403 (2011).

[80] R. P. Smith *et al.*, Phys. Rev. Lett. **107**, 190403 (2011).

[81] N. N. Bogoliubov, J. Phys. (USSR) **11**, 23 (1947).

[82] C. Mora and Y. Castin, Phys. Rev. A **67**, 053615 (2003).

[83] Y. Kagan and B. V. Svistunov, Phys. Lett. A **79**, 3331 (1997).

[84] Y. Castin *et al.*, JOURNAL OF MODERN OPTICS **47**, 2671 (2000), 7th Meeting on Laser Phenomena, TYROL, AUSTRIA, JAN 16-21, 2000.

[85] M. J. Davis and P. B. Blakie, Phys. Rev. Lett. **96**, 060404 (2006).

[86] E. P. Gross, Il Nuovo Cimento **20**, 454 (1961).

[87] L. P. Pitaevskii, Sov. Phys. JETP **13**, 451 (1961).

[88] S. Nazarenko, M. Onorato, and D. Proment, Phys. Rev. A **90**, 013624 (2014).

[89] M. E. Fisher, M. N. Barber, and D. Jasnow, Phys. Rev. A **8**, 1111 (1973).

[90] V. L. Berezinskii, Soviet Physics JETP **32**, 493 (1971).

[91] V. L. Berezinskii, Soviet Physics JETP **34**, 610 (1972).

[92] M. Holzmann, G. Baym, J. P. Blaizot, and F. Laloë, P.N.A.S. **104**, 1476 (2007).

[93] M. Holzmann and G. Baym, Phys. Rev. B **76**, 092502 (2007).

[94] B. Josephson, Physics Letters **21**, 608 (1966).

[95] J. M. Kosterlitz, Journal of Physics C: Solid State Physics **7**, 1046 (1974).

[96] N. V. Prokof'ev, O. Ruebenacker, and B. V. Svistunov, Phys. Rev. Lett. **87**, 270402 (2001).

[97] N. Berloff and B. V. Svistunov, Physics **2**, 61 (2009).

[98] N. V. Prokof'ev and B. V. Svistunov, Phys. Rev. A **66**, 043608 (2002).

[99] M. Holzmann, M. Chevallier, and W. Krauth, Phys. Rev. A **81**, 043622 (2010).

[100] R. N. Bisset, M. J. Davis, T. P. Simula, and P. B. Blakie, Phys. Rev. A **79**, 033626 (2009).

[101] Z. Hadzibabic *et al.*, New Journal of Physics **10**, 045006 (2008).

[102] M. Holzmann and W. Krauth, Phys. Rev. Lett. **100**, 190402 (2008).

[103] T.-L. Ho and Q. Zhou, Nature Physics **6**, 131 (2010).

[104] M. Holzmann, M. Chevallier, and W. Krauth, Europhys. Lett. **82**, 30001 (2008).

[105] L. Chomaz *et al.*, Nature Communications **6**, (2015).

[106] C.-L. Hung, V. Gurarie, and C. Chin, Science **341**, 1213 (2013).

[107] S. T. Bramwell and P. C. W. Holdsworth, Phys. Rev. B **49**, 8811 (1994).

[108] I. Shvarchuck *et al.*, Phys. Rev. Lett. **89**, 270404 (2002).

[109] P. A. Murthy *et al.*, Phys. Rev. A **90**, 043611 (2014).

[110] A. L. Gaunt *et al.*, Phys. Rev. Lett. **110**, 200406 (2013).

[111] I. Bloch, Nature Physics **1**, 23 (2005).

[112] N. L. Smith *et al.*, Journal of Physics B **38**, 223 (2005).

[113] N. Tammuz, Ph.D. thesis, Cambridge, UK, 2011.

[114] R. L. D. Campbell, Ph.D. thesis, Cambridge, UK, 2011.

[115] D. S. Petrov, M. Holzmann, and G. V. Shlyapnikov, Phys. Rev. Lett. **84**, 2551 (2000).

[116] D. S. Petrov and G. V. Shlyapnikov, Phys. Rev. A **64**, 012706 (2001).

[117] W. Ketterle, D. S. Durfee, and D. M. Stamper-Kurn, in *Bose–Einstein condensation in atomic gases, Proceedings of the International School of Physics Enrico Fermi, Course CXL*, edited by M. Inguscio, S. Stringari, and C. Wieman (IOS Press, Amsterdam, 1999), p. 67.

[118] R. N. Bisset, D. Baillie, and P. B. Blakie, Phys. Rev. A **79**, 013602 (2009).

[119] C. J. Foot, *Atomic Physics* (Oxford University Press, Oxford, 2004).

[120] C. Ockeloen, A. Tauschinsky, R. Spreeuw, and S. Whitlock, Phys. Rev. A **82**, 061606 (2010).

[121] D. A. Tiecke (unpublished).

[122] J. Man, Master's thesis, Cambridge, UK, 2014.

[123] A. Dareau, Master's thesis, Cambridge, UK, 2010.

[124] N. Navon, A. L. Gaunt, R. P. Smith, and Z. Hadzibabic, Science **347**, 167 (2015).

[125] R. Loudon, *The Quantum Theory of Light* (Clarendon, Oxford, 1983).

[126] T. G. Steck (unpublished).

[127] T. Haugset, H. Haugerud, and J. O. Andersen, Phys. Rev. A **55**, 2922 (1997).

[128] V. S. Bagnato and D. Kleppner, Phys. Rev. A **44**, 7439 (1991).